HIGH-FIDELITY NUMERICAL SIMULATION AND EMULATION OF BI-FLUID SWIRL INJECTOR FLOW AND COMBUSTION DYNAMICS

A Dissertation
Presented to
The Academic Faculty

by

Yixing Li

In Partial Fulfillment
of the Requirements for the Degree
Doctor of Philosophy in the
School Aerospace Engineering

Georgia Institute of Technology
August 2019

HIGH-FIDELITY NUMERICAL SIMULATION AND EMULATION OF BI-FLUID SWIRL INJECTOR FLOW AND COMBUSTION DYNAMICS

Approved by:

Dr. Vigor Yang, Advisor
School of Aerospace Engineering
Georgia Institute of Technology

Dr. Joseph Oefelein
School of Aerospace Engineering
Georgia Institute of Technology

Dr. Timothy Lieuwen
School of Aerospace Engineering
Georgia Institute of Technology

Dr. Jeff Wu
School of Industrial & Systems Engineering
Georgia Institute of Technology

Dr. Lakshmi N Sankar
School of Aerospace Engineering
Georgia Institute of Technology

Dr. Xingjian Wang
School of Aerospace Engineering
Georgia Institute of Technology

Date Approved: April 29, 2019

“I lift up my eyes to the hills, from where does my help come? My help comes from the LORD, who made heaven and earth.”

Psalm 121:1-2 (ESV)

ACKNOWLEDGEMENTS

I would like to express my gratitude to my thesis advisor, Dr. Vigor Yang for his continuous help and support. His patience, motivation, enthusiasm and immense knowledge guided me in the course of my Ph.D. study. It has been a pleasant and memorable experience to work with him as one of his students, and I could not imagine having a better advisor and mentor for my Ph.D. study.

Besides my advisor, I want to thank the rest of my thesis committee: Dr. Timothy Lieuwen, Dr. Joseph Oefelein, Dr. Lakshmi Sankar, Dr. Jeff Wu and Dr. Xingjian Wang, for their encouragements, inspiring questions and insightful comments.

I am especially grateful to Dr. Xingjian Wang for his support and guidance, for kind help in coding, writing, and research. He has been a wonderful mentor and a great friend. I would also like to thank Dr. Yanxing Wang for many inspiring discussions and kind help.

I want to express my gratitude to my colleagues, Dr. Liwei Zhang, Dr. Prashant Khare, Dr. Dilip Sundaram, Dr. Yu-Hung Chang, Dr. Suo Yang, Dr. Shiang-Ting Yeh, Dr. Murali Gopal Muraleedharan, Dr. Chris Lioi, Umesh Unnikrishnan, Tim Dawson, Zhaoyi Xu, Bichuan Mo, Petro Milan, Haoxiang Huang; my collaborators from ISyE, Dr. Simon Mak, Dr. Chih-li Sung and Li-Hsiang Lin.

I would also like to thank my supervisors during my internship at Siemens, Dr. Frederic Villeneuve, Dr. Yan Guo and Dr. Tsz Ling Elaine Tang, for their guidance and help. Special thanks go to Dr. Frederic Villeneuve and Dr. Tsz Ling Elaine Tang, who have been always kind, always encouraging and always inspiring.

Thanks to my friends and family in Atlanta, including Jason Chen, Jasmine Shi, Bin Wu, Mengzhen Chen and Helga Wang, who sustained me with love, encouragements and support.

My deep appreciations belong to my parents, Wen Zeng and Jian Li, who have constantly loved me and unselfishly supported me, and also to my girlfriend Tutu Wang, for her constant love, patience and understanding.

Finally, thanks be to God who have loved me and prepared blessings and plans for me in ways that I could never imagine.

Table of Contents

LIST OF TABLES

LIST OF FIGURES

LIST OF SYMBOLS AND ABBREVIATIONS

a	flow strain rate
d	design parameters
D	mass diffusivity
Da	Damköhler number
E	specific total energy
e	specific internal energy
f	mixture fraction
h	specific enthalpy
H	number of training cases
k_l	reaction rate constant
$\dot{m}$	mass flow rate
MW	molecular weight
N	total number of species
p	pressure
Pr	Prandtl number
$\dot{q}$	heat release rate
q_i	heat flux in the direction of i
R_u	universal gas constant
SGS	subgrid scale
Sc	Schmidt number
t	physical time
T	temperature
u	velocity component
$U_{i,j}$	diffusive velocity of species i in j direction
$w_{i,new}$	weighting number of i-th case to new case
x	physical coordinate
X	flow field in matrix notation
Y_k	mass fraction of species k

Z	compressibility factor

Greek Symbols

β	POD coefficients
ρ	density
ρ_i	density of species i
σ	stress tensor
τ	viscous stress tensor
δ	Dirac delta
ϕ	POD modes
μ	molecular dynamic viscosity
ν_t	turbulent eddy viscosity
λ	thermal conductivity
$\dot{\omega}_i$	mass production rate of species i
χ	scalar dissipation rate

SUMMARY

Injectors are critical components of combustion devices in liquid-fueled propulsion systems. By controlling the atomization and mixing of propellants, injectors can affect combustion efficiency, combustion instabilities and engine lifespan. This work conducts a comprehensive study of the gas-centered liquid-swirl coaxial (GCLSC) injectors, operating at supercritical conditions, and is composed of two parts. The first part investigates flow and combustion dynamics of GCLSC injectors based on high-fidelity large eddy simulations (LES), and the second part presents a high-fidelity emulation framework for the prediction of spatiotemporally evovling flow field for both non-reacting and reacting cases in a significantly shorter turnaround time.

For the first part of the study, LES simulations are conducted to study supercritical fluid flow dynamics and combustion characteristics of GCLSC injectors. Gaseous oxygen is axially injected into the center post at a temperature of 687.7K, while kerosene is tangentially introduced into the coaxial annulus at a temperature of 492.2K. The operating pressure is 25.3 MPa, well above the thermodynamic critical points of the propellants involved. Multiple cases are simulated to study the influence of recess length on flow and combustion dynamics. Based on LES results, for non-reacting flows, detailed flow physics and structures are identified, followed by comprehensive analyses of key dynamic characteristics and corresponding mechanisms. The mechanisms include vortex shedding near the fuel injection slit, the shear layer instability in the recess region, and vortical expansion and merging in the taper region. For each case, mixing efficiency is quantified and compared. For reacting flows, the flow field is categorized into four regions: propellant

injection, flame initialization, flame development, and intensive combustion. Flow structures and the flame evolution are elaborated in detail. Moreover, the effects of the recess length on mixing, flow dynamics and combustion dynamics are investigated.

The second part presents a high-fidelity data-driven emulation framework, which utilizes training data from LES and enables flow field emulation in reasonable turnaround time. The framework employs common kernel-smoothed proper orthogonal decomposition (CKSPOD) as the surrogate model, which is able to extract dominant coherent flow structures through hadamard-based POD and kriging, and reconstruct them to predict the flow field of a new case. Significant improvements, including common grid interpolation and physics-based conditions, are incorporated to the this framework to accommodate the prediction of complicated mixing and combustion dynamics. In the current study, CKSPOD utilizes LES results of GCLSC injectors as training data, and recess length is chosen as the varying design parameter. The predicted flow fields from CKSPOD are evaluated, and the current framework is able to capture both intantaneous and time-averaged flow fields with high accuracy. Moreover, the improved CKSPOD presents uncertainty quantification (UQ) of the predicted flow field, providing a metric for model fit. The proposed framework is further extended to injector design and optimization, based on the objective functions of mixing efficiency and injector wall thermal protection. The current work significantly reduces the computational time for efficient survey of the design space, and will serve as a promising tool in the early design stages.

CHAPTER 1.

INTRODUCTION

1.1 Background and Motivation

Bi-fluid injectors are critical components of combustion devices for high-performance power generation and propulsion systems [1-4]. By controlling the injection, atomization and mixing processes of fuel and oxidizers, injectors are able to affect combustion efficiency, combustion dynamics and engine life cycle [5, 6].

The design of injectors is a sophisticated process that is dependent on numerous factors, including combustion efficiency, thermal protection of the device, the suppression of combustion instabilities, throttling capability, high affordability, high reliability, etc. Conventional design paradigm, with insufficient knowledge about the whole design space, demands a lot of trial and error tests in the resource-intensive detailed design stage. The development of F-1 rocket engine in the Apollo lunar-landing project, for example, conducted more than 1,300 components and engine tests to mitigate combustion instabilities, which results in tremendous design cost [7]. To remedy the limitations of the conventional design practices, in the current study, a thorough understanding of mixing and combustion characteristics under supercritical conditions is desired.

High-fidelity simulations can be employed to provide spatiotemporally evolving flow field that is otherwise difficult to obtain via either theoretical analyses or experiments [8, 9]. Numerical simulations of the high-pressure physicochemical processes occurring at supercritical combustion, on the other hand, pose a variety of challenges, which involve all

of the classical difficulties in simulating turbulent reacting flow, and the unique problems associated with thermodynamic non-ideality and transport abnormality for supercritical combustion. From the classical point of view, turbulent reacting flow is characterized with a broad range of length and time scales, including the time scales of chemical reactions and those of various turbulent motions. The scales of the former are dependent on the species concentration, temperature and pressure of the flow. They could be smaller than one nano-second or approach infinity (as for chemically frozen flow, i.e. non-reacting flow). For the latter, the time scales are highly dependent on the local flow dynamics and can range from an even smaller time scale (infinitely large Reynolds number) to infinity (as for stagnant reacting flow). The length scales ranges from the smallest Kolmogorov scales, the flamelet thickness, all the way to the characteristic length of a combustion chamber. The modeling of turbulent reacting flows are themselves open research issues at atmospheric pressures. Secondly, thermodynamic properties and transport properties behave abnormally at transcritical conditions as discussed above. As a result, compressibility effects (i.e., volumetric changes induced by pressure variations) and variable inertial effects (i.e., volumetric changes induced by heat addition and/or variable composition) play a dominant role in the flow evolution [10]. Thirdly, Reynolds number increases and the flame thickness decreases with increasing pressure. The reduction of Kolmogorov scale and flame thickness may change the turbulence / chemistry interaction mechanism and thus the flow evolution. Finally, the resolution of rapid variation of thermodynamic and transport properties requires extremely fine grid, and resultant the high density gradient also affects the turbulence anisotropy in this region and changes the flow characteristics.

Comprehensive reviews of the knowledge on supercritical mixing and combustion were given by [10] and [11].

With the challenges of high-fidelity numerical simulation of supercritical mixing / combustion in mind, if successfully implemented, the numerical framework is able to provide insights of flow dynamics and combustion characteristics that are otherwise difficult to obtain from either experiments or numerical simulations. On the other hand, the high-fidelity framework is also numerically expensive and time-consuming. A recent study applied Large Eddy Simulation (LES) to a 42-injector engine using a 70 M elements mesh. Although the authors described the mesh to be "relatively coarse", it nevertheless requires 100,000 CPU hours for the simulation of 1 ms [12]. When the high-fidelity simulation is employed to survey the whole design space, the total amount of resources required is formidable. An efficient surrogate model that is able to conduct flow field emulation with sufficient accuracy in reasonable turnaround time is desired.

A generic surrogate model, which conducts 'offline' model reduction based on the existing data, is able to reduce 'online' calculations and provide predictions with limited loss of accuracy [13, 14]. Surrogate models are categorized into data-fit models, projection-based models, and simplified models (or hierarchical models) [15]. Data-fit models are formulated directly from the data, utilizing interpolation or regression of simulation data to fit a model. They are nonintrusive, which means that the models treat high-fidelity models as "black-box", independent of any formulations or prerequisite assumptions. The modeling of dynamic evolution of flow field poses challenges to these approaches, as they are more suitable to predict aggregate variables. Simplified models are

extracted from high-fidelity models through simplification of physical assumptions or linearization. These approaches may retain more physics, but might not be available in all cases. Moreover, they require sophisticated simplification process. Projection-based models, which project high-fidelity model into a low-dimensional space, are able to retain the underlying structure of the high-fidelity data, but requires innovative algorithms and sophisticated calibrations to retain sufficient accuracy. The selection and appropriate calibration of surrogate models pose challenges to high-fidelity flow emulation

The complexity and challenges of high-fidelity simulation and emulation are outlined above. This dissertation represents an attempt to enhance understanding fluid dynamics of bi-fluid injectors at supercritical conditions, and develop efficient emulation tools for injector design.

1.2 Literature Review

1.2.1 High-Pressure Fluid Injection, Mixing and Combustion

Jet Injector

Researchers and scientists in Europe and the United States have conducted many studies on cryogenic fluid injection under supercritical conditions. Because the rocket engines developed in these countries primarily implement impinging jet injectors (F-1 engine for the Saturn V) or shear coaxial injectors (SSME and Vulcain engine). Extensively experimental studies were conducted to visualize the flow and flame structures using optical diagnostic techniques, including shadowgraph, excited CH, OH chemiluminescence, and planar laser induced fluorescence (PLIF) of OH. The extreme

operating conditions and working environment of contemporary rocket engines pose severe challenges on experimental measurements. In spite of limitations of flow visualization and data acquisition techniques, experimental efforts on the characteristics of propellant injection, mixing, and combustion processes at near-critical conditions have led to a better qualitative understanding of the fundamental mechanisms involved [16-20] in the last few decades.

It was found that shear-coaxial injection processes in liquid rocket engines exhibit two distinct modes of combustion. At subcritical pressures, injected liquid jets undergo the classical cascade of processes associated with atomization. Dynamic forces and surface tension promote the formation of a heterogeneous spray that evolves continuously. As a consequence, spray flames are formed and lifted away from the injector post in a manner consistent with the combustion mechanisms exhibited by local drop clusters. As the chamber pressure approaches or exceeds the critical pressure of a particular propellant, however, injected liquid jets undergo a transcritical change of state as interfacial fluid temperatures rise above the critical temperature of the local mixture. For this situation, diminished inter-molecular forces promote diffusion-dominated processes prior to atomization, and jets vaporize in the presence of exceedingly large thermophysical gradients. Well-mixed diffusion flames evolve and are anchored by small but intensive recirculation zones that exist in the shear-layers between adjacent propellant streams.

In parallel to experimental studies, attempts were made both theoretically and numerically to explore the underlying mechanisms of high-pressure fluid mixing and combustion. Oefelein and Yang [21] modeled two-dimensional mixing and combustion of

oxygen and hydrogen streams at supercritical conditions using large-eddy-simulation technique and outlined the fundamental difficulties associated with modeling mixing and combustion processes at near-critical conditions. Zong et al. [22] conducted a comprehensive numerical study of nitrogen injection and mixing under supercritical conditions. The model accommodates full conservation laws and general-fluid thermodynamics and transport phenomena. All the thermophysical properties were evaluated directly from fundamental thermodynamics theories over the entire regime of fluid states of concern. Furthermore, a unified treatment of numerical algorithms based on general fluid thermodynamics was established to improve computational accuracy and efficiency.

Oefelein [23] studied the thermal characteristics of oxygen/hydrogen shear-coaxial jet flames at supercritical pressure. Significant real-gas effects and transport anomalies occurs in colder regions of the flow, while ideal-gas thermodynamic and transport characteristics are dominant in the flame zone. The flame anchors itself in the interfacial region of high shear between the liquid oxygen core and annular hydrogen jet as shown in Figure 1.1. The vortical expansion of low-density hydrogen stream induces strong recirculating backflow in the vicinity of the LOX-post. Inside this recirculation zone is an unsteady stagnation point that provides the flame-holding mechanism. Zong and Yang [24] later studied near-field and flame dynamics of LOX/methane shear-coaxial injectors. The LOX/methane flame is anchored between two counter-rotating wake recirculating zones, unlike LOX/hydrogen flame close to the LOX jet boundary because of high-diffusivity of hydrogen.

The extinction limits of the flame generated around the LOX jet boundary were studied by Juniper et al. [25] by constructing a one-dimensional counterflow diffusion flame model. The results indicated that the flame was fairly stable in the near injector region and could not easily be extinguished by the strain rate, even at a very low hydrogen stream temperature. Since the typical strain rates encountered in rocket engines were insufficient to punch a hole in the flame, the edge of this diffusion flame sheet should be stabilized behind the lip of the LOX post. Following this suggestion, a two-dimensional simulation was performed to investigate the flame stabilization mechanism behind a step over a liquid reactant surface [26]. It was reported that the most influential parameter regarding flame stabilization was the height of the step with respect to the flame thickness. If the flame was thicker than the step, it could not remain in the recirculation zone behind the step and was readily blown off.

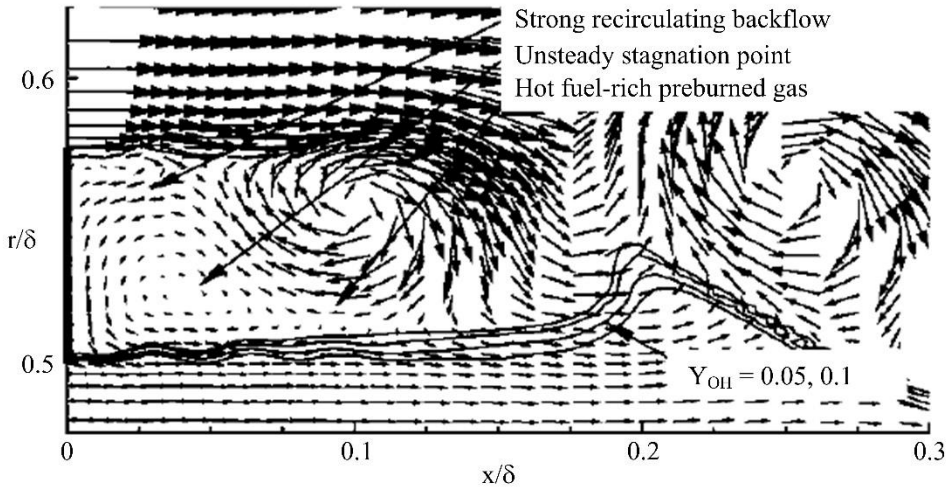

Figure 1.1 Schematic of flame-holding mechanism for oxygen-hydrogen shear-coaxial injection.

Masquelet et al. [27] simulated the LOX/H_2 combustion in a subscale multi-injector liquid rocket engine. A sub-grid eddy break-up (EBU) model was used to limit chemical

reaction rates with a mixing rate dependent on the dissipation rate of turbulent eddies. Heat flux along the chamber wall showed deviation from experiment measurements. Masquelet and Menon [28] later studied the GOX/GH_2 combustion of a single-element shear coaxial injector. Chemical reactions were calculated directly from the resolved temperature and species, without consideration of turbulence/chemistry interactions. The three-dimensional results captured the trend of heat flux profile of the experimental data, and were much better compared to their two-dimensional cases.

Swirl Injectors

Swirl injectors have recently drawn increasingly attention in the rocket community in US to achieve efficient mixing and combustion in many propulsion and power-generation systems [29, 30], especially those developed in Russia. The swirling motion can improve flame stability by producing toroidal recirculation zones and reduce combustion length by inducing high rates of the ambient fluid entrainment and fast mixing [4, 31]. Design of injectors highly affects the occurrences of combustion instability in the combustion chamber, because all feedback couplings of combustion chamber with other engine components take place through the injection process [5, 32].

Compared to jet injectors, swirl injectors in liquid-propellant rocket engines distinguish themselves in several aspects [33]. First, the non-uniform mixing of propellants in the jet core region is avoided and the intra-element mixing is significantly improved because of the outward spreading of the liquid spray. High mixing efficiency is, thus, possible even for a large injector flowrate. Second, the large flow passage in a swirl injector

renders the atomization characteristics to be less sensitive to manufacturing errors. The injector is also less susceptible to choking and cavitation. Third, the injected fluid is discharged into the chamber as a hollow spray cone. The thickness of the liquid film becomes thinner as it swirls and spreads outward. Most existing studies [34-37] on swirl injectors has focused on liquid film thickness, spray cone angle, liquid sheet breakup, and mixing efficiency under various controlling parameters such as backpressure and recess length. The fluid dynamics inside swirl injectors have been much less investigated.

Bazarov and Yang [5] applied linear theory to study the dynamics of swirl injectors and showed that the overall response function of a swirl injector can be represented by transfer characteristics of each individual element of the injector, the coupling of pressure and velocity pulsations in the tangential entries causes not only fluctuations of liquid free surface propagating at the speed of axial velocity component, but the energy disturbance in the form of fluctuations of circumferential velocity component propagating through the entire liquid layer in both the radial and axial directions. Richardson et al. [38] implemented a nonlinear model based on the boundary element method to evaluate the dynamic response of swirl injectors and compared their computational results with those of the linear theory [5]. Ismailov and Heister [39, 40] performed both analytical linear theory and nonlinear numerical computations to investigate wave reflection and resonance inside the swirl injector using abrupt convergence resonance model and conical convergence resonance model. Injector responses at resonant conditions behave as a quarter-wave oscillator. The dimensions of vortex chamber and mass flow rates have strong

effects on injector responses, while the nozzle convergence angle and nozzle length have negligible effects on injector responses.

The above studies were carried out under inviscid flow conditions. The pressure and temperature of working fluids were not explicitly specified. Thermodynamic properties of injection fluids and their variations at various pressures and temperatures were also not taken into account. Liquid rocket engines normally operate at pressures much higher than critical pressures of liquid propellants, hence accurate property evaluations are critical in numerical simulations. Cho et al. [41] conducted an experimental study on surface instability of cryogenic nitrogen swirling flow at both sub- and supercritical conditions. They found the different mechanisms of flow instability between cryogenic fluids and water swirl flows. The former is dominated by precessing vortex core (PVC) in the center-recirculation zone (CTRZ) while the latter is caused by Kelvin-Helmholtz instability. For the nitrogen swirling flow, the phase change and subsequent density change differs and flow characteristics, such as the behavior of the downstream flow, spray angle, wavelength, and propagation velocity, change dramatically when the ambient pressure varies from subcritical to supercritical conditions.

Zong and Yang [42] first studied cryogenic fluid dynamics of swirl injectors at supercritical conditions. Liquid oxygen (LOX) was injected tangentially into a simplex swirl injector and mixed with gaseous oxygen in the chamber in the two-dimensional axisymmetric flow configuration. The internal flow pattern was divided into three different regimes with distinct characteristics, developing, stationary, and accelerating regimes. Hydrodynamic instabilities in the LOX, acoustic waves in the gaseous core, shear layer

instabilities, and center recirculation zone induced by sudden expanding swirling film at the injector exit were identified and analyzed comprehensively. Huo et al. [43] further extended the study by imposing external forcing to pulsate the mass flow rate at the tangential inlet. External forcing drives the flow to fluctuate at its forcing frequency and suppresses other frequencies of fluctuations generated by the original non-pulsated flow. However, these axisymmetric studies failed to provide azimuthal variations of flow properties and three-dimensional vortex-stretching mechanism. The propagation of hydrodynamic waves in azimuthal direction was thus not included. Huo et al. [44] have shown that the importance of three-dimensional flow effects in the swirl injector, which motivates the present study.

Understanding the dynamics of swirling fluid injection is a prerequisite of exploring flow physics and flame dynamics of swirl coaxial injectors, which are actually encountered more frequently in practical applications. Various injector parameters and chamber conditions have been examined to explore the injector mixing and combustion characteristics [45-50]. Sasaki et al. [45] performed a cold experiment of water/nitrogen swirl coaxial injectors at room conditions. Special attention was given to the effect of the center post recess, which tends to narrow the spreading angle and cause a deformation of the spray cone. Han et al [47] investigated the recess effects of the center element on the mixing characteristics of a swirl coaxial injector using water and kerosene. Four different recess numbers in the range of 0.71-1.37, defined as the ratio of the recess length to the post thickness, were considered. The mixing efficiency and propellant mass distribution

were found to be very sensitive to the recess length. The Sauter mean diameter decreases slightly with increasing recess length and can be correlated with the empirical equations.

The aforementioned studies were conducted at low pressures without considering the effects of the elevated pressures typically encountered in operational liquid-propellant rockets engines. And most existing studies at high pressures have been focused on shear coaxial injectors using simple fluids, hydrogen and methane as fuel propellant. The investigation of swirl coaxial injectors using kerosene, which have been broadly used in Russian rocket engines such as RD-0110 and RD-107/108, are less-well documented in terms of experiments and numerical simulations.

Kim et al. [51] showed that as the recess length of injector post for a liquid oxygen (LOX)/kerosene bi-swirl injector increases the mechanism of propellants' mixing shifts from external mixing to internal mixing. The latter mechanism significantly improves the mixing and combustion efficiency. Ahn et al. [52, 53] conducted a set of experiments to study combustion characteristics of LOX/kerosene bi-swirl coaxial injectors at near-critical and transcritical conditions. They found that the longer injector recess promotes the interactions of propellants and improves combustion performance, and that the injector recess scarcely affects the pressure fluctuation at supercritical pressure while it might induce strong low-frequency combustion instability at subcritical pressure. The lack of flow visualization and enough data in these experimental studies restricts our understanding on detailed flame dynamics and flame-holding mechanism for swirl coaxial injectors at supercritical pressure.

Gas-centered Liquid-swirl Coaxial Injectors

Gas-centered liquid-swirl coaxial (GCLSC) injectors have been extensively used as main combustion chamber injectors in many oxidizer-rich staged-combustion cycle engines [54], such as in NK-33, RD-170 and RD-180 [55-57]. As sketched in Figure 1.2, High-temperature gaseous oxygen (GOX) is axially injected into the GOX post, and liquid kerosene is tangentially delivered into the outer annulus. GCLSC injectors offer excellent combustion efficiency and stability behaviors, and relatively simple configurations. Although these engines and their constituent injectors have been in service for decades, performance assessment and in-depth understanding of their fundamental mechanisms remains limited in the open literature, especially for practical operating conditions.

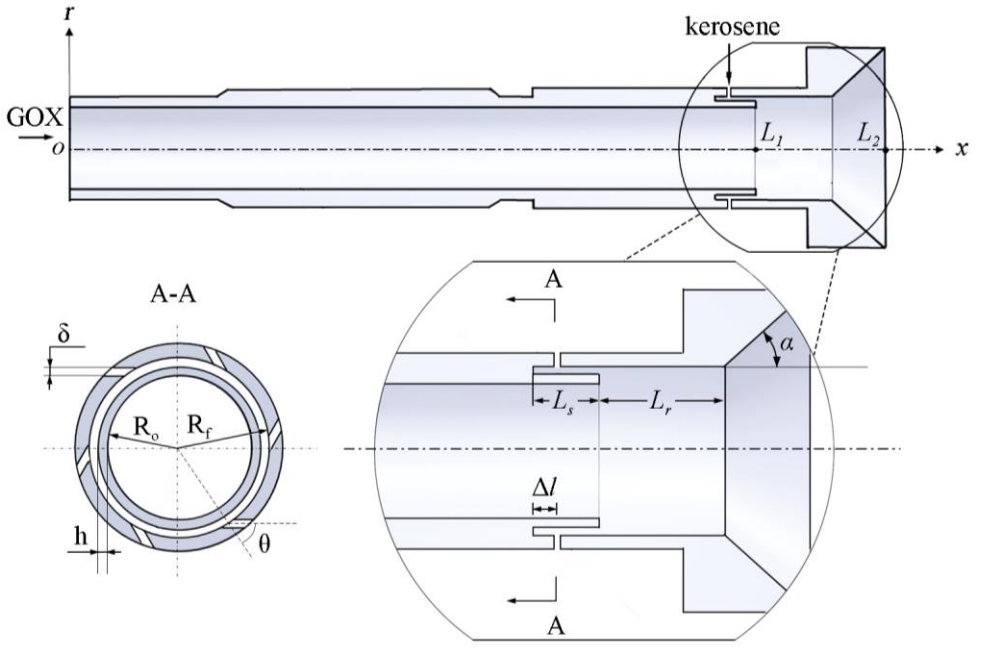

Figure 1.2 Schematic of Gas-Centered Liquid-Swirl Coaxial injector

A comprehensive literature review has been conducted to previous works on GCLSC injectors, as listed in Table 1.1. Soller et al. [58] investigated the combustion stability

characteristics in a subscale test facility. They found that the recess length L_r, defined as the distance between the end of the central post and the entrance of the taper region (or the entrance of the combustion chamber, if no taper is considered), plays a critical role in determining the acoustic dynamics of the chamber. Miller et al.[59] studied combustion dynamics by changing the combustor length. Lightfoot et al.[60] examined the spray behaviors of injectors with different mixing cups, and identified flow non-uniformities caused by disturbances in the upstream region. Schumaker et al.[61] found negligible impact of the mixing cup length on the liquid film thickness for the gas-to-liquid momentum flux ratio, *J*, over 400. Im et al.[50] compared the spray characteristics in a GCLSC injector and a liquid-centered, gas-swirl coaxial (LCGSC) injector, over a wide range of *J*. The spray angle was found to decrease with increasing *J* for the LCGSC injector, while the angle for the GCLSC injector initially decreases at relatively low *J* but the trend is reversed with high *J*. Kulkarni et al.[62] examined un-recessed GCLSC injectors.

Table 1.1 Studies on Gas-Centered, Liquid-Swirl Coaxial (GCLSC) injectors

References	Fluids	Cold or Reacting CFD or Experiment	Chamber Pressure
Soller et al. [58]	GOX/kerosene	reacting, expt	40-85 bar
Miller et al.[59]	superheated water and GOX/kerosene	reacting, expt	21-24 bar
Lightfoot et al.[60]	N_2/water	cold, expt	atmospheric
Schumaker et al.[61]	N_2/water	cold, expt	atmospheric
Im et al.[50]	air/water	cold, expt	atmospheric
Kulkarni et al.[62]	air/water	cold, expt	atmospheric
Jeon et al.[63]	N_2/water	cold, expt	atmospheric

Table 1.1 continued

Schummaker et al.[64]	N_2/water	cold, expt	atmospheric
Trask et al.[65]	N_2/water	cold, expt and 2D CFD	atmospheric
Kim et al.[66]	N_2/water	cold, expt	atmospheric and 59 bar
Matas et al.[67]	air/water	cold, expt and theoretical	atmospheric
Sisco et al.[68]	decomposed H_2O_2/JP-8	reacting, expt	28 bar
Morgan et al.[69]	decomposed H_2O_2/RP-1	reacting, expt and CFD	8-10 bar
Park et al.[70]	air/water	cold, expt	atmospheric

GOX: gaseous oxygen; MR: mixture ratio; J : gas-to-liquid momentum flux ratio

Many of the existing studies on GCLSC injector flow dynamics were performed with water and air/nitrogen as working fluids under atmospheric conditions, without consideration of the effects of the elevated pressure encountered in operational engines. As observed by Kim et al.,[66] however, the flow and mixing behaviors vary noticeably at high pressures. The present study aims to investigate the flow dynamics and mixing effectiveness of a GCLSC injector under supercritical conditions. The chamber pressure substantially exceeds the thermodynamic critical point of the fluid, in order to mimic the situations in practical rocket engines. The effect of recess length L_r on the injector evolution[71, 72] is examined.

1.2.2 Surrogate Model

Low-order surrogate models are categorized into data-fit models, projection-based models, and simplified models (or hierarchical models) [15], as review in the previous section. With features and limitations of each model in mind, this study employs projection-based models, which project high-fidelity model into a low-dimensional space. These models are able to retain the underlying structure of the high-fidelity data, and are applicable to the prediction of spatiotemporally evolving field. In the current study, the authors concentrate on projection-based methods that are dependent on proper orthogonal decomposition (POD), a well-accepted model reduction method that extracts spatial modes and corresponding temporal coefficients based on their energy norms.

One example of projection-based model is POD-Galerkin method [73, 74], which, as the name implies, applies Galerkin projection to the basis functions extracted by POD. This method reduces the number of equations, and transforms the governing equations from PDEs to ODEs. On the other hand, POD-Galerkin is intrusive, requiring additional sophisticated case-specific theoretical derivations and programming efforts to calibrate the ODEs, and some calibration techniques are based on the assumptions like ideal gas, non-reacting flow, etc. A non-intrusive model with greater flexibility is desired.

The applications of data-driven tools to projection-based models have been discussed in many works. In an early attempt, Ly et al. [75] applied POD to the temperature field in a Rayleigh–Bénard convection problem, and then uses a cubic spline interpolation to model and predict the POD coefficients. Audouze et al. [76] employed radial basis functions to model POD coefficients, and validated the proposed method against non-linear steady-state convection-diffusion-reaction problems. Mainini et al. [77] proposed a surrogate modeling

approach to support real-time structural assessment of an unmanned aerial vehicle, where POD coefficients are modelled by self-organizing maps and local response surface. The above works provide useful ideas on non-intrusive projection-based models, but are constrained by significant limitations. All the studies are based on either steady-state systems or time-evolving parameters, with limited work on spatiotemporally evolving flow field. Moreover, all the proposed methods focus on POD coefficients, with less concentration on POD modes, which will be problematic when applied to cases with complicated dynamics characteristics.

In our previous works, to address the aforementioned issues, a few POD-based high-fidelity emulation methodologies for the prediction of spatiotemporally evolving flow field have been proposed and tested. Yeh and colleagues [78, 79] proposed a data-driven framework, including key design parameter sensitivity analysis, physics-guided classification of design parameter set, and a novel flow evolution modeling technique, called Common Proper Orthogonal Decomposition (Common POD). Later, Chang et al. developed kernel-smoothed POD (KSPOD) [80]. Both methods are able to predict spatiotemporally evolving flow field, and detailed explanations of these method can be found in the referenced studies.

Recently, Chang et al [81] proposed CKSPOD, which combines advantages of CPOD and KSPOD, and outperforms both. The method extracts dominant coherent flow structures through hadamard-based POD, conducts kriging-based training of the POD coefficients, and then reconstructs the structures to predict the flow field of a new case. The referenced study validated CKSPOD based on nonreacting flow field of 30 simplex

swirl injectors, whose geometric parameters are selected by Design of Experiments (DOE). CKSPOD is able to predict spatiotemporally evolving flow field with high accuracy.

1.3 Research Objectives

The primary objective of this dissertation is to conduct a comprehensive study of bi-fluid injectors using LES-based simulation and POD-based emulation. The theoretical LES model is based on full-conservation laws of mass, momentum, energy, and species, and accommodates real-fluid thermodynamics and transport phenomena over the entire range of fluid states of concern. This work focus on both non-reacting and reacting flow of GCLSC injectors at supercritical conditions.

The complex non-reacting flow dynamics of GCLSC injectors are explored. Dominant flow structures are identified. Various underlying mechanisms dictating the flow evolution, including Kelvin-Helmholtz instability, centrifugal instability, shear layer roll-up, vortex pairing and their interactions are studied. A parametric study is performed to examine the influence of recess length on dynamic characteristics and mixing efficiencies, with special focus on fully recess and fully non-recessed injectors.

The combustion characteristics of GCLSC injectors are also numerically investigated. The entire flowfield can be divided into four regimes: propellant injection, flame initialization, flame development, and intensive combustion. The flame is anchored in the wake of the GOX post and further enhanced in the taper region, and the flame-holding mechanism is discussed in detail. The effects of recess length on flow and flame evolution are explored in depth.

The high-fidelity data-driven emulation framework that is able to predict spatiotemporally evolving flow field is proposed and validated. Common kernel-smoothed proper orthogonal decomposition (CKSPOD), a high-fidelity emulation technique, is employed as the surrogate model. Significant improvements, including common grid interpolation and physics-based conditions, are incorporated to accommodate the prediction of complicated flow dynamics and mixing characteristics. The framework is applied to predict non-reacting and reacting flow fields of GCLSC injectors. Detailed evaluations of the predicted flow fields are carried out, and the current framework is able to capture spatio-temporally evolving flow field, as well as the corresponding uncertainties. Good agreements are also observed for the time-averaged flow fields and mixing efficiencies.

Another objective of the current thesis is to propose a data-driven framework of combustion instability identification. Based on the traditional framework of identifying combustion instability through extraction and application of flame transfer function, this work proposes a novel method for the uncertainty quantification (UQ) of combustion instability. The method is implemented to estimate the UQ of thermoacoustic instability in a full-scale liquid rocket engine combustor, which comprises of 91 bi-swirl injectors burning kerosene and liquid oxygen. The tendency of each mode to become unstable is quantified and analyzed, and compared with results from traditional framework.

1.4 Dissertation Outline

The thesis is structured as follows. Chapter 2 describes the theoretical formulation and numerical framework of high-fidelity Large Eddy Simulation. Chapter 3 presents the numerical framework of the high-fidelity flow emulation, and the implemented surrogate model. Chapter 4 explores the flow dynamics of GCLSC injectors at supercritical conditions, as well as the underlying mechanisms and mixing characteristics. Combustion dynamics of GCLSC injectors at supercritical conditions are numerically investigated in Chapter 5. Chapter 6 applies the high-fidelity emulation framework to non-reacting GCLSC flow fields, and validated the framework using both spatiotemporally evolving flow field and time-averaged flow field. Chapter 7 applies high-fidelity emulation framework to reacting GCLSC flow fields, and extends the framework to injector design optimization based on the objective functions of mixing efficiency and injector wall thermal protection. Chapter 8 systematically investigates combustion instability identification framework and applies the framework to a 91 bi-injectors combustor. Conclusions of the current dissertation and recommendations for future works are provided in Chapter 9.

CHAPTER 2.

LARGE EDDY SIMULATIONS

2.1 Theoretical Formulation for Large Eddy Simulations

2.1.1 Governing Equations

The conservative equations of mass, momentum, energy, and species concentrations are employ as governing equations in the current study. In fluid mechanics, with assumption of continuum and negligible body forces, the differential questions for the governing equations are given by

$$\frac{\partial \rho}{\partial t} + \frac{\partial \rho u_i}{\partial x_i} = 0 \,, \tag{2.1}$$

$$\frac{\partial \rho u_i}{\partial t} + \frac{\partial (\rho u_i u_j)}{\partial x_j} = \frac{\partial \sigma_{ij}}{\partial x_j}, \quad (i = 1,\ 2,\ 3) \tag{2.2}$$

$$\frac{\partial \rho E}{\partial t} + \frac{\partial \left[(\rho E + p) u_i \right]}{\partial x_i} = -\frac{\partial q_i}{\partial x_i} + \frac{\partial (u_i \tau_{ij})}{\partial x_j}, \tag{2.3}$$

$$\frac{\partial \rho Y_k}{\partial t} + \frac{\partial \rho Y_k u_j}{\partial x_j} = \dot{\omega}_k + \frac{\partial \left(\rho D_k \nabla_j Y_k \right)}{\partial x_j}, \qquad (k = 1,\ \cdots,\ N\text{-}1) \tag{2.4}$$

Here, *i* and *j* are indices for spatial coordinates, *k* denotes species, and the repeated indices imply a summation. For a Newtonian fluid with Stokes' hypothesis, the viscous stress tensor, σ_{ij} in Eq. (2.2) is expressed as

$$\sigma_{ij} = -p\delta_{ij} + \tau_{ij} = -p\delta_{ij} + \mu \left(\frac{\partial u_i}{\partial x_j} + \frac{\partial u_j}{\partial x_i} \right) - \frac{2}{3} \mu \frac{\partial u_k}{\partial x_k} \delta_{ij} \,. \tag{2.5}$$

The Dufour effect, which is the heat flux due to concentration gradient, is generally very small and thus neglected in the current study. Then q_j in Eq. (2.3) is defined as

$$q_j = -\lambda \frac{\partial T}{\partial x_j} + \rho \sum_{k=1}^{N} \hat{h}_k Y_k U_{k,j} \ . \tag{2.6}$$

The specific total energy is defined as the sum of specific internal energy and kinetic energy, given by

$$E = e + \frac{u_j u_j}{2} \ , \tag{2.7}$$

where the specific internal energy is calculated from specific enthalpy, pressure, and density, given by

$$e = h - \frac{p}{\rho} \ , \tag{2.8}$$

where h is determined by the mixture concentration and partial-mass based enthalpies, $\hat{h}_k$, for which the definition will be given later.

$$h = \sum_{k=1}^{N} Y_K \hat{h}_k \ . \tag{2.9}$$

The chemical source term in Eq. (2.4) is determined from the selected chemistry kinetics. For an elementary reaction mechanism, with L-step reaction and N species,

$$\sum_{k=1}^{N} \boldsymbol{\nu'_{kl} \chi_k} \underset{k_{bl}}{\overset{k_{fl}}{\Leftrightarrow}} \sum_{k=1}^{N} \boldsymbol{\nu''_{kl} \chi_k} \ , \boldsymbol{l = 1, 2, \dots, L} \tag{2.10}$$

the reaction rate constants of the forward and backward reactions, k_{fl} and k_{bl}, may take the following form according to the modified Arrhenius's equation:

$$k_l\left(T\right) = A_l T^b \exp\left(-E_l / R_u T\right) . \tag{2.11}$$

The net production rate for each species in a multi-step mechanism is given by

$$\dot{\omega}_k = MW_k \sum_{i=1}^{L} \left(\nu''_{kl} - \nu'_{kl}\right) \left[k_{fl} \prod_{k=1}^{N} \left[x_k\right]^{\nu'_{kl}} - k_{bl} \prod_{k=1}^{N} \left[x_k\right]^{\nu''_{kl}} \right], \ \mathrm{k} = 1,\ 2,\ \ldots,\ N. \tag{2.12}$$

In non-premixed combustion studies, mixture fraction is an important conserved variable. In the current study, which is based on bi-fluid system, mixture fraction is defined as the ratio of the local mass originating from the fuel (denoted by 1) to total mass (with mass from the oxidizer stream denoted by 2),

$$Z = \frac{\dot{m}_1}{\dot{m}_1 + \dot{m}_2} . \tag{2.13}$$

It is worth mentioning that the definition of mixture fraction may be ambiguous when there are more than two multiple inlets, which is beyond the scope of the current study.

From Eq. (2.4) and Eq. (2.13), the transport equation for the mixture fraction is written as:

$$\frac{\partial \rho Z}{\partial t} + \frac{\partial (\rho u_j Z)}{\partial x_j} = \frac{\partial}{\partial x_j}\left(\rho D \frac{\partial Z}{\partial x_j}\right) . \tag{2.14}$$

2.1.2 Equation of State

In order to close the aforementioned governing equations, equations of states (EOS), thermodynamic and transport properties should be defined. Ideal-gas model is not capable of handling property evaluations over a large temperature range at high pressures, and an equation of state that is able to handle real fluid properties is desired. The thermodynamic and transport properties have to be evaluated in a consistent manner to provide a unified treatment. In this section, the selected equation of state is first presented, followed by a brief description of real-fluid thermodynamics treatment and the methodology to evaluate real fluid mixture transport properties.

The commonly used EOS for computing real-fluid properties under high-pressure conditions includes Benedict-Webb-Rubin (BWR) [82], Peng-Robinson (PR)[83], and Soave-Redlich-Kwong (SRK) [84]. All of them can predict thermodynamic properties of vapor and liquid phases with excellent accuracy. In the present study, SRK EOS is implemented to evaluate the derivative terms in thermodynamic relations, and BWR EOS accompanied with an extended corresponding state principle is used to estimate transport properties, which will be discussed in a later section. The formula of SRK EOS is given by,

$$p = \frac{\rho R_u T}{MW - b\rho} - \frac{a\alpha}{MW}\frac{\rho^2}{MW + b\rho} \tag{2.15}$$

where a and b account for the attractive and repulsive forces between molecules. α is a modeling parameter and a function of temperature and acentric factor. For a mixture, these parameters are expresses as,

$$a\alpha = \sum_{i=1}^{N}\sum_{j=1}^{N} x_i x_j \alpha_{ij} a_{ij} \tag{2.16}$$

$$b = \sum_{i=1}^{N} x_i b_i \tag{2.17}$$

where x_i is the mole fraction of species *i*. The product $\alpha_{ij} a_{ij}$ in Eq. (2.16) is given by,

$$\alpha_{ij} a_{ij} = \sqrt{\alpha_i \alpha_j a_i a_j}\,(1-\kappa_{ij}) \tag{2.18}$$

where κ_{ij} is the binary interaction coefficient. a_i , b_i, and other parameters are determined by critical properties and expressed as follows,

$$a_i = 0.42747 \frac{R_u^2 T_{ci}^2}{p_{ci}} \tag{2.19}$$

$$b_i = 0.08664 \frac{R_u T_{ci}}{p_{ci}} \tag{2.20}$$

$$\alpha_i = [1 + S_i(1-\sqrt{T_{ri}})]^2 \tag{2.21}$$

$$T_{ri} = \frac{T}{T_{ci}} \tag{2.22}$$

$$S_i = 0.48508 + 1.5517\omega_i - 0.15613\omega_i^2 \tag{2.23}$$

Here ω_i represents the acentric factor of species *i*. For hydrogen, to account for the quantum-gas behavior, Eq. (2.21) is modified as,

$$\alpha_{H_2} = 1.202 \exp(-0.30228 T_r) \tag{2.24}$$

This correlation is expected to be accurate for hydrogen at temperature higher than 83K, applicable in liquid rocket.

2.1.3 Thermodynamic Properties

Thermodynamic properties can be derived directly from fundamental thermodynamic relations, which are valid for all thermodynamic states. These properties are generally taken as the sum of the low-pressure limit value using ideal-gas model and a departure function accounting for the dense-fluid corrections at high pressures. Taking advantage of the path-independence of state properties, specific internal energy, enthalpy, entropy, and specific heat capacity can be calculated as:

$$e(T,\rho) = e_0(T) + \int_{\rho_0}^{\rho} \left[\frac{p}{\rho^2} - \frac{T}{\rho^2}\left(\frac{\partial p}{\partial T}\right)_{\rho} \right]_T d\rho, \tag{2.25}$$

$$h(T,\rho) = h_0(T) + \int_{p_0}^{p} \left[\frac{1}{\rho} + \frac{T}{\rho^2}\left(\frac{\partial \rho}{\partial T}\right)_{p} \right]_T dp, \tag{2.26}$$

$$s(T,\rho) = s_0(T,\rho_0) - \int_{\rho_0}^{\rho} \left[\frac{1}{\rho^2}\left(\frac{\partial p}{\partial T}\right)_{\rho} \right]_T d\rho, \tag{2.27}$$

$$C_p(T,\rho) = C_{V_0}(T) - -\int_{\rho_0}^{\rho} \left[\frac{T}{\rho^2}\left(\frac{\partial^2 p}{\partial T^2}\right)_{\rho} \right]_T d\rho + \frac{T}{\rho^2}\left(\frac{\partial p}{\partial T}\right)_{\rho}^2 \Bigg/ \left(\frac{\partial p}{\partial \rho}\right)_T . \tag{2.28}$$

The subscript 0 refers to an ideal state at low-pressure limit and the integral terms are the departure functions. All the partial derivatives in these functions can be estimated from SRK EOS, as written in the referenced study [85], and is not discussed in detail in the current study.

2.1.4 Transport Properties

In addition to the modification of thermodynamic properties, transport properties are needed to be evaluated accurately by taking into account high-pressure effects. As originally proposed by van der Waals in 1873, the law of corresponding states conclude that equilibrium properties can be related to the critical properties in a universal manner [86]. It expresses that the reduced *P-V-T* relationships are the same for all substances. The property of any fluid can be thus estimated by relating to its counterpart of a reference substance, whose properties can be easily obtained [87]. Chung et al.'s method [86], which also falls into the corresponding state theory category, is used in the current study to evaluate dynamic viscosity and thermal conductivity due to its good accuracy, relative simplicity, availability of parameters, and consistency. As for the binary mass diffusivity, as discussed by Poling et al. [86], there are only a few proposed methods to account for high-pressure effect on the diffusion coefficients, and the Takahashi method is used in the current study.

2.1.4.1 Dynamic Viscosity

According to Chung et al's method, dynamic viscosity of mixtures at high pressures are calculated based on the general formulations derived from elementary kinetic theory, as written below:

$$\mu_m = \mu^* \frac{36.344\left(MT_c\right)^{1/2}}{V_c^{2/3}} \ , \tag{2.29}$$

$$\mu^* = \frac{\left(T^*\right)^{1/2}}{\Omega_v}\left\{F_c\left[\left(G_2\right)^{-1} + E_6 y\right]\right\} + \mu^{**} \ , \tag{2.30}$$

$$y = \frac{\rho V_c}{6} \ , \tag{2.31}$$

$$G_1 = \frac{1-0.5y}{\left(1-y\right)^3} \ , \tag{2.32}$$

$$G_2 = \frac{E_1\left\{\left[1-e^{-E_4 y}\right]/\, y\right\} + E_2 G_1 e^{E_5 y} + E_3 G_1}{E_1 E_4 + E_2 + E_3} \ , \tag{2.33}$$

$$\mu^{**} = E_7 y^2 G_2 \exp\left[E_8 + E_9\left(T^*\right)^{-1} E_{10}\left(T^*\right)^{-2}\right] , \tag{2.34}$$

$$E_i = a_i + b_i\omega + c_i\mu_r^4 + d_i\kappa \ . \tag{2.35}$$

where the coefficients given by Table 2.1.

Table 2.1: Coefficients to calculate E_i in Eq. (2.35)

i	a_i	b_i	c_i	d_i
1	6.324	50.41	-51.68	1189
2	1.21×10^{-3}	-1.154×10^{-3}	-6.257×10^{-3}	0.03728
3	5.283	254.2	-168.5	3898
4	6.623	38.10	-8.464	31.42
5	19.75	7.630	-14.35	31.53
6	-1.900	-12.54	4.985	-18.15
7	24.28	3.450	-11.29	69.35
8	0.7972	1.117	0.01235	-4.117
9	-0.2382	0.06770	-0.8163	4.025
10	0.06863	0.3479	0.5926	-0.7270

Table 2.2: Coefficients to calculate E_i in Eq. (2.42)

i	a_i	b_i	c_i	d_i
1	2.4166E+0	7.4824E-1	-9.1858E-1	1.2172E+2
2	-5.0924E-1	-1.5094E+0	-4.9991E+1	6.9983E+1
3	6.6107E+0	5.6207E+0	6.4760E+1	2.7039E+1
4	1.4543E+1	-8.9139E+0	-5.6379E+0	7.4344E+1
5	7.9274E-1	8.2019E-1	-6.9369E-1	6.3173E+0
6	-5.8634E+0	1.2801E+1	9.5893E+0	6.5529E+1
7	9.1089E+1	1.2811E+1	-5.4217E+1	5.2381E+2

2.1.4.2 Thermal Conductivity

Thermal conductivity is derived in a similar manner. The final expression for thermal conductivity is given by:

$$\lambda = \frac{31.2\lambda^{\circ}\Psi}{M'}\left(G_2^{-1} + B_6 y\right) + qB_7 y^2 T_r^{1/2} G_2 \ . \tag{2.36}$$

With λ = thermal conductivity, W/(m·K)

λ° = low pressure gas viscosity, N·s/m

M' = molecular weight, kg/mol

$$q = 3.586 \times 10^{-3}(T_c M')^{1/2}/V_c^{2/3}$$

$$\Psi = 1 + \alpha\left\{\left[0.215 + 0.28288\alpha - 1.061\beta + 0.26665z\right]/\left[0.6366 + \beta z + 1.061\alpha\beta\right]\right\} \ , \tag{2.37}$$

$$\alpha = \frac{C_v}{R} - \frac{3}{2} \ , \tag{2.38}$$

$$\beta = 0.7862 - 0.7109\omega + 1.3168\omega^2 \ , \tag{2.39}$$

$$z = 2.0 + 10.5T_r^2 \ , \tag{2.40}$$

$$G_2 = \frac{(B_1 / y)\left[1 - e^{-B_4 y}\right] + B_2 G_1 e^{B_5 y} + B_3 E_1}{B_1 B_4 + B_2 + B_3} \ , \tag{2.41}$$

$$B_i = a_i + b_i\omega + c_i\mu_r^4 + d_i\kappa \ . \tag{2.42}$$

where the coefficients listed in Table 2.2.

2.1.4.3 Binary Mass Diffusivity

There are only a few estimation methods for binary mass diffusivity. In this study, lower-pressure values of binary mass diffusivity are evaluated with Fuller et al.'s empirical correlation, recommended by Poling et al. [86]. Then a very simple method, which is also a corresponding-state method, suggested by Takahashi is adopted in the current study to account for high-pressure effect.

At low pressures, the binary mass diffusivity is given by Fuller et al. [86],

$$D_{ij} = \frac{0.00143T^{1.75}}{pM_{ij}^{1/2}\left[(\Sigma_v)_i^{1/3} + (\Sigma_v)_j^{1/3}\right]^2} \ , \tag{2.43}$$

whereD_{ij} is binary mass diffusivity with unit of cm^2/s, Σ_v is found for each component by summing atomic diffusion volumes, which is tabulated in Poling et al. [86], Table 11-1). The data of interest are listed in Table 2.3.

Table 2.3: Diffusion volumes for selected atoms and molecules.

Atoms	Diffusion volume increments	Molecules	Diffusion volumes
C	15.9	O_2	16.3
H	2.31	Air	19.7
O	6.11	CO	18.0
N	4.54	CO_2	26.9
Aromatic Ring	-18.3	H_2O	13.1

Then high-pressure correction is evaluated based on Takahashi's correlation, which is given by:

$$\frac{D_{ij}\,p}{\left(D_{ij}\,p\right)^{+}} = f\left(T_r, p_r\right) , \tag{2.44}$$

where the superscript + indicates the low-pressure values given by Eq. (2.43). The function $f(T_r, p_r)$ represents a pressure scaling factor.

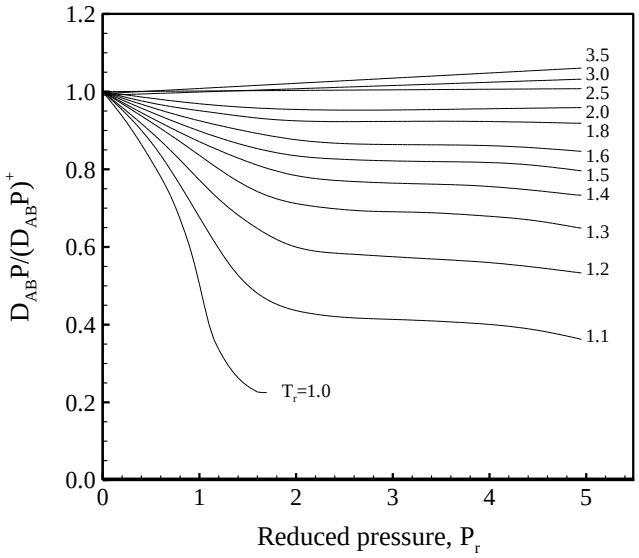

Figure 2.1 Correlation for high-pressure diffusivity using Takahashi method

The combining rules to calculate the reduced temperature and reduced pressure are given by:

$$T_c = x_i T_{c,i} + x_j T_{c,j} \ , \tag{2.45}$$

$$p_c = x_i p_{c,i} + x_j p_{c,j} \ . \tag{2.46}$$

2.1.5 Large Eddy Simulation and Turbulence Closure

Although turbulence has been studied for more than ten decades after Osborne Reynolds' experiments, it is still a big challenge in fluid mechanics due to its strong nonlinear behavior [88]. Numerical simulations of turbulent motions fall into three major categories: Direct Numerical Simulation (DNS), Reynolds-Aaveraged Navier-Stokes Equation Simulation (RANS), and Large-Eddy Simulation (LES) [89].

DNS is the most straightforward method. The governing equations are discretized with enough resolution and solved numerically; it resolves the smallest scales of motion and does not require any modeling. This makes it possible to compute and visualize any quantity of interest, and it has been a very useful research tool to obtain insight on detailed kinematics and dynamics of turbulent flows [90]. DNS has been applied to supercritical mixing layers [91, 92] and combustion studies [93] to reveal physical and/or chemical processes that would not have been possible with other approaches. The database created by DNS can be used to validate existing turbulent models and turbulent/combustion models. However, the implementation of DNS requires extensively computational resources. To resolve all scales of motion in three-dimensional space, the number of grid

points are proportional to $Re_L^{9/4}$, e.g., 9 billion grid points for Re_L = 10000. Therefore, DNS is limited to small Reynolds number flows and is infeasible for industry-interested applications.

In contrast to DNS, RANS has been commonly applied method to solve turbulent flow problems, especially in engineering applications. In RANS, only statistical quantities, i.e., the ensemble or time-averaged mean quantities are predicted. The effect of all the scales of motion is modeled (except for Unsteady-RANS, in which coherent motions are partially resolved) [89]. Although RANS is inherently less expensive and has moderate success in industrial applications, it fails to account for a very wide range of scales. Based on Kolmogorov's hypothesis, at sufficiently high Reynolds number, the small-scale motions are statistically isotropic and tend to be universal to model [94]. However, the large-scale motions are strongly dependent on flow conditions and geometric boundaries, thus it is impossible for RANS to achieve a universal model that can cover a range of scales in turbulent flows [88].

As a trade-off between the accuracy and computational cost of RANS and DNS, an intermediate technique known as Large-Eddy Simulation (LES) has been developed. LES features higher accuracy than RANS, while it requires much less computational effort compared to DNS. In LES, energy-containing large-scale motions are fully resolved with the grid and filter employed, while the effect of the smallest-scale motions of turbulence is modeled [88]. Since the small-scale motions are more isotropic and universal, they can be modeled in universal manner with much less adjustments in model coefficients, as

compared with the turbulent models for RANS simulations. The demanding computational cost to resolve all scales of motions explicitly and accurately in DNS is avoided.

In the current study, the LES technique is used to achieve turbulent closure. The small-scale motions are not resolved in LES; however, based on the energy cascade analysis, it is in this range of scales that viscous dissipations drain turbulent kinetic energy to internal energy. This part of turbulent motions has to be modeled with appropriate SGS models.

2.1.5.1 Filtered Governing Equations

In LES, large-scale motions, which carry most of the kinetic energy are fully resolved, while small-scale motions, which are more universal and appropriate to model, are simulated with SGS models. To separate the large-scale motions from the small-scale ones, a low-pass filtering operation is performed explicitly or implicitly. A filtered (or resolved) variable is defined as,

$$\tilde{f}(\boldsymbol{x}) = \int_{\infty} f(\boldsymbol{x}) G_f(\boldsymbol{x} - \boldsymbol{x}') d\boldsymbol{x}' , \tag{2.47}$$

where G is the filter function and satisfies $\int G(\boldsymbol{x}) d\boldsymbol{x} = 1$. The filter function determines the size and structure of the small scales. Leonard [95] indicated that if G is only a function of $\boldsymbol{x} - \boldsymbol{x}'$, the differentiation and filtering operations could commute with each other. Although for stretched grids, the commutation between filtering and differentiation is not strictly valid [96, 97], the commutation error is usually neglected for moderately stretched grids [98, 99]. The modeling error is found to be generally smaller than the discretization

error [98]. One of the most commonly used filter functions, the box filter, which is also employed in the current study, is defined as:

$$\bar{\boldsymbol{f}}(\boldsymbol{x}) = \frac{\mathbf{1}}{\boldsymbol{\Delta V}} \int \boldsymbol{f}(\boldsymbol{x}) \boldsymbol{dx} \,. \tag{2.48}$$

With the box filter, any filtered quantity is simply its average in the control volume. A detailed description of properties of various filters can be found in standard textbooks [94].

Based on the Favre-averaging [100], any instantaneous variable (f) can be expressed as the sum of a Favre-averaged filtered scale ($\tilde{f}$) and a sub-filter scale (f'')

$$\boldsymbol{f} = \tilde{\boldsymbol{f}} + \boldsymbol{f}'', \tag{2.49}$$

where

$$\tilde{f} = \frac{\overline{\rho f}}{\bar{\rho}} \,. \tag{2.50}$$

Since $\overline{f'} \neq 0$ and $\widetilde{f''} \neq 0$, the filtering operation in LES is different from the conventional Reynolds averaging in time domain. The filtered Favre-averaged mass, momentum, energy, mixture fraction, and progress variable transport equations in conservative form can be written as

$$\frac{\partial \bar{\rho}}{\partial t} + \frac{\partial \bar{\rho} \tilde{u}_i}{\partial x_i} = 0 \,, \tag{2.51}$$

$$\frac{\partial \bar{\rho}\tilde{u}_i}{\partial t}+\frac{\partial(\bar{\rho}\tilde{u}_i\tilde{u}_j)}{\partial x_j}=-\frac{\partial \bar{p}}{\partial x_i}+\frac{\partial(\tilde{\tau}_{ij}-\tau_{ij}^{SGS})}{\partial x_j}\ ,\ i=1,2,3, \tag{2.52}$$

$$\frac{\partial \bar{\rho}\tilde{E}}{\partial t}+\frac{\partial\left[(\bar{\rho}\tilde{E}+\bar{p})\tilde{u}_i\right]}{\partial x_i}=\frac{\partial}{\partial x_i}\left(\bar{q}_i+\tilde{u}_j\tilde{\tau}_{ij}-Q_i^{SGS}-H_i^{SGS}+\sigma_i^{SGS}\right), \tag{2.53}$$

$$\frac{\partial \bar{\rho}\tilde{f}}{\partial t}+\frac{\partial(\bar{\rho}\tilde{u}_j\tilde{f})}{\partial x_j}=\frac{\partial}{\partial x_j}\left(\bar{\rho}D\frac{\partial \tilde{f}}{\partial x_j}-\Phi_j^{SGS}\right), \tag{2.54}$$

$$\frac{\partial \bar{\rho}\tilde{C}}{\partial t}+\frac{\partial(\bar{\rho}\tilde{u}_j\tilde{C})}{\partial x_j}=\frac{\partial}{\partial x_j}\left(\bar{\rho}D\frac{\partial \tilde{C}}{\partial x_j}-\Psi_j^{SGS}\right)+\overline{\dot{\omega}_C}\ , \tag{2.55}$$

where the SGS terms are defined as:

$$\tau_{ij}^{SGS}=\overline{\rho u_i u_j}-\bar{\rho}\tilde{u}_i\tilde{u}_j\ , \tag{2.56}$$

$$Q_i^{sgs}=(\bar{q}_i-\tilde{q}_i)\ , \tag{2.57}$$

$$H_i^{SGS}=\left(\overline{\rho E u_i}-\bar{\rho}\tilde{E}\tilde{u}_i\right)+\left(\overline{pu_i}-\bar{p}\tilde{u}_i\right), \tag{2.58}$$

$$\sigma_{ij}^{SGS}=\left(\overline{u_j\tau_{ij}}-\tilde{u}_j\tilde{\tau}_{ij}\right), \tag{2.59}$$

$$\Phi_j^{SGS}=\left(\overline{\rho u_j f}-\bar{\rho}\tilde{u}_j\tilde{f}\right), \tag{2.60}$$

$$\Psi_j^{SGS}=\left(\overline{\rho u_j C}-\bar{\rho}\tilde{u}_j\tilde{C}\right). \tag{2.61}$$

The SGS stress term τ_{ij}^{SGS}, SGS energy flux term H_i^{SGS}, and SGS scalar flux terms Φ_j^{SGS}, and Ψ_j^{SGS}, result from filtering the corresponding convective terms. The SGS viscous work term σ_{ij}^{SGS}, comes from correlations of the velocity field with the viscous stress tensor. The resolved-scale progress variable production rate $\overline{\dot{\omega}_C}$, is also unclosed. The modeling of these SGS terms is discussed in detail in the following subsections.

In addition to the conservation equations, the equation of state must also be filtered. By introducing the compressibility factor, *Z*, the alternative form of EOS can be written as

$$p = \frac{Z\rho R_u T}{MW} = \rho R_u ZT \sum_{k=1}^{N} \frac{Y_k}{MW_k} \tag{2.62}$$

Filtering Eq. (2.62) gives us

$$\bar{p} = \bar{\rho} R_u \sum_{k=1}^{N} \frac{\tilde{Z}\tilde{T}\tilde{Y}_k}{MW_k} + \bar{\rho} R_u \sum_{k=1}^{N} \frac{ZTY_k - \tilde{Z}\tilde{T}\tilde{Y}_k}{MW_k} \tag{2.63}$$

For ideal gas without heat release, the correlations (second term in the right hand side) in the filtered equation of state can be neglected [101]. This may not be true for high-pressure, real-fluid mixtures. However, due to the difficulty and uncertainty in modeling those correlations, they are neglected without justification.

The filtered total energy, $\tilde{E}$ can be approximated as

$$\tilde{E} = \tilde{h} - \frac{\tilde{p}}{\bar{\rho}} + \frac{\tilde{u}_k^2}{2} + k^{SGS} = \tilde{\psi} + \int_{p_0}^{p} \left[\frac{1}{\rho} + \frac{T}{\rho^2} \left(\frac{\partial \rho}{\partial T} \right)_p \right] dp - \frac{\tilde{p}}{\bar{\rho}} + \frac{\tilde{u}_k^2}{2} + k^{SGS} \ , \tag{2.64}$$

where $\psi = \sum_{k=1}^{N} Y_k h_k^0$ and $k^{sgs} = \frac{\tau_{kk}^{SGS}}{2\bar{\rho}} = \frac{1}{2}\left(\frac{\overline{\rho u_k u_k}}{\bar{\rho}} - u_k^{\ 2} \right)$.

2.1.5.2 Subgrid-Scale Model

In LES, the unresolved motions of sub-grid scales have to be represented by an appropriate SGS model. Most of SGS models use the concept of eddy viscosity, ν_t, which

is similar to dynamic viscosity but generally with much higher value. Using eddy viscosity, the subgrid viscous shear stress can be written as,

$$\tau_{ij}^{SGS} - \frac{\delta_{ij}}{3}\tau_{kk}^{SGS} = -2\nu_t \tilde{S}_{ij} \ , \tag{2.65}$$

where $\tilde{S}_{ij}$ is the symmetric part of velocity gradient tensor, $\tilde{S}_{ij} = \frac{1}{2}\left(\partial\tilde{u}_i / \partial\tilde{x}_j + \partial\tilde{u}_j / \partial\tilde{x}_i\right)$. In this study, a compressible version of Smagorinsky model is employed.

The Smagorinsky SGS model [102] has been widely used because of its simplicity and good accuracy. The eddy viscosity is obtained algebraically to avoid solving additional equations. The model uses the equilibrium hypothesis, which claims that the small-scale motions with much short time scales can rapidly adjust to the flow perturbations and recover equilibrium nearly instantaneously. A balance equation between turbulent kinetic energy production and viscous dissipation thus exists: $-\tau_{ij}\tilde{S}_{ij} = \varepsilon_v$. Followed by this assumption, the Smagorinsky model is written as,

$$\nu_t = \left(C_S\bar{\Delta}\right)^2 \left|\tilde{S}\right| \ , \tag{2.66}$$

$$\left|\tilde{S}\right| = \sqrt{2\tilde{S}_{ij}\tilde{S}_{ij}} \ , \tag{2.67}$$

$$\bar{\Delta} = \sqrt[3]{\Delta_1\Delta_2\Delta_3} \ , \tag{2.68}$$

where $\bar{\Delta}$ is the filter width, proportional to the grid size. The coefficient C_s can be determined from a priori test on decaying isotropic turbulence [103] with C_s=0.16. Erlebacher et al. [104] extended the above model to compressible flows,

$$\tau_{ij}^{SGS} = -2\bar{\rho}\nu_t\left(\tilde{S}_{ij} - \frac{\delta_{ij}}{3}\tilde{S}_{kk}\right) + \frac{2}{3}\bar{\rho}k^{SGS}\delta_{ij}\ , \tag{2.69}$$

$$\nu_t = \left(C_R \Delta D\right)^2 \left|\tilde{S}\right|\ , \tag{2.70}$$

$$k^{SGS} = C_I(\Delta D)^2 \tilde{S}_{ij}\tilde{S}_{ij}, \tag{2.71}$$

where the dimensionless quantities C_R and C_I represent the compressible Smagorinsky constants. The Van-Driest damping function (D) is used to take into account the inhomogeneities near the wall [105], and is expressed as

$$D = 1 - \exp\left(-\left(y^+/25\right)^2\right), \tag{2.72}$$

where $y^+ = yu_\tau/\nu$ and u_τ is friction velocity.

The subgrid energy flux term H_j^{sgs} is modeled based on the gradient transport assumption

$$H_i^{SGS} = --\bar{\rho}\frac{\nu_t}{Pr_t}\frac{\partial\tilde{H}}{\partial x_i} = -\bar{\rho}\frac{\nu_t}{Pr_t}\left(\frac{\partial\tilde{h}}{\partial x_i} + \tilde{u}_j\frac{\partial\tilde{u}_j}{\partial x_i} + \frac{1}{2}\frac{\partial k^{SGS}}{\partial x_i}\right) \tag{2.73}$$

where Pr_t represents the turbulent Prandtl number, and a standard value 1.0 is used. The SGS viscous work term, σ_{ij}^{sgs}, is neglected due to its small contribution to the total energy equation [88, 106].

The convective mixture fraction flux term is usually approximated as

$$\Phi_j^{sgs} = -\bar{\rho}\frac{\nu_t}{Sc_t}\frac{\partial \tilde{f}}{\partial x_j} \tag{2.74}$$

where Sc_t is the turbulent Schmidt number. However, the use of the gradient transport assumption for reactive species is questionable.

The algebraic Smagorinsky model described above is the most widely used model in LES. However, as pointed out by Germano et al. [107], it has several limitations. First, the optimal model constant must be changed for a different class of flows. The model does not have the accurate limiting behavior near the wall [108]. The SGS stress does not vanish in laminar flow and the model is found to be very dissipative in the laminar/transition region. In addition, the model does not account for the backscatter of energy from small to large scale, which has been shown to be of importance in the transition region.

2.1.6 Turbulence Combustion Models

In LES, although the energy-carrying eddy motions are resolved with sufficient grid resolution, motions of small scales, such as the Kolmogorov scale, are not resolved, which plays a crucial role in reactant mixing at molecular levels. The chemical reaction rate is a very strong nonlinear function of local species concentration and temperature at the molecular level, which are highly dependent on the turbulent mixing. Chemical reactions release heat and alter species concentration and temperature gradients of the smallest turbulent eddies, which in turn change the turbulent mixing process. Chemical reaction occurring at different time scales may interact with turbulence eddies of different length/time scales, which further complicates the picture. The interaction of these two

processes occurs at length scales from the smallest turbulent scales to much larger inertial sub-range scales, which cannot be completely resolved in LES studies. The physical processes associated with these interactions are modeled with turbulent combustion models.

There are several combustion models for the LES of non-premixed turbulent combustion. The most straightforward way is to evaluate the filtered reaction rate from the filtered quantities, without consideration of the sub-grid interactions of turbulence and chemistry. This method has been used by several researchers due to the simplicity [21, 28].

Conditioned Momentum Closure (CMC) was developed by Klimenko [109] and Bilger [110] independently for non-premixed turbulent combustion. Variables of interest are conditioned with mixture fraction before the Favre averaging to obtain conditional moment equations. However, this method solves conditional species equations for all species; the computational cost increases with the number of species, which may become prohibitively costly when detailed chemical mechanism is involved. The Linear-Eddy Model (LEM) was developed by Kerstein [111, 112] has been used by the author, Menon and colleagues [113, 114]. The one-dimensional laminar reactive scalar field is combined with stochastically independent rearrangement events to mimic turbulence/chemistry interactions. However, this model suffers from prohibitive computational costs in applications. The Monte Carlo method for PDF transport equations was developed by Pope and extensively tested in RANS and LES [115]. However, the formulation is very complicated, and the computation cost is considerably high for even a moderate number of species. Dynamically thickened flame was developed by Légier et al. [116] for both

premixed and non-premixed combustion. This model can account for unsteady combustion such as extinction, re-ignition etc. However, it has similar difficulties when detailed chemistry is used. Flamelet concept proposed by Peters [115] has been extensively studied. In the current study, the steady flamelet model is employed in order to account for turbulence/chemistry interactions and identify the flame stabilization mechanism for supercritical combustion.

2.1.6.1 Basic Assumptions and Formulations for Flamelets

The basic assumption of the laminar flamelet model is that the chemical time scales are shorter than that of the smallest turbulent eddies: Kolmogorov scales. Consequently, a turbulent flame can be envisioned as a synthesis of thin reaction zones (i.e., flamelets) embedded in an otherwise inert turbulent flow field. The inner structure of the flame can be handled separately from turbulent flow simulations. Instead of directly treating the reactive scalar (i.e., species concentration), the focus is placed on the identification of the flame surface in the flow-field, which can be obtained by solving the conservation equation of the mixture fraction together with the mass, momentum, and energy equations.

The flame thickness is smaller than the grid size employed in LES and is not actually resolved. Therefore, the filtered species mass fraction of the i^{th} species, $\tilde{Y}_i(x,t)$, in each computational cell should be evaluated by convoluting the state relationships, $Y_i(f,\chi_{st})$, with the *SGS* Filtered Density Function (*FDF*) of mixture fraction, $\tilde{P}(f)$, and the *SGS FDF* of scalar dissipation rate, $\tilde{P}(\chi_{st})$, as shown below:

$$\tilde{Y}_i(x,t) = \int_0^1 \int_0^\infty Y_i(f, \chi_{st}) \tilde{P}(\chi_{st}) \tilde{P}(f) d\chi_{st} df . \quad (2.75)$$

It should be noted that a statistical independence is intrinsically assumed in Eq. (2.75) between the *SGS* variations of mixture fraction and scalar dissipation. The unresolved *SGS* fluctuation of the mixture fraction is commonly represented by a presumed β-shaped Probability Density Function (PDF) parameterized by the filtered mixture fraction and its *SGS* variance, which takes the following form,

$$\boldsymbol{P}\left(\boldsymbol{f};\ \tilde{\boldsymbol{f}}, \boldsymbol{f''^2}\right) = \frac{\boldsymbol{f}^{(\alpha-1)}(\boldsymbol{1}-\boldsymbol{f})^{\beta-1}}{\boldsymbol{\Gamma(\alpha)\Gamma(\beta)}} \boldsymbol{\Gamma(\alpha+\beta)} , \quad (2.76)$$

where Γ is the γ-function. The parameters α and β are defined as

$$\boldsymbol{\alpha} = \tilde{\boldsymbol{f}}\left(\frac{\tilde{\boldsymbol{f}}(\boldsymbol{1}-\tilde{\boldsymbol{f}})}{\boldsymbol{f''^2}} - \boldsymbol{1}\right) , \quad (2.77)$$

$$\boldsymbol{\beta} = (\boldsymbol{1}-\tilde{\boldsymbol{f}})\left(\frac{\tilde{\boldsymbol{f}}(\boldsymbol{1}-\tilde{\boldsymbol{f}})}{\boldsymbol{f''^2}} - \boldsymbol{1}\right) . \quad (2.78)$$

The *SGS* variance of mixture fraction, f''^2, is modeled based on the scale similarity assumption [117],

$$\boldsymbol{f''^2} = \boldsymbol{K_b}\overline{\boldsymbol{\rho}\left(\tilde{\boldsymbol{f}} - \tilde{\overline{\boldsymbol{f}}}\right)^2} / \overline{\boldsymbol{\rho}} , \quad (2.79)$$

where K_b is a model constant chosen as 3. It has been validated by many researchers that the β-function *PDF* provides an excellent estimation of the *SGS* mixture fraction distribution for non-premixed reacting turbulent flows [118]. For simplicity, the *SGS* FDF of the scalar dissipation rate, $\tilde{P}(\chi_{st})$, which is typically assumed to be a lognormal, is considered as a Dirac peak at the filtered scalar dissipation rate. Further investigation is

required to validate this assumption. The filtered rate of scalar dissipation, $\tilde{\chi}$, is modeled based on the eddy viscosity approach as suggested by Girimaji and Zhou [119]

$$\tilde{\chi} = 2(\frac{\nu}{Sc} + \frac{\nu_t}{Sc_t})(\frac{\partial f}{\partial x_j}\frac{\partial f}{\partial x_j}) \,. \tag{2.80}$$

The thermo-chemistry state relation is established through a steady-state flamelet approach. Taking advantage of the fact that the flamelet library only needs to be calculated once for every specified case, chemistry kinetics with any number of species and reaction steps can be used for the establishment of the flamelet library. The flamelet library should cover a broad range of strain rates, from near chemistry equilibrium to near-extinction limit. For all the calculations, the pressure is fixed at the same as the application; and the inlet temperatures of the fuel and oxidizer take the corresponding inlet temperature of the application cases. Consistent with the flamelet assumption, the corresponding scalar dissipation rate, χ, for each solution is evaluated as a function of filtered mixture fraction. The solutions are then integrated based on Eq. (2.75) and tabulated as functions of $\tilde{\chi}$, $\tilde{f}$, and f''^2. The calculated filtered mixture fraction, mixture fraction variance, and the scalar dissipation rate from LES simulation are used to determine the appropriate entry in the table.

Although the laminar flamelet method is easy to implement and fairly inexpensive, it has several drawbacks. Firstly, the mixture fraction essentially does not carry information about the chemical reaction state. The flamelet method uses the scalar dissipation rate as an additional parameter to account for the flame stretching and quenching effect. However,

the scalar dissipation rate does not provide a unique mapping from the mixture fraction to the corresponding chemical state. A pure mixing of fuel and oxidizer cannot be accounted for in the flamelet method if the local scalar dissipation is smaller than the quenching limit. This drawback is due to the lack of information regarding the local chemical state in the flow field. The Flamelet/Progress-Variable (FPV) method is able to overcome the limitations of the flamelet method by incorporating an additional transport equation for tracking a scalar in the form of a progress variable. This method has been developed to account for extinction, ignition, and unsteady mixing effect [120]. It will be interesting to examine the performance of these two methods in the future work

2.2 Numerical Framework for Large Eddy Simulations

In the current work, the numerical framework, with a pre-conditioning scheme and a unified treatment of real-fluid thermodynamic properties, is capable of solving the three dimensional governing equations in a general curvilinear coordinate system. The solver uses finite volume approach with structured grid system. It employs a density-based finite-volume methodology along with a dual-time-stepping integration technique, with a Runge-Kutta integration in pseudo-time iterations. Temporal discretization is achieved using a second-order backward difference scheme, and the inner loop pseudo-time term is integrated with a four-step Runge-Kutta scheme. Spatial discretization is obtained by a fourth-order central difference scheme in generalized coordinates. A fourth-order matrix dissipation is employed to ensure numerical stability with a minimal contamination of the solution. A multi-block domain decomposition technique with message passing interfaces

at domain boundaries is used to facilitate parallel programming and optimize computational speed.

2.2.1 Preconditioning Scheme for Real-Fluid Mixtures

The three-dimensional, unsteady, Favre-filtered governing equations listed in the previous section can be re-written in a vector form:

$$\frac{\partial \mathbf{Q}}{\partial t}+\frac{\partial\left(\mathbf{E}-\mathbf{E}_{\mathbf{v}}\right)}{\partial x}+\frac{\partial\left(\mathbf{F}-\mathbf{F}_{\mathbf{v}}\right)}{\partial y}+\frac{\partial\left(\mathbf{G}-\mathbf{G}_{\mathbf{n}}\right)}{\partial z}=\mathbf{H}, \tag{2.81}$$

where the vectors $\mathbf{Q, E, F, G, E_n, F_v, G_n,}$ and $\mathbf{H}$ are defined as:

$$\mathbf{Q}=\left(\bar{\rho}, \bar{\rho}\tilde{u}, \bar{\rho}\tilde{v}, \bar{\rho}\tilde{w}, \bar{\rho}\tilde{E}, \bar{\rho}\,\tilde{f}\right)^{T}, \tag{2.82}$$

$$\mathbf{E}=\left(\bar{\rho}\tilde{u}, \bar{\rho}\tilde{u}^{2}+\bar{p}, \bar{\rho}\tilde{u}\tilde{v}, \bar{\rho}\tilde{u}\tilde{w}, \left(\bar{\rho}\tilde{E}+\bar{p}\right)\tilde{u}, \bar{\rho}\tilde{u}\tilde{f}\right)^{T}, \tag{2.83}$$

$$\mathbf{F}=\left(\bar{\rho}\tilde{v}, \bar{\rho}\tilde{u}\tilde{v}, \bar{\rho}\tilde{v}^{2}+\bar{p}, \bar{\rho}\tilde{v}\tilde{w}, \left(\bar{\rho}\tilde{E}+\bar{p}\right)\,\tilde{v}, \bar{\rho}\tilde{v}\tilde{f}\right)^{T}, \tag{2.84}$$

$$\mathbf{G}=\left(\bar{\rho}\tilde{w}, \bar{\rho}\tilde{u}\tilde{w}, \bar{\rho}\tilde{v}\tilde{w}, \bar{\rho}\tilde{w}^{2}+\bar{p}, \left(\bar{\rho}\tilde{E}+\bar{p}\right)\tilde{w}, \bar{\rho}\tilde{w}\tilde{f}\right)^{T}, \tag{2.85}$$

$$\mathbf{E}_{v}=\begin{pmatrix} 0, \bar{\tau}_{xx}-\tau_{xx}^{sgs}, \bar{\tau}_{xy}-\tau_{xy}^{sgs}, \bar{\tau}_{xz}-\tau_{xz}^{sgs}, \tilde{u}\bar{\tau}_{xx}+\tilde{v}\bar{\tau}_{xy}+\tilde{w}\bar{\tau}_{xz}+\bar{q}_{x}-H_{x}^{sgs}+\sigma_{x}^{sgs}, \\ \bar{\rho}D\tilde{f}_{x}+\bar{\rho}\dfrac{\nu_{t}}{Sc_{t}}\,\tilde{f}_{x} \end{pmatrix}^{T}, \tag{2.86}$$

$$\mathbf{F}_{v}=\begin{pmatrix} 0, \bar{\tau}_{xy}-\tau_{xy}^{sgs}, \bar{\tau}_{yy}-\tau_{yy}^{sgs}, \bar{\tau}_{yz}-\tau_{yz}^{sgs}, \tilde{u}\bar{\tau}_{xy}+\tilde{v}\bar{\tau}_{yy}+\tilde{w}\bar{\tau}_{yz}+\bar{q}_{y}-H_{y}^{sgs}+\sigma_{y}^{sgs}, \\ \bar{\rho}D\tilde{f}_{y}+\bar{\rho}\dfrac{\nu_{t}}{Sc_{t}}\,\tilde{f}_{y} \end{pmatrix}^{T}, \tag{2.87}$$

$$\mathbf{G}_v = \begin{pmatrix} 0, \bar{\tau}_{xz} - \tau_{xz}^{sgs}, \bar{\tau}_{yz} - \tau_{yz}^{sgs}, \bar{\tau}_{zz} - \tau_{zz}^{sgs}, \tilde{u}\bar{\tau}_{xz} + \tilde{v}\bar{\tau}_{yz} + \tilde{w}\bar{\tau}_{zz} + \bar{q}_z - H_z^{sgs} + \sigma_z^{sgs}, \\ \bar{\rho} D\tilde{f}_z + \bar{\rho}\dfrac{\nu_t}{Sc_t}\tilde{f}_z \end{pmatrix}^T , \qquad (2.88)$$

$$\mathbf{H} = \left(0,0,0,0,0,0\right)^T , \qquad (2.89)$$

where the superscript T stands for the transpose of the vector.

There are two severe numerical challenges in solving these equations for high-pressure mixing and combustion. First, thermodynamic non-idealities and transport anomalies take place as the fluid transits from subcritical to supercritical conditions. Treating these abnormal changes in a manner consistent with the intrinsic characteristics of the numerical algorithm presents a major obstacle. Second, the rapid variation of the fluid state and wide range of characteristic time and length scales pose the well-known stiffness problem. The stiffness of the system results from: 1) ill-conditioned eigenvalues; 2) competing convective and diffusion processes; and 3) pressure singularities in the momentum equation.

The Mach number in present simulations is relatively small, and thus the dynamic pressure is negligibly smaller than the static pressure (high-pressure situations). This could cause the computer round-off error override the dynamic pressure in the momentum equation, i.e., the pressure singularity problem. To overcome this difficulty, the static pressure is decomposed into a constant reference pressure and a gauge pressure [121, 122],

$$p = p_0 + p_g \ . \qquad (2.90)$$

Here the averaged pressure in the flowfield is generally selected as the reference pressure, while the gauge pressure is the fluctuating part induced by unstable flow motions.

With this decomposition, p is replaced with p_g in the momentum equations. To solve the ill-conditioned eigenvalue problem, let us look at the following equations:

$$\frac{\partial \boldsymbol{Q}}{\partial \boldsymbol{t}} + \mathbf{A}\frac{\partial \boldsymbol{Q}}{\partial \boldsymbol{x}} + \mathbf{B}\frac{\partial \boldsymbol{Q}}{\partial \boldsymbol{y}} + \mathbf{C}\frac{\partial \boldsymbol{Q}}{\partial \boldsymbol{z}} = 0 \,, \tag{2.91}$$

where $\mathrm{A} = \frac{\partial \mathrm{E}}{\partial \mathrm{Q}}$, $\mathrm{B} = \frac{\partial \mathrm{F}}{\partial \mathrm{Q}}$, and $\mathrm{C} = \frac{\partial \mathrm{G}}{\partial \mathrm{Q}}$ are the Jacobian matrices. Analysis shows that the eigenvalues of matrix **A** is:

$$\lambda_1 = \tilde{u} + \tilde{c}, \lambda_2 = \tilde{u} - \tilde{c}, \lambda_{3,4,5,6} = \tilde{u} \,. \tag{2.92}$$

In low Mach number flows, $\mathrm{M} \ll 1$, the ratio of the largest eigenvalue to the smallest one is close to inverse of Mach number, indicating that the eigenvalues are order of magnitude different. For a given CFL number, the maximum local time step determined by the largest eigenvalue hence is extremely small, resulting in a very slow convergence. It becomes unacceptable for even lower-Mach number or time accurate simulations.

To cure the eigenvalue disparity problem in low Mach number flows, the time-derivative preconditioning method [121-124] are implemented associated with the methodologies developed by Meng and Yang [125] for handling general fluid thermodynamics, to take full account of the thermodynamic non-idealities and transport anomalies in the whole fluid state of concern. Zong and Yang [126] made further improvement by changing primitive variable *h* to *T*, getting rid of the cost intensive computation associated with iterative calculations to get temperature from enthalpy. A

unified treatment of thermodynamic properties and associated preconditioning matrix makes the numerical scheme accurate, robust, and efficient.

The basic idea of the preconditioning method is to add a pseudo time differential term in Eq. (2.81), with multiplication factor of a preconditioning matrix:

$$\Gamma \frac{\partial \mathbf{Z}}{\partial t} + \frac{\partial \mathbf{Q}}{\partial t} + \frac{\partial \left(\mathbf{E} - \mathbf{E}_{\mathbf{v}} \right)}{\partial x} + \frac{\partial \left(\mathbf{F} - \mathbf{F}_{\mathbf{v}} \right)}{\partial y} + \frac{\partial \left(\mathbf{G} - \mathbf{G}_{\mathbf{n}} \right)}{\partial z} = \mathbf{H}, \tag{2.93}$$

$$\mathbf{Z} = \left(\bar{\mathbf{p}}_{\mathbf{g}}, \tilde{u}, \tilde{v}, \tilde{w}, \tilde{T}, \tilde{f} \right)^{T} . \tag{2.94}$$

If Γ is chosen carefully so that the eigenvalues of these matrixes are of the same order of magnitude, the resulting equations have well-conditioned eigenvalues and converge efficiently in all Mach number flows. When pseudo time approaches infinity, (steady state solutions are achieved with respect to pseudo time), the original governing equations are recovered. It can be seen that the efficiency of preconditioning method is largely determined by the selection of the preconditioning matrix.

Following Zong [127], the transfer matrix is derived as:

$$T = \frac{\partial \mathbf{Q}}{\partial \mathbf{Z}} . \tag{2.95}$$

In this matrix, a common term $\left(\frac{\partial \mathrm{p}}{\partial \rho} \right)_{\mathrm{T,Y_i}}$ can be related to speed of sound and specific heat capacity ratio:

$$\left(\frac{\partial\rho}{\partial p}\right)_{T,Y_i} = \frac{C_p}{C_v}\left(\frac{\partial\rho}{\partial p}\right)_{s,Y_i} = \frac{\gamma}{a^2} \ . \tag{2.96}$$

a^2 is replaced with β to define the preconditioning matrix,

$$\Gamma = \begin{pmatrix} \frac{\gamma}{\beta} & 0 & 0 & 0 & \rho_T & \rho_f \\ \frac{\gamma}{\beta}\tilde{u} & \bar{\rho} & 0 & 0 & \tilde{u}\rho_T & \tilde{u}\rho_f \\ \frac{\gamma}{\beta}\tilde{v} & 0 & \bar{\rho} & 0 & \tilde{v}\rho_T & \tilde{v}\rho_f \\ \frac{\gamma}{\beta}\tilde{w} & 0 & 0 & \bar{\rho} & \tilde{w}\rho_T & \tilde{w}\rho_f \\ \frac{\gamma}{\beta}\tilde{h}_t + \frac{\tilde{T}}{\bar{\rho}}\rho_T & \bar{\rho}\tilde{u} & \bar{\rho}\tilde{v} & \bar{\rho}\tilde{w} & \bar{\rho}c_p + h_t\rho_T & \rho_f E + \bar{\rho}E_f \\ \frac{\gamma}{\beta}\tilde{f} & 0 & 0 & 0 & \rho_T\tilde{f} & \bar{\rho} + \tilde{f}\rho_f \end{pmatrix}, \tag{2.97}$$

where $\tilde{h}_t$ is the total specific enthalpy, $\rho_T = \left(\partial\rho/\partial T\right)_{p,y_i}$, $\rho_f = \partial\rho/\partial f$, and $E_f = \partial E/\partial f$.

β is defined as

$$\beta = \frac{\gamma\varepsilon a^2}{1+(\gamma-1)\varepsilon} \ , \tag{2.98}$$

where ε $(0 < \varepsilon \le 1)$ is the preconditioning factor. Unlike the definition of preconditioning matrix by other researchers, all of the off-diagonal terms in Eq. (2.97) have been retained. By keeping these terms, the unaltered system is identically restored as $\varepsilon \to 1$;

$$\lim_{\varepsilon\to 1}\Gamma = T \ . \tag{2.99}$$

The conditioned governing equations in the pseudo-time space are characterized by the new Jacobian matrices, $\Gamma^{-1}A_v$, $\Gamma^{-1}B_v$, and $\Gamma^{-1}C_v$, the eigenvalues of which are given by:

$$\begin{aligned}
\lambda_1 &= \frac{1}{2}[U(\varepsilon+1)+\sqrt{U^2(1-\varepsilon)^2+4\varepsilon a^2}]\,, \\
\lambda_2 &= \frac{1}{2}[U(\varepsilon+1)-\sqrt{U^2(1-\varepsilon)^2+4\varepsilon a^2}]\,, \\
\lambda_{3,4,5,6} &= U\,,
\end{aligned} \tag{2.100}$$

where U represents $\tilde{u}$, $\tilde{v}$, and $\tilde{w}$ in x-, y- and z-direction, respectively. If ε is small enough, the first two eigenvalues can be of the same order of magnitude as others. Note that no assumption is made to the form of the equation of state, it can be applied to any fluid state without loss of accuracy.

From the definition of the preconditioning matrix, and the resulting system eigenvalues, it is clear that the effectiveness of the preconditioning method is totally determined by the choice of the preconditioning factor, ε. The value of ε in each computational cell is crucial to get well-conditioned eigenvalues and thus the fast convergence of the numerical scheme.

Various time scales are associated with each computational cell in each direction, due to local flow convection, acoustic propagation, momentum, and thermal and mass diffusion processes. The non-dimensional numbers that characterize these physical processes, including CFL number, Mach number, von Neumann number, cell Reynolds number, Prandtl number, and Schmidt number, should also be considered when choosing the preconditioning factor.

In the current study, the preconditioning factor is selected based on the methodology developed by Choi and Merkel [121], Buelow et al. [128], and Venkateswaran and Merkel [129]. Optimal values are specified locally as:

$$\varepsilon = \min[1, \max(\varepsilon_{inv}, \varepsilon_{vis})] \,. \tag{2.101}$$

ε_{inv} and ε_{vis} are the inviscid and viscous preconditioning factors, respectively. The criteria employed to evaluate these terms are elaborated in [130], and is not discussed here.

2.2.2 Spatial Discretization

The conservation laws of fluid motion presented in the previous sections can be expressed in differential or integral form. The former can be solved by finite differencing approach, but it has inherent difficulties associated with irregular gird system [131]. Integral methods, including finite volume and finite element methods, can ensure the conservation of properties in each computational cell. In the current study, finite volume approach is thus implemented.

To utilize the finite-volume approach, the governing equations are integrated over the control volume V enclosed by the surface S in the physical domain as

$$\iiint_V \left(\mathbf{\Gamma} \frac{\partial \mathbf{Z}}{\partial \tau} + \frac{\partial \mathbf{Q}}{\partial t} + \frac{\partial (\mathbf{E} - \mathbf{E}_v)}{\partial x} + \frac{\partial (\mathbf{F} - \mathbf{F}_v)}{\partial y} + \frac{\partial (\mathbf{G} - \mathbf{G}_v)}{\partial z} - \mathbf{H} \right) dV = 0. \tag{2.102}$$

The generalized control volume in a structured grid system is a hexahedron formed by eight nodes as shown in Figure 2.2, where $\vec{n}_\xi$, $\vec{n}_\eta$ and $\vec{n}_\zeta$ are area unit vectors normal to the surfaces in the ξ-, η-, and ζ-directions, respectively. In order to enhance numerical

efficiency and minimize the complexity arising from the irregular shape of the computational mesh, a grid transformation is made to convert a curvilinear coordinate system in the physical space into a uniform grid system in the computational space.

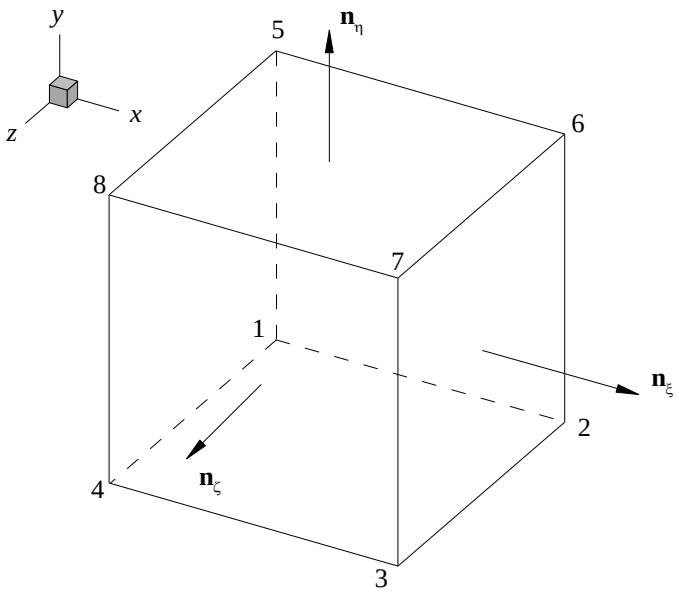

Figure 2.2 Schematic of three-dimensional computational cell

Upon applying the Gauss' divergence theorem over a hexahedral cell as shown in Figure 2.2, Eq. (2.102) can be re-written as:

$$\iiint_V (\mathbf{\Gamma}\frac{\partial \mathbf{Z}}{\partial \tau}+\frac{\partial \mathbf{Q}}{\partial t})dV+\int_{S_\xi}\vec{\mathbf{W}}\bullet\vec{\mathbf{n}}_\xi dS_\xi+\int_{S_\eta}\vec{\mathbf{W}}\bullet\vec{\mathbf{n}}_\eta dS_\eta+\int_{S_\zeta}\vec{\mathbf{W}}\bullet\vec{\mathbf{n}}_\zeta dS_\zeta=\iiint_V \mathbf{H}dV\ , \quad (2.103)$$

where

$$\vec{\mathbf{W}}=\left(\mathbf{E}-\mathbf{E}_v\right)\vec{\mathbf{i}}+\left(\mathbf{F}-\mathbf{F}_v\right)\vec{\mathbf{j}}+\left(\mathbf{G}-\mathbf{G}_v\right)\vec{\mathbf{k}}\ . \quad (2.104)$$

S_ξ, S_η, and S_ζ are the surface areas that are perpendicular to the surface vectors $\vec{n}_\xi$, $\vec{n}_\eta$ and $\vec{n}_\zeta$, respectively. These areas can be combined with the area unit vectors $\vec{n}_\xi$, $\vec{n}_\eta$ and $\vec{n}_\zeta$ into a vector form given by:

$$\begin{aligned}
\vec{S}_\xi &= S_\xi \vec{n}_\xi = S_{\xi x}\vec{i} + S_{\xi y}\vec{j} + S_{\xi z}\vec{k} \ , \\
\vec{S}_\eta &= S_\eta \vec{n}_\eta = S_{\eta x}\vec{i} + S_{\eta y}\vec{j} + S_{\eta z}\vec{k} \ , \\
\vec{S}_\zeta &= S_\zeta \vec{n}_\zeta = S_{\zeta x}\vec{i} + S_{\zeta y}\vec{j} + S_{\zeta z}\vec{k} \ .
\end{aligned} \tag{2.105}$$

And the unit area vectors are related to cell surface areas as

$$\begin{aligned}
\vec{n}_\xi &= \left(S_{\xi x}\vec{i} + S_{\xi y}\vec{j} + S_{\xi z}\vec{k}\right) / \left|\vec{S}_\xi\right| \ , \\
\vec{n}_\eta &= \left(S_{\eta x}\vec{i} + S_{\eta y}\vec{j} + S_{\eta z}\vec{k}\right) / \left|\vec{S}_\eta\right| \ , \\
\vec{n}_\zeta &= \left(S_{\zeta x}\vec{i} + S_{\zeta y}\vec{j} + S_{\zeta z}\vec{k}\right) / \left|\vec{S}_\zeta\right| \ .
\end{aligned} \tag{2.106}$$

The surface vectors and the cell volume can be calculated directly from the grid points [132]:

$$\begin{aligned}
\vec{S}_\xi &= \frac{1}{2}\left(\vec{r}_{72} \times \vec{r}_{36}\right) = \frac{1}{2}\begin{vmatrix} \vec{i} & \vec{j} & \vec{k} \\ x_2 - x_7 & y_2 - y_7 & z_2 - z_7 \\ x_6 - x_3 & y_6 - y_3 & z_6 - z_3 \end{vmatrix} \ , \\
\vec{S}_\eta &= \frac{1}{2}\left(\vec{r}_{86} \times \vec{r}_{75}\right) = \frac{1}{2}\begin{vmatrix} \vec{i} & \vec{j} & \vec{k} \\ x_6 - x_8 & y_6 - y_8 & z_6 - z_8 \\ x_5 - x_7 & y_5 - y_7 & z_5 - z_7 \end{vmatrix} \ , \\
\vec{S}_\zeta &= \frac{1}{2}\left(\vec{r}_{74} \times \vec{r}_{83}\right) = \frac{1}{2}\begin{vmatrix} \vec{i} & \vec{j} & \vec{k} \\ x_4 - x_7 & y_4 - y_7 & z_4 - z_7 \\ x_3 - x_8 & y_3 - y_8 & z_3 - z_8 \end{vmatrix} \ ,
\end{aligned} \tag{2.107}$$

$$\Delta V = \frac{1}{3}\vec{r}_{17}\left(\vec{S}_\xi + \vec{S}_\eta + \vec{S}_\zeta\right) .$$

Assuming that the increments $\Delta\xi=\Delta\eta=\Delta\zeta=1$ in the body-fitted coordinate system and substituting Eq. (2.104) and Eq. (2.106) into Eq. (2.103) yields the following governing equation in the general coordinates

$$\left\{\mathbf{\Gamma}\frac{\partial \mathbf{Z}}{\partial \tau}+\frac{\partial \mathbf{Q}}{\partial t}\right\}+\left(\mathbf{E}_\xi-\mathbf{E}_{\xi\nu}\right)\Big|_{i-1/2,j,k}^{i+1/2,j,k}+\left(\mathbf{F}_\eta-\mathbf{F}_{\eta\nu}\right)\Big|_{i,j-1/2,k}^{i,j+1/2,k}+\left(\mathbf{G}_\zeta-\mathbf{G}_{\zeta\nu}\right)\Big|_{i,j,k-1/2}^{i,j,k+1/2}=\mathbf{H}\ , \qquad (2.108)$$

where the vectors $\mathbf{E}_\xi, \mathbf{F}_\eta, \mathbf{G}_\zeta, \mathbf{E}_{\xi\nu}, \mathbf{F}_{\eta\nu},$ and $\mathbf{G}_{\zeta\nu}$ are defined as

$$\begin{aligned}
\mathbf{E}_\xi &= \left(\tilde{S}_{\xi x}\mathbf{E}+\tilde{S}_{\xi y}\mathbf{F}+\tilde{S}_{\xi z}\mathbf{G}\right), \quad & \mathbf{E}_{\xi\nu} &= \left(\tilde{S}_{\xi x}\mathbf{E}_\nu+\tilde{S}_{\xi y}\mathbf{F}_\nu+\tilde{S}_{\xi z}\mathbf{G}_\nu\right),\\
\mathbf{F}_\eta &= \left(\tilde{S}_{\eta x}\mathbf{E}+\tilde{S}_{\eta y}\mathbf{F}+\tilde{S}_{\eta z}\mathbf{G}\right), \quad & \mathbf{F}_{\eta\nu} &= \left(\tilde{S}_{\eta x}\mathbf{E}_\nu+\tilde{S}_{\eta y}\mathbf{F}_\nu+\tilde{S}_{\eta z}\mathbf{G}_\nu\right),\\
\mathbf{G}_\zeta &= \left(\tilde{S}_{\zeta x}\mathbf{E}+\tilde{S}_{\zeta y}\mathbf{F}+\tilde{S}_{\zeta z}\mathbf{G}\right), \quad & \mathbf{G}_{\zeta\nu} &= \left(\tilde{S}_{\zeta x}\mathbf{E}_\nu+\tilde{S}_{\zeta y}\mathbf{F}_\nu+\tilde{S}_{\zeta z}\mathbf{G}_\nu\right),
\end{aligned} \qquad (2.109)$$

The quantities $\mathbf{E}_{\xi,i\pm1/2,j,k}$, $\mathbf{E}_{\xi\nu,i\pm1/2,j,k}$, $\mathbf{F}_{\eta,i,j\pm1/2,k}$, $\mathbf{F}_{\eta\nu,i,j\pm1/2,j,k}$, $\mathbf{G}_{\zeta,i,j,k\pm1/2}$, and $\mathbf{G}_{\zeta\nu,i,j,k\pm1/2}$ represent the numerical fluxes associated with each cell interface. $\tilde{S}$ represents cell surface areas per cell volume. In fact, the above analysis describes the transformation of a quadrilateral cell with a volume ΔV in x-y-z coordinates to a cubic cell with unit volume in the general coordinate (i.e., ξ-η-ζ coordinates).

To accelerate convergence, the pseudo-time integration is based on the local time step in the computational domain. The maximum pseudo-time increment $\Delta\tau$ of each cell can be evaluated by

$$\Delta\tau = \frac{\Delta\tau_\xi \quad \Delta\tau_\eta \quad \Delta\tau_\zeta}{\Delta\tau_\xi \quad \Delta\tau_\eta + \Delta\tau_\eta \quad \Delta\tau_\zeta + \Delta\tau_\zeta \quad \Delta\tau_\xi} \ , \tag{2.110}$$

where

$$\begin{aligned}
\Delta\tau_\xi &= \frac{CFL\cdot \ \Delta V}{\left|\rho(\lambda_x)S_{\xi x} + \rho(\lambda_y)S_{\xi y} + \rho(\lambda_z)S_{\xi z}\right| / \left|\vec{S}_\xi\right|} \ , \\
\Delta\tau_\eta &= \frac{CFL \ \cdot \Delta V}{\left|\rho(\lambda_x)S_{\eta x} + \rho(\lambda_y)S_{\eta y} + \rho(\lambda_z)S_{\eta z}\right| / \left|\vec{S}_\eta\right|} \ , \\
\Delta\tau_\zeta &= \frac{CFL \ \cdot \Delta V}{\left|\rho(\lambda_x)S_{\zeta x} + \rho(\lambda_y)S_{\zeta y} + \rho(\lambda_z)S_{\zeta z}\right| / \left|\vec{S}_\zeta\right|} \ .
\end{aligned} \tag{2.111}$$

For the discretization of convective fluxes $\mathbf{E}_{\xi,i\pm1/2,j,k}$, $\mathbf{F}_{\xi,i,j\pm1/2,k}$, $\mathbf{G}_{\xi,i,j,k\pm1/2}$ and viscous fluxes fluxes $\mathbf{E}_{\xi v,i\pm1/2,j,k}$, $\mathbf{F}_{\xi v,i,j\pm1/2,k}$, $\mathbf{G}_{\xi v,i,j,k\pm1/2}$, the present work utilizes second-order overall accuracy for spatial discretization with the exception of first order accuracy close to the physical boundaries, and artificial dissipation with similar orders is also applied [130].

2.2.3 Temporal Discretization

The physical time derivatives in Eq. (2.109) are evaluated by backward differencing

$$\frac{\partial Q}{\partial t} = \frac{1}{\Delta t}[a_1 Q^{m+1} - \phi(Q^n, Q^{n-1}, \cdots)] \ . \tag{2.112}$$

The coefficient a_1 and function ϕ in Eq. (2.112) can be specified to any level of temporal accuracy desired. In the current work, a three-point backward difference with second-order accuracy is employed. For this situation

$$a_1 = \frac{3}{2},\ \phi = \frac{1}{2}(4Q^n - Q^{n-1})\ . \tag{2.113}$$

The superscripts m and n denote iterations within the pseudo-time domain (inner-loop) and physical time domain (outer-loop), respectively. The physical time term Q^{m+1} can be linearized as

$$Q^{m+1} = Q^m + T\Delta Z^{m+1}\ . \tag{2.114}$$

Substituting Eq. (2.112) and Eq. (2.114) into Eq. (2.109) yields the following discretized system

$$\begin{aligned}&\left\{\Gamma + a\frac{\Delta\tau}{\Delta t}T\right\}\Delta Z + \frac{\Delta\tau}{\Delta V}\left(\left(\mathrm{E}_{\xi} - \mathrm{E}_{\xi v}\right)\Big|_{i-1/2,j,k}^{i+1/2,j,k} + \left(\mathrm{F}_{\eta} - \mathrm{F}_{\eta v}\right)\Big|_{i,j-1/2,k}^{i,j+1/2,k} + \right.\\ &\left.\left(\mathrm{G}_{\zeta} - \mathrm{G}_{\zeta v}\right)\Big|_{i,j,k-1/2}^{i,j,k+1/2}\right) = \mathrm{H}^{m+1}\Delta\tau - \frac{\Delta\tau}{\Delta t}(a_1 Q^m - \phi)\ .\end{aligned} \tag{2.115}$$

A fourth-order Runge-Kutta (RK-4) scheme is used to solve the governing equation (2.115) in the pseudo-time space due to its higher temporal accuracy and relatively larger CFL number requirement (i.e., $2\sqrt{2}$ for an Euler calculation using RK-4). A thorough investigation of the stability characteristics of the RK-4 method, based on convection of the turbulence energy-spectrum, has been performed by Apt and Yang [133] to establish its creditability and accuracy. Using the four-step Runge-Kutta scheme, each pseudo-time integration is completed through four consecutive intermediate steps, as given below

$$\boldsymbol{Z_0} = \boldsymbol{Z^m}, \tag{2.116}$$

$$\boldsymbol{Z_0 = Z^m + \Delta Z_1,\ \left(\Gamma + \frac{\Delta\tau}{\Delta t}T - \Delta\tau D\right)\Delta Z_1 = 1/4 \cdot \Delta\tau \cdot R(Z_0),}$$

$$\boldsymbol{Z_2 = Z^m + \Delta Z_2,\ \left(\Gamma + \frac{\Delta\tau}{\Delta t}T - \Delta\tau D\right)\Delta Z_2 = 1/3 \cdot \Delta\tau \cdot R(Z_1),}$$

$$\boldsymbol{Z_3 = Z^m + \Delta Z_3,\ \left(\Gamma + \frac{\Delta\tau}{\Delta t}T - \Delta\tau D\right)\Delta Z_3 = 1/2 \cdot \Delta\tau \cdot R(Z_2),}$$

$$\boldsymbol{Z_m = Z^m + \Delta Z^{m+1},\ \left(\Gamma + \frac{\Delta\tau}{\Delta t}T - \Delta\tau D\right)\Delta Z^{m+1} = \Delta\tau \cdot R(Z_3),}$$

where

$$R(z) = \mathrm{H}^{\mathrm{m}} - \frac{1}{\Delta t}(a_1 Q^m - \phi) - [\left(\mathrm{E}_{\xi} - \mathrm{E}_{\xi v}\right)\Big|_{i-1/2,j,k}^{i+1/2,j,k} + \left(\mathrm{F}_{\eta} - \mathrm{F}_{\eta v}\right)\Big|_{i,j-1/2,k}^{i,j+1/2,k} + \left(\mathrm{G}_{\zeta} - \mathrm{G}_{\zeta v}\right)\Big|_{i,j,k-1/2}^{i,j,k+1/2}] \,. \tag{2.117}$$

Superscripts 'm' and 'm+1' stand for the solution at the 'm^{th}' and '$(m+1)^{\text{th}}$' pseudo-time steps, respectively. The iteration begins from pseudo-time steps (inner-loop). At convergence in pseudo-time step, the solution proceeds one physical time step (outer-loop).

2.2.4 Boundary Conditions

In all cases considered, second-order accurate boundary conditions are implemented. The inlet and exit conditions are specified using the method-of-characteristics (MOC). Adiabatic and noslip conditions are imposed at the solid wall. Elsewhere conditions are specified using second-order extrapolated values. These conditions produce zero normal gradients with respect to pressure, velocity, temperature, and species mass fraction.

2.2.4.1 Characteristic Boundary Conditions

At the inlet and outlet boundary, care must be taken when specifying the numerical boundary conditions. One has to ensure that the unphysical spurious wave reflections are avoided at the boundary and the flow is capable of relaxing to ambient conditions in the prescribed ways, which can be satisfied using the MOC proposed by Poinsot and Lelef [134]. In the absence of a significant diffusion processes, the MOC method provides correct number of conditions that must be specified, as well as conditioned information from the interior domain.

Implementation of the MOC procedure involves diagonalizing the governing system to a quasi-one-dimensional characteristic form

$$[S + LM^{-1}\Gamma^{-1}(\Gamma + \frac{\Delta\tau}{\Delta t}T - \Delta\tau D)]\Delta Z = -LM^{-1}\Gamma^{-1}$$
$$\left\{(\frac{\partial E}{\partial x} + \frac{\partial F}{\partial y} + \frac{\partial G}{\partial z}) + \tilde{\Omega} + \frac{\Delta\tau}{\Delta t}(a_1 Q^m - \phi) - H\right\} . \qquad (2.118)$$

All of the terms in Eq. (2.118) are evaluated at cell centroids using the finite difference methodology. The term $\tilde{\Omega}$ is the vector of specified boundary conditions. The term L is a selection matrix that singles out the desired characteristics at respective boundaries. The Jabobian matrix S is defined as $S = \partial\tilde{\Omega} / \partial Z$.

In the absence of significant diffusion processes, the MOC procedure dictates the correct number of conditions that must be specified at each boundary and provides well-conditioned information from the interior domain. In this study, the conditions imposed at the inlet and exit planes remain subsonic. At the inlet, there is one outgoing characteristic

and N+3 conditions must be specified. Here the temperature, velocity, and species concentrations are employed assuming fully-developed turbulent channel flow. These conditions are given by

$$\tilde{\Omega}_{inlet} = \Delta V \begin{pmatrix} 0 \\ \tilde{u} - \tilde{u}_{ref} \\ \tilde{v} - \tilde{v}_{ref} \\ \tilde{w} - \tilde{w}_{ref} \\ \tilde{T} - \tilde{T}_{ref} \\ \tilde{Y}_1 - \tilde{Y}_{1_{ref}} \\ \vdots \\ \tilde{Y}_N - \tilde{Y}_{N-1_{ref}} \end{pmatrix}, \; L_{inlet} = \begin{pmatrix} 1 & 0 & 0 & 0 & 0 & 0 & \cdots & 0 \\ 0 & 0 & 0 & 0 & 0 & 0 & \cdots & 0 \\ 0 & 0 & 0 & 0 & 0 & 0 & \cdots & 0 \\ 0 & 0 & 0 & 0 & 0 & 0 & \cdots & 0 \\ 0 & 0 & 0 & 0 & 0 & 0 & \cdots & 0 \\ 0 & 0 & 0 & 0 & 0 & 0 & \cdots & 0 \\ \vdots & \vdots & \vdots & \vdots & \vdots & \vdots & \ddots & \vdots \\ 0 & 0 & 0 & 0 & 0 & 0 & \cdots & 0 \end{pmatrix}. \tag{2.119}$$

where $\tilde{u}_{ref}$, $\tilde{v}_{ref}$, $\tilde{w}_{ref}$, and $\tilde{T}_{ref}$, $\tilde{Y}_{1_{ref}}$, …, $\tilde{Y}_{N-1_{ref}}$ represent the specified values of velocity components, temperature, and species mass fraction, respectively. At the exit, there are N+3 outgoing characteristics and one condition must be specified. Here a far-field pressure condition is simulated using the methodologies proposed by Rudy and Strikwerda [135], Poinsot and Lele [134], and Baum et al. [136].

To simulate the far-field boundary the incoming characteristic given by Eq. (2.118) is modified to provide a nonreflecting outflow condition. The equation of interest is given by the selection matrix

$$L = \begin{pmatrix} 1 & 0 & 0 & 0 & 0 & 0 & \cdots & 0 \\ 0 & 0 & 0 & 0 & 0 & 0 & \cdots & 0 \\ 0 & 0 & 0 & 0 & 0 & 0 & \cdots & 0 \\ 0 & 0 & 0 & 0 & 0 & 0 & \cdots & 0 \\ 0 & 0 & 0 & 0 & 0 & 0 & \cdots & 0 \\ 0 & 0 & 0 & 0 & 0 & 0 & \cdots & 0 \\ \vdots & \vdots & \vdots & \vdots & \vdots & \vdots & \ddots & \vdots \\ 0 & 0 & 0 & 0 & 0 & 0 & \cdots & 0 \end{pmatrix} . \tag{2.120}$$

Associated with this equation is the term

$$\boldsymbol{\Pi_2 = \lambda_2 \left[\frac{1}{\varepsilon} \frac{u-\lambda_2}{a} \frac{\partial p}{\partial x} - \rho a \frac{\partial u}{\partial x} \right]} , \tag{2.121}$$

which characterizes the time variation of the normal component of acoustic waves that propagate from an infinitely distant downstream source into the computational domain. The term λ_2 is the acoustic eigenvalue. Conceptually, a perfectly non-reflecting subsonic outflow condition can be obtained if this term is set equal to zero. Specifying such a condition, however, eliminates the information provided by the acoustic waves and leads to an ill-posed problem. To simulate this information Rudy and Strikwerda [135], Poinsot and Lele [134], and Baum et al. [136] proposed that Eq. (2.121) be replaced with the term

$$\boldsymbol{\Pi_2^k = k(p - p_\infty)} , \tag{2.122}$$

where k is a constant that determines the speed with which the average pressure in the computational domain relaxes towards the imposed pressure at infinity p_∞. This condition introduces small amplitude acoustic waves using scaling arguments that are based on known quantities at the exit. Rudy and Strikwerda [135] proposed that optimal values of k are given by

$$\boldsymbol{k = 2\frac{\sigma}{x_c}\frac{\varepsilon a^2(1-\bar{M}^2)}{\sqrt{u(1-\varepsilon)^2+4\varepsilon a^2}}}. \tag{2.123}$$

The factor presented here has been modified from that given by Rudy and Strikwerda [135] to accommodate the dual-time preconditioned system. Here $\bar{M}^2$ represents the maximum Mach number in the computational domain, x_c is the characteristic axial length of the domain, e is the local preconditioning factor, and a is the local speed of sound. The term σ is a scaling factor used for optimization. Poinsot and Lele [134], and Baum et al. [136] have shown that values ranging from 0.25 to 0.5 provide the best results. When lower values are specified, solutions tend to drift away from the reference pressure. When larger values are specified, flow oscillations are introduced.

To implement the MOC methodology with the far field pressure condition described above, the $N + 3$ outgoing characteristics are selected and the incoming characteristic is modified by replacing the incoming wave amplitude given by Eq. (2.121). These conditions are given by

$$\tilde{\Omega}_{outlet} = \Delta V \begin{pmatrix} p - p_{ref} \\ 0 \\ 0 \\ 0 \\ 0 \\ 0 \\ \vdots \\ 0 \end{pmatrix}, \; L_{outlet} = \begin{pmatrix} 0 & 0 & 0 & 0 & 0 & 0 & \cdots & 0 \\ 0 & 1 & 0 & 0 & 0 & 0 & \cdots & 0 \\ 0 & 0 & 1 & 0 & 0 & 0 & \cdots & 0 \\ 0 & 0 & 0 & 1 & 0 & 0 & \cdots & 0 \\ 0 & 0 & 0 & 0 & 1 & 0 & \cdots & 0 \\ 0 & 0 & 0 & 0 & 0 & 1 & \cdots & 0 \\ \vdots & \vdots & \vdots & \vdots & \vdots & \vdots & \ddots & \vdots \\ 0 & 0 & 0 & 0 & 0 & 0 & \cdots & 1 \end{pmatrix}. \tag{2.124}$$

The far-field pressure condition has been shown to be effective in reducing reflections at the subsonic exit boundary and is relatively accurate and stable.

2.2.5 Parallel Implementation

Since the explicit time-stepping numerical scheme is applied in the current study, only the data from neighboring cells instead of the whole computational domain were required during the calculation of variables in each cell. Since the data dependence is weak, the domain decomposition technique is best suited for this kind of application. It is also commonly implemented in distributed-memory parallel computer systems. In the field of computational fluid dynamics (CFD), it is generally referred to as mesh partitioning, based on the geometric substructure of the computational domain. In the domain-decomposition technique, the physical domain is divided into several sub-domains. Variables in each cell are updated to the next time step simultaneously. In order to calculate the spatial derivatives at the sub-domain boundaries, ghost cells or halo data around the computing cells are introduced. Figure 2.3 shows an example of a two-dimensional sub-domain with ghost cells. Because the variables in the ghost cell are updated in another sub-domain, message passing is required to synchronize data between different sub-domains. The communication overhead is directly proportional to the volume-to-surface ratio of the grid system in that sub-domain. Maximizing the computation-to-communication ratio leads to higher parallel execution efficiency.

High Performance Computing (HPC) clusters used to conduct the large-scale computations required in the current studies. The in-house program is highly paralleled, and each decomposed sub-domain is computed by one CPU core. Communication at the domain boundary is made through a message passing interface (MPI).

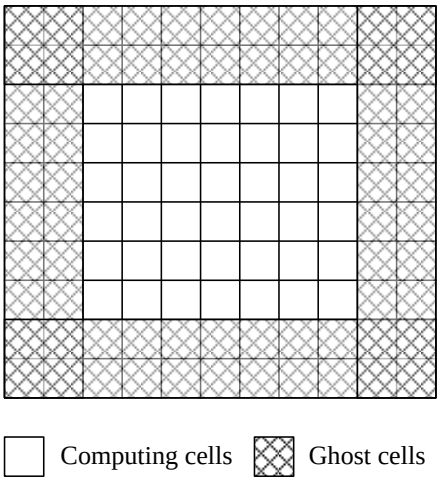

Figure 2.3 Schematic of a two-dimensional sub-domain with ghost cells

2.3 Injector Configuration

Figure 1.2 shows a schematic sketch of the Gas-Centered Liquid-Swirl Coaxial (GCLSC) injector, mimicking the main chamber injector of the staged-combustion rocket engine RD-170/180 [57, 137-140]. This injector is composed of four regions: center cylindrical tube, coaxial annular fuel passage, recess region, and taper region. High-temperature GOX is introduced axially into the center tube (known as GOX post), and kerosene is tangentially injected into the coaxial annulus through a total of 12 tangential orifices distributed in two arrays. The configuration is simplified here to a single circular slit. Its width $\Delta l = 2.0$ mm is carefully chosen to ensure that the mass and momentum flow rates are identical to the original design of 12 fuel ports. Mixing of GOX and kerosene begins directly after the shielding collar rim, and the mixing layer develops in the recess region and taper region. Table 2.4 and Table 2.5 list the geometric parameters and operating conditions of the injector.

Table 2.4 Geometric parameters of baseline injector

δ, mm	h_1, mm	R_g, mm	R_{if}, mm	R_f, mm	L_1, mm	L_2, mm	Δl_n, mm	α
0.66	5.76	5.62	6.36	7.03	93	113.1	2	42°

Table 2.5 Injection operating conditions for fuel and oxidizer

	Oxidizer	Fuel
Mass flow rate, kg/s	1.33	0.48
Static pressure, MPa	25.3	25.3
Temperature, K	687.7	492.2
Density, kg/m^3	131.4	640.8
Inlet velocity, m/s	102.0	U_r = 24.5, U_θ = 49.0

In the present work, ten different recess lengths (L_r) are considered in a range of 0-16 mm. First six cases are important for analyses of fluid dynamics and combustion dynamics, and the other four cases are implemented for the emulation studies. The distance from the headend of the fuel annulus to the entrance of the taper region is fixed at 16 mm. The length of the annulus inner surface (i.e., shielding, L_s) thus changes according to the variation of the recess length L_r. Table 2.6 lists the lengths of recess and shielding for all cases. The recess length decreases with increasing case number. Case 3, with a recess length of 5.5 mm, is considered as the baseline, while Case 1 is fully recessed and Case 6 has no recess. Other geometric parameters and operating conditions remain identical as listed in Table 2.4 and Table 2.5.

Table 2.6 Lengths of recess and shielding for all cases

Case	1	2	3	4	5	6	7	8	9	10
L_s, mm	0.0	3.0	5.5	9.0	12.5	16.0	7.25	4.25	10.75	8.125
L_r, mm	16.0	13.0	10.5	7.0	3.5	0.0	8.75	11.75	5.25	7.875

The momentum flux ratio between GOX and fuel stream is defined as $\rho_o U_o^2 / \rho_f U_f^2$. The densities of oxidizer and fuel at the entrance are 131.4 and 640.8 kg/m^3, respectively. The axial velocity of the incoming oxidizer stream is 102 m/s. The reference entrance velocity of kerosene needs to be evaluated carefully. For Case 1, without shielding, the kerosene radially penetrates into the axial GOX stream. U_f is taken as the radial velocity component at the inlet, 24.5 m/s. For other cases with shielding, kerosene flows axially at the point of mixing, and U_f is most appropriately represented by the axial velocity in the coaxial outer annulus, 26.6 m/s. The momentum flux ratio is thus obtained as 3.5 for Case 1 and 3.0 for Cases 2-10. The Reynolds numbers are 1.89×10^6 and 4.14×10^4 for the GOX and kerosene flows, respectively, based on the center post diameter and outer annulus width.

For each case, the computational domain is comprised of the injector (shown in Figure 1.2) and the downstream region, which spans 90 and 158 mm in the radial and axial directions, respectively. The present study considers a cylindrical sector of the three-dimensional domain, with periodic boundary conditions in the azimuthal direction. Acoustically non-reflecting boundary conditions are applied at the GOX and kerosene inlets. In the downstream region, a sponge-layer treatment [141] is implemented in both the axial and radial directions. No-slip and adiabatic conditions are enforced at the injector walls. White noise with 5% intensity is applied to the inlet velocities of both propellant streams.

CHAPTER 3.

HIGH-FIDELITY EMULATION

3.1 Data sets and Geometric Design Parameter

As mentioned in the previous sections, for GCLSC injectors, recess length L_r has significant impacts on flow structure, flow dynamics and mixing of non-reacting cases and combustion dynamics of reacting cases [142]. For all injectors, the distance from the headend of the fuel annulus to the entrance of the taper region is fixed at 16 mm, and recess lengths are in the range of 0-16 mm. Table 2.6 lists the recess lengths and shielding lengths for all cases. Numerical simulations of these GCLSC injectors with varying recess lengths have been carried out using LES, both non-reacting and reacting cases. Among the 10 cases listed in Table 2.6, both Case 1 (fully recessed) and Case 6 (fully non-recessed) are excluded from the training dataset due to their fundamentally different dynamics from all other cases [142]. The time-evolving flow fields of the remaining 8 cases are selected. In this study, Case 7 is close to the center of the design space, and is thus selected as the testing case, and the remaining 7 cases are the training cases.

3.2 Kriging Model

Kriging is a commonly-used GP-base model, and has been successfully applied to a variety of fields [143]. The data are a set of observations of some variable(s) of interest, with some spatial correlation present. Usually, the results of kriging are the expected value ("kriging mean") and variance ("kriging variance") computed for every point within a region. Unlike other traditional interpolation methods in statistics, such as inverse distance

weighting and spline, to use the kriging effectively involves an interactive investigation of the spatial behavior of the phenomenon (prediction) represented by training data sets (observation) before selecting the best estimation method for generating the output surface. The inverse distance weighting and Spline interpolation methods are considered deterministic interpolation methods, in that they are directly based on the surrounding measured values or on specified mathematical formulas that determine the smoothness of the resulting surface. Conversely, kriging can build a statistical model that includes autocorrelation. A kriging model considers the statistical relationships among all the measured points; hence, a kriging model not only has the capability of producing a prediction surface but also decreases the errors and provides better certainty or accuracy of the predictions.

3.2.1 Basics of Kriging

All kriging estimators are based on the basic linear regression estimator $\hat{f}(\boldsymbol{d}^*)$, which is defined as

$$\hat{f}(\boldsymbol{d}^*) - \mu(\boldsymbol{d}^*) = \sum_{i=i}^{n} \lambda_i [f(\boldsymbol{d}_i) - \mu(\boldsymbol{d}_i)] \quad \textbf{(3.1)}$$

where $\boldsymbol{d}^*$ and $\boldsymbol{d}_i$ are location vectors for estimation point and one of the neighboring data points, indexed by i. In the current study, $\boldsymbol{d}^*$ and $\boldsymbol{d}_i$ correspond to design parameters, as will be described below. $\mu(\boldsymbol{d}^*)$ and $\mu(\boldsymbol{d}_i)$ are trend components of $f(\boldsymbol{d}^*)$ and $f(\boldsymbol{d}_i)$; λ_i is kriging weight assigned to datum $f(\boldsymbol{d}_i)$ for estimation location $\boldsymbol{d}^*$; same datum will

receive different weight for different estimation location; and n is the total number of data points in local neighborhood used for estimation of $\hat{f}(\boldsymbol{d}^*)$ [144].

The estimation error $\hat{f}(\boldsymbol{d}^*) - f(\boldsymbol{d})$ is a linear combination of random variables at the points $\boldsymbol{d_i}$ and the estimation point $\boldsymbol{d}^*$:

$$\begin{aligned}\hat{f}(\boldsymbol{d}^*) - f(\boldsymbol{d}^*) &= \left[\hat{f}(\boldsymbol{d}^*) - \boldsymbol{m}\right] - [f(\boldsymbol{d}^*) - \boldsymbol{m}] \\ &= \sum_{i=i}^{n} \lambda_i(\boldsymbol{d}^*) R(\boldsymbol{d}_i) - R(\boldsymbol{d}^*) = R^*(\boldsymbol{d}^*) - R(\boldsymbol{d}^*)\end{aligned} \quad \textbf{(3.2)}$$

Eq. (3.3) is the basic form of the kriging estimator. The goal is to determine weights, λ_i, that minimize the variance of the estimator

$$\sigma^2(\boldsymbol{d}^*) = \mathrm{Var}\left[\hat{f}(\boldsymbol{d}^*) - f(\boldsymbol{d}^*)\right] \quad \textbf{(3.3)}$$

Under the unbiasedness constraint $\mathrm{E}\left[\hat{f}(\boldsymbol{d}^*) - f(\boldsymbol{d}^*)\right] = 0$.

The field $f(\boldsymbol{d}^*)$ is decomposed into residual component $R(\boldsymbol{d}^*)$ and trend components $\mu(\boldsymbol{d}^*)$, $f(\boldsymbol{d}^*) = R(\boldsymbol{d}^*) + \mu(\boldsymbol{d}^*)$, with the residual component treated as a random field with a stationary mean of 0 and a stationary covariance (i.e., a function of lag, $\boldsymbol{h}$):

$$\mathrm{E}[R(\boldsymbol{d}^*)] = 0 \quad \textbf{(3.4)}$$

$$\mathrm{cov}[R(\boldsymbol{d}^*), R(\boldsymbol{d}^* + \boldsymbol{h})] = \mathrm{E}[R(\boldsymbol{d}^*) \cdot R(\boldsymbol{d}^* + \boldsymbol{h})] = \mathrm{cov_R}[\boldsymbol{h}] \quad \textbf{(3.5)}$$

The three main kriging variants (i.e., simple kriging, ordinary kriging, and kriging with a trend), all of them follows the equations listed above, but differs in the treatment of trend components $\mu(\boldsymbol{d}^*) = \mathrm{E}[f(\boldsymbol{d}^*)]$. Simple kriging is first introduced, followed by a description of ordinary kriging, which is utilized in the current study. A detailed description of other methods can be found in the referenced study [145].

3.2.2 Simple Kriging

For simple kriging, the trend component is assumed as a constant and known: $\mu(\boldsymbol{d}) = \mathrm{E}[f(\boldsymbol{d})] = m$. Therefore,

$$\hat{f}(\boldsymbol{d}^*) = m + \sum_{i=i}^{n} \lambda_i(\boldsymbol{d}^*)[f(\boldsymbol{d}_i) - m] \tag{3.6}$$

This estimation is automatically unbiased, since $\mathrm{E}[f(\boldsymbol{d}) - m] = 0$; hence, $\mathrm{E}\left[\hat{f}(\boldsymbol{d}^*)\right] = m = \mathrm{E}[f(\boldsymbol{d})]$. Define residual as $R(\boldsymbol{d}) = f(\boldsymbol{d}) - m$. The estimation error $\hat{f}(\boldsymbol{d}^*) - f(\boldsymbol{d})$ is a linear combination of random variables representing residuals at the data points, $\boldsymbol{d_i}$, and the estimation point, $\boldsymbol{d}^*$:

$$\begin{aligned} \hat{f}(\boldsymbol{d}^*) - f(\boldsymbol{d}^*) &= \left[\hat{f}(\boldsymbol{d}^*) - m\right] - [f(\boldsymbol{d}^*) - m] \\ &= \sum_{i=i}^{n} \lambda_i(\boldsymbol{d}) R(\boldsymbol{d}_i) - R(\boldsymbol{d}^*) = R^*(\boldsymbol{d}^*) - R(\boldsymbol{d}^*) \end{aligned} \tag{3.7}$$

Using rules for the variance of a linear combination of random variables, the error variance is then given by

$$\sigma_E^2(\boldsymbol{d}) = \mathrm{Var}[R^*(\boldsymbol{d}^*)] + \mathrm{Var}[R(\boldsymbol{d}^*)] - 2\mathrm{cov}[R^*(\boldsymbol{d}^*), R(\boldsymbol{d}^*)]$$
$$= \sum_{i=1}^{n}\sum_{j=i}^{n}\lambda_i(\boldsymbol{d}^*)\lambda_j(\boldsymbol{d}^*)\mathrm{cov}_{\mathrm{R}}(\boldsymbol{d_i} - \boldsymbol{d_j}) + \mathrm{cov}_{\mathrm{R}}(0) - \quad \textbf{(3.8)}$$
$$2\sum_{i=i}^{n}\lambda_i(\boldsymbol{d}^*)\mathrm{cov}_{\mathrm{R}}(\boldsymbol{d_i} - \boldsymbol{d}^*)$$

To minimize the error variance, we take the derivation of the above expression with respect to each of the kriging weights and set each derivative to zero. This leads to the following system of equations:

$$\sum_{j=1}^{n}\lambda_j(\boldsymbol{d}^*)\mathrm{cov}_{\mathrm{R}}(\boldsymbol{d}_i - \boldsymbol{d}_j) = \mathrm{cov}_{\mathrm{R}}(\boldsymbol{d}_i - \boldsymbol{d}^*), \quad i = 1, \dots, n \qquad \textbf{(3.9)}$$

Because of the constant mean, the covariance function for $f(\boldsymbol{d})$ is the same as that for the residual component, $\mathrm{cov}(h) = \mathrm{cov}_{\mathrm{R}}(h)$, so that we can write the simple kriging system directly in terms of $\mathrm{cov}(h)$:

$$\sum_{j=1}^{n}\lambda_j(\boldsymbol{d}^*)\mathrm{cov}(\boldsymbol{d}_i - \boldsymbol{d}_j) = \mathrm{cov}(\boldsymbol{d}_i - \boldsymbol{d}^*), \quad i = 1, \dots, n \qquad \textbf{(3.10)}$$

This can be denoted in matrix form as

$$\boldsymbol{\mathcal{K}}\lambda(\boldsymbol{d}^*) = \mathbf{k} \qquad \textbf{(3.11)}$$

where $\boldsymbol{\mathcal{K}}$ is the matrix of covariances between data points, with elements $\boldsymbol{\mathcal{K}_{i,j}} = \mathrm{cov}(\boldsymbol{d}_i - \boldsymbol{d}_j)$, $\mathbf{k}$ is the vector covariances between the data points and the estimation point, with elements given by $\mathbf{k} = \mathrm{C}(\boldsymbol{d}_i - \boldsymbol{d}^*)$, and $\lambda(\boldsymbol{d}^*)$ is the vector of simple kriging weights

for the surrounding data points. If the covariance model is licit (meaning the underlying semi-variogram model is licit) and no two data points are collocated, then the data covariance matrix is positive definite, and we can solve for the kriging weights using

$$\lambda(\boldsymbol{d}^*) = \boldsymbol{\mathcal{K}}^{-1}\mathbf{k} \tag{3.12}$$

Once the kriging weights are evaluated, the kriging estimate and the kriging variance can be both computed by substituting the kriging weights into the error variance expression below:

$$\sigma_E^2(\boldsymbol{d}) = \mathrm{C}[0] - \lambda(\boldsymbol{d}^*)\mathbf{k} = \mathrm{C}[0] - \sum_{j=1}^{n} \lambda_j(\boldsymbol{d}^*)\mathrm{cov}(\boldsymbol{d}_i - \boldsymbol{d}^*). \tag{3.13}$$

The simple kriging finds a set of weights for estimating the variable value $f(\boldsymbol{d}^*)$ at point $\boldsymbol{d}^*$ from values at a set of neighboring data points. The weight on each data point generally decreases with increasing distance to that point, in accordance with the decreasing data-to-estimation covariances specified in the right-hand vector, $\mathbf{k}$. However, the set of weights is also designed to account for redundancy among the data points, represented in the data point-to-data point covariances in the matrix $\boldsymbol{\mathcal{K}}$. Multiplying $\mathbf{k}$ by $\boldsymbol{\mathcal{K}}^{-1}$ will downweigh points falling in clusters relative to isolated points at the same distance.

3.2.3 Ordinary Kriging

For ordinary kriging, constant trend value is assumed in the local neighborhood of each estimation point, that is $\mu(\boldsymbol{d_i}) = \mu(\boldsymbol{d}^*)$ for each nearby data value, $f(\boldsymbol{d}_i)$, that we are using to estimate $f(\boldsymbol{d}^*)$. In this case, the kriging estimator can be written as

$$\begin{aligned}\hat{f}(\boldsymbol{d}^*) &= \mu(\boldsymbol{d}^*) + \sum_{i=i}^{n} \lambda_i(\boldsymbol{d}^*)\,[f(\boldsymbol{d}_i) - \mu(\boldsymbol{d}^*)] \\ &= \sum_{i=i}^{n} \lambda_i(\boldsymbol{d}^*) f(\boldsymbol{d}_i) + \left[1 - \sum_{i=i}^{n} \lambda_i(\boldsymbol{d}^*)\right] \mu(\boldsymbol{d}^*)\end{aligned} \tag{3.14}$$

in order to filter out the unknown local mean $\mu(\boldsymbol{d}^*)$, we require the sum of kriging weights to be 1, leading to an ordinary kriging estimator of

$$\hat{f}(\boldsymbol{d}^*) = \textstyle\sum_{i=i}^{n} \lambda_i(\boldsymbol{d}^*) f(\boldsymbol{d}_i) \quad \text{with} \quad \sum_{i=i}^{n} \lambda_i(\boldsymbol{d}^*) = 1\,. \tag{3.15}$$

A technique called maximum-likelihood estimation (MLE), a ubiquitous estimation technique in statistical literature [146], is employed. The key concept in MLE is to discover the optimal parameter setting that minimizes the likelihood function of the GP model. In order to minimize the error variance subject to the unit-sum constraint on the weights, we actually set up the system minimize the error variance with an additional term involving a Lagrange parameter, $\mu(\boldsymbol{d}^*)$. After applying Eq (3.2) and (3.3) to the equation:

$$L = \sigma_E^2(\boldsymbol{d}^*) + 2\mu(\boldsymbol{d}^*)\left[1 - \sum_{i=i}^{n} \lambda_i(\boldsymbol{d}^*)\right] \tag{3.16}$$

$$= Var(R^*(\boldsymbol{d}^*) - R(\boldsymbol{d}^*)) + 2\mu(\boldsymbol{d}^*)\left[1 - \sum_{i=i}^{n} \lambda_i(\boldsymbol{d}^*)\right]$$

$$= Var[R^*(\boldsymbol{d}^*)] + Var[R(\boldsymbol{d}^*)] - 2cov[R^*(\boldsymbol{d}^*), R(\boldsymbol{d}^*)]$$

$$+ 2\mu(\boldsymbol{d}^*)\left[1 - \sum_{i=i}^{n} \lambda_i(\boldsymbol{d}^*)\right]$$

$$= \sum_{i=1}^{n}\sum_{j=i}^{n} \lambda_i(\boldsymbol{d}^*)\lambda_j(\boldsymbol{d}^*)cov\big(\boldsymbol{d} - \boldsymbol{d_j}\big) + cov(0)$$

$$- 2\sum_{i=i}^{n} \lambda_i(\boldsymbol{d}^*)cov(\boldsymbol{d_i} - \boldsymbol{d}^*) + 2\mu(\boldsymbol{d}^*)\left[1 - \sum_{i=i}^{n} \lambda_i(\boldsymbol{d}^*)\right]$$

to minimize the error variance, we take the derivation of the above expression with respect to each of the kriging weights and set each derivative to zero. This leads to the following system of equations

$$\tfrac{1}{2}\tfrac{\partial \mathcal{L}}{\partial \mu} = 1 - \textstyle\sum_{i=i}^{n} \lambda_i(\boldsymbol{d}^*) = 0, \qquad \textbf{(3.17)}$$

$$\tfrac{1}{2}\tfrac{\partial \mathcal{L}}{\partial \lambda_i} = -\textstyle\sum_{j=1}^{n} \lambda_j(\boldsymbol{x}^*)cov\big(\boldsymbol{d}_i - \boldsymbol{d}_j\big) - \mu(\boldsymbol{d}^*) + cov(\boldsymbol{d}_i - \boldsymbol{d}^*) = 0. \qquad \textbf{(3.18)}$$

In the present work, optimization is achieved by means of the L-BFGS algorithm [147], a method employed for many training algorithms. A more detailed explanation can be found in Santner et al. [148].

Once the kriging weights (and Lagrange parameter) are obtained, the ordinary kriging error variance is given by:

$$\sigma_E^2(\boldsymbol{x}^*) = cov(0) - \sum_{i=1}^{n} \lambda_i(\boldsymbol{d}^*)\mathrm{cov}(\boldsymbol{d}_i - \boldsymbol{d}^*) + \mu(\boldsymbol{d}^*). \quad \textbf{(3.19)}$$

3.3 Surrogate models

The current section will start with a brief review of Proper Orthogonal Decomposition (POD), followed by descriptions of a few POD-based emulation techniques that are recently proposed and implemented.

3.3.1 Review of Proper Orthogonal Decomposition (POD)

POD is a model reduction method that is able to extract spatial modes and corresponding temporal coefficients based on the energy norms [149]. This method is able to provide valuable insights into the dynamic characteristics of the flow field. The equation can be written in the following form

$$\hat{f}(\boldsymbol{x}, t) = \sum_{i=1}^{n} \beta^i(t)\phi^i(\boldsymbol{x}) \quad \textbf{(3.20)}$$

$\hat{f}(\boldsymbol{x}, t)$ is the flow field at spatial location $\boldsymbol{x}$ and time t, and there are n snapshots in total. $\beta^i(t)$ and $\phi^i(\boldsymbol{x})$ represent the time-varying coefficient and basis function for the i-th mode. The basis function (POD mode) $\phi^i(\boldsymbol{x})$ can be interpreted as the extracted spatial coherent structure of flow field. The temporal coefficient $\beta^i(t)$ can be interpreted as the dynamic evolving of this mode, and a spectral analysis of $\beta^i(t)$ is able to identify flow periodicity and quantify dominant frequencies of the specific mode. The total number of the extracted POD modes is equal to the number of available snapshots n. And as indicated

in Eq. (3.20), the reconstruction process with all modes is able to recover the flow field with no truncation error.

From the matrix notation, the flowfield $f(x,t)$ can be denoted as $X \in R^{n\times m}$,

$$X = \begin{bmatrix} f_{1,t=1} & f_{2,t=1} & \cdots & f_{m,t=1} \\ f_{1,t=2} & f_{2,t=2} & \cdots & f_{m,t=2} \\ \vdots & \vdots & \ddots & \vdots \\ f_{1,t=n} & f_{2,t=n} & \cdots & f_{m,t=n} \end{bmatrix} \tag{3.21}$$

while n is the number of temporal snapshots, and m is the mesh size. Flow field X can be uniquely decomposed in the form of Singular Value Decomposition (SVD) as:

$$f(x,t) = X = U\Lambda V^T \tag{3.22}$$

where U is a $n \times k$ orthonormal matrix spanning A's column space $\mathrm{im}(A)$, Λ is a $k \times k$ diagonal matrix of singular values, and V is $m \times k$ orthonormal matrix spanning A's row space $\mathrm{im}(A^T)$. k represents the first k ranked modes, and in this study, $k = n$.

If we multiply X by X^T, then

$$\begin{aligned} XX^T &= U\Lambda V^T (U\Lambda V^T)^T \\ &= U\Lambda \mathrm{V}^{\mathrm{T}} V \Lambda^T U^T \\ &= U\Lambda^2 U^T \end{aligned} \tag{3.23}$$

multiply both sides by U

$$XX^T U^T = U\Lambda^2 U^T U$$
$$= \Lambda^2 U \quad \textbf{(3.24)}$$

So eigenmatrix (the collection of eigenvectors) for XX^T is $U \in R^{n\times n}$, the eigenvalues are the diagonal terms of $\lambda = \Lambda^2 \in R^{n\times n}$

Correspondingly, modes and coefficients from conventional POD can be written as:

$$\Phi = X^T U \, , \quad \textbf{(3.25)}$$

$$B = \frac{(\phi)^T X}{\Lambda^2} = \frac{(XU)^T X}{\Lambda^2} = \frac{U^T X^T X}{\Lambda^2} = U^T \frac{U\Lambda^2 U^T}{\Lambda^2} = U^T \, , \quad \textbf{(3.26)}$$

$\Phi \in R^{m\times n}$ is the representation of Multiplication of POD modes and coefficients with full modes will guarantee a reconstruction with no error.

$$\Phi B = X^{\mathrm{T}} \quad \textbf{(3.27)}$$

If the reconstruction is written in index notation,

$$\hat{f}(\boldsymbol{x}, t) = \sum_{k=1}^{n} \phi_k(\boldsymbol{x})\beta_k(t) \quad \textbf{(3.28)}$$

3.3.2 Common Proper Orthogonal Decomposition (CPOD)

Common Proper Orthogonal Decomposition (CPOD) was first proposed by Mak et al. [78] and Yeh et al. [79]. The kriging surrogate model combines machine-learning techniques, statistical modeling, and a physics-driven data-reduction method.

The mathematical details for CPOD are provided below [78]. It is supposed that n simulations are conducted at various design geometries $\boldsymbol{d}_1, \dots, \boldsymbol{d}_n$ and $f(\boldsymbol{x}, t; \boldsymbol{d}_i)$ is the simulated flowfield at design point $\boldsymbol{d}_i$ for a given time *t* and spatial coordinate $\boldsymbol{x}$. The *k*-th CPOD mode is defined as

$$\begin{aligned} \phi_k(\boldsymbol{x}) = \underset{\psi:\|\psi\|_2=1}{\operatorname{argmax}} \sum_{i=1}^{n} \int \left[\int \phi(\boldsymbol{x}) f(\boldsymbol{x}, t; \boldsymbol{d}_i) d\boldsymbol{x} \right]^2 dt\,, \\ s.t. \int \phi(\boldsymbol{x}) \phi_l(\boldsymbol{x}) d\boldsymbol{x} = 0, \forall\, l < k. \end{aligned} \tag{3.29}$$

Here, the map $\mathcal{M}_i$: $\mathbb{R}^2 \rightarrow \mathbb{R}^2$ is the transformation that linearly scales spatial features from the common geometry $\boldsymbol{d}$ to the *i*-th geometry $\boldsymbol{d}_i$. The sequence of POD coefficients is defined as

$$\beta_k(\boldsymbol{d}_i, t) = \int \phi(\boldsymbol{x}) f(\boldsymbol{x}, t; \boldsymbol{d}_i) d\boldsymbol{x} \tag{3.30}$$

with the corresponding POD expansion using *K* modes given by

$$f^{(K)}(\boldsymbol{x}, t; \boldsymbol{d}_i) = \sum_{k=1}^{K} \beta_k(\boldsymbol{d}_i, t) \phi_k(\boldsymbol{x}) \tag{3.31}$$

The transformation allows for the extraction of common basis functions. In addition, the obtained modes can be used to identify key mechanisms of flow dynamics. It should

be noted that reacting-flow simulations are characterized by additional dimensionless parameters, and linear mapping may not perform well when combustion is involved.

Two computational challenges must be addressed to implement this methodology. As previously mentioned, to calculate the inner product of the snapshots from different simulation cases, a common set of spatial grid points is needed. Not only does the calculation of the inner product become a computational bottle-neck, as the covariance matrix consists of snapshots from each simulation, the number of modes required to capture a certain energy level is significantly increased relative to an individual simulation, which can capture more than 95% of the total energy with approximately six modes [150]. The computation of CPOD modes and associated time-varying coefficients requires eigen-decomposition of a $nT \times nT$ matrix, where n is the number of simulation cases and T is the number of snapshots. This usually requires $O(n^3T^3)$ computation work. A typical value for T is 1,000 snapshots spanning 10 ms, which achieves a frequency resolution of 100 Hz. An iterative method of eigen-decomposition based on periodic restarts of Arnoldi decompositions is then used here to quickly calculate the first few eigen-vectors with the largest eigenvalues. These eigenvalues can also be interpreted as the amount of "energy," as defined by the inner product used to calculate the covariance matrix. For a particular data reconstruction using a linear combination of POD modes and associated time-varying coefficients, there is reconstruction error, which decreases when more eigen-vectors, or POD modes, are included.

After the data decomposition step, a kriging model is applied to the CPOD time-varying coefficients $\beta_k(\boldsymbol{d}_i, t)$, k-th CPOD coefficient at setting $\boldsymbol{d}$ and time step t,. With

the mean and variance computable in closed form, UQ and confidence intervals (CI) can be calculated easily. The mathematical approach of kriging is described in Section 3.2. For notational simplicity, let $\beta(\boldsymbol{d})$ denote $\beta_k(\boldsymbol{d}, t)$, the k-th CPOD coefficient at setting $\boldsymbol{d}$ and time step t.

It is supposed that the function values $\boldsymbol{\beta}^{(n)} = [\beta(\boldsymbol{d}_i)]_{i=1}^{n}$ are observed at input settings $\{\boldsymbol{d}_i\}_{i=1}^{n}$ and that $\boldsymbol{d}_{new}$ is a new setting for which prediction is desired. Conditional on the observed values $\boldsymbol{\beta}^{(n)}$, the best linear unbiased estimator of $\beta_k(\boldsymbol{d}_{new}, t)$, k-th CPOD coefficient at setting $\boldsymbol{d}$ and time step t, can be shown to be [148]

$$\hat{\beta}_k(\boldsymbol{c}_{new}, t) = \mu + \boldsymbol{r}_{new}^T \boldsymbol{R}^{-1}\left(\boldsymbol{\beta}^{(n)} - \mu \mathbf{1}\right) \tag{3.32}$$

Here, $\mathbf{1}$ is the n x 1 vector of ones, $r_{new} = [R(\boldsymbol{d}_i, \boldsymbol{d}_{new})]_{i=1}^{n}$ is the n x 1 vector of correlations between the new point and sampled points, and $\boldsymbol{R} = \left[R\left(\boldsymbol{d}_i, \boldsymbol{d}_j\right)\right]_{i=1}^{n}{}_{j=1}^{n}$ is the covariance matrix for the sampled points. Such a predictor minimizes the mean-squared prediction error, a commonly-used criterion for prediction error. In the context of flowfield prediction, employing this kriging estimator allows for obtaining accurate flow predictions from the CPOD coefficients.

In CPOD emulation process, the kriging models are trained independently over each time step, due to the inherent fine-scale temporal resolution of the simulation. This time-independence assumption is made for two reasons. First, the fully developed flow is treated as statistically stationary and has high-frequency resolution, so no practical value exists for estimating temporal correlations. Second, as in the high-fidelity simulation

procedure, the assumption of time-independence allows the exploitation of parallel computation in training the emulator model. Once the model is trained, the predictor is used with the CPOD expansion to predict the flow evolution at a new design point:

$$\hat{f}(\boldsymbol{x}, t; \boldsymbol{d}_{new}) = \sum_{k=1}^{K} \hat{\beta}_k(\boldsymbol{d}_{new}, t)\phi_k(\boldsymbol{x}) \,. \tag{3.33}$$

It is worth noting that the computation time of the proposed model is orders of magnitude smaller than that of LES. Simulation data that typically takes a week, or around 30,000 CPU hours, to acquire can be predicted by the model with an associated uncertainty in under an hour. The procedure of CPOD is stated in Algorithm 1.

Algorithm 1 Common proper orthogonal decomposition (CPOD)

DATA:		For each design setting in $\{\boldsymbol{x}_i\}_{i=1}^{H}$, the flow evaluation at each spatial location and time step $f(\boldsymbol{x}_i, \boldsymbol{u}_j, t_q)$ is provided, where $\{\boldsymbol{u}_j\}_{j=1}^{K}$ is the spatial location and $\{t_q\}_{q=1}^{m}$ is the time step. $\boldsymbol{x}_i \in \mathbb{R}^{n\times m}$ and $n \gg m$.
TRAINING:	*Step 1:*	Concatenate all *H* set of training cases along the time direction and create a huge matrix $\boldsymbol{X} \in \mathbb{R}^{n\times mH}$. Then, calculate the CPOD covariance by $\mathcal{C} = \frac{\boldsymbol{X}^T\boldsymbol{X}}{n-1}$ and $\mathcal{C} \in \mathbb{R}^{mH\times mH}$. Proper orthogonal decomposition (POD) based on singular-value decomposition (SVD) with $\mathcal{C}$ is performed and can be written as $f(\boldsymbol{X}, \boldsymbol{U_j}, T_Q) = \sum_{k=1}^{K} \hat{\beta}^k(\boldsymbol{X}, T_Q)\tilde{\phi}^k(\boldsymbol{X}, \boldsymbol{U_j})$ for the first dominated K mode, $T_Q = \{t_{1,q}^T, \dots, t_{H,q}^T\}^T$, and $t_q \in \mathbb{R}^{m\times K}$

		Note: $\hat{\beta}^k(\boldsymbol{X}, T_Q) \in \mathbb{R}^{mH\times K}$ and $\tilde{\phi}^k(\boldsymbol{X}, \boldsymbol{U_j}) \in \mathbb{R}^{n\times K}$
	Step 2:	For each time step, t_q, and each mode, k, perform an ordinary kriging model on $\{\tilde{\beta}^k(\boldsymbol{X}, t_{1,q}), \dots, \tilde{\beta}^k(\boldsymbol{X}, t_{H,q})\}$ with inputs $\{\boldsymbol{x}_1, \dots, \boldsymbol{x}_H\}$ and the predictive function at an untried setting, x_{new}, $\hat{\beta}^k(\boldsymbol{x}_{new}, t_q)$.
	Step 3:	Since all training cases are concatenated together to create a huge matrix, $\boldsymbol{X} \in \mathbb{R}^{n\times mH}$, for CPOD covariance, all training cases share the same set of POD modes, $\tilde{\phi}^k(\boldsymbol{X}, \boldsymbol{U_j}) \in \mathbb{R}^{n\times K}$, which is also applied for the new prediction case.
PREDICTION:	At an untried setting x_{new}, compute $\hat{\beta}^k(\boldsymbol{x}_{new}, t_q), q = 1, \dots, m; k = 1, \dots, K$, and $\tilde{\phi}^k(\boldsymbol{X}, \boldsymbol{U_j}), j = 1, \dots, J; k = 1, \dots, K$, then $f(\boldsymbol{x}_{new}, \boldsymbol{U_j}, t_q) = \sum_{k=1}^{K} \hat{\beta}^k(\boldsymbol{x}_{new}, t_q)\tilde{\phi}^k(\boldsymbol{X}, \boldsymbol{U_j})$, where $j = 1, \dots, J$ and $q = 1, \dots, m$.	

3.3.3 Kernel-Smoothed Proper Orthogonal Decomposition (KSPOD)

This section introduces the idea of KSPOD, which combines statistical modeling with a data-reduction method to obtain a reduced-basis model. The proposed KSPOD method can be viewed as a generalization of POD used for flow emulation; POD decomposes the flowfield into an expansion of spatial eigenfunctions, called POD modes, and corresponding time-varying coefficients. For n snapshots, such a decomposition can be written in the following form:

$$f(\boldsymbol{x}, t) = \sum_{k=1}^{n} \beta_k(t)\phi_k(\boldsymbol{x}) \,. \tag{3.34}$$

The approximation form is

$$f(\boldsymbol{x},t) \approx \sum_{k=1}^{K} \beta^k(t)\phi^k(\boldsymbol{x}) \,, \tag{3.35}$$

where $f(\boldsymbol{x},t)$ is the simulated flowfield at spatial location $\boldsymbol{x}$ and time t, and $\beta^k(t)$ and $\phi^k(\boldsymbol{x})$ represent the time-varying coefficient and basis function for the i-th mode, respectively. As indicated in Equation (3.35), the expansion is typically truncated at the first K terms, where $K < n$ is chosen such that the reconstructed flowfield retains a desired degree of accuracy. In practice, the time-varying coefficients and basis functions are obtained through an eigen-decomposition of the inner product of a flowfield variable [151]. Equation (3.35) can be viewed as the optimal decomposition of $f(\boldsymbol{x},t)$ using a basis expansion of K terms.

In CPOD, the emulator cannot predict detailed structures of spatiotemporal evolving flow. The goal of building an improved emulator is to employ the flow features extracted using POD within a statistical framework, allowing the training of an emulator for flow prediction. To this end, the popular machine-learning technique GPR, kriging, which is described in the previous sections, is employed to predict POD modes and time-varying coefficients at a new design setting. The equation is written as

$$\hat{\beta}_k(\boldsymbol{c}_{new},t) = \mu + \boldsymbol{r}_{new}^T \boldsymbol{R}^{-1}\left(\boldsymbol{\beta}^{(n)} - \mu\mathbf{1}\right). \tag{3.36}$$

Here, $\mathbf{1}$ is the n x 1 vector of ones, $r_{new} = [R(\boldsymbol{d}_i, \boldsymbol{d}_{new})]_{i=1}^{n}$ is the n x 1 vector of correlations between the new point and sampled points, and $\boldsymbol{R} = \left[R\left(\boldsymbol{d}_i, \boldsymbol{d}_j\right)\right]_{i=1}^{n}{}_{j=1}^{n}$ is the covariance matrix for the sampled points.

While the predictor in Equation (3.36) is simple to evaluate when the desired function $\hat{\beta}_k(\boldsymbol{c}_{new}, t)$ is a scalar function, it becomes much more difficult to evaluate for the problem at hand, where the desired function is spatiotemporal. In particular, there are over 400,000 grid points and 1,000 timesteps for each simulation case, and performing kriging for each grid point and time step would be impractical and time consuming. From a statistical perspective, the use of separate kriging models over each grid point and time step also leads to a serious problem of over-parametrization (as each model requires d correlation parameters), which then results in poor prediction performance for the trained model. Accounting for these challenges and the grid systems remaining static for all simulated cases, an improved kriging-based model is introduced that combines the POD information from each case in the form of a "*weighting number*."

The key idea in KSPOD is to apply the kriging equation, to predict the weight of each POD mode at a new design setting. To this end, the observations of $\hat{\beta}_k(\boldsymbol{c}_{new}, t)$ are now assumed to be the unit vector $\boldsymbol{e_i}$, where $\boldsymbol{e_i}$ is an n-vector with 1 in its i-th element and 0 elsewhere. Intuitively, this quantifies the fact that the POD information extracted in the i-th design setting corresponds to only that setting and not the other $n-1$ settings. With this in mind, the resulting predictor in Equation (3.36) can be viewed as the predicted weight for that particular POD term at a new design setting $\boldsymbol{d}_{new}$, which is denoted as $\widehat{w}_{new,i}$. This procedure is repeated for each of the n unit vectors, $(\boldsymbol{e_i})_{i=1}^{n}$, from which the n weighting numbers $\left(\widehat{w}_{new,i}\right)_{i=1}^{n}$ can be obtained. They are subsequently used to predict the new POD modes and coefficients through a weighted average of the extracted modes

and coefficients at the new design settings. Once the model is trained, the predictor is used with the KSPOD expansion to predict the flow evolution at a new design point, that is,

$$\hat{f}(\boldsymbol{x}, t; \boldsymbol{d}_{new}) = \sum_{k=1}^{K} \hat{\beta}_k(\boldsymbol{d}_{new}, t)\hat{\phi}^k(\boldsymbol{d}_{new}, \boldsymbol{x}) \,, \tag{3.37}$$

and

$$\hat{\phi}^k(\boldsymbol{d}_{new}, \boldsymbol{x}_j) = \frac{\sum_{i=1}^{n} \hat{w}_i(\boldsymbol{d}_{new})\phi^k(\boldsymbol{d}_i, \boldsymbol{x}_j)}{\sum_{i=1}^{n} \hat{w}_i(\boldsymbol{d}_{new})} \,. \tag{3.38}$$

Algorithm 2 outlines the detailed steps in the KSPOD algorithm. First, POD is performed for each simulated geometry to extract the coherent structures. Next, the coefficients of POD modes are trained by ordinary kriging models using the Gaussian kernel as the correlation function, with the correlation parameter tuned using MLE. The predictive function can be constructed. The weighting numbers are also trained using the procedure described above. Lastly, the POD modes and coefficients are predicted, which are used to "reconstruct" the flowfield at the new design setting $\boldsymbol{d}_{new}$.

Algorithm 2 Kernel-smoothed proper orthogonal decomposition (KSPOD)

DATA:	For each design setting in $\{\boldsymbol{c}_i\}_{i=1}^{n}$, the flow evaluation at each spatial location and time step $f(\boldsymbol{x}_j, t_q; \boldsymbol{c}_i)$ is provided, where $\{\boldsymbol{x}_j\}_{j=1}^{J}$ is the spatial location and $\{t_q\}_{q=1}^{m}$ is the time step.	
TRAINING:	*Step 1:*	For each design setting $\boldsymbol{x}_i$, proper orthogonal decomposition (POD) is performed and can be written as $f(\boldsymbol{x}_j, t_q; \boldsymbol{c}_i) = \sum_{k=1}^{K} \beta^k(\boldsymbol{c}_i, t_q)\phi^k(\boldsymbol{c}_i, \boldsymbol{x}_j)$.
	Step 2:	For each time step t_q and each mode k, an ordinary kriging model is performed on

		$\{\beta^k(\boldsymbol{c}_1, t_q), \dots, \beta^k(\boldsymbol{c}_n, t_q)\}$ with inputs $\{\boldsymbol{c}_1, \dots, \boldsymbol{c}_n\}$. The predictive function at an untried setting x_{new} is $\hat{\beta}^k(\boldsymbol{c}_{new}, t_q)$.
	Step 3:	For$i = 1, \dots, n$, an ordinary kriging model is performed on $\boldsymbol{e}_{\mathrm{i}}$ with inputs $\{\boldsymbol{c}_1, \dots, \boldsymbol{c}_n\}$, and the predictive function at an untried setting $\boldsymbol{x}_{new}$ is $\widehat{w}_i(\boldsymbol{c}_{new})$. Therefore, for each spatial location u_j and each mode k, the predictive function of $\phi^k(\boldsymbol{c}_{new}, \boldsymbol{x}_j)$ is $\hat{\phi}^k(\boldsymbol{c}_{new}, \boldsymbol{x}_j) = \sum_{i=1}^{n} \widehat{w}_i(\boldsymbol{c}_{new})\phi^k(\boldsymbol{c}_i, \boldsymbol{x}_j) / \sum_{i=1}^{n} \widehat{w}_i(\boldsymbol{c}_{new})$.
PREDICTION:	At an untried setting x_{new} is computed as $\hat{\beta}^k(\boldsymbol{c}_{new}, t_q), q = 1, \dots, m; k = 1, \dots, K$ and $\hat{\phi}^k(\boldsymbol{c}_{new}, \boldsymbol{x}_j), j = 1, \dots, J; k = 1, \dots, K$. Then, $f(\boldsymbol{x}_j, t_q; \boldsymbol{c}_{new}) = \sum_{k=1}^{K} \hat{\beta}^k(\boldsymbol{c}_{new}, t_q)\hat{\phi}^k(\boldsymbol{c}_{new}, \boldsymbol{x}_j)$, where $j = 1, \dots, J$ and $q = 1, \dots, m$.	

This method is termed KSPOD, because the kriging here does not apply the weighting number $\widehat{w}_{new,i}$ to the flowfield directly. The vortex structures within the flowfield are a combination of waves with different frequencies, amplitudes, and phases. If the weighting number is used on the flowfield directly, the two datasets may cancel each other out during the regression process, thereby eliminating useful information. The phase difference can be observed in POD modes as well. Application of weighting functions to POD modes with a kernel-smoothed algorithm can prevent the phase cancelation and retain important flow physics. Once the emulator model is trained, it can be used with the KSPOD model for predicting the flow evolution at a new design point. The computation cost is reduced by several orders of magnitude. The high-fidelity original simulations take around

107,000 CPU hours for each case. The trained model can evaluate a new flowfield in 0.02 CPU hours.

3.3.4 Common Kernel-Smoothed Proper Orthogonal Decomposition (CKSPOD)

CPOD, KSPOD are reviewed in the previous sections. As reviewed in the Introduction, CKSPOD outperforms both methods in terms of its ability to provide better prediction of instantaneous flow field in reasonable turnaround time [81]. In this section, the algorithms and implementations of CKSPOD will be described in detail.

A schematic diagram of the framework for the CKSPOD methodology is shown in Figure 3.1. The framework is composed of four steps, data manipulation, reduction, training, and reconstruction. Compared with the previous study [81], significant improvements have been made to CKSPOD, including the introduction of common grid technique and physics-based constraints (denoted in Figure 3.1 in red). These novelties will be discussed in the remainder of the current section.

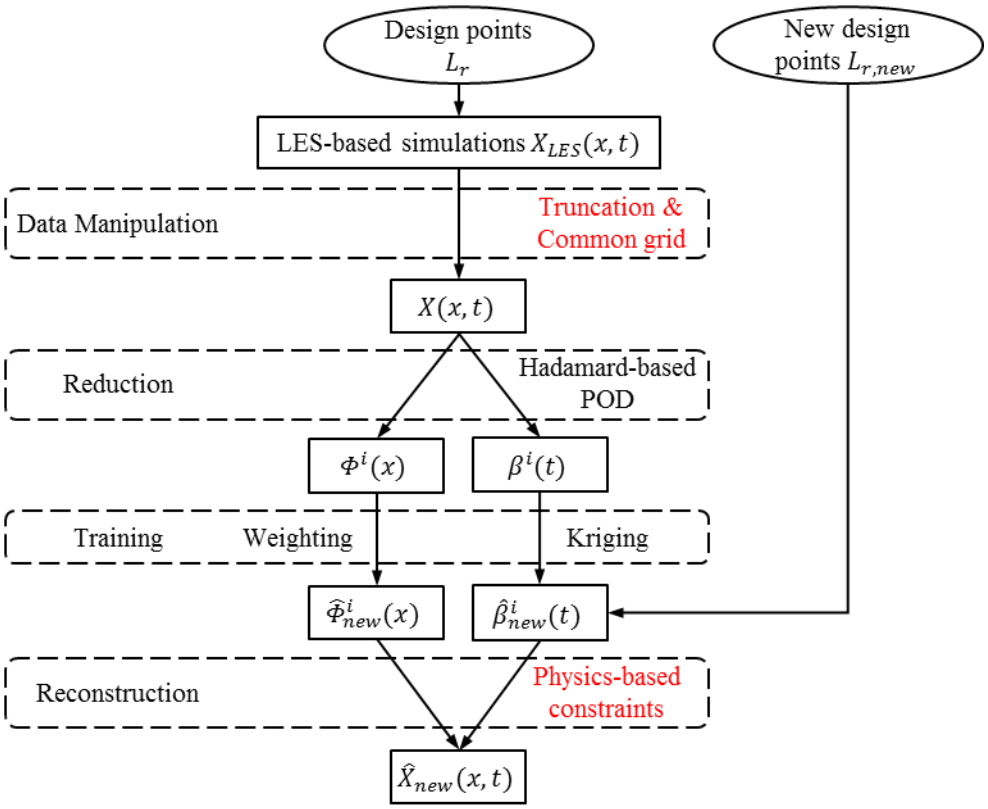

Figure 3.1 CKSPOD Methodology

In the data manipulation step, training data for each case is truncated to the region of interest. As shown in Figure 3.2a, the high-fidelity simulation utilizes a large computational domain (black line) to avoid the significant influences of boundary conditions on the flow field, while in this study, only the region of interest (red line) is emulated. Moreover, as each individual case has a unique geometry and a unique grid system, this study introduces the concept of common grid interpolation, as specified in Figure 3.2b. A common grid system, with the densest mesh among all cases, is selected as the benchmark. For each case, the region of interest is divided into four regions, shown with different colors. Each region is adjusted and rescaled to fit to the common grid.

In the reduction step, the flow field is reduced into a set of modes. Among many reduction techniques, proper orthogonal decomposition (POD) [149] is considered due to its successful application to similar injectors [8, 152]. Moreover, when using full modes, POD is able to reconstruct the flow field with no error. In the present study, a POD-like mode decomposition method is employed. In this following paragraphs, the authors will first overview the conventional POD method, followed by the mathematical description of the current POD-like approach.

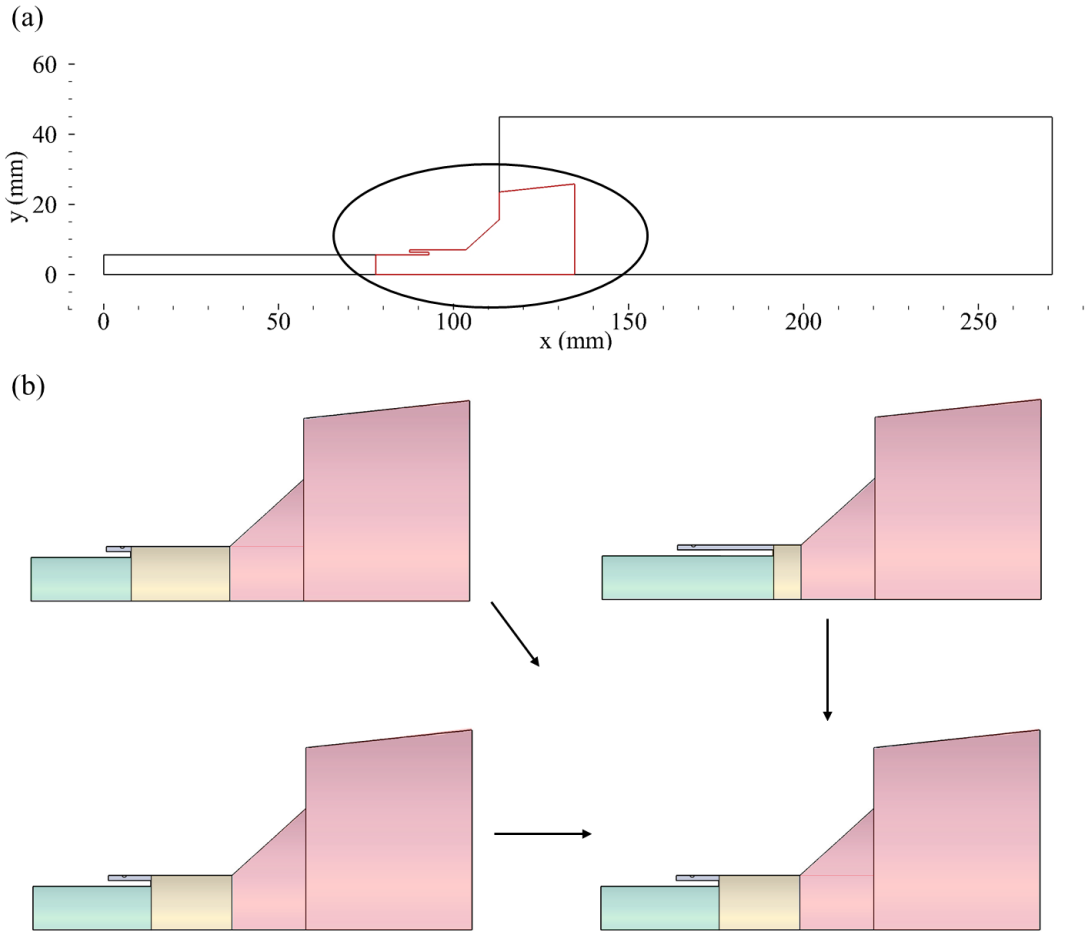

Figure 3.2 Sketch for (a) computational domain and (b) common grid technique

For CKSPOD, different from the conventional POD, the common covariance matrix $\mathbb{C}$ is constructed by the Hadamard product of the covariance matrix of each case. Hadamard, denoted as $\circ$, is the operation that takes two matrices of the same dimensions and conducts point-to-point multiplication, as indicated in Eq. (3.39)

$$\begin{bmatrix} a_{11} & a_{12} \\ a_{21} & a_{22} \end{bmatrix} \circ \begin{bmatrix} b_{11} & b_{12} \\ b_{21} & b_{22} \end{bmatrix} = \begin{bmatrix} a_{11}b_{11} & a_{12}b_{12} \\ a_{21}b_{21} & a_{22}b_{22} \end{bmatrix}. \tag{3.39}$$

Based on the definition of Hadamard product, the common covariance matrix can be written as

$$\begin{aligned} \mathbb{C} = C_1 \circ C_2 \circ \ldots \circ C_H &= \left(\frac{V_1 \Lambda_1^2 V_1^T}{n-1}\right) \circ \ldots \circ \left(\frac{V_H \Lambda_1^2 V_H^T}{n-1}\right) \\ &= \left(\frac{1}{n-1}\right)^H (V_1 L_1 V_1^T) \circ \ldots \circ (V_H L_H V_H^T) = \mathbb{V}\mathbb{L}\mathbb{V}^T \end{aligned} \tag{3.40}$$

C_i represents the covariance matrix for case i, L_i denotes the square of eigenvalues, $L_i = \Lambda_i^2$, and H is the total number of cases.

We define Π as the notation of Hadamard product, and the covariance $\mathbb{C}$ can be organized as:

$$\mathbb{C} = \Pi_{j=1}^{H} C_j = C_i \circ \Pi_{\substack{j=1 \\ j \neq i}}^{H} C_j = \frac{V_i L_i V_i^T}{n-1} \circ \Pi_{\substack{j=1 \\ j \neq i}}^{H} C_j = \mathbb{V}\mathbb{L}\mathbb{V}^T \tag{3.41}$$

Based on the common covariance $\mathbb{C}$, the new modes for Case i can be represented as:

$$\tilde{\phi}_i(x) = X_i\mathbb{V} = X_i V_i \frac{L_i V_i^T}{n-1} \circ \left(\Pi_{\substack{j=1 \\ j\neq i}}^{H} C_j \right) \mathbb{V}\mathbb{L}^{-1} \cong X_i V_i \mathcal{T} = \phi(x)\mathcal{T} \tag{3.42}$$

therefore,

$$\mathcal{T} = \frac{L_i V_i^T}{n-1} \circ \left(\Pi_{\substack{j=1 \\ j\neq i}}^{H} C_j \right) \mathbb{V}\mathbb{L}^{-1}\,, \tag{3.43}$$

can be viewed as a CKSPOD transfer matrix that is imposed on the conventional POD mode. After normalization, the new basis function and coefficients for mode k of case i can be written as

$$\tilde{\Phi}_i^k(x) = \frac{\tilde{\phi}^k(x)}{norm(\tilde{\phi}^k(x))} \tag{3.44}$$

$$\tilde{\beta}_i^k(t) = \mathbb{V}^T norm(\tilde{\Phi}^k(x)) \tag{3.45}$$

After Hadamard-based data reduction, kriging is then employed in the third step of Figure 3.1. The basic idea of kriging is to model unobserved responses using a Gaussian Process (GP) governed by a preset covariance function. The response surface of the trained kriging model can then be obtained by applying data-tuned weights to radial basis functions centered at observed points. The design variable (in this study, recess length) is the predictor variable, and the coefficient for a specific mode is the response variable. Given a new design point, kriging is able to predict new coefficient based on the equations in [81].

Another important issue in the training step, the prediction of new mode $\hat{\phi}_{new}^k(x)$, is solved through the introduction of "weighting number" $\widehat{w}_i$, as denoted in the equation below

$$\hat{\phi}_{new}^{k}(x) = \sum_{i=1}^{n} \widehat{w}_i(d_{new}, d_i)\tilde{\phi}_i^k(x) \,/\, \sum_{i=1}^{n} \widehat{w}_i(d_{new}, d_i) \tag{3.46}$$

d_i denotes the design point of Case i. The idea of weighting number $\widehat{w}_i(d_{new}, d_i)$ is based on the assumption that the cases close in the design space have similar flow dynamics. $\widehat{w}_i(d_{new}, d_i)$ is a function of only the new design point and existing point of Case i, and in this study, inverse distance weighting is applied to this number $\widehat{w}_i(d_{new}, d_k) = \frac{1}{|d_{new} - d_k|^2}$.

For the last step, the trained POD coefficients and weighted POD modes are employed to reconstruct the spatiotemporal flow field of the new case. This reconstruction process is able to capture detailed coherent structures, provide accurate 'relative' flow field, but it does not guarantee fluid properties in the flow field to be physical. For example, the reconstructed density field is able to capture the detailed flow structure, but some snapshots may have non-physical local negative densities. A physics-based correction f is thus implemented to avoid such circumstances. The flow variable (density, velocity, etc) at the kerosene and GOX inlets are constant regardless of the design parameter and operating conditions, and are chosen as benchmark values. Based on the two values, an interpolation is implemented to the flow field to ensure a physical reconstruction, as indicated in the equation below

$$\hat{X}_{new}(x, t) = f\left(\sum_{i=1}^{n} \hat{\beta}_{new}^{k}(t)\hat{\phi}_{new}^{k}(x)\right) \tag{3.47}$$

The detailed steps of the CKSPOD are outlined in Algorithm 3. First, POD is performed for each simulated flow to extract the coherent structures (step 1 of training process in Algorithm 3). Next, in step 2 of training process, the coefficients of POD modes are trained by ordinary kriging models using the Gaussian kernel as correlation function,

with correlation parameter θ trained with maximum-likelihood. In step 3 of training process, the weighting numbers are trained using the procedure described above. Lastly, in the prediction process, the POD modes and coefficients are predicted at the new design setting $\boldsymbol{x}_{new}$, which yields the flow field at setting $\boldsymbol{x}_{new}$ by reconstruction.

As is the case for any physical or statistical model, there are several implicit assumptions for the proposed method. First, by predicting the i-th POD term of the new design setting using only the information for the i-th POD terms extracted from observed design settings, we assume the ranking of the extracted flow physics from POD to be invariant over different geometry settings. In other words, the flow instability for the first POD mode corresponds to the same coherent structure for all design points, and the same holds for the second modes, third modes, etc. This implicit assumption, as will be reviewed in the following sections, is actually guaranteed by the nature of CKSPOD.

Second, as the weighting function is calculated based on the inverse distance weighting of distance between design points, it should be assumed that cases with similar dynamic characteristics should cluster in the design space, which is also confirmed in the following sections.

The computational efficiency of the similar emulation methods have been described in previous studies [79-81]. For the current study, the high-fidelity simulation of GCLSC injector takes ~100,000 CPU hours for the simulation of 10ms (1000 snapshots). For CKSPOD, the computational time is composed of the offline part and online part. The offline calculation, which includes preprocessing, reduction and training, takes ~1 CPU

hour. The online part, when given a new design, takes around 60 seconds of CPU time per snapshot. For both parts, the computational time are dependent on the size of the training data. For the current dataset, the speedup of CKSPOD is in the order of ~60,000.

Algorithm 3 Common Kernel-smoothed POD (CKSPOD)

DATA:		For each design setting in $\{\boldsymbol{x}_i\}_{i=1}^{H}$, the flow evaluation at each spatial location and time-step $f(\boldsymbol{x}_i, \boldsymbol{u_j}, t_q)$ is provided, where $\{\boldsymbol{u}_j\}_{j=1}^{J}$ is the spatial location and $\{t_q\}_{q=1}^{m}$ is the time-step.
TRAINING:	Step 1:	Calculate hadamard product with covariance matrices from each design setting $\boldsymbol{x}_i$, $\mathbb{C} = \mathrm{cov}(f(\boldsymbol{x}_1), f(\boldsymbol{x}_1)) \circ \mathrm{cov}(f(\boldsymbol{x}_1), f(\boldsymbol{x}_1)) \circ \ldots \circ \mathrm{cov}(f(\boldsymbol{x}_H), f(\boldsymbol{x}_H)) = \mathrm{C}_1 \circ \mathrm{C}_2 \circ \ldots \circ \mathrm{C}_\mathrm{H}$. Proper Orthogonal Decomposition (POD) based on SVD with $\mathbb{C}$ is performed and can be written as $f(\boldsymbol{x}_i, \boldsymbol{u}_j, t_q) = \sum_{k=1}^{K} \hat{\beta}^k(\boldsymbol{x}_i, t_q)\tilde{\phi}^k(\boldsymbol{x}_i, \boldsymbol{u_j})$. Note that: $\widetilde{\Phi}^k(\boldsymbol{x}_i, \boldsymbol{u_j}) = \frac{\tilde{\phi}^k(\boldsymbol{u})}{norm(\tilde{\phi}^k(\boldsymbol{u}))}$ and $\tilde{\phi}^k(\boldsymbol{u}) = A_i\mathbb{V}$; $\tilde{\beta}^k(\boldsymbol{x}_i, t_q) = \mathbb{V}^{\mathrm{T}} norm(\hat{\phi}^k(\boldsymbol{x}_i, \boldsymbol{u_j}))$.
	Step 2:	For each time-step t_q and each mode k, perform an ordinary kriging model on $\{\tilde{\beta}^k(\boldsymbol{x}_1, t_q), \ldots, \tilde{\beta}^k(\boldsymbol{x}_H, t_q)\}$ with inputs $\{\boldsymbol{x}_1, \ldots, \boldsymbol{x}_H\}$, and the predictive function at an untried setting x_{new} is $\hat{\beta}^k(\boldsymbol{x}_{new}, t_q)$
	Step 3:	For $i = 1, \ldots, H$, perform inverse distance weighting of the weighting number of each case based on the design variables $$\widehat{w}_i(d_{new}, d_k) = \frac{1}{\lvert d_{new} - d_k \rvert^2}$$

PREDICTION:	At an untried setting x_{new}, compute $\hat{\beta}^k(\boldsymbol{x}_{new}, t_q), q = 1, \dots, m; k = 1, \dots, K$, and $\hat{\phi}^k(\boldsymbol{x}_{new}, u_j), j = 1, \dots, J; k = 1, \dots, K$, then $f(\boldsymbol{x}_{new}, u_j, t_q) = \sum_{k=1}^{K} \hat{\beta}^k(\boldsymbol{x}_{new}, t_q)\hat{\phi}^k(\boldsymbol{x}_{new}, u_j)$, where $j = 1, \dots, J$ and $q = 1, \dots, m$.

CHAPTER 4.

GAS-CENTERED LIQUID-SWIRL COAXIAL INJECTOR FLOW DYNAMICS

The flow dynamics of gas-centered, liquid-swirl coaxial injectors at supercritical conditions are systematically investigated using the large eddy simulation technique. Gaseous oxygen is axially injected into the center post at a temperature of 687.7K, while kerosene is tangentially introduced into the coaxial annulus at a temperature of 492.2K. The operating pressure is 25.3 MPa, well above the thermodynamic critical points of the propellants involved. Detailed flow physics and structures are identified, followed by comprehensive analyses of mechanisms controlling key dynamic characteristics. Special attentions are given to recess region and taper section, where primary mixing occurs. Six cases with varying recess lengths from zero to the maximum possible value are evaluated. Results indicate that the recess length plays a critical role in determining the flow dynamics and mixing behaviors, and the impacts of recess length on dynamic characteristics, momentum and mass transfer, and mixing efficiencies are discussed in detail.

4.1 Grid Independence Study

The theoretical/numerical framework has previously been validated against a variety of supercritical fluid flow problems [21, 125, 150, 153, 154]. In order to ensure appropriate resolution of flow physics, a grid independence study was carried out for Case 3 (the baseline case). Three different grid levels were tested. As the grid level increases by one, the grid size decreases by half in both the axial and radial directions. The total number of

grid points thus increases four times accordingly, ranging from 0.58×10^5 (Level 1) to 9.26×10^5 (Level 3). Table 4.1 summarizes the numbers of finite-volume cells in the GOX post, fuel passage, mixing cup, and downstream domain, respectively. The grid points are clustered in regions with stiff flow variable gradients and toward the walls, to adequately treat boundary layers. The Reynolds number based on the width of the fuel annulus ξ and kerosene properties is

$$Re_\delta = \frac{\rho_f U_f \delta}{\mu_f} = 4.14 \times 10^4 \quad \textbf{(4.1)}$$

The corresponding Kolmogorov and Taylor microscales are:

$$\eta = \delta \cdot Re_\delta^{-3/4} = 0.24\ \mu m \quad \textbf{(4.2)}$$

$$\lambda = \sqrt{10}\delta \cdot Re_\delta^{-1/2} = 10.88\ \mu m \quad \textbf{(4.3)}$$

The intermediate Level 2 grid has a grid size of 5 μm near the injector wall in the mixing cup, and 10 μm near the fuel shielding collar rim in the radial direction. Both sizes are comparable with the Taylor microscale and fall in the inertial subrange of the turbulent kinetic energy spectrum.

Table 4.1 Numerical grid matrices

	GOX post	Fuel passage	Mixing cup	Downstream	Total cell number
Level 1	224×64	56×24	160×112	160×160	0.58×10^5
Level 2	448×128	122×48	320×224	320×320	2.31×10^5
Level 3	896×256	224×6	640×448	640×640	9.26×10^5

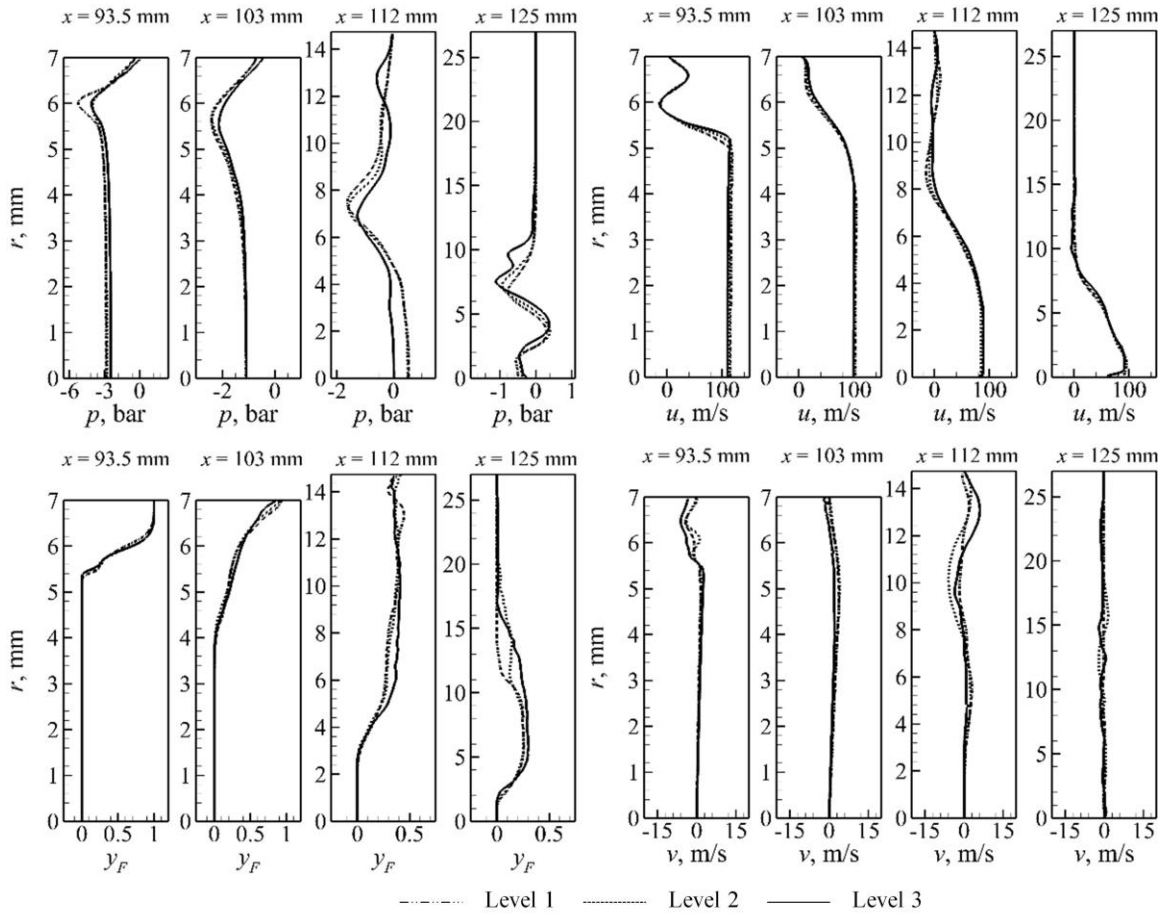

Figure 4.1 Effect of grid resolution on radial distributions of mean gauge pressure, kerosene mass fraction, and axial and radial velocity components at different axial locations for three different grid levels (Case 3)

Figure 4.1 compares the radial distributions of the mean gauge pressure, kerosene mass fraction, and axial and radial velocities at different axial locations for the three different grid levels for Case 3. The reference pressure is set as 253.0 bar. Good agreement is observed among the mean profiles, except at x = 112 mm in the taper section and x = 125 mm at the injector exit, where sudden geometric change induces strong flow distortions. The discrepancy in the fuel mass fraction at these regions is especially apparent because of the unsteady mixing process, which is not fully captured by the LES calculations. Among the three grid resolutions, Level 2 is selected for subsequent

calculations in the present study as a tradeoff between computational efficiency and accuracy. The time step is fixed at 2.0×10^{-7}s to ensure sufficient temporal accuracy. The local Courant-Friedrichs-Lewy (CFL) number varies in the range of 0.1-0.5, depending on local flow velocities and grid sizes.

4.2 Flow Structures

For all of the cases, calculations are initiated by the injection of GOX into GOX post at $t = 0$. Kerosene injection is activated at $t = 9.0\ ms$, after the GOX flow has completed its transient stage. The flowfield reaches its stationary state at around t = 12.0 ms, when the kerosene/GOX mixing field is fully established. Figure 4.2 shows instantaneous fields of kerosene mass fraction, gauge pressure, and temperature at t = 15.0 ms for Case 1 (no kerosene fuel shielding). Figure 4.3 shows the corresponding distributions of density, kerosene mass fraction, vorticity, and pressure gradient in the mixing zone. High-speed, high-temperature GOX flows through the center post, and low-speed, high-density kerosene is discharged from the tangential entry, rendering complicated flow structures in the mixing zone. The injector wall confines the shear layer before the entrance to the taper section. This type of configuration often generates absolute instability and may induce self-sustained global instabilities.[155] Kerosene mixes rapidly with GOX while traveling downstream, and forms large-scale structures. The intricate interactions among fluid injection, mixing, and acoustic resonance induce well-defined pressure oscillations in the GOX post, which gradually lose regularity in the downstream region due to viscous damping and turbulent diffusion.

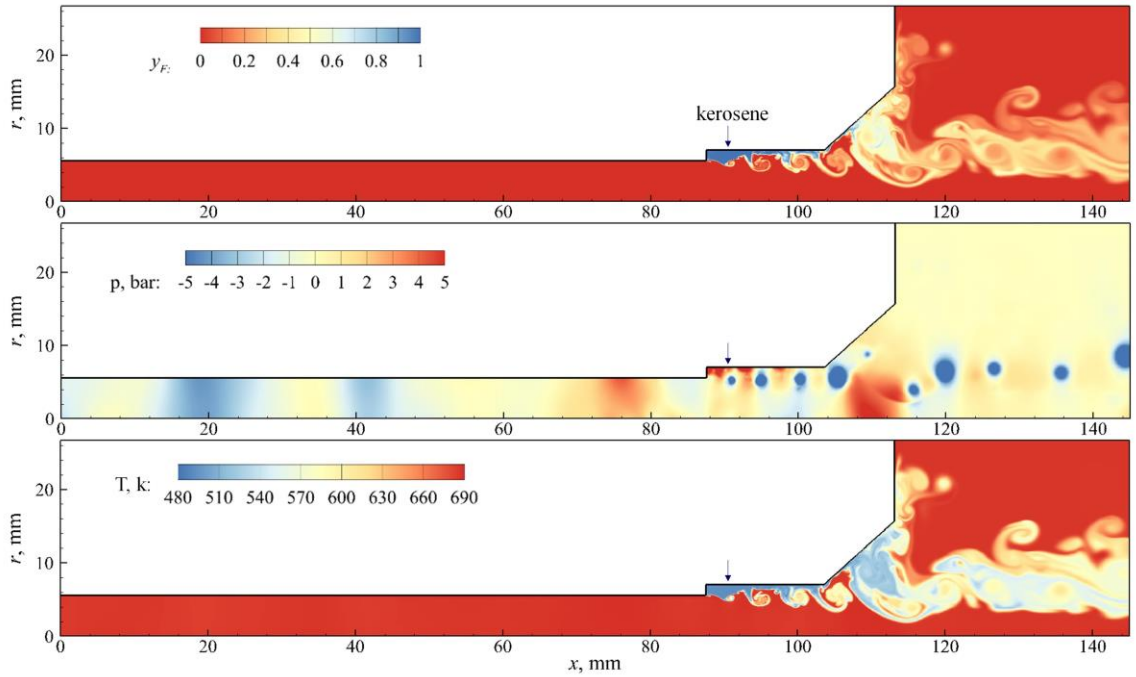

Figure 4.2 Snapshots of kerosene mass fraction, gauge pressure, and temperature fields at t = 15.0 ms (Case 1)

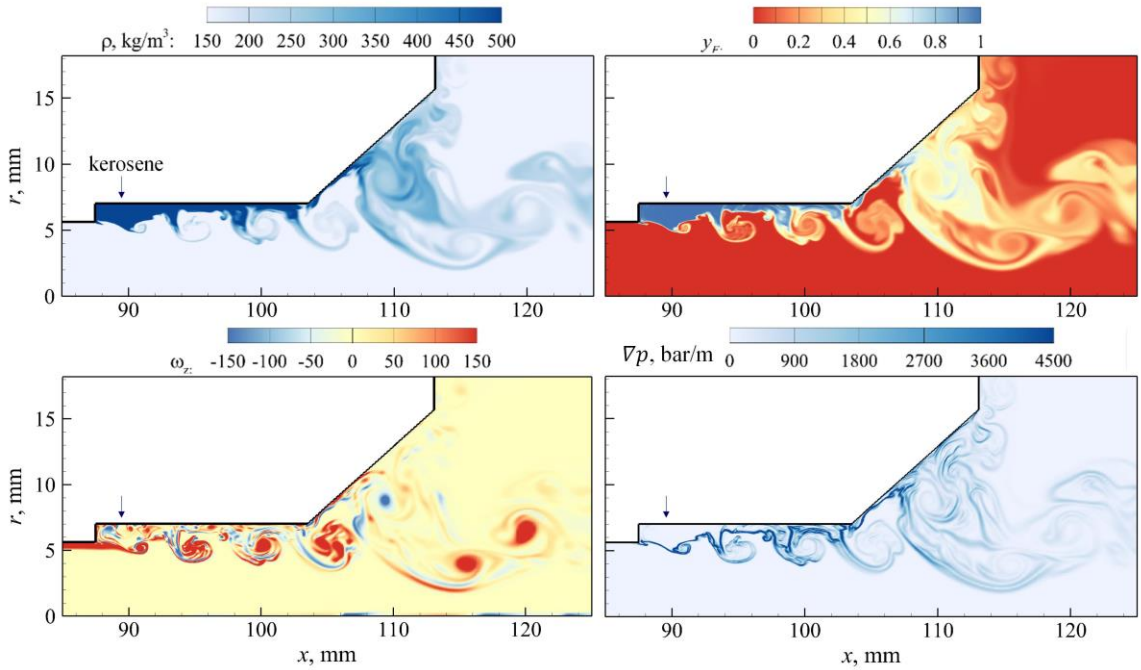

Figure 4.3 Snapshots of density, kerosene mass fraction, vorticity, and pressure-gradient fields at t = 15.0 ms (Case 1)

In the following sections, the flowfield and major flow structures will be analyzed in detail to characterize the mixing layer development. Special attention is given to the region near the GOX post exit, to identify the formation and initial development of the mixing layer.

4.2.1 Density Field

Figure 4.4 shows the evolution of the density field in the mixing zone for Cases 1 and 4, and Figure 4.5 shows the corresponding close-up views near the GOX post exit. At the entrance of the mixing cup, a kerosene film forms along the injector wall because of the swirl-induced centrifugal force. The interface between the low-speed kerosene and the high-speed GOX is intrinsically unstable and features hydrodynamic instability waves.[150] A short distance downstream of the post exit, the longitudinal mode of the hydrodynamic instability grows, forming large-scale billows as the interface moves toward the taper section. Since the GOX stream travels faster than kerosene, the velocity gradient leads to momentum transfer and shear stress on the interface. The resultant vorticity (shown in Figure 4.8 and Figure 4.9) in the azimuthal direction induces counterclockwise-rotating roll-ups in the mixing layer. As these forward-rolling vortices travel downstream, they grow in size and the spacing between successive vortices increases. In Case 1 the vortices are well structured and measure up to 3 mm in diameter before they enter the taper. The traveling speed of the vortices, based on the core locations, is estimated to be 60 m/s, approximately equal to the average of the GOX and kerosene speeds, and consistent with classical mixing layer theories [156]. In Case 4, the kerosene film appears thicker, and the vortices are smaller and less coherent, mainly because of a shorter travel distance.

In a swirling flow, there is a radially outward centrifugal force acting on the mass ($f \sim mu_\theta^2/r$). In order to move the mass closer to the axis (say from r_1 to r_2, where $r_1 = r_2 + \Delta r$ and Δr has an infinitesimal positive value), work must be done, and hence, the mass gains potential as it moves inwards

$$W = -\int_{r_1}^{r_2} f\, dr = -\int_{r_1}^{r_2} \frac{mu_\theta^2}{r} dr = m\overline{u}_\theta^2 \cdot ln\left(\frac{r_1}{r_2}\right) > 0 \qquad \textbf{(4.4)}$$

Note that kerosene has a substantially larger density than GOX. When a disturbance moves a small amount of kerosene inwards, displacing an equal volume of GOX outwards, a mass has been moved toward the axis. Therefore, the combined potential energy of the flow increases, and the disturbance will diminish and revert back to the original equilibrium state of the system—an inverse of the development of Rayleigh-Taylor instabilities. This eliminates the contribution of density gradient to the mixing layer development in the present study.

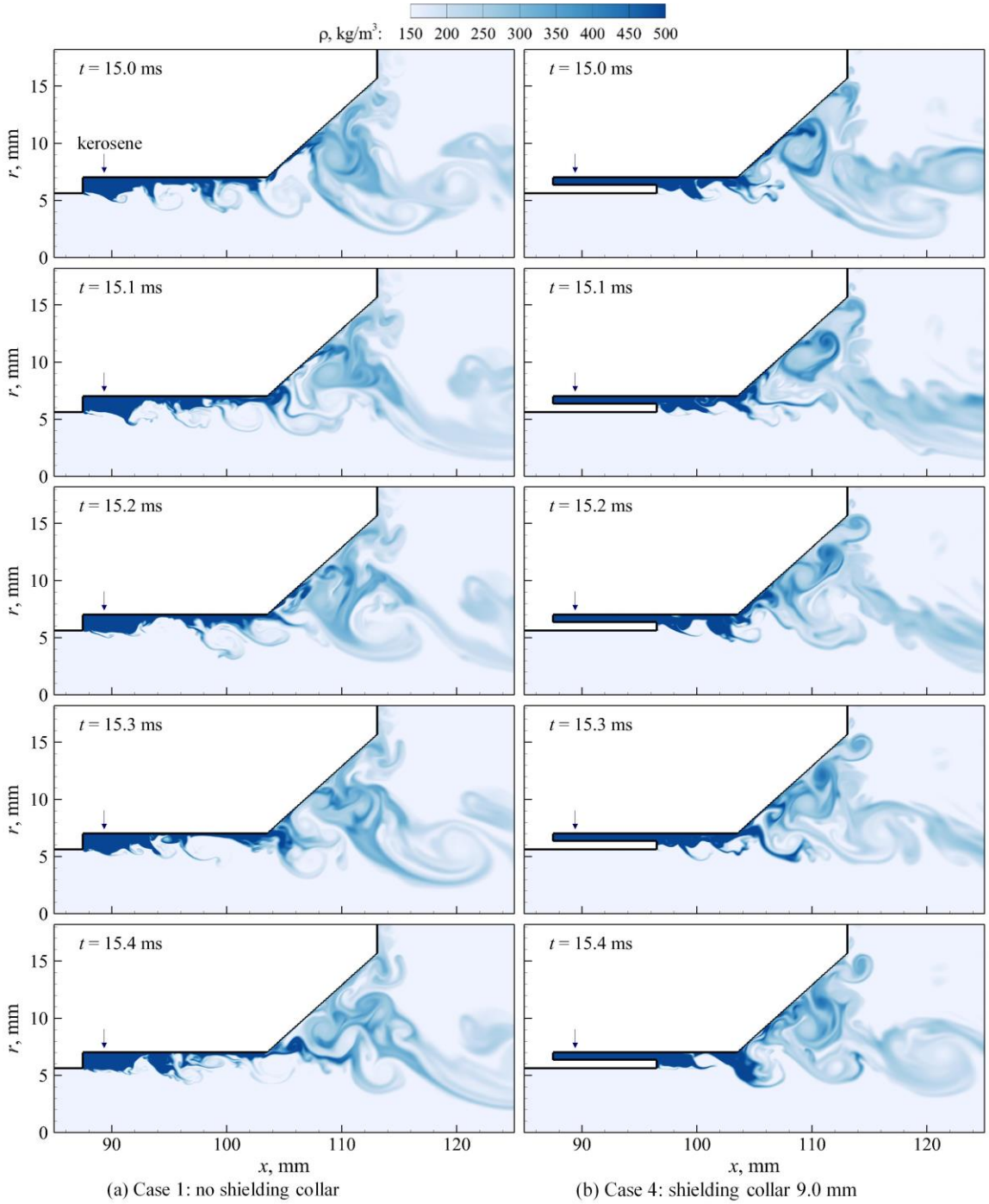

(a) Case 1: no shielding collar (b) Case 4: shielding collar 9.0 mm

Figure 4.4 Temporal evolution of density field in the mixing section

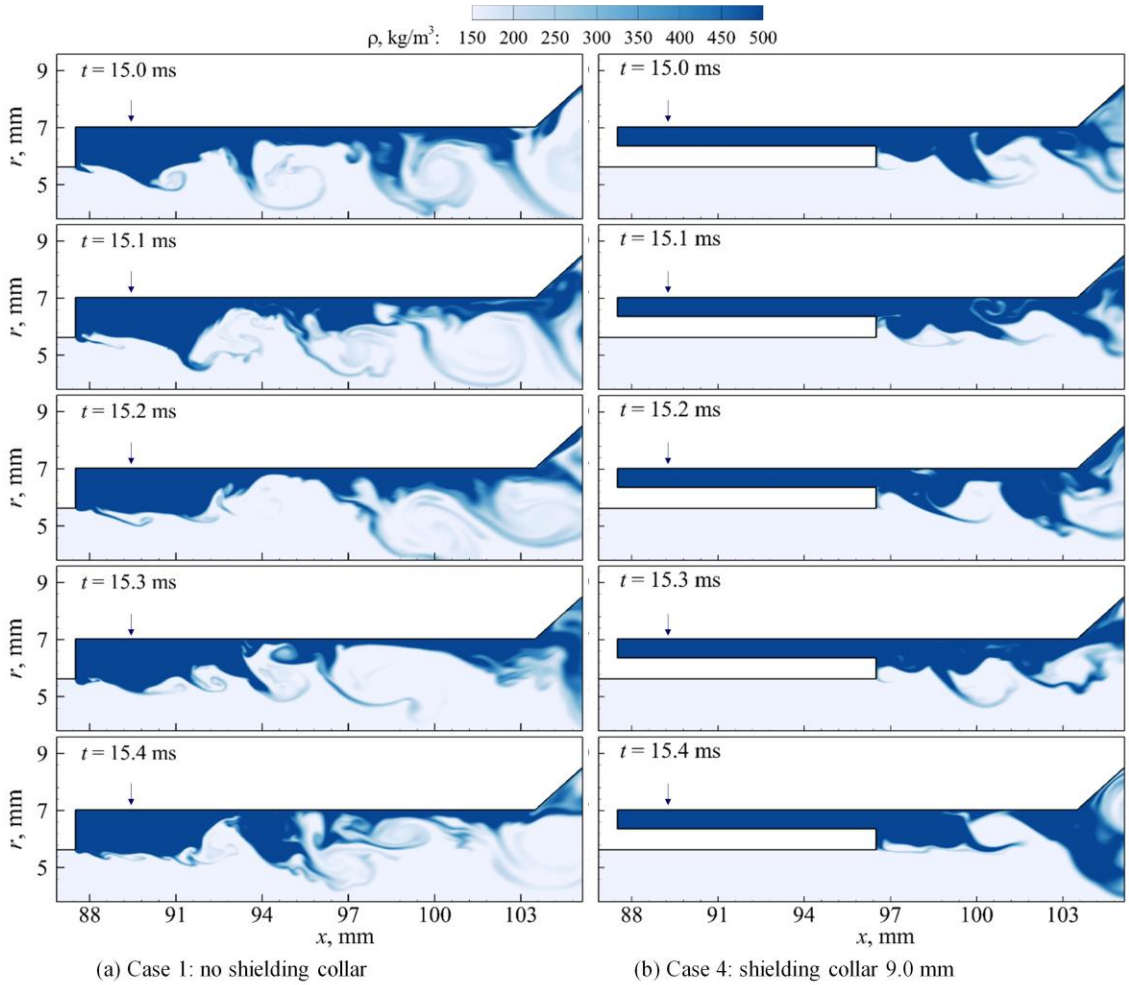

Figure 4.5 Temporal evolution of density field near the GOX post exit

4.2.2 Kerosene Mass-Fraction Field

Figure 4.5 shows the evolution of the kerosene mass-fraction field in the mixing zone for Cases 1 and 4. The isolines show the kerosene mass fraction of 0.4 (dashed lines) and 0.6 (solid lines). The unsteadiness of the kerosene injection and the intrinsic hydrodynamic instabilities in the kerosene/GOX shear layer lead to the formation of large-scale vortices. These structures engulf GOX bulk and draw it into the shear layer (macromixing). They also stretch the interface between the unmixed fluids, increasing the interfacial area and steepening the local concentration gradients, and enhance the diffusive micro-mixing. As

shown in Figure 4.6, GOX entrains the kerosene film and macromixing takes place in the early mixing region. As the mixing layer travels downstream, large-scale vortices grow and fine structures emerge, promoting the disintegration and the dispersion of the kerosene stream. This phenomenon is especially prominent in the taper region, and as a result, a sizeable part of the injector has a kerosene mass fraction between 0.4 and 0.6 (also shown in Figure 4.20).

Figure 4.6 shows close-up views of the kerosene mass-fraction field near the GOX post exit. Since kerosene is tangentially introduced into the injector (Case 1) or the fuel passage (Case 4), the centrifugal force prevents it from penetrating deeply into the injector center. The local kerosene mass faction holds at unity near the wall for both cases. In Case 1, the transverse motion of the injected kerosene and the recirculating flow further constrains the fuel to the corner region, and only a slight amount of GOX is observed near the head end. At the GOX post tip, on the other hand, a thin kerosene stream entrains the otherwise smooth GOX flow and rolls up a small volume of GOX as it convects downstream, forming the very early mixing layer. The crest marked by A at the devolved kerosene/GOX interface subsequently increases in size as the GOX flow passing the crest accelerates and decreases the local static pressure. Downstream of x = 90 mm, the transverse kerosene stream meets these crests, generating more coherent structures, marked by B, C, and D. In Case 4, the rim of the fuel-shielding collar plays an important role in the initialization of the mixing layer. As the outer kerosene and the inner GOX expand immediately downstream of the rim, recircularization occurs behind the rim, and kerosene entrainment takes place. The unsteadiness in the kerosene stream induces strong disruptions on the kerosene/GOX

interface, creating large crests and engulfing GOX bulk. This macro-mixing process near the GOX post exit defines the early-stage mixing characteristics and has a significant impact on the subsequent flow development.

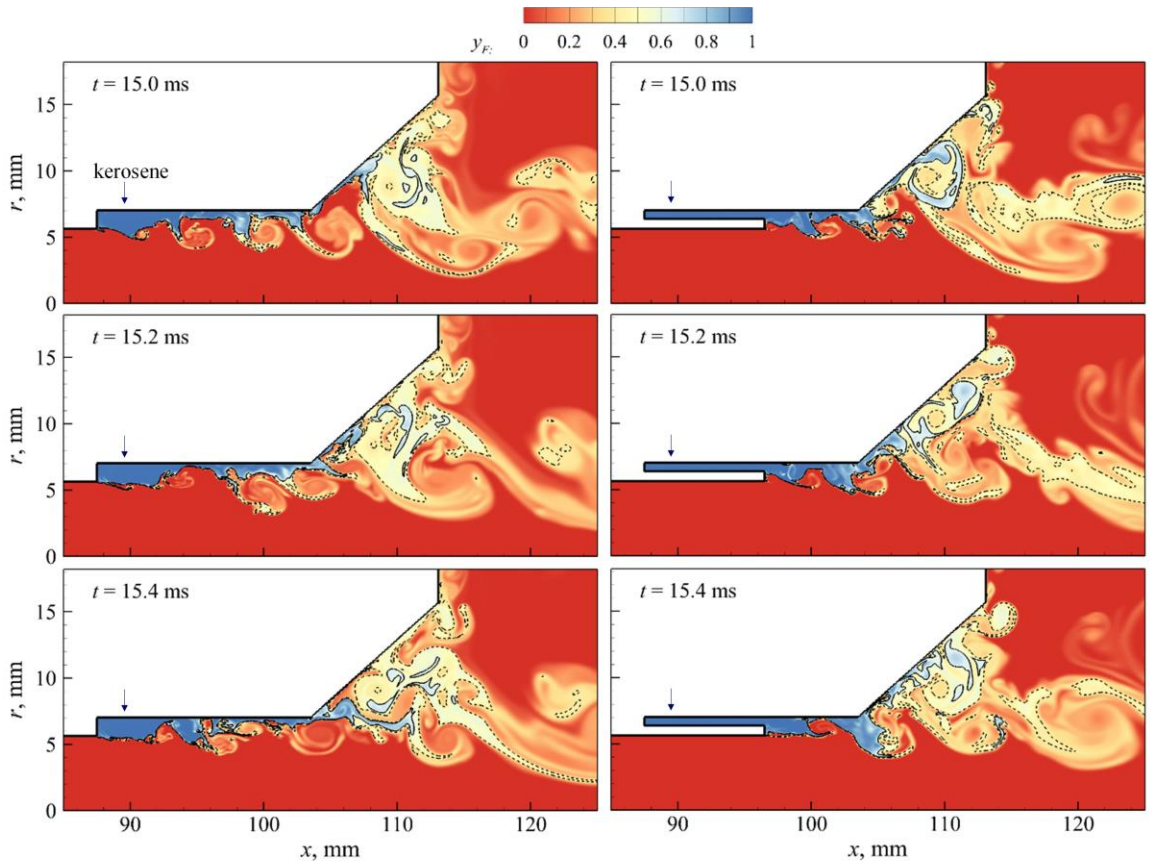

Figure 4.6 Temporal evolution of kerosene mass fraction in the mixing section

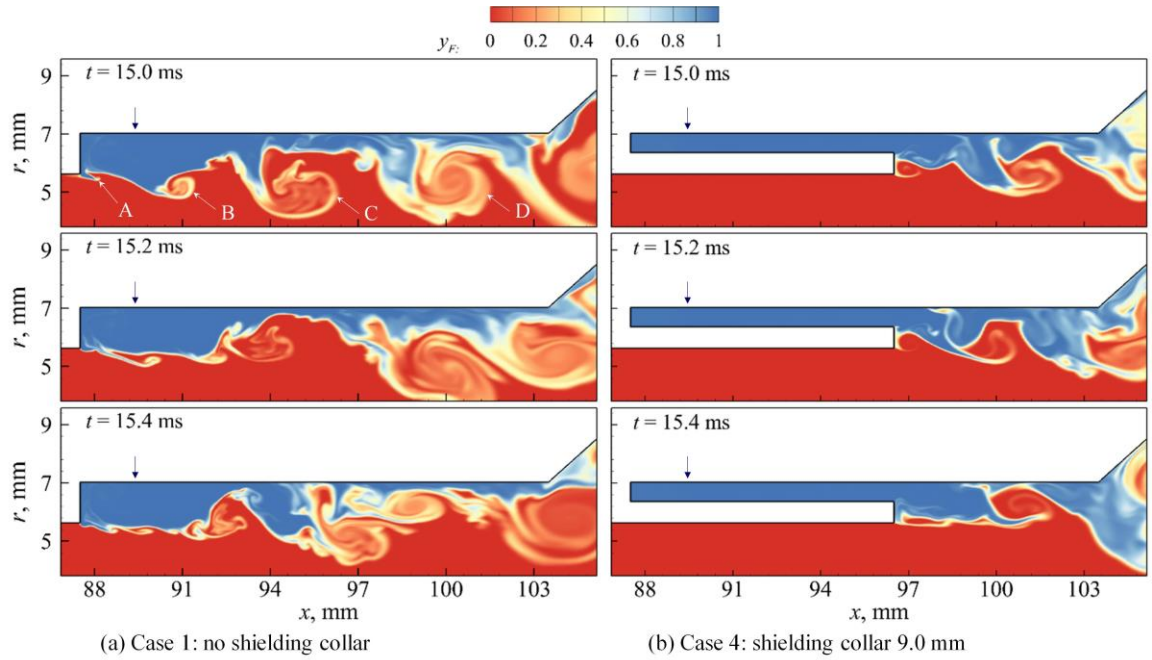

(a) Case 1: no shielding collar (b) Case 4: shielding collar 9.0 mm

Figure 4.7 Temporal evolution of kerosene mass fraction near the GOX post exit

4.2.3 Vorticity Field

Figure 4.8 shows the evolution of the vorticity field in the mixing zone for Cases 1 and 4. The bright red regions mark the locations of high, positive azimuthal vorticity, mainly generated in the boundary layer of the incoming GOX stream and supplemented by minor production at the kerosene/GOX interface. As positive vorticity continuously sheds from the GOX post tip, a vortex train forms in the mixing cup. A noticeably smaller amount of negative vorticity is produced near the kerosene injection slit in Case 1, and along the inner wall of the fuel passage in Case 4, as well as in small separation zones at the center. As the kerosene/GOX mixing layer develops, both negative and positive vorticities entangle and disperse, tracing the two streams to some extent. Flow recirculation occurs in the fuel passage for Case 4, and in the upstream part of the mixing cup for both cases. Close-up views of instantaneous streamlines are shown near the wall at the taper entrance

in Figure 4.8b, visualizing the localized flow separation and reattachment. Once the flow enters the taper region, the coherent vortical structures rapidly enlarge, creating a wide vorticity plume that occupies most of the injector cross section. The observed behavior results from the flow expansion in the taper section; the flow speed decreases and the vortices also travel slowly. Since the lumps of vorticity persist, the incoming eddies stretch and/or amalgamate into larger structures. Each pairing interaction redistributes vorticity into larger vortices, with doubled wavelength and halved frequency. Flow recirculation occurs at the taper region and the injector exit, and the sizes and axial locations of the vortices are closely related to their evolution. The time-averaged structures of the recirculating flows are shown in Figure 4.18.

Figure 4.9 shows close-up views of the vorticity distribution in the wake of the GOX post. Also shown are the instantaneous streamlines near the kerosene inlet in Case 1 (Figure 4.9c) and near the collar rim in Case 4 (Figure 4.9d). In both cases, a large amount of vorticity is generated in the wall boundary of the GOX post. In Case 1, the transverse momentum of the kerosene leads to the formation of a small separation zone immediately ahead of the jet, a large recirculation zone in the corner, and an inward flow near the head end. As the GOX travels downstream of the post, it expands radially. The transverse motion of the kerosene jet, however, suppresses such expansion. Early stage GOX entrainment into the kerosene is only possible near the head end, and the axial momentum of the GOX stream deflects the kerosene jet. The two streams meet at x = 90 mm, where significant mixing between GOX and kerosene occurs. A large vortex appears at x = 90.5 mm at t = 15.0 ms.

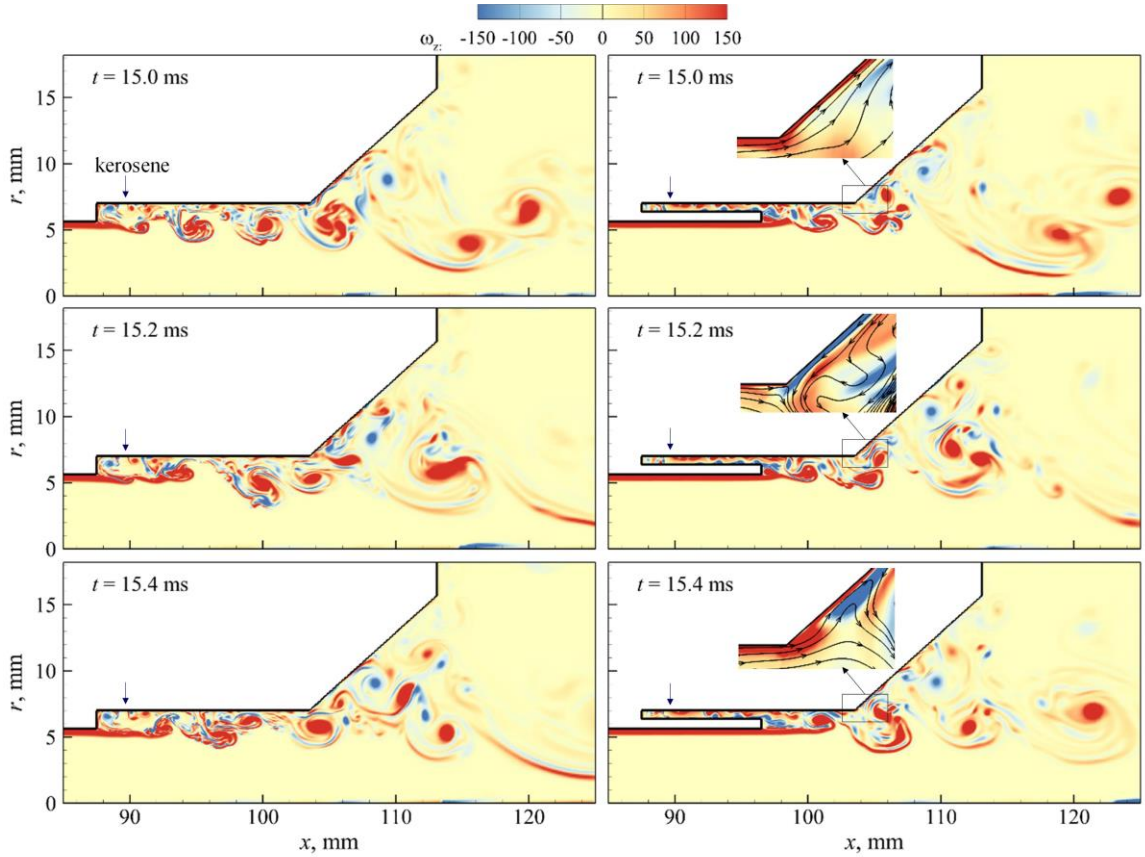

Figure 4.8 Temporal evolution of vorticity in the mixing section

In Case 4, the wall boundaries of the fuel passage provide another source of vorticity. Because of intrinsic flow oscillations, vorticity enters the mixing cup intermittently, forming a wavy vorticity plume downstream of the shielding collar. Both the kerosene and GOX streams expand rapidly when entering the mixing cup, as visualized by the curved vorticity trajectories and the streamlines in Figure 4.9d. The highly unsteady kerosene flow induces the shedding of a series of vortices from the outer collar rim, which subsequently varies the flow direction. Near the collar rim, two counter-rotating recirculating zones are produced, as is typical in the wake flow behind a splitter plate.[157] They are strongly influenced by the incoming streams and constantly change in shape and size. Consequently, the contact point of the main kerosene and GOX streams varies between x = 97.5 and 98.5

mm as marked by E1, E2, and E3. These two streams have distinct velocities, densities, and vorticities, and this leads to dynamic structures in the mixing layer in the downstream region.

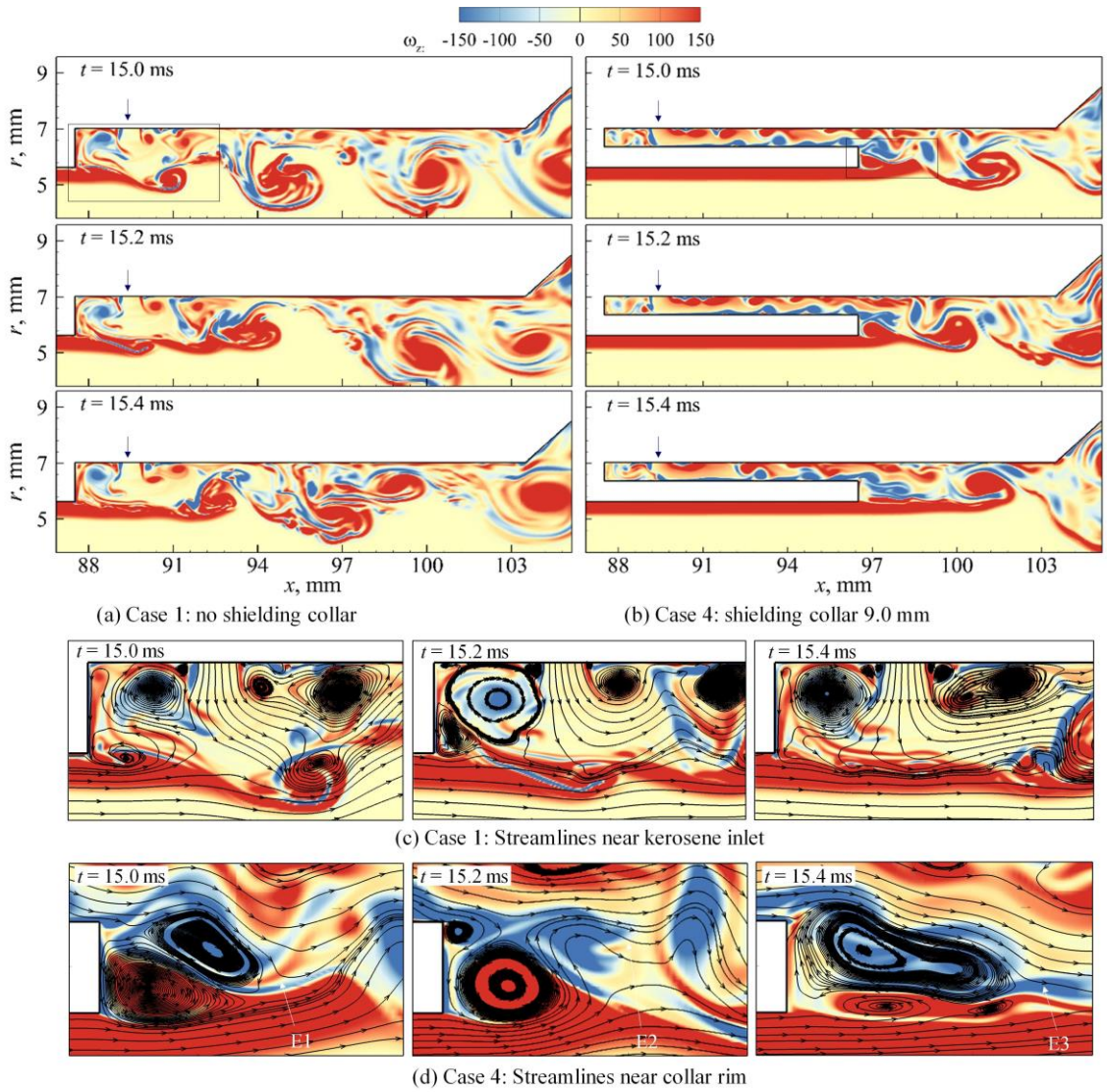

Figure 4.9 Temporal evolution of vorticity near the GOX post exit and closeup views of streamlines

4.2.4 Pressure Field

Figure 4.10 shows the evolution of gauge pressure with radial velocity isolines near the GOX post exit for Cases 1 and 4. The dashed lines denote negative radial velocity. In Case 1, the transverse momentum of kerosene causes a negative radial velocity field near the fuel inlet and a time-evolving radial gradient in the pressure field. Pressure in the near-wall region peaks at t = 15.0 ms and decreases to a much lower value at t = 15.2 ms. As the kerosene jet penetrates into the GOX stream, a small separation zone occurs ahead of the injection slit, as suggested by the positive-negative variation of velocity marked by F. The corner flow then moves to the center region, as indicated by the negative radial velocity near the head end. In Case 4, since kerosene is first introduced into the fuel passage, where it is shielded by the collar, the flow is predominantly axial before it enters the mixing zone at x = 95.5 mm. Therefore, the pressure field does not exhibit radial gradient; the observed variations are mainly induced by the interaction between the GOX and kerosene flows. Note that since the pressure is slightly higher in the kerosene flow than in the GOX flow, the radial velocity close to the post tip is negative.

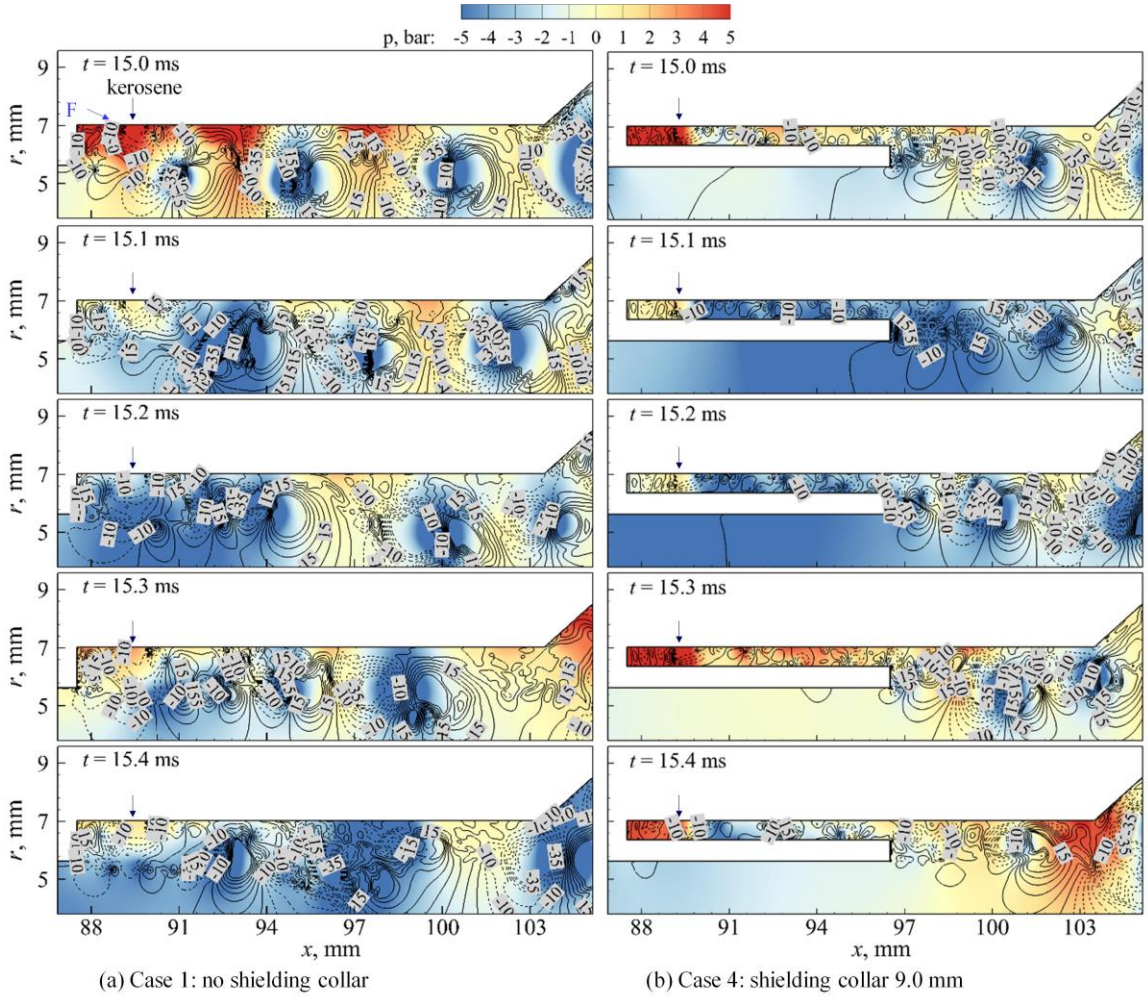

Figure 4.10 Temporal evolution of pressure field near the GOX post exit (with radial velocity contours)

4.3 Flow Dynamics

As mentioned above, the injection and mixing of GOX and kerosene renders complicated flow dynamics, which will be elaborate in the current session. Figure 4.11 depicts the various salient features of the GCLSC injector flow dynamics. The color contour represents an instantaneous density field. Lines and arrows in orange denote some of the important flow structures, as described in the previous section. The flow dynamics in the fuel annulus are featured by shear layer roll-up and vortex shedding near the injection

slit. As GOX and kerosene mix in the recess region, inside the shear layer, Kelvin-Helmholtz (K-H) instability in both axial and azimuthal directions becomes prominent due to strong velocity gradients between the two flows. Strongly influenced by the shear layer instability, centrifugal instability further induces liquid film thickness oscillations. Further downstream, area expansion, combined with centrifugal instability, leads to the formation of recirculation bubbles attached to the taper wall, which bring kerosene back to the GOX stream. Vortices undergo intricate processes of expansion, interaction, and merging. All these dynamic characteristics will be described in detail in the following sections.

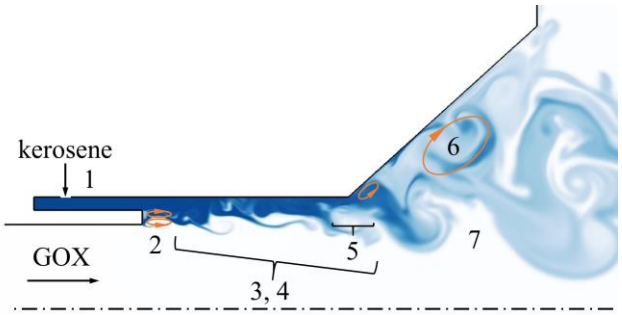

1. shear layer roll-up
2. counter-rotating recirculation
3. axial shear layer instability
4. azimuthal shear layer instability
5. centrifugal instability
6. taper recirculation
7. vortex merging

Figure 4.11 Schematics of flow dynamics in the baseline case

4.3.1 Fuel Passage

Figure 4.12 shows the temporal evolution of the azimuthal vorticity field overlaid by streamlines near the fuel injection slit within one cycle of flow oscillations for the baseline case. Five plots are presented, with time interval (Δt) of 0.04ms. Shear layers form on both

sides of the fuel jet. They roll up and results in the development of recirculation bubbles, as depicted in green.

At time t_o, the recirculation bubble on the left side of the injection slit starts to evolve. It expands in the radial direction and eventually separates into two bubbles at t_o+0.16ms. The inner one travels downstream, while the outer one continues to grow and repeats the same process. The shedding frequency is 5.6 kHz. Immediate downstream of the injection slit, similar vortex dynamics are observed. The counter-clockwise recirculation bubble grows and horizontally splits into two bubbles. The one in the upstream region evolves again while the other convects downstream. The shedding frequency is estimated to be 13 kHz, and is not shown in the figure. Both frequencies are approximately constant for all cases.

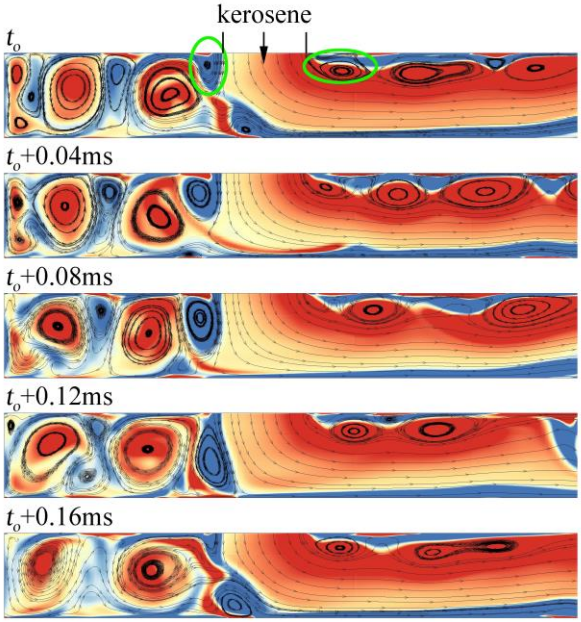

Figure 4.12 Temporal evolution of azimuthal vorticity overlaid by streamlines near fuel injection slit for the baseline case

4.3.2 Recess Region

The shielding collar allows for the development and shedding of vortices generated from both the GOX and kerosene streams. Figure 4.13 shows the temporal evolution of fuel mass fraction overlaid by streamlines in the near field of the GOX post exit of the baseline case. Counter-clockwise vortices generated from the oxidizer side are stronger due to the larger velocity. The shear layer instability induced by the velocity gradient is clearly observed. At time t_o, immediately downstream of the shielding collar rim, the GOX stream rolls up, forms a counterclockwise rotating recirculation bubble. After 0.04ms, while the bubble is being convected downstream, it detaches from the rim and entrains liquid kerosene stream into the GOX flow. At t_o+0.08ms, the bubble further grows and facilitates the liquid entrainment and subsequent mixing between GOX and kerosene.

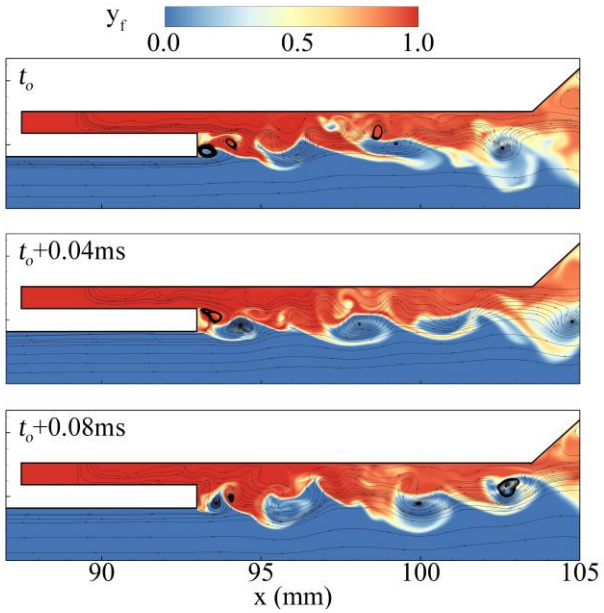

Figure 4.13 Temporal evolution of fuel mass fraction overlaid by streamlines in the recess region for the baseline case

Figure 4.14 shows the temporal evolution of azimuthal vorticity in the recess region for the baseline case. The propagation speed of the bubbles is approximately $\bar{u} = 60$ m/s, the average velocity of the GOX and kerosene flows. The distance between neighboring

bubbles is around $\Delta l = 4$ mm. The corresponding frequency is estimated to be in the order of $f = \bar{u}/\Delta l = 15$ kHz.

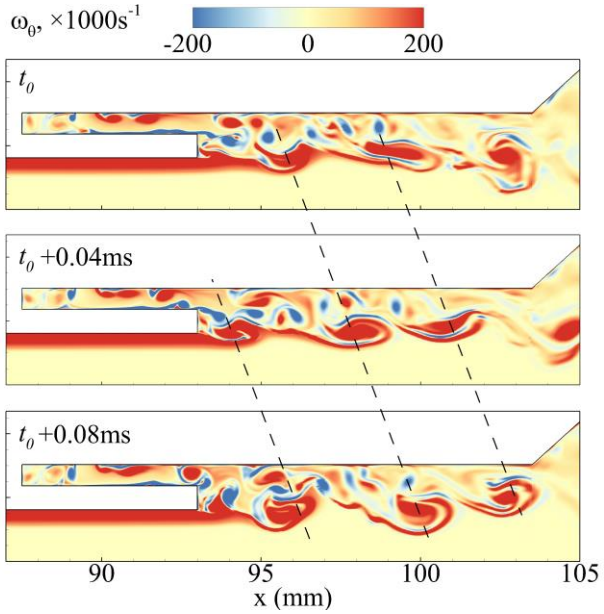

Figure 4.14 Temporal evolution of azimuthal vorticity in recess region for the baseline case

To obtain in-depth understanding of the flow dynamic characteristics, the spectral contents of the pressure oscillations in both recess and taper regions are presented in Figure 4.15. Probe locations are depicted in a), and the power spectral densities of pressure are shown in b) and c). In the recess region, two probes are placed near the mixing layer, located at GOX and fuel sides, respectively. Dominant frequencies (or frequency ranges) of 1.9 kHz, 3.6 kHz, 6.2 – 6.6 kHz and 11–13 kHz are observed. Similar dominant frequencies can be observed in both probes.

The dominant frequency of Kelvin-Helmholtz instability follows

$$f = St \cdot \bar{u}/\delta \tag{4.5}$$

$\bar{u} = 1/2 \times (u_1 + u_2)$ is the average velocity, u_1 and u_2 are the velocities of streams at two sides of the shear layer, respectively. δ is the initial momentum thickness of the shear layer, defined as one fourth of vorticity thickness, $\delta = 1/4 \times (u_1 - u_2)/(du/dy)_{max}$ [158, 159]. For baseline case, the averaged axial velocity is $\bar{u} = 60\mathrm{m/s}$. The estimated δ is approximately 0.25mm. If we take $f = 11.1$ kHz, then according to Eq. (4.5), the Strouhal number is $\mathrm{St} \approx 0.046$. This is within the range of $St \approx 0.044 - 0.048$, which is the Strouhal number of the most unstable mode of an unforced planar shear layer in turbulent flows [160]. Similarly, the authors identify 3.6 kHz as the dominant frequency in the azimuthal direction. If we take $f = 3.6$ kHz and take azimuthal velocities of both flows as u_1 and u_2, following the similar approach, the Strouhal number is estimated as $\mathrm{St} = 0.041$, still close to the same Strouhal number range. The frequency range of 6.2 – 6.6 kHz is roughly half of 11 – 13 kHz, and is identified as sub-harmonics of the shear layer instability. The sub-harmonics process can be attributed to the vortex merging process, which starts in the recess region and later becomes prominent in the taper region. Details about the merging process will be further elaborated in the following section. For the same reason, since 1.9 kHz is nearly half of 3.6 kHz, the authors conjectured that 1.9 kHz corresponds to the sub-harmonics of shear layer instability in the azimuthal direction. Another possible mechanism for oscillations at 1.9 kHz can be travelling acoustic wave, which progresses from recess region to the non-reflecting boundary of GOX inlet. The details need to be further explored in future works.

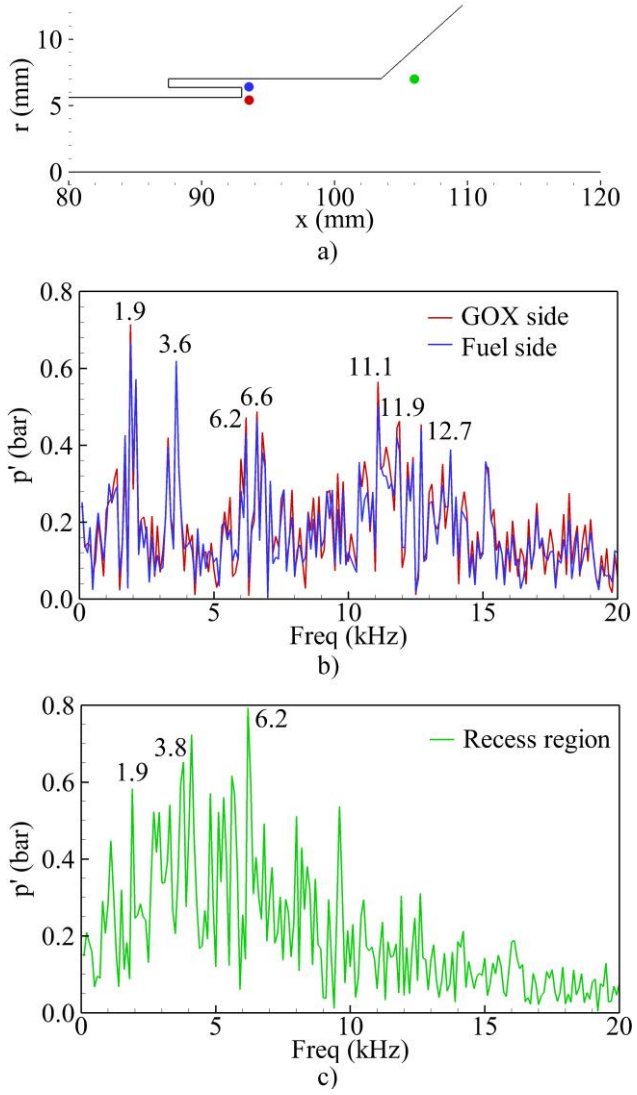

Figure 4.15 Power spectral densities of pressure oscillations at different probes in recess and taper regions for the baseline case

The influence of recess length on shear layer instability is summarized in Table 4.2, where instabilities in both axial and azimuthal directions are listed. The effects of recess length on both instabilities are quite different, and will be analyzed separately. For axial shear layer instability, all six cases can be categorized into three groups (Case 1-2, Case 3-5, Case 6). For cases with longer recess length (Case 1, Case 2), the fuel injection process is exposed to the GOX flow, and the recess length has a strong impact on the axial velocity

of fuel stream and consequently influences the shear layer instability. Figure 4.16a shows the radial distribution of time-mean axial velocities at the shielding collar rim for Case 2-6. The velocity profile does not include Case 1, as there is no shielding collar for this case. For Case 2, kerosene flow is not fully developed, and recirculation zone can be observed near the upper wall. Axial velocity of kerosene flow in Case 2 is larger than in Case 3-5. Moreover, the radial location of maximum axial velocity of fuel stream is also closer to the GOX flow, resulting in a smaller δ. According to $f \propto u_x/\delta$, Case 2 has a larger frequency. For injectors with shorter recess length (Case 3-5), kerosene flow is fully developed in the fuel annulus, and the influence of recess length on shear layer instability is diminished. For non-recessed injector (Case 6), dominant frequency of 12.3 kHz can be observed in the taper region. For this case, shear layer instability is accompanied by complicated vortex expansion and interaction processes induced by area expansion. Detailed discussion about flow dynamics in taper region is conducted in the next session. On the other hand, the frequency of shear layer instability in the azimuthal direction decreases with decreasing recess length (except Case 1). This trend can be explained by the time-mean azimuthal velocities at the shielding collar rim, as depicted in Figure 4.16b. Since azimuthal velocity decreases with decreasing recess length, $f \propto u_\theta/\delta$, the frequency decreases accordingly.

Table 4.2 Shear layer instability frequency for Case 1-6

Case No	1	2	3	4	5	6
Axial (kHz)	13.0	15.6	11.1	10.9	11.8	12.3
Azimuthal (kHz)	5.1	5.2	3.6	3.4	3.2	2.8

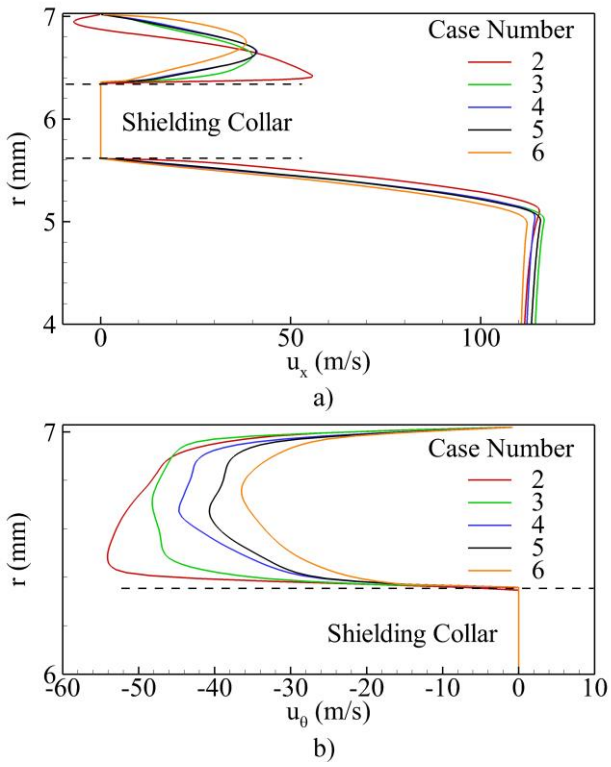

Figure 4.16 Radial distribution of time-mean axial and azimuthal velocities at end of shielding collar for Case 2-6

During the mixing process, as depicted in Figure 4.13, while recirculating bubbles roll up and shed downstream periodically, oscillations of liquid film thickness can be observed in the nearby region of each bubble. This can be attributed to the influence of centrifugal force, which is induced by swirling kerosene flow. Inside the flow, spatiotemporally varying azimuthal velocity results in pressure gradient, which affects liquid film thickness. In this study, this centrifugal instability is influenced by the shear layer instability, and leads to complicated flow dynamics, including the liquid film thickness oscillations and the fuel ligament breakup.

4.3.3 Taper Region

In taper region, the conservation of azimuthal momentum $u_\theta r$ is observed near the taper wall, thus the azimuthal velocity u_θ is inversely proportional to radial distance r. In the radial direction,

$$\frac{\partial p}{\partial r} \sim f_c \sim \frac{\rho u_\theta^2}{\mathrm{r}} = \frac{\rho (u_\theta r)^2}{\mathrm{r}} \qquad \textbf{(4.6)}$$

f_c is the centrifugal force. The decrease of azimuthal velocity causes the pressure to recover in the downstream region. The resultant axial positive pressure gradient leads to axial deceleration of the GOX stream. A large clockwise rotating recirculation zone thus forms near the taper wall. A similar phenomenon, commonly known as vortex breakdown, is observed in the flow fields of swirl injectors [150, 152], where a central recirculation zone is developed. For GCLSC injectors, the recirculation flow is located between the outer kerosene and central GOX streams.

Figure 4.17 depicts temporal evolution of fuel mass fraction in the taper region. Near-wall vortices are rotating at roughly stationary positions, while other vortices undergo complex interactions, including propagation, disintegration and merging. At time t_o, two vortices, denoted as 1 and 2, are convected downstream from recess region. Influenced by centrifugal force, vortex 1 remains radially outward, where it is decelerated by the low-speed main stream. For vortex 2, centrifugal force is balanced by the influence from the first vortex, and it flows axially downstream. Due to the difference in axial velocity, the merging process starts at t_o+0.03ms and ends at t_o+0.06ms.

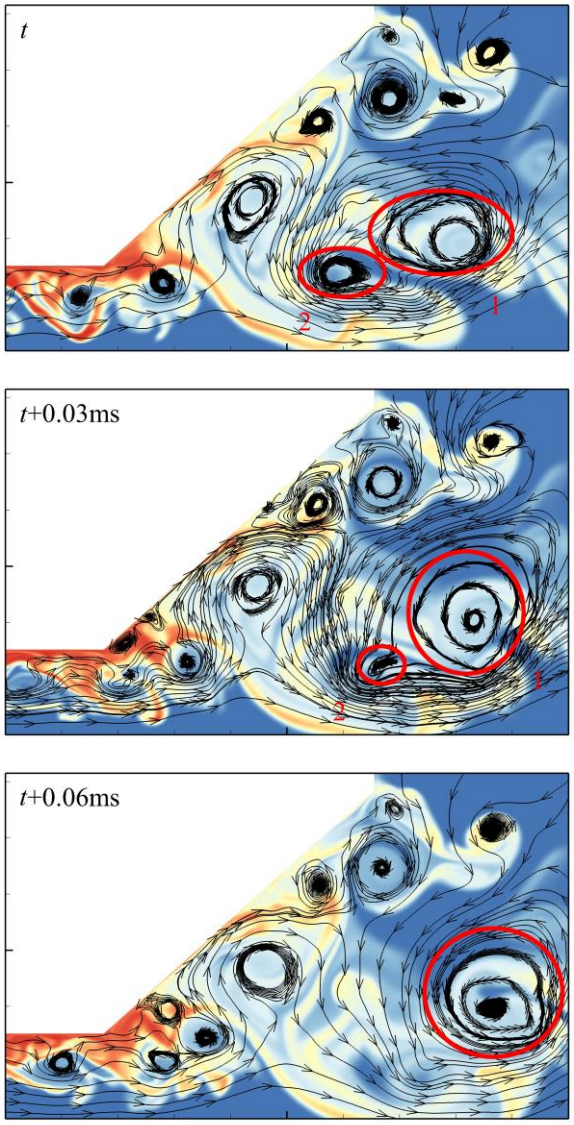

Figure 4.17 Temporal evolution of fuel mass fraction and streamlines in taper region

Complexity of flow dynamics in the taper region is further illustrated in Figure 4.15c, where spectral information of a probe inside the taper region is plotted. Multiple peaks are also observed. Dominant frequency of 6.2 kHz is identified in the taper region, and is attributed to the vortex merging process, as 6.2 kHz is approximately half of the shear layer instability frequency in the axial direction.in the recess region. Multiple peaks at other

frequencies are also observed, indicating the complexity of flow field and the influences of multiple flow dynamics mechanisms.

4.4 Mean Flow Properties

4.4.1 Mean Flow Field

The flow characteristics are further examined in the light of time-averaged properties. Figure 4.18 shows the streamlines in the mixing cup and its downstream region. Close-up views near the GOX post tip are shown in Figs.14 (c) and (d). In Case 1, the transverse injection of kerosene directly into the injector creates a recirculation zone in the head end, as well as a small area of separation immediately ahead of the injection slit. Because of the small momentum flux ratio between the kerosene and GOX, and swirl-induced centrifugal force, the kerosene stays close to the wall and fills the entire corner region and the near-wall zone. Immediately downstream of the injection slit, the kerosene flow separates and then reattaches to the wall, creating a stagnation point with a locus of positive divergence (node) at x = 90.6 mm; this structure is typical of a transverse jet in crossflow.[161, 162] The swirl-induced centrifugal force and the expanding GOX stream push the kerosene toward the wall, as shown by the slightly tilted streamlines between x = 93 and 103.5 mm. As the flow enters the taper region, the geometric change causes flow expansion, and the otherwise smooth streamlines curve upward, forming a small separation zone at the divergent point and a large recirculation zone in the downstream region. Secondary recirculation bubbles also appear.

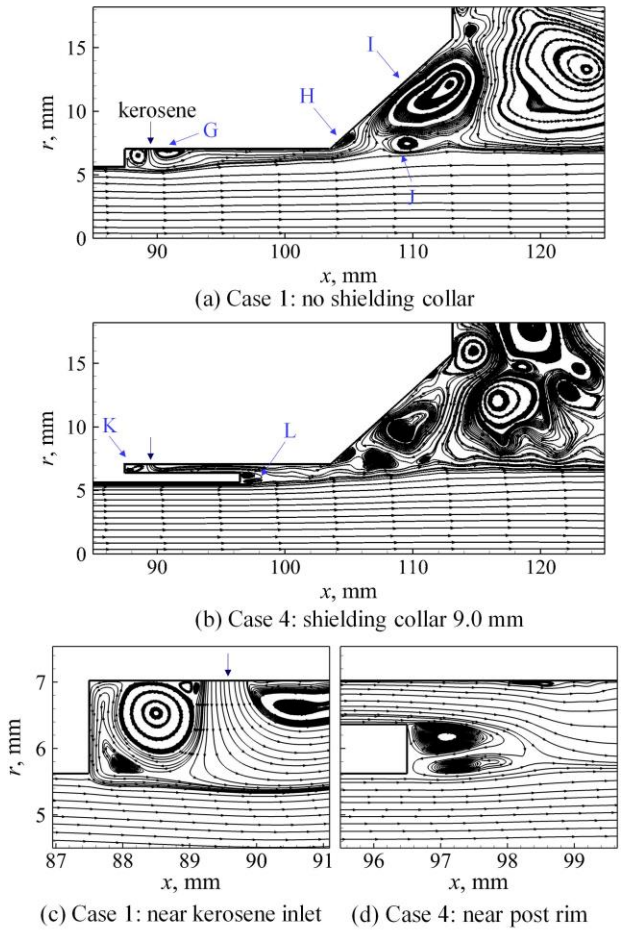

Figure 4.18 Time-mean streamlines in the mixing section

In Case 4, wavy streamlines visualize the unsteady kerosene flow in the fuel passage. A small recirculation bubble forms at the head end. As the kerosene and the GOX streams expand downstream of the post, two recirculation bubbles occur behind the shielding collar rim. Because of the limited recess length L_r, the near-wall streamlines originating in the kerosene stream are not flattened before the flow enters the taper region. A complicated vortical flowfield appears in the taper region, featuring multiple toroidal recirculation zones and secondary vortex structures.

Figure 4.19 shows the radial distributions of gauge pressure, kerosene mass fraction, and velocity components at five different axial locations in the time-averaged flowfield. The first axial location is 0.5 mm downstream of the GOX post end, x = 88 mm for Case 1 and x = 97 mm for Case 4. Case 1 has a slightly lower pressure and a larger axial velocity near the center. The pressure remains nearly uniform in the center region (r < 5.4 mm), and then increases continuously toward the wall at r = 7.0 mm, where the kerosene injection occurs. In the fuel passage (r > 5.6 mm), the axial velocity decreases substantially for both cases, while in Case 1 the radial velocity increases up to 15 m/s. Within the post, Case 1 has a negative radial velocity, suggesting a weak kerosene movement toward the GOX stream near the head end as observed in Figure 4.18c. In Case 4, the recirculation zone downstream of the collar rim (5.6 < r < 6.4 mm) is characterized by a local pressure reduction, a negative axial velocity, and a wavy radial velocity profile.

The second axial location, x = 103 mm, is located 0.5 mm upstream of the entrance of the taper. In the kerosene/GOX mixing region (r > 4.0 mm), pressure and axial velocity decrease, while the radial velocity increases; this is especially noticeable in Case 4. The third axial location, x = 112 mm, is located 1.1 mm ahead of the injector exit. As the flow expands in the taper region, pressure increases and axial velocity decreases. Kerosene spreads inward and reaches the radial location of r = 2 mm, as evidenced in the mass fraction profile; the small axial velocity and negative radial velocity mark the existence of a large recirculation flow in the kerosene plume. The fourth axial location, x = 115 mm, is located 1.9 mm downstream of the injector exit, where the flow expands rapidly. The GOX core shrinks and only covers the region of r < 3 mm, and kerosene spreads broadly,

reaching the radial location r > 20 mm. The radial velocity is negative in the region of 5 < r < 15 mm, under the influence of flow recirculation. At x = 125 mm, which is 11.9 mm downstream of the injector exit, the GOX core further decreases, as indicated by the weakened axial velocity in the region of r > 2 mm; the recirculating flow extends broadly, leading to a sizable radial velocity up to r = 18 mm in Case 1 and r = 22 in Case 4.

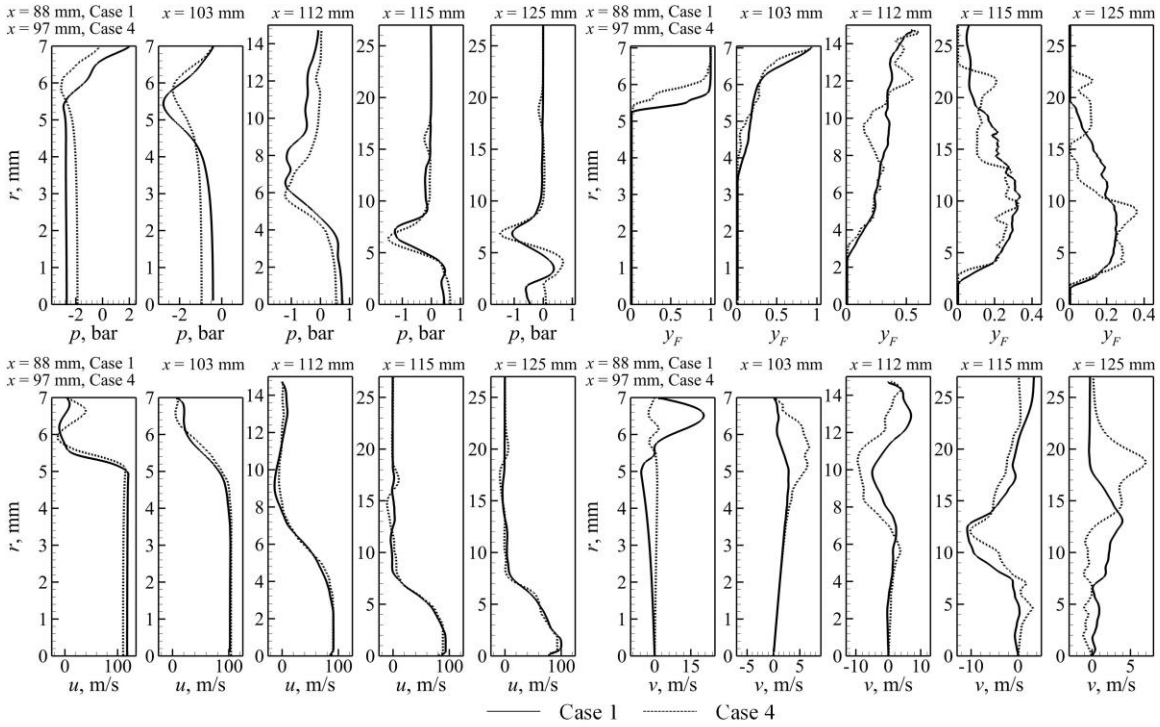

Figure 4.19 Radial distributions of mean gauge pressure, kerosene mass fraction, and velocity components at different axial locations in mixing section and initial chamber

Figure 4.20 shows distributions of kerosene mass fraction in the time-averaged flowfield for all six cases. Also shown are the isolines of $\overline{y_F}$ = 0.2, 0.4, 0.6, and 0.8. In Cases 1 and 2, kerosene is well distributed in the taper region and near the injector exit. As the length of the fuel shielding collar increases (the recess length decreases), the near-wall kerosene mass fraction increases and the plume shrinks, especially in Cases 5 and 6.

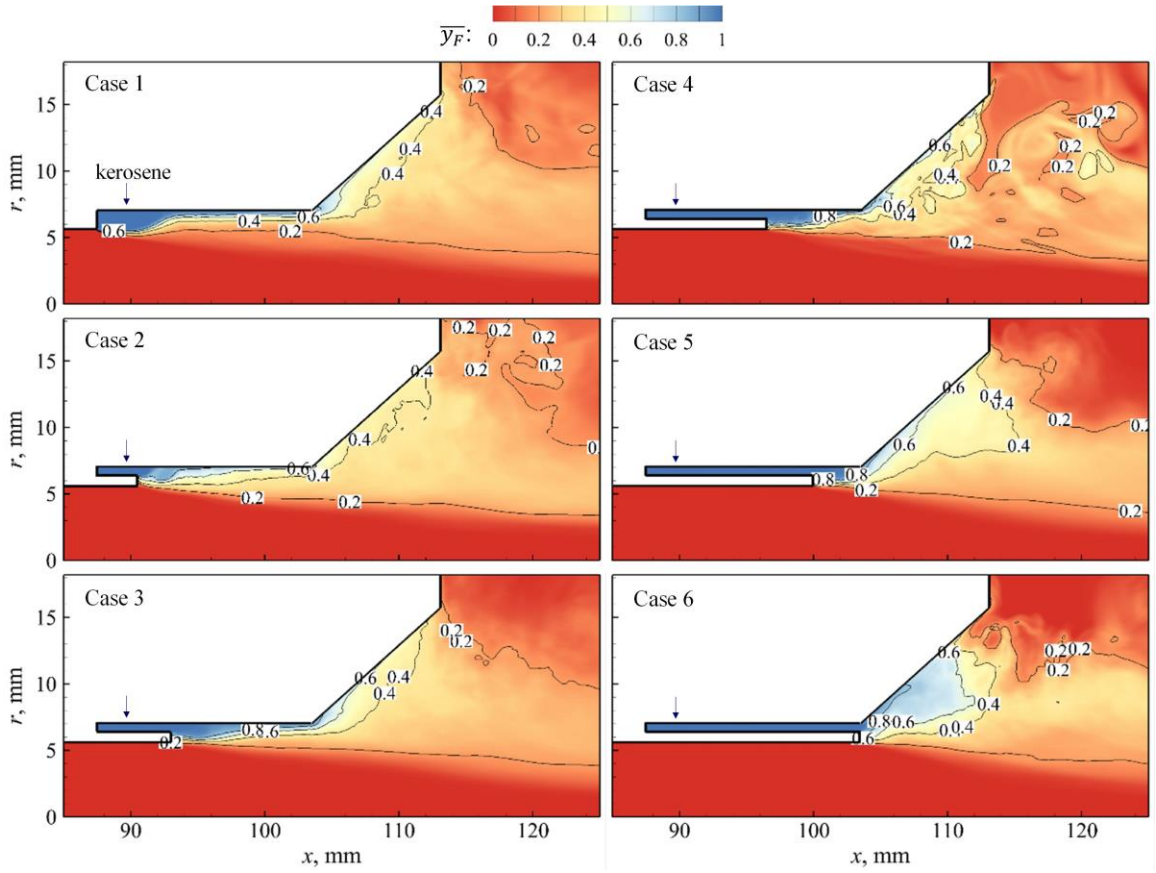

Figure 4.20 Distributions of kerosene mass fraction in the time-mean flowfield (Cases 1-6)

4.4.2 Mixing Layer Evolution

The mixing process allows for the dynamic momentum exchange between GOX and kerosene in both axial and azimuthal directions. This process is shown in Figure 4.21, which depicts the radial distributions of time-mean axial and azimuthal velocities at different axial positions for the baseline case. Directly downstream of GOX post, mean axial velocities of GOX and kerosene are 110 m/s and 20 m/s, respectively. In the mixing process, axial momentum is transfer from GOX flow to kerosene flow, the azimuthal momentum is transferred the other way around. The entrainment of kerosene leads to the diminishing of liquid film thickness, and the radial expansion of shear layer.

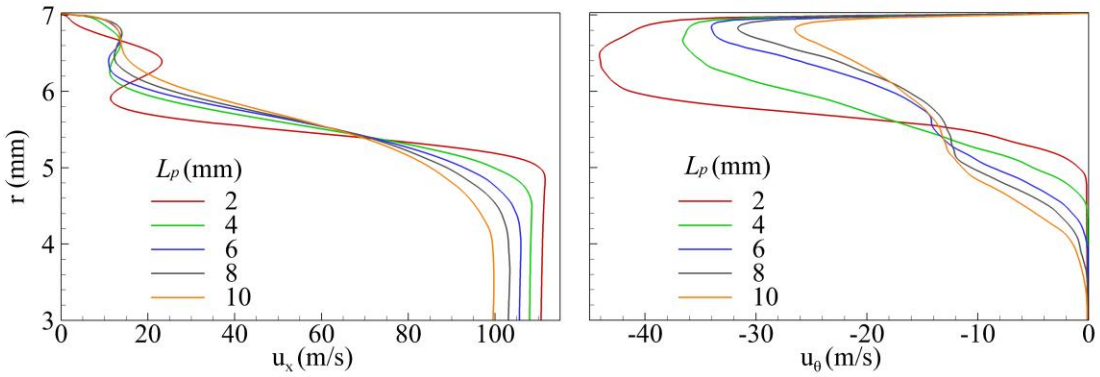

Figure 4.21 Radial distributions of time-mean axial and azimuthal velocities at different axial positions for the baseline case (L_P stands for distance after GOX post)

Figure 4.22 further presents the dynamic evolving of mixing layer structure. u_θ is azimuthal velocity, and r is radius. At the location of 2mm from the GOX post, flowfield in the recess region can be radially divided into four sub-regions. Under supercritical conditions, liquid-gas interface is characterized by a continuous transition region, which poses challenges to the accurate definition of liquid surface. To facilitate discussion, liquid surface is defined at the location of maximum radial density gradient [152], and is marked as small circles.

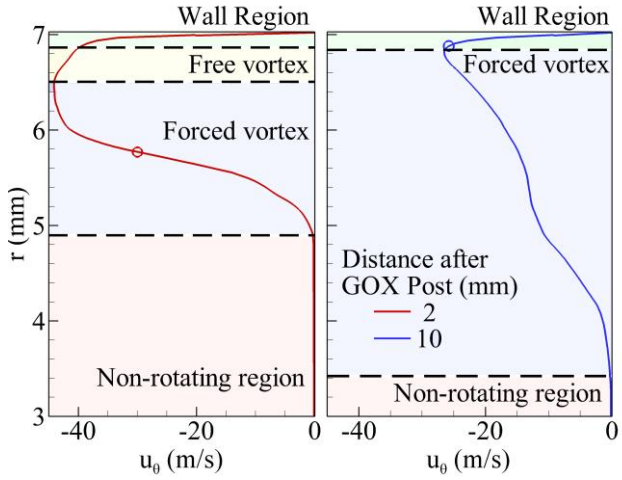

Figure 4.22 Flow regions in recess region for the baseline case at 2 and 10mm after GOX post

As axial velocity of the GOX flow is high, a non-rotating core can be observed inside the GOX flow. Outside of the non-rotating core, a forced region is formed, where GOX is forced to rotate, and u_θ increases with the radial distance from the centerline. At the location of kerosene flow, a free vortex is identified, where the azimuthal momentum, $u_\theta r$, remains constant. Near the wall, a boundary layer is formed and u_θ reaches zero rapidly.

As shown in the right plot of Figure 4.22, further downstream, the azimuthal momentum transfer from kerosene to GOX results in rapid radial expansion of forced vortex region, whereas free vortex region disappears, and non-rotating region is compressed. The mixing process also decelerate the azimuthal velocity of kerosene flow. Immediately after mixing, the liquid surface lies forced vortex region. While at 10 mm from GOX post, this surface falls in wall region, due to mass and azimuthal momentum transfer.

In this study, in order to quantify and compare mixedness among all cases, spatial mixing deficiency (SMD) [161, 163] is calculated at several cross sections in the near field. The SMD index corresponds to a planar average and measures the spatial heterogeneity of the mixture. SMD can be based on any instantaneous flow variable, and mass fraction of fuel is used as *y* in this study. Over *m* snapshots, SMD in one specific plane is calculated as

$$SMD = \frac{RMS_{plane}(<y_i>)}{Avg_{plane}(<y_i>)} \quad \textbf{(4.7)}$$

$$Avg_{plane}(< y_i >) = \frac{1}{m}\sum_{i=1}^{m} < y_i > \quad \textbf{(4.8)}$$

$$RMS_{plane}(< y_i >) = \sqrt{\frac{1}{m-1}\sum_{i=1}^{m}\left(< y_i > - Avg_{plane}(< y_i >)\right)^2} \qquad \textbf{(4.9)}$$

From the definitions, smaller values of SMD indicate more complete mixing, and a zero SMD corresponds to perfect mixing. The evolution of mixture-fraction-based SMD at multiple axial locations for all cases are depicted in Figure 4.23. For each case, SMD covers recess and taper region with an axial interval of 0.5mm. Mixing is promoted as mixture flows downstream, so SMD generally decreases with the increase of axial location. The only exception is in Case 1, where SMD drops gradually at the beginning of recess region, but slightly increases due to the fuel injection and its direct penetration into GOX flow. From Figure 4.23, it can be observed that Case 2 has the best mixing efficiency. From Case 3 through 6, mixing efficiency decreases with the decrease of recess length.

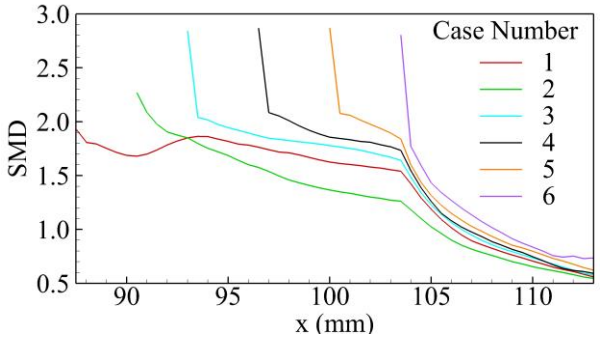

Figure 4.23 SMD in recess region and taper region for all cases

Figure 4.24 provides a better illustration of the comparison between Case 1 and Case 2. In Case 1, with no shielding, kerosene flows radially inward and penetrates into GOX flow. Thick liquid film forms at the head end, and the kerosene is gradually entrained by GOX. For Case 2, on one hand, short fuel passage leads to the conversion of radial velocity to axial velocity, thus the initial liquid film thickness is thinner than Case 1. On the other hand, shielding collar rim ends at the same axial location of the center of recirculation

bubble. The direct exposure of kerosene reattachment process to flow penetration results in deeper penetration of GOX flow into kerosene film.

To conclude, for injectors whose kerosene injection process is fully covered by shielding (Case 3-6), longer recess length leads to improvement of mixing efficiency. On the other hand, a GCLSC injector with short fuel passage (Case 1-2) can achieve better mixing efficiency than fully-recessed GCLSC injector.

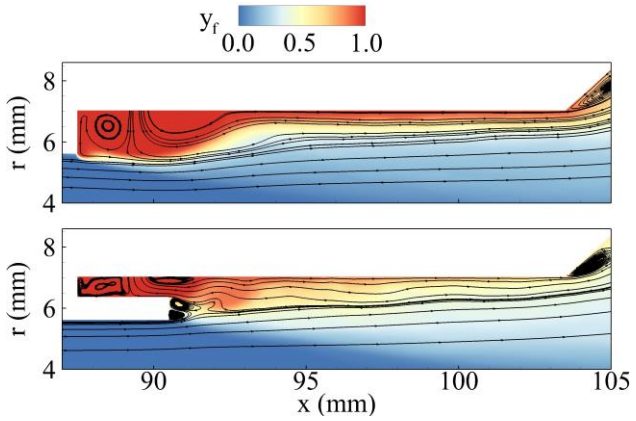

Figure 4.24 Time-averaged kerosene mass fraction distribution and streamlines for Case 1 and 2

4.5 Conclusions

Supercritical fluid flow characteristics and mixing behaviors of gas-centered, liquid-swirl coaxial (GCLSC) injectors have been studies extensively. Gaseous oxygen (GOX) and kerosene are used as the working fluids at a chamber pressure of 253.0 bar. The end of the center GOX post is recessed from the entrance of the taper region. Cases with different recess length (and correspondingly, fuel-shielding collar length) are studied to identify the influences of geometric attributes on the flow evolution and mixing.

Both instantaneous and time-averaged flow properties are examined systematically. In the case without the fuel-shielding collar, the initial kerosene/GOX interaction resembles a swirling transverse jet into a crossflow, and flow recirculation occurs near the kerosene injection slit and the head end. In other cases with the fuel-shielding collar, the kerosene flow is predominately axial before it enters the mixing zone; the coflow kerosene and GOX streams expand radially and form flow recirculation in the wake of the GOX post. Flow unsteadiness occurs during fluid injection and mixing. Vorticity production takes place in the boundary layer of the incoming GOX stream, along the wall of the fuel passage, and at the kerosene/GOX interface. As a result, the flowfield is characterized by salient vortical structures, such as forward-rolling vortices whose sizes and spacing change as they convect downstream. Depending on the travel distance, as determined by recess length, these vortices assume different levels of spatial coherence and macro-mixing capability that defines the early-stage mixing characteristics. As the flow enters the taper region, the vortices rapidly enlarge via stretching and/or amalgamation, changing the acoustic features and mixing effectiveness of the injectors. The flowfield is further complicated by another geometric change at the injector exit, and the downstream computational domain features multiple toroidal recirculation zones, flow separation, and reattachment, whose locations and structures vary according to the geometry.

Key flow dynamic characteristics in GCLSC are also identified and analyzed. After GOX injection, longitudinal acoustic waves can be observed in GOX post and recess region. Inside recess region, entrainment of low-speed, high-density kerosene to high-speed, low-density GOX induces shear layer instability, in both axial and azimuthal

directions. The influence of recess length on shear layer instability is explored in detail. In the taper region, the vortices undergo propagation, disintegration and merging processes.

The momentum and mass transfer between GOX flow and kerosene flow of all cases are examined through the analyses of the mixing layer evolution. Mixing layer expands as mixture flows downstream. Influence of recess length on mixing efficiency is also elaborated. Mixedness at different axial locations among all cases are quantified and compared. Case 2 achieves the most efficient mixing, and Case 6 achieves the least efficient mixing.

CHAPTER 5.

GAS-CENTERED LIQUID-SWIRL COAXIAL INJECTOR COMBUSTION DYNAMICS

The combustion characteristics of GCLSC injectors are numerically investigated in the current section. As mentioned in the previous section, GOX at 687.7 K is injected into the center post while kerosene at 492.2 K is delivered tangentially into the coaxial annulus. The initial operating pressure is 25.3 MPa. Figure 5.1 shows a global view of instantaneous temperature distributions for Cases 1, 3, and 6. The geometry-dependent flame dynamics are clearly observed. The entire flowfield can be divided into four regimes: propellant injection, flame initialization, flame development, and intensive combustion, as shown schematically in Figure 5.2. The injection regime consists primarily of the center tube and coaxial annulus, where GOX and kerosene are injected separately. The flame is initialized and anchored in the wake of the GOX post and develops further in the recess region. Intensive combustion then takes place and becomes well-distributed in the downstream region for the cases with recess region. For Case 6 without recess, the interaction of GOX and kerosene is delayed to the taper region. Combustion resides primarily in the upper end of the downstream region close to the injector faceplate, because of the insufficient entrainment of kerosene into the GOX stream. The details of flow evolution and flame dynamics in these regions, as well as the influences of recess length on combustion dynamics, will be discussed in the following sections.

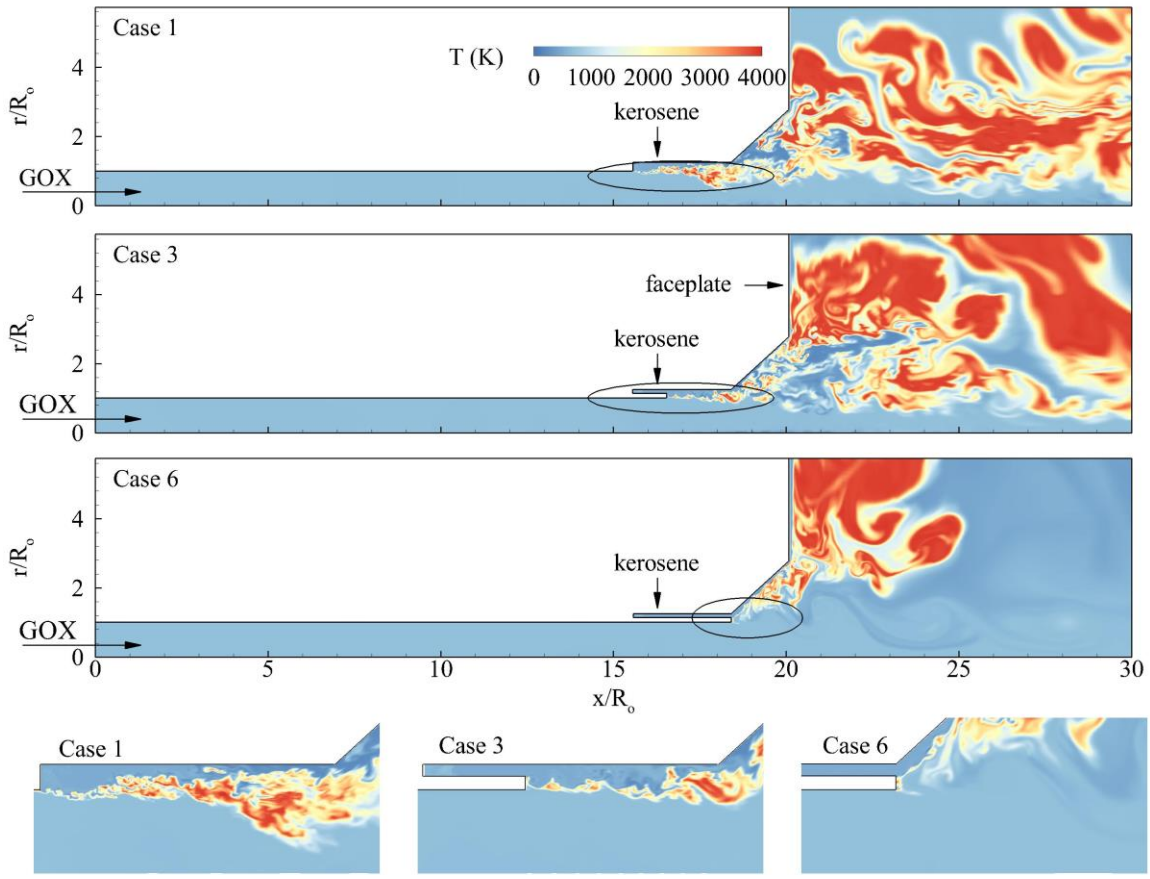

Figure 5.1 Global and zoom-in views of instantaneous temperature field for Cases 1, 3, and 6

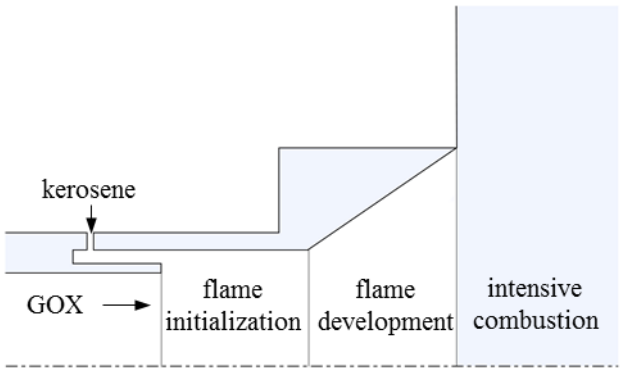

Figure 5.2 Schematic of flow regimes

5.1 Propellant Injection Region

Figure 5.3 shows the radial profiles of time-averaged axial velocity immediately downstream (Case 1) or upstream (Cases 2-6) of the GOX post tip. The vertical dashed line

represents zero velocity, and the horizontal dashed line denotes the center of the coaxial annulus. The region of $1.0 < r/R_o < 1.13$ is a continuous flow zone in Case 1, but is displaced by the fuel shielding in Cases 2-6. As the recess length decreases (the shielding length increases accordingly), the axial velocity decreases slightly within the GOX post ($r/R_o \leq 1.0$). This is attributed partly to the increasing viscous loss along the GOX post surface and partly to the pressure change in the downstream flame zone with different geometries. Different flow profiles are observed in the coaxial fuel annulus ($1.13 \leq r/R_o \leq 1.25$). Because of the lack of shielding in Case 1, kerosene is radially injected into the GOX stream, which has a stronger axial momentum. The kerosene stream must adjust its direction and merges into the GOX flow. The negative profile in the region of $1.13 \leq r/R_o \leq 1.25$ in Figure 5.3 is caused by flow reversal in the corner region.

In Cases 2 and 3 ($L_r \geq 10.5$ mm, $L_s \leq 5.5$ mm), the distribution of axial velocity in the fuel annulus resembles that of a channel flow with significant angular momentum. The shielding is too short to allow for the full development of the kerosene stream in the annulus. As the shielding length increases (Cases 4 and 5), the residence time for kerosene in the annulus increases, rendering a fully developed flow, as manifested by the axisymmetric velocity profiles in Fig. 4. In spite of the longest residence time in the fuel annulus in Case 6, the profile of axial velocity ($L_r = 0$) is asymmetric, with the peak value shifting to above the center. The phenomenon is caused by two contributing factors: 1) the kerosene stream spreads upwards due to the sudden expansion in the entrance of the taper region and the swirl-induced centrifugal force; and 2) the expansion of hot products in the wake of the GOX post drives kerosene to flow along the taper surface.

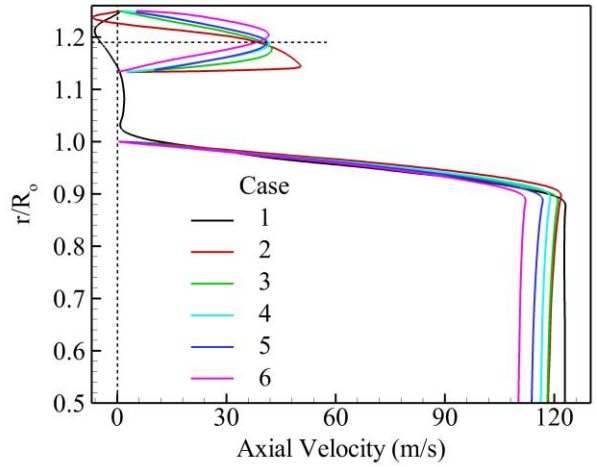

Figure 5.3 Radial profiles of time-averaged axial velocity immediately downstream (Case 1) or upstream (Cases 2-6) of the GOX post tip.

Figure 5.4 shows the time-averaged bulk axial momentum immediately upstream of the end of the GOX post as a function of recess length. It is obtained by integrating axial momentum flux in the radial direction. The axial momentum in the fuel annulus is not plotted for Case 1, because the fuel stream penetrates radially into the GOX flow with the lack of shielding. The axial momentum decays gradually with increasing fuel shielding (decreasing recess length) in the inner tube, due to increasing viscous loss along the post surface. The axial momentum in the fuel annulus follows a similar trend until the recess length approaches zero, and increases slightly. This distinction is attributed to the dynamic process near the taper region when there is no recess (Case 6). The sudden expansion of the swirling kerosene stream at the exit of the fuel annulus triggers momentum transfer from the angular to the axial component [150]. This gain overshadows the viscous loss along the annulus surface, and leads to the slight increase in axial momentum at the annulus exit.

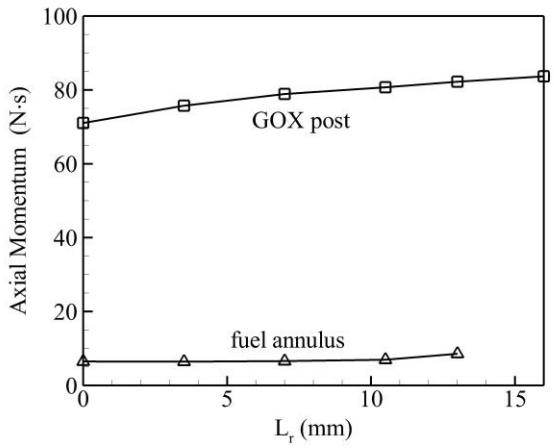

Figure 5.4 Time-averaged bulk axial momentum immediately upstream of the end of GOX post as a function of recess length.

5.2 Recess Region

Figure 5.5 shows snapshots of the temperature and mixture-fraction fields in the recess region for all cases. The arrow denotes the location of the kerosene injection slit. The flame is always anchored near the GOX post tip, the axial location of which moves downstream with decreasing recess length. It then develops in the mixing layer between the GOX and kerosene. The flame structures are largely induced by the shear-layer instabilities, originating from various mechanisms of flow convection, baroclinicity, and volume dilation. The latter two were found to be significant in vorticity production at supercritical conditions [164]. Kerosene is entrained into the GOX stream through various sizes of vortical motions, while GOX expands radially into the kerosene stream through mass diffusion and turbulent mixing. The kerosene stream forms a thin liquid film along the annulus outer surface due to the swirl-induced centrifugal force. The axial velocity of the film is significantly accelerated by the shear-layer growth as the film convects

downstream. The film thickness decreases because of mass conservation, and the mixing region increases accordingly.

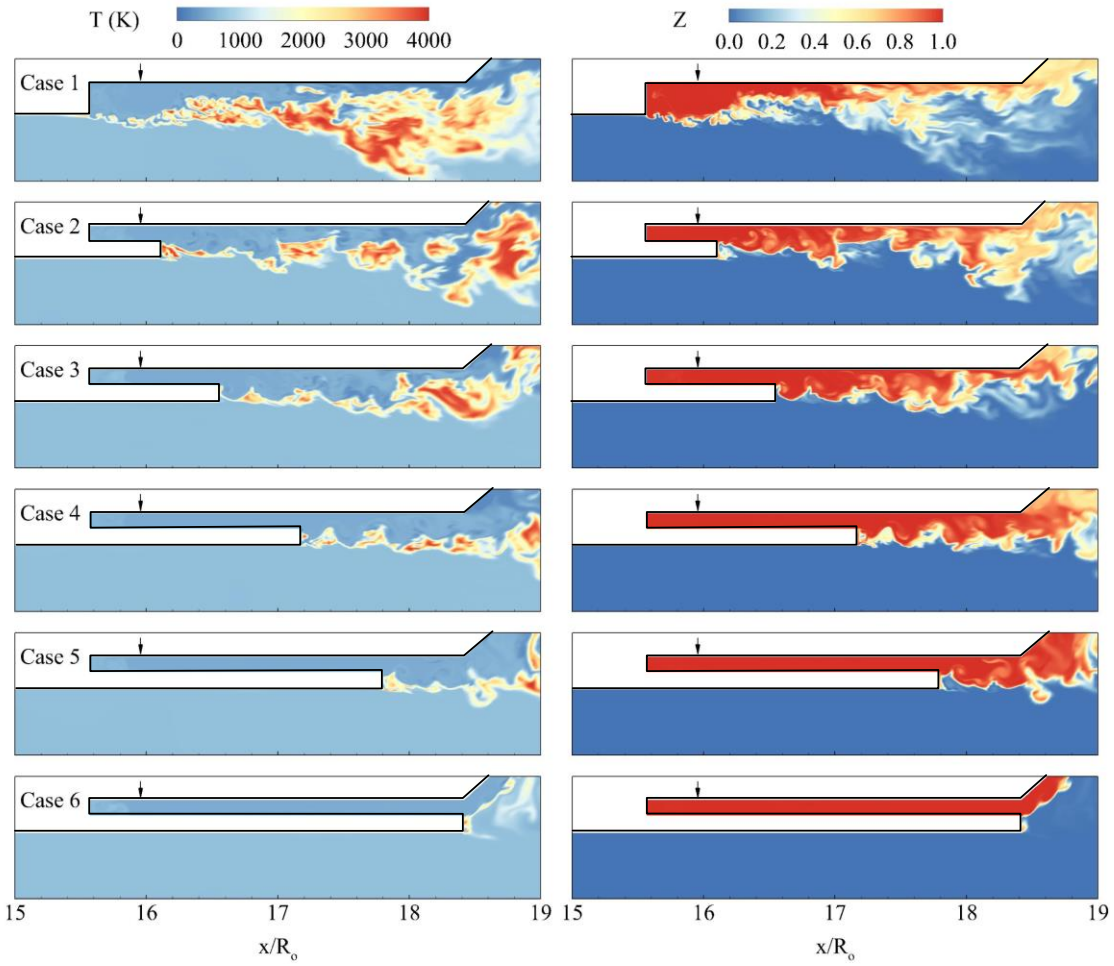

Figure 5.5 Snapshots of temperature (left) and mixture fraction (right) fields in recess region for all cases

The mixing efficiency at the exit of the injector increases with recess length. Figure 5.6 shows the radial distribution of mixture fraction at the exit of the recess region for all cases. The pink dashed line for Case 6 represents a discontinuity (GOX post), where GOX in the inner tube has not yet interacted with kerosene in the annulus. The region with finite gradient of mixture fraction indicates the presence of a mixed state. Case 1 has the widest radial span of finite gradient among the six cases. This span decreases with decreasing

recess length, and becomes zero for Case 6. The maximum mixture fraction on the outer surface of the annulus (R_f/R_o = 1.25) is much less than unity for Cases 1-3. Therefore, the longer the recess, the higher the mixing efficiency. This observation is also supported by the increase of flame area with recess length, as seen in Figure 5.5. Intensive combustion is initiated in the recess region, while it is delayed to the taper region for Case 6 (with no recess).

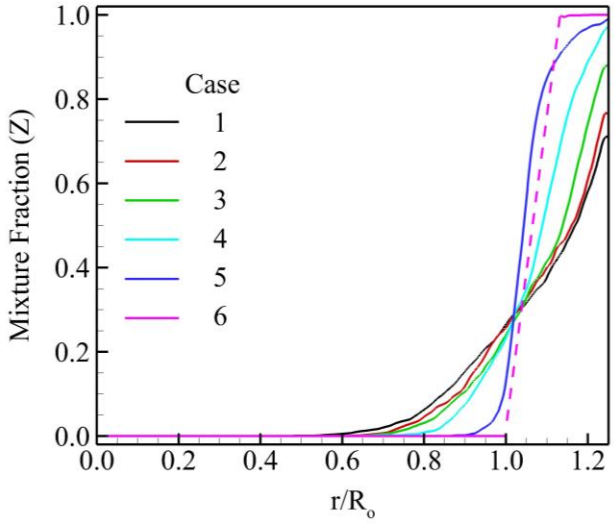

Figure 5.6 Radial distributions of mixture fraction at exit of recess region for all cases

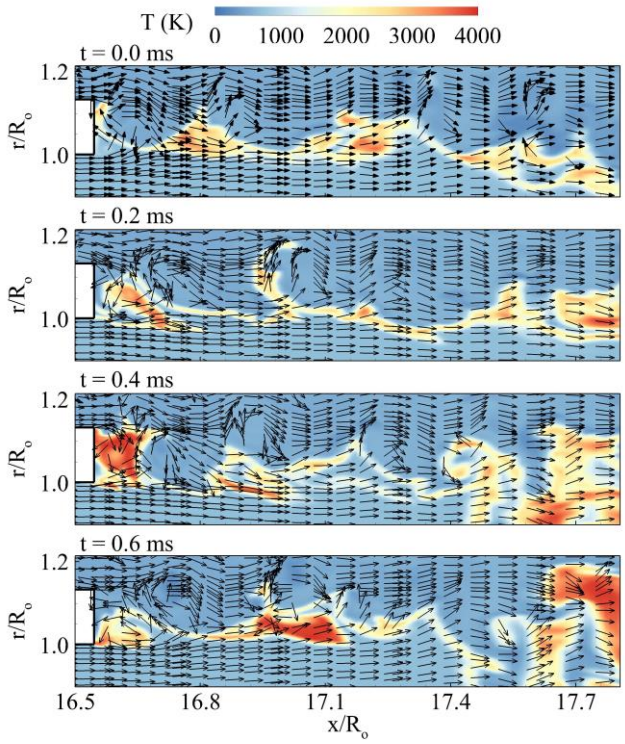

Figure 5.7 Temporal evolution of temperature field overlaid by velocity vectors in recess region for Case 3

The flow evolution offers more insight into the flame initialization process. Figure 5.7 shows the temporal evolution of the temperature field overlapped by the velocity vectors for Case 3. Here t = 0 ms is an arbitrary reference point after the flame is sufficiently developed. At t=0 ms, the flame is detached from the GOX post tip. Between them, a recirculation zone is formed, and it in turn enhances the mixing between GOX and kerosene. At t = 0.2 ms, the flame moves up stream, as a result of the enhanced mixing, but remains detached. It becomes fully attached to the post at 0.4 ms, at which point the mixing reaches the optimal state. After extensive consumption of the reactants, the flame shifts downstream and another flame cycle begins. Large vortical motions arising from the shear-layer instability in the mixing region play an important role in stabilizing the flame. These vortices provide a longer residence time for the interaction of GOX and kerosene. It is

concluded that the flame is initiated and stabilized by the intensive vortical motions in the wake of the GOX post. This observation was corroborated qualitatively using optical diagnostics, in a recent study of the flame dynamics of a geometrically similar injector [165]. The wrinkled flame is transported downstream and induces a broader combustion zone in the taper region, where the propellants have been sufficiently mixed.

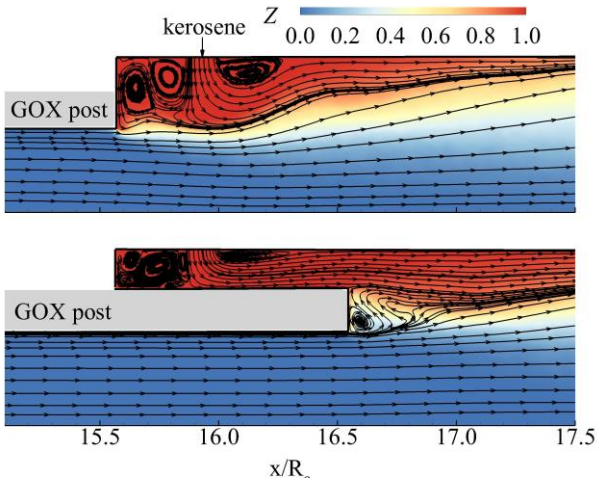

Figure 5.8 Time-averaged mixture fraction distribution superimposed by streamlines for Cases 1 (top) and 3 (bottom)

Figure 5.8 shows the time-averaged distribution of the mixture fraction, superimposed with streamlines in the recess region for Cases 1 and 3. For Case 1 with no fuel shielding (L_r = 16 mm), the end of the GOX post is radially aligned with the headend of the fuel annulus. The flow pattern is similar to that of a liquid jet in a crossflow. The kerosene penetration depth is roughly equivalent to the height of the rear-facing step. The injected kerosene is divided into two branches. One flows upstream to the headend and generates two large recirculating bubbles. The flow residence time in this zone is on the order of magnitude of the ignition time delay of reactants, allowing sufficient mixing between GOX and kerosene to activate ignition. The other branch, containing the majority

of the kerosene stream, travels downstream along with the GOX stream. Case 3 presents a significantly different flow pattern due to the presence of fuel shielding. The swirling fuel flow moves downstream in the annulus. A small recirculating bubble with an oxygen-rich mixture is established next to the lower part of the GOX post tip. The situation differs from that in a bi-swirl injector in which two-counter rotating bubbles occurs in the wake of the inner swirler [166].

5.3 Taper Region

The flame is further developed in the taper region, and this serves several purposes. First, the taper adjusts the fuel spreading angle to a desired value to facilitate inter-injector element mixing (42° in the present study). Note that the original spreading angle of the fuel injected into an open environment should exceed the taper angle, so that fuel flows along the injector surface to provide thermal protection. Second, the taper region provides necessary damping of acoustic oscillations originating from the intensive combustion in the chamber. The acoustic energy can be dissipated and/or convected by the vortex motions in the taper region.

Figure 5.9 shows snapshots of the mixture fraction field in the taper region for all cases. As previously discussed in connection with Figure 5.6, the mixing near the entrance of the taper region improves as the recess length increases. The mixture fraction along the taper surface decreases accordingly. In particular, for Case 6 (no recess, $L_r = 0$), the kerosene stream travels along the taper surface and then along the injector faceplate in the downstream region, due to the swirl-induced centrifugal force. The kerosene and GOX

barely mix. The GOX flows primarily in the axial direction, but the kerosene spreads outward. This situation is undesirable in practical applications, and underlines the necessity of a recess for the current injector prototype.

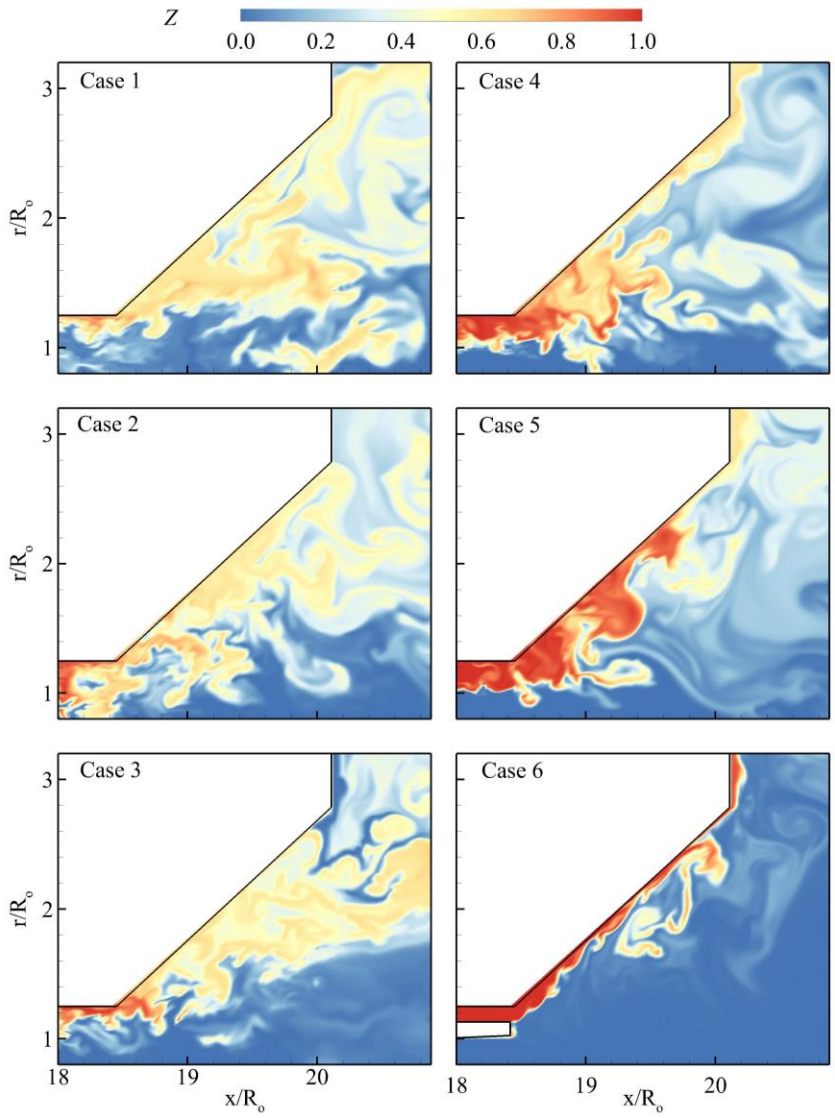

Figure 5.9 Snapshots of mixture fraction field in taper region for all cases

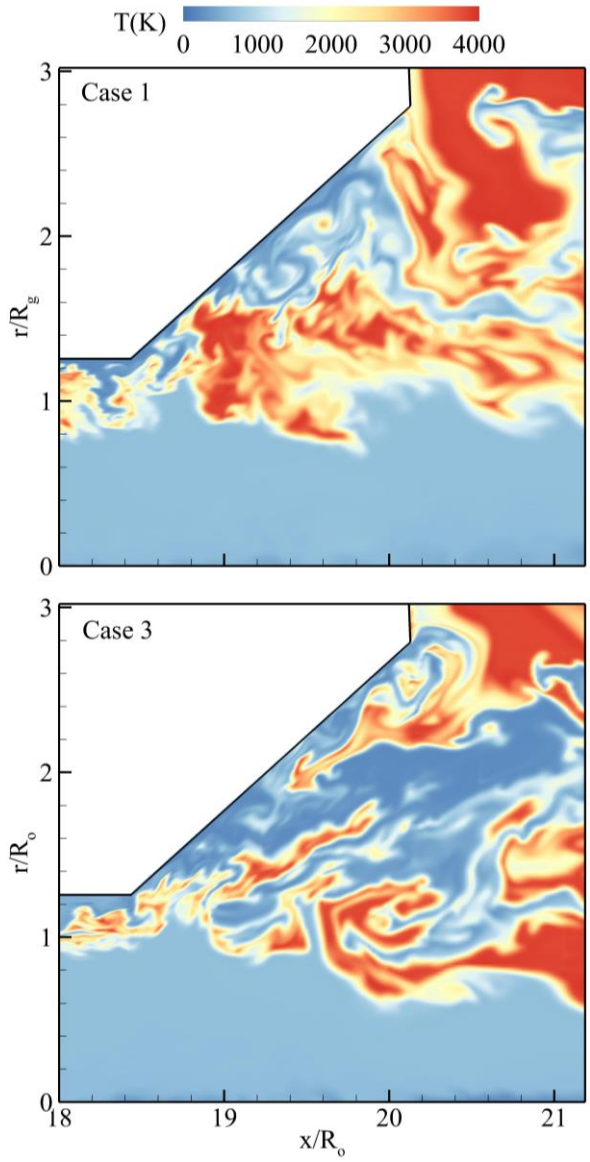

Figure 5.10 Snapshots of temperature field in taper region for Cases 1 and 3

For Cases (1-5), with a recess region, a certain level of mixedness is established upstream of the taper region. Although the mixture fraction along the taper surface decreases from Case 1 to Case 6, it is always larger than the stoichiometric mixture fraction. The temperature near the taper surface is thus relatively low. This is demonstrated by the snapshot of the temperature field in Figure 5.10. The kerosene-rich mixture protects the taper surface from being overheated by the hot products in the flame region, reducing

cooling requirements and prolonging the life of the device. Case 1 shows a more distributed burning area than does Case 3, and this is consistent with the earlier observation that Case 1 achieves better mixedness in the recess region.

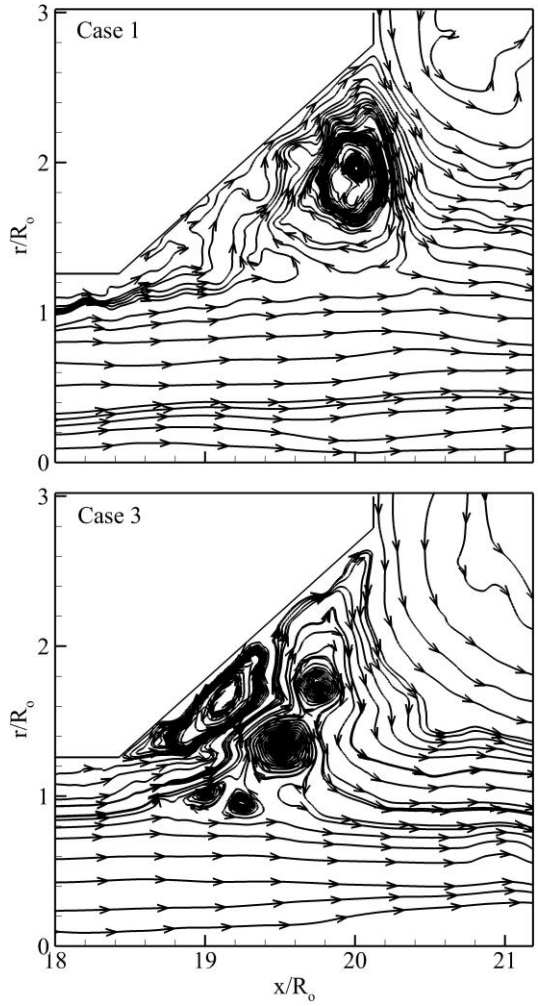

Figure 5.11 Instantaneous streamlines in taper region for Cases 1 and 3

Another important role of the taper is to stabilize the flame. Figure 5.11 shows instantaneous streamlines in the taper region for Cases 1 and 3. Various recirculation zones next to the taper surface are produced by flow separation, due to the decaying swirl strength and adverse pressure gradient in the streamwise direction. These zones contain burned

products and act as a heat pool to preheat the cold propellant and sustain the combustion. The combined recess and taper regions provide the major flame stabilization mechanism. A small flame is initiated next to the GOX post tip in the recess region. When transported to the taper region, the flame is further developed and stabilized, leading to intensive combustion in the downstream region.

5.4 Downstream Region

Figure 5.12 shows instantaneous temperature distributions in the downstream region for Cases 3 and 6. Intensive combustion occurs over a broad area in both radial and axial directions in Case 3, while burning takes place only along a radial layer next to the injector faceplate in Case 6. As discussed above, there is insufficient mixing between GOX and kerosene in the taper and recess regions in Case 6. Kerosene flows along the taper surface and then the faceplate, and the GOX in the inner tube is transported downstream axially without much kerosene entrainment. In Case 6, kerosene reacts with oxygen primarily in the initial downstream environment, and combustion ends when the oxygen is depleted locally. The recess is thus crucial for achieving effective mixing of propellants in an early stage and subsequent intensive combustion in the downstream region.

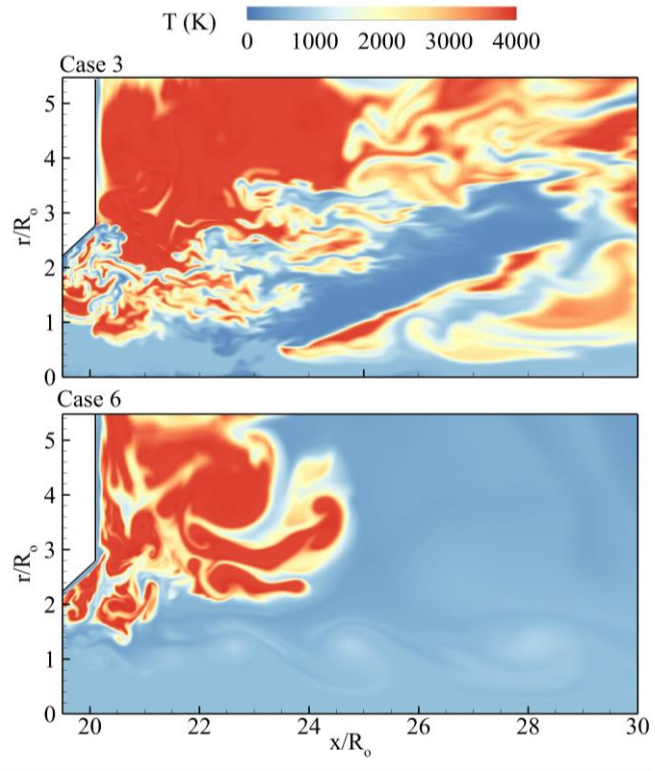

Figure 5.12 Snapshots of temperature in downstream region for Cases 3 and 6

Figure 5.13 shows instantaneous distributions of the volumetric heat release rate for Cases 3 and 6. Positive values represent the release of chemical energy from combustion, while negative values denote endothermic reactions in the kerosene pyrolysis process. The latter is consistent with the experimental observation of soot formation in locally kerosene-rich regions of combustion [165]. In Case 3, endothermic reactions are observed in multiple areas, and small hydrocarbons are generated and transported downstream for further oxidization. In Case 1, heat release is confined to the vicinity of the faceplate region.

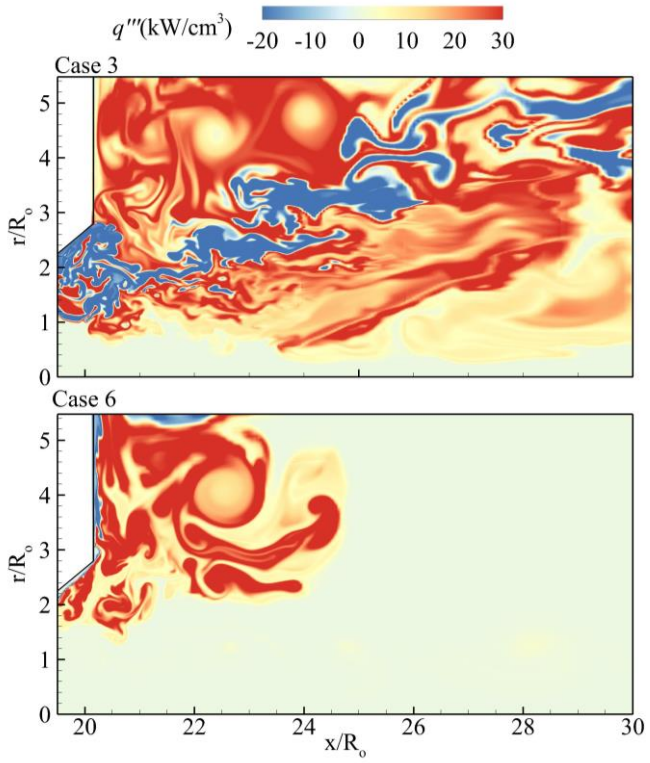

Figure 5.13 Snapshots of volumetric heat release rate in downstream region for Cases 3 and 6

CHAPTER 6.

HIGH-FIDELITY EMULATION OF NON-REACTING FLOW DYNAMICS AND MIXING

CKSPOD, which is introduced in Section 3.3, is implemented and applied to high-fidelity emulation of non-reacting flow dynamics and mixing. This method has been successfully applied to simplex swirl injector [145], which is an abstraction of injectors in many power generation and propulsion systems. The practical injectors, however, are usually featured by more complicated geometries and richer dynamic characteristics, including mixing, combustion, etc. CKSPOD is then employed to predict non-reacting flow field of GCLSC injectors, depicted in Figure 1.2. In this Chapter, CKSPOD is applied to quantify both spatiotemporally evolving flow field and time-averaged flow field.

6.1 CKSPOD Modes and Coefficients

According to previous studies [81], CKSPOD, which employs Hadamard-based POD, is able to provide better predictions of flow field than emulation methods based on conventional POD. In this section, the authors will evaluate both methods, and provide a detailed explanation of CKSPOD's superiority.

The modal energy percentages for both cases are listed in Table 6.1. As elaborated in the Methodology, Hadamard-based POD shares the same set of eigenvalues among all cases. For conventional POD, the energy percentages for the test case (Case 7) are presented in the table. For both Hadamard-based POD and conventional POD, the total number of modes is equal to the number of snapshots n. Both methods can preserve the

flow field with no error when reconstructed with all modes. According to the definition, conventional POD is able to extract the most energetic modes in the flow field. This means that with same number of ranked modes, conventional POD is able to accumulate more energy than Hadamard-based POD, as shown in this table.

Table 6.1: Modal Energy Percentage of Hadamard-based POD and conventional POD

Modes	Hadamard-based POD	POD (Case 7)
1	45.60	88.70
1-10	51.59	92.47
1-50	66.28	96.31
1-100	77.18	97.94
1-200	91.81	99.44
1-1000	100.00	100.00

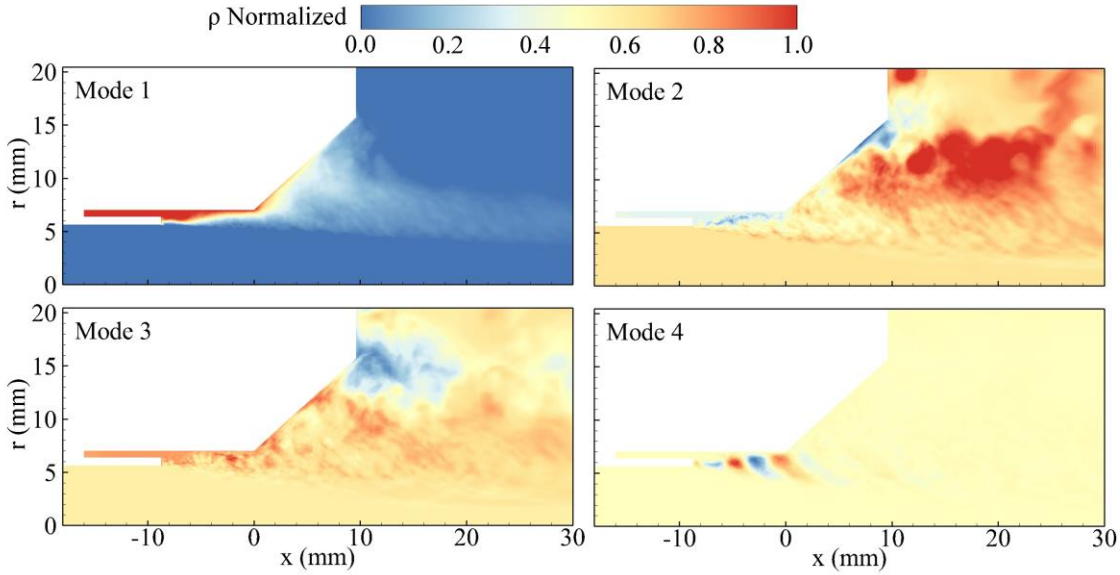

Figure 6.1 First four POD modes extracted from CKSPOD

First four normalized modes for CKSPOD are plotted in Figure 6.1. Mode 1 is an extraction of average flow field. Mode 2 and 3 extract similar physics with phase

differences. In both modes, the evolving mixing layer and complicated mixing structures in the recess and downstream regions can be observed. For Mode 4, vortex bubbles and the corresponding fuel ligaments structures are observed near the end of the shielding collar. This figure indicates that extracted CKSPOD modes are able to retain significant flow structures and dynamics.

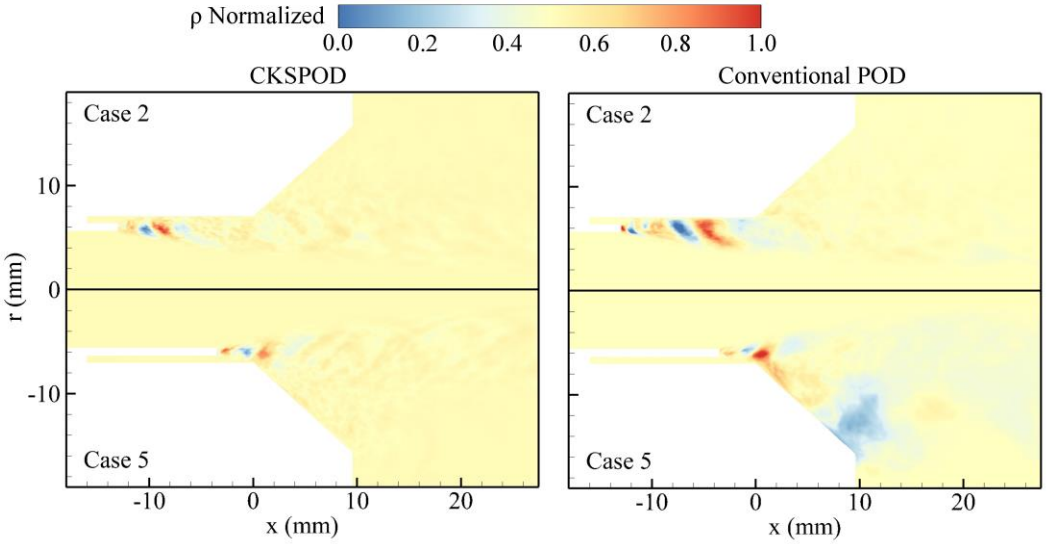

Figure 6.2 Mode 4 of CKSPOD and Conventional POD for Case 2 and Case 5

Moreover, for CKSPOD, the same set of POD coefficients leads to similar pattern of POD mode for all cases. As an example, Figure 6.2 shows mode 4 extracted by CKSPOD and KSPOD for two cases, Case 2 and Case 5, with maximum and minimum recess lengths among all training cases. Despite the differences in recess lengths, for CKSPOD, Mode 4 for Case 2 and Case 5 shows similar dynamic characteristics. This is desired, as it ensures that weighed interpolation is conducted among modes with same dynamic characteristics, and thus is able to retain physics. Conventional POD, on the other hand, exhibits different dynamics in the same mode, as illustrated on the right of Figure 6.2. The similar phenomenon can be observed for other modes and other cases (not shown here). To

conclude, with the sacrifice of modal energy percentages, Hadamard-based POD "transfers" and relocates significant dynamic structures among different modes, so that the extracted modes that are consistent across all cases.

6.2 Results and Discussions

6.2.1 Prediction of Non-reacting Instantaneous Flow Field and Flow Dynamics

A comparison of instantaneous density field between high-fidelity LES and CKSPOD is shown in Figure 6.3. As described in the previous section, the mixing process is featured by the entrainment of swirling kerosene into high-speed GOX flow. The entrainment process leads to the formation and evolution of fuel ligaments. The fuel ligaments roll up and form GOX-rich counterclockwise rotating recirculation bubbles. The bubbles develop while convecting downstream, facilitating the liquid entrainment and subsequent mixing between GOX and kerosene. In Figure 6.3, CKSPOD-based emulator is able to successfully predict the essential flow structures. Each fuel ligament is mark with vertical dotted line, which indicates that CKSPOD is able to accurately capture the location and spacing between nearby periodic structures. CKSPOD is also able to recover the density distributions in the taper region, but the accuracy decreases in further downstream in terms of predicting fine flow structure, due to the influence complicated flow dynamics and secondary flow instabilities. Moreover, for the simulation flow field, in the recess region, the fuel ligaments are thin and sharp, while for the predicted flow field, the fuel ligaments are slightly thicker, blurred with regions of intermediate density.

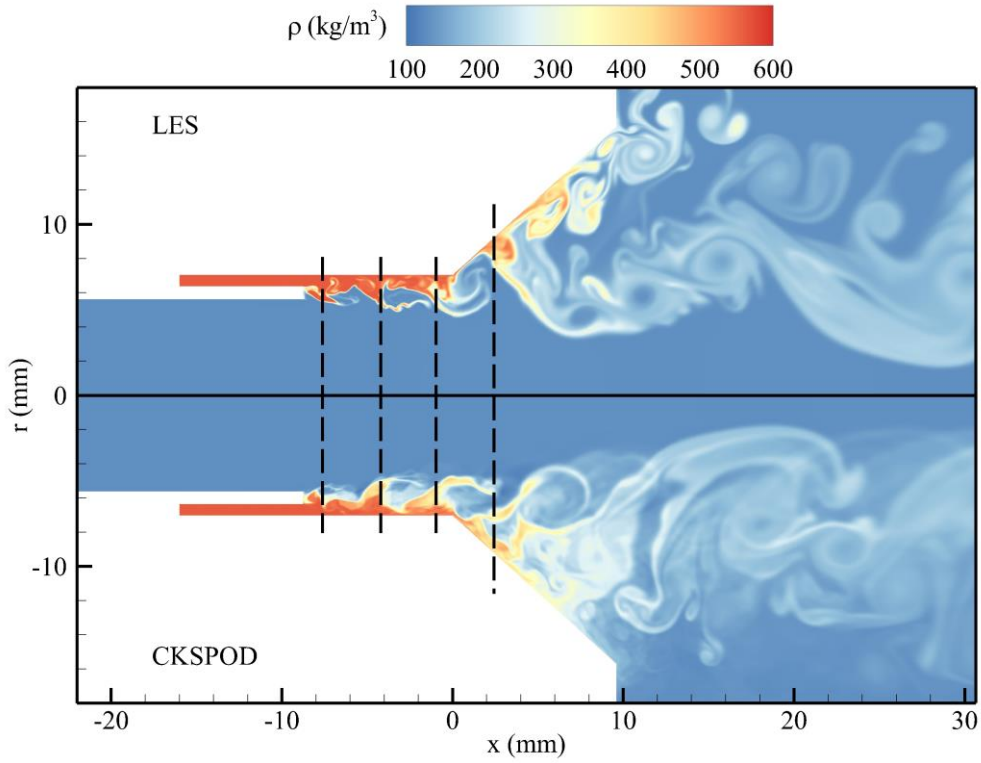

Figure 6.3 Comparison of instantaneous density field by LES and CKSPOD

The same framework can be applied to any other flow variable. As an example, the comparison of instantaneous pressure distribution is shown in Figure 6.4. A high pressure core is observed at the head end of recess region, and the periodic low pressure cores, which corresponds to the recirculating bubble, are observed in the flow field. CKSPOD is able to capture the propagation of the pressure cores in the recess region, and their interactions in the downstream region.

To further investigate the dynamic characteristics of both methods, temporal evolution of density field is plotted in Figure 6.5. The instantaneous density distributions from both LES and CKSPOD at the same temporal instants t, $t + 0.05\text{ms}$ and $t + 0.10\text{ms}$ are shown. Black dotted line indicates the propagation process of each recirculation bubble, and similar propagation speeds are observed for both LES and CKSPOD. In the taper

region, the recirculation bubbles undergo intricate processes of expansion, interaction and merging, and the fuel ligaments disintegrate. All these key time-evolving flow structures and dynamics are captured by CKSPOD.

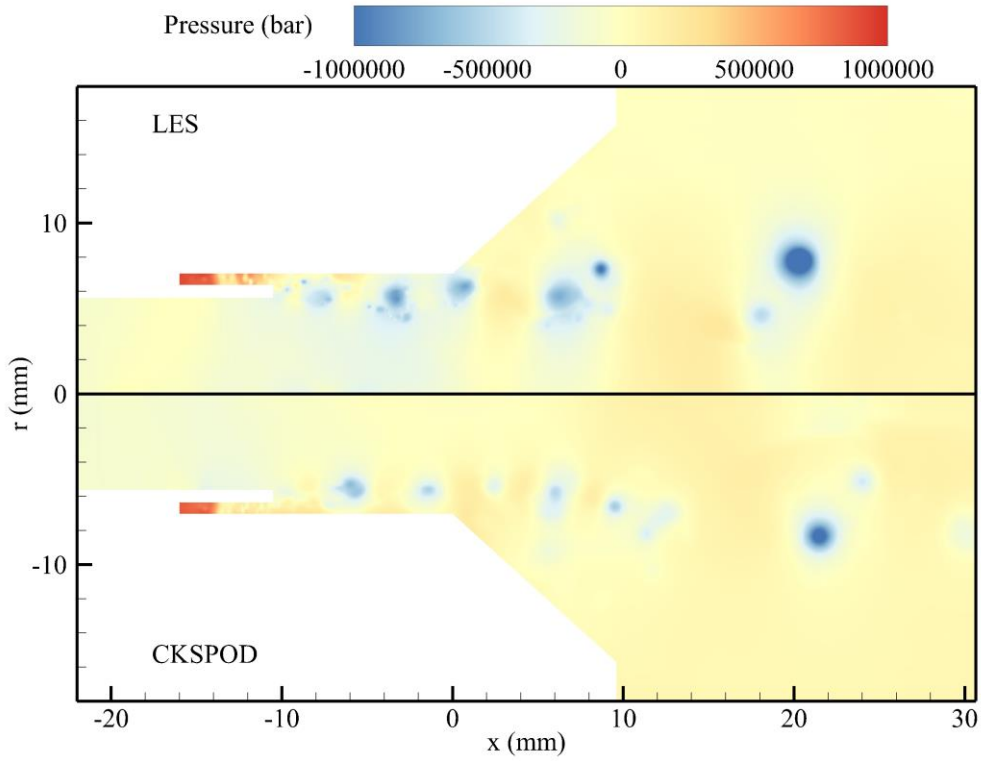

Figure 6.4 Comparison of instantaneous pressure distribution by LES and CKSPOD

One important measure of the GCLSC injector is the liquid film thickness δ. Figure 6.6 shows the probability density distribution of liquid film thickness at the end of recess region, which is estimated from the kernel smoothing function. Under supercritical conditions, liquid-gas interface is characterized by a continuous transition region, which poses challenges to the accurate definition of liquid surface. In this study, interface between GOX and liquid kerosene is defined as the location of maximum radial density gradient [142]. The estimated mean liquid film thicknesses from LES and CKSPOD are 1.25 and

1.266, respectively, and the error is within 1.3%. In Figure 6.6, probability densities from both methods exhibit similar trend and pattern. Some errors are observed for smaller δ, but is within reasonable range. Overall, CKSPOD is able to accurately capture the probability density of the time-evolving mixing layer thickness.

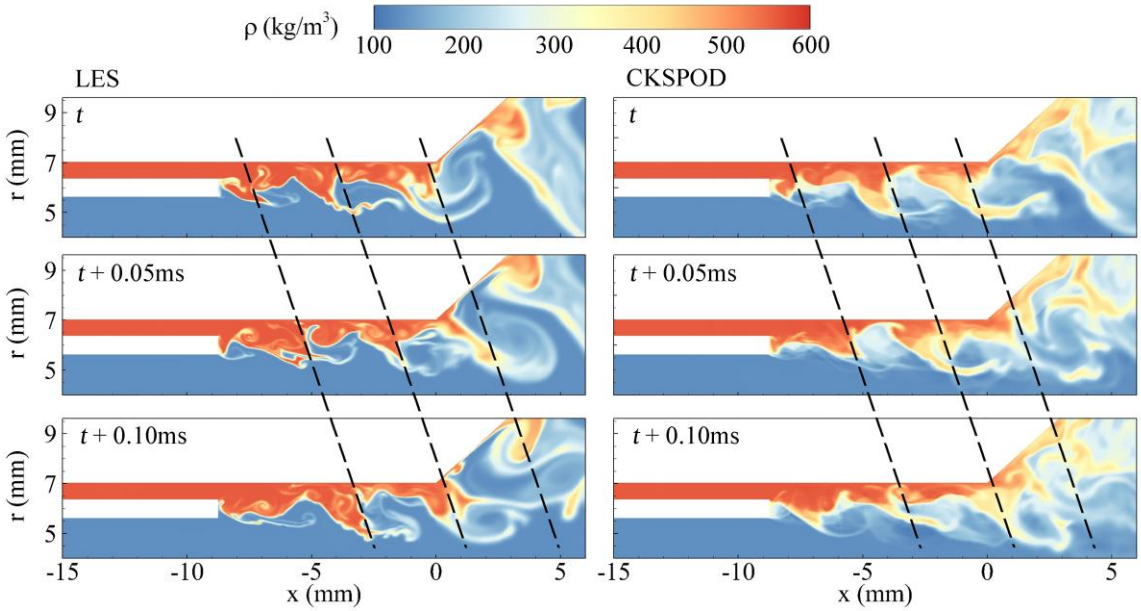

Figure 6.5 Temporal evolution of density field in the recess and taper region by LES and CKSPOD

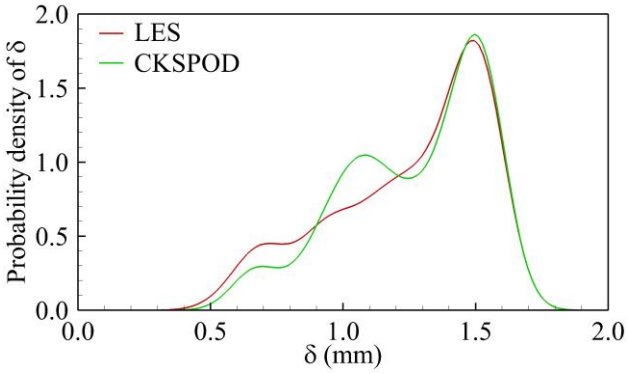

Figure 6.6 Probability density of liquid film thickness at the end of recess region

CKSPOD allows for uncertainty quantification of the predicted flow fields, and the standard deviation of the emulated instantaneous density field is presented in Figure 6.7. In the recess region, the area with higher uncertainty lies immediately behind the shielding

collar rim, and gradually expands in the radial direction. This corresponds to the GOX-kerosene mixing layer. In the taper region, the area of high uncertainty splits into two branches, one flows axially downstream, which can be attributed to the further development of mixing layer; the other branch stays attached to the wall, due to the influence of centrifugal instability. Regions of high uncertainty matches the areas with richer dynamic characteristics, which further validates the current CKSPOD method.

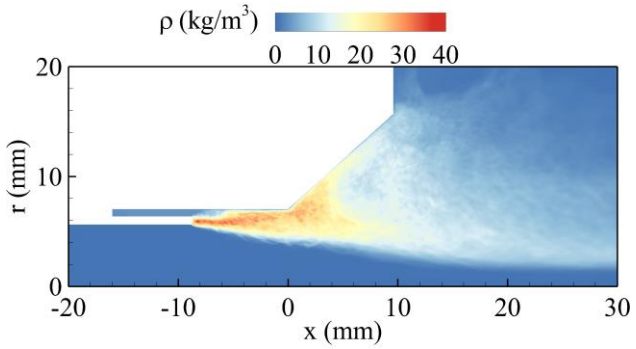

Figure 6.7 Uncertainty quantification of predicted instantaneous density flow field by CKSPOD

The computational efficiency of the similar emulation methods have been described in previous studies [79-81]. For the current study, the high-fidelity simulation of GCLSC injector takes ~100,000 CPU hours for the simulation of 10ms (1000 snapshots). For CKSPOD, the computational time is composed of the offline part and online part. The offline calculation, which includes preprocessing, reduction and training, takes ~1 CPU hour. The online part, when given a new design, takes around 60 seconds of CPU time per snapshot. For both parts, the computational time are dependent on the size of the training data. For the current dataset, the speedup of CKSPOD is in the order of ~60,000.

6.2.2 Prediction of Time-averaged Flow Field

A comparison of time-averaged density field between high-fidelity simulation and CKSPOD is presented in Figure 6.8. In the recess region, the liquid film thickness gradually decreases, accompanied by the dynamic evolving and expansion of mixing layer. In the taper region, a portion of kerosene stays attached to the taper wall, and the remainder flows axially downstream. The predicted density field from CKSPOD is able to accurately capture the time-averaged flow structures in both recess and taper regions.

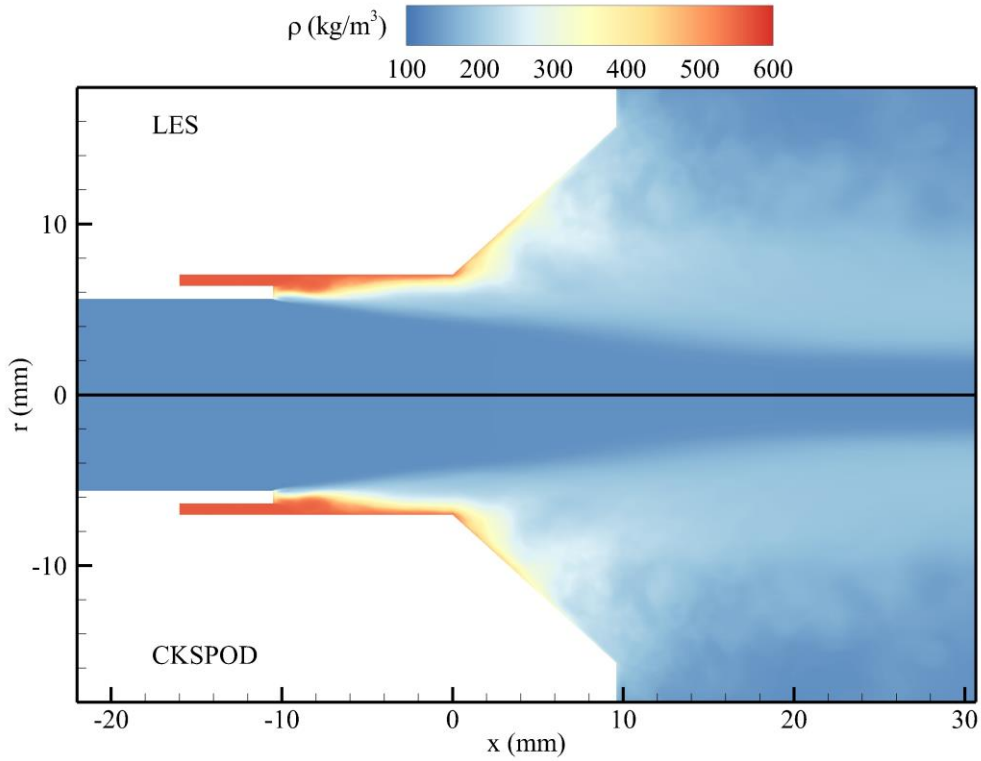

Figure 6.8 Comparison of time-averaged density field by LES and CKSPOD

In order to quantify the accuracy of CKSPOD-based emulations, two performance measures, thickness of density contours and mixing efficiency, are evaluated and compared. Figure 6.9 shows time-averaged density contours of 200, 300, 400 and 500 kg/m^3. These contours quantify the development of the shear layer, which starts from the shielding collar rim, and gradually expands in the downstream. For each contour, a close match is observed

between the results obtained from simulation and emulation. For all density contours, the error is within 1% in the recess region, and is within 5% in the taper region.

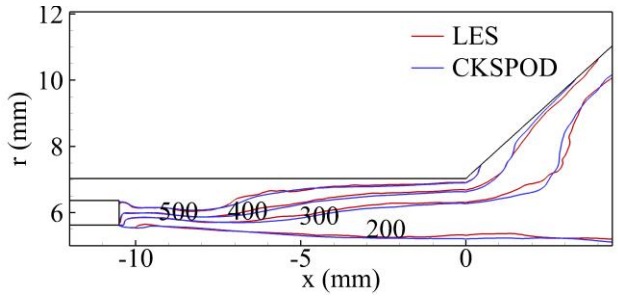

Figure 6.9 Density contours by LES and CKSPOD

In this study, mixing efficiencies are quantified and analyzed through estimation of spatial mixing deficiency (SMD) [142, 163] at multiple cross sections in the near field. SMD is defined in Section 4.4.2. From the definitions, smaller values of SMD indicate more complete mixing, and a zero SMD corresponds to perfect mixing. The evolution of SMD at multiple axial locations from both LES and CKSPOD are depicted in Figure 6.10. For each case, SMD covers recess and taper region with an axial interval of 0.5mm. Mixing efficiency is promoted as mixture flows downstream, thus SMD generally decreases with increasing axial location. From the figure, SMD of CKSPOD agrees well with that of simulation, in both recess region and taper region, and the error is within 2%. Both density contours and mixing efficiencies verified the accuracy of CKSPOD when predicting the time-averaged flow field.

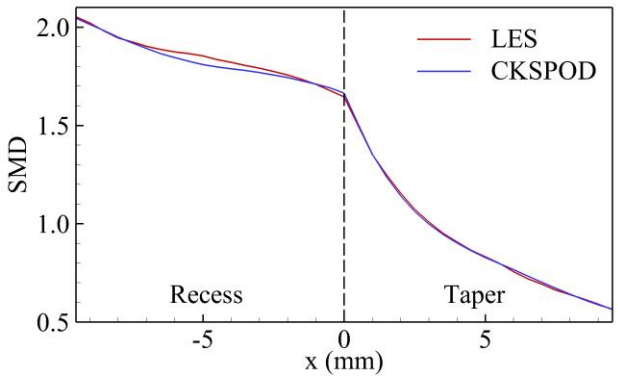

Figure 6.10 SMD in recess region and taper region by LES and CKSPOD

6.2.3 Applicability of CKSPOD

In the previous works, surrogate models are widely applied to fully developed flow, when the flow field reaches statistically stationary state. The current study extends the application to transient state. In Figure 6.11, the process of kerosene injection is shown through three snapshots with 0.3ms interval. After injection, the kerosene flow develops in the fuel annulus, interacts with GOX flow in the recess region, and propagates downstream. The comparisons indicate that CKSPOD is able to capture the flow structure and dynamic characteristics in unsteady and transient processes.

In the previous sections, the predicted instantaneous and time-averaged flow fields are based on Case 7, whose design variable is close to the center of design space. This framework is also applicable to other cases. In Figure 6.12, CKSPOD is applied to Case 4, which has longer recess length. Similar to Case 7, the proposed methodology is able to capture major flow structures and dynamics in Case 4, including the formation of fuel ligaments and recirculation bubbles, the mixing characteristics, etc. CKSPOD is also applied to many other cases (not shown here), and good agreements are observed among these cases.

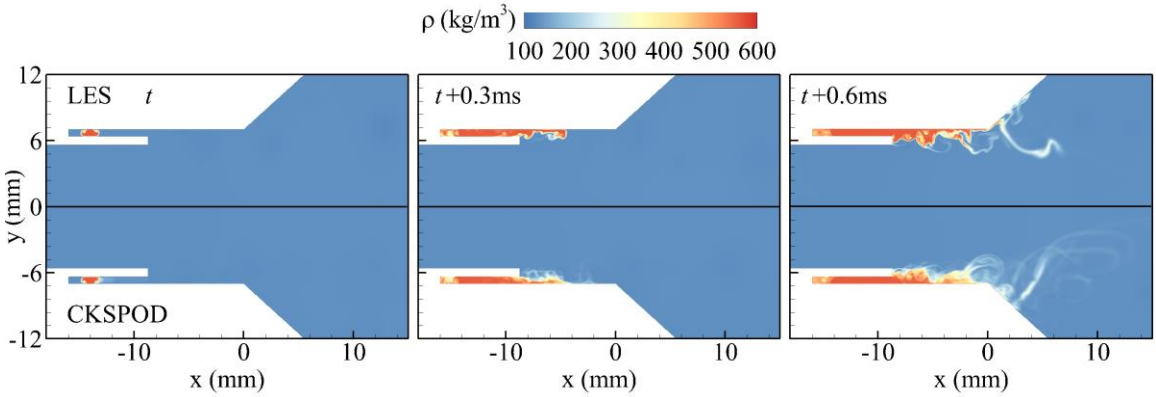

Figure 6.11 Comparison of density field from LES and CKSPOD during transient process

One exception of the CKSPOD application is to the "edge" cases, with minimum and maximum recess lengths. In this study, Case 2, with maximum recess length, is selected as an example. The recess lengths of all training cases are shorter than Case 2. This means that in the design space, all training points are clustered on one side of test point. The comparison of instantaneous density fields of Case 2 is plotted in Figure 6.13. CKSPOD is able to capture some dynamic characteristics. On the other hand, local spots with unnatural density can be observed in the emulated field. This can be attributed to lack of training case whose recess length is larger than Case 2.

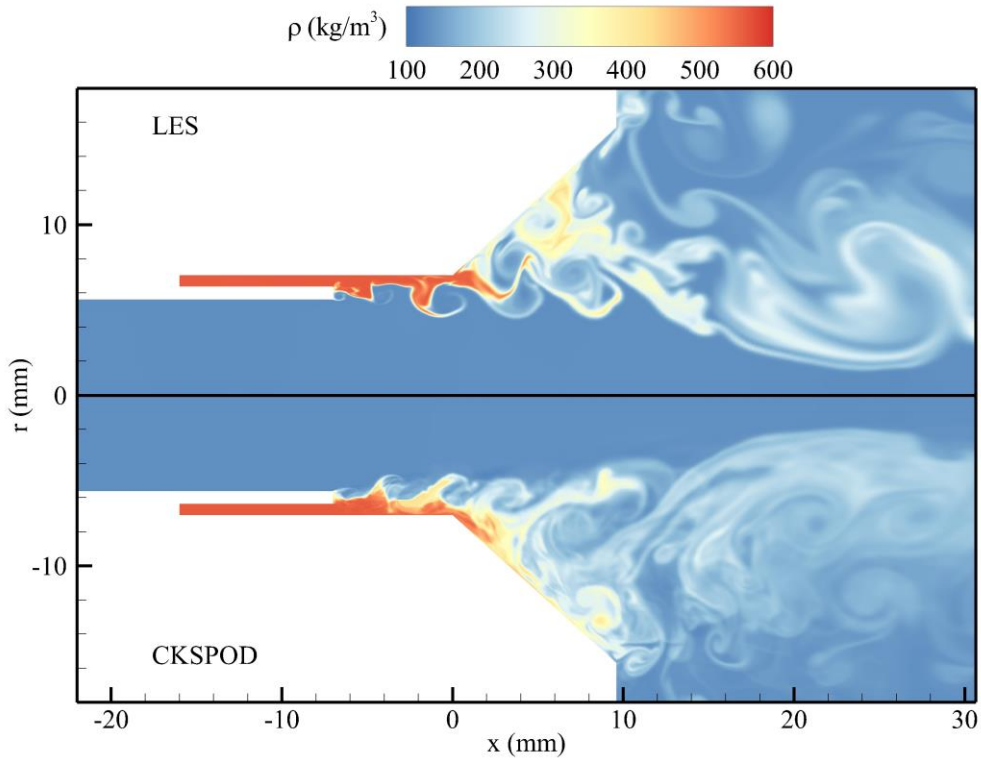

Figure 6.12 Comparison of instantaneous density field by LES and CKSPOD for Case 4

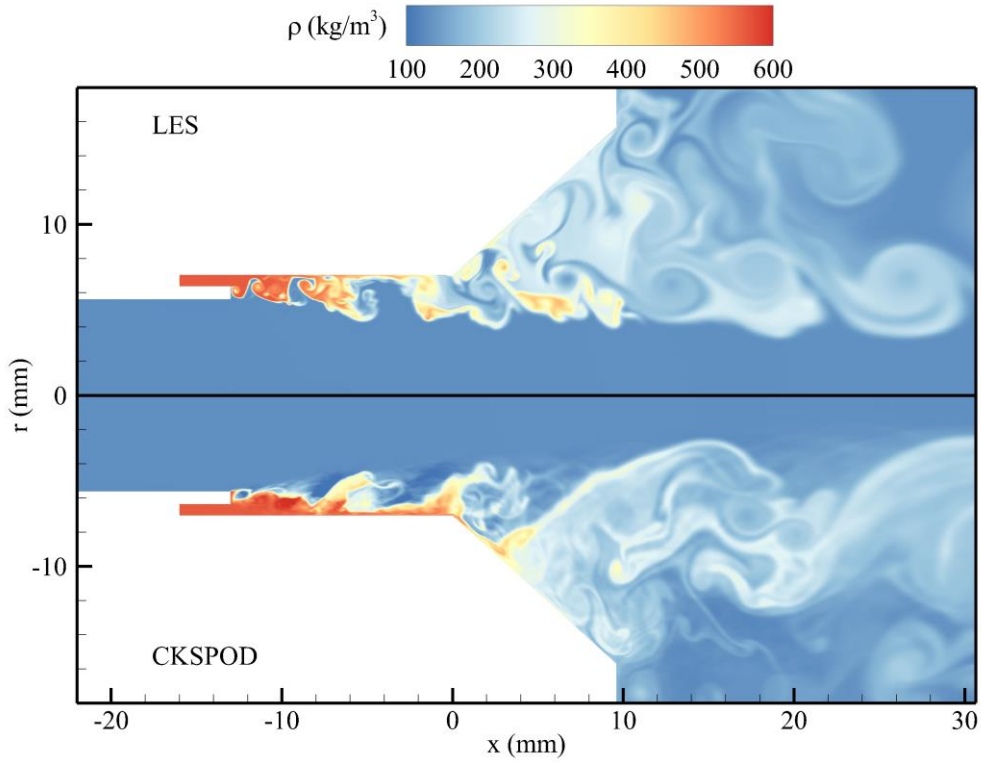

Figure 6.13 Comparison of instantaneous density field by LES and CKSPOD for Case 2

6.3 Conclusions

This study proposes and implements a high-fidelity emulation framework to predict flow dynamics and mixing. The current framework improves and employs CKSPOD, which utilizes training dataset from high-fidelity LES to enable flow field emulation in reasonable turnaround time. This model utilizes hadamard-based POD, which allows for extraction of dominant coherent flow structures. CKSPOD is applied to gas-centered, liquid-swirl coaxial (GCLSC) injectors, which are operating at supercritical conditions. Detailed comparisons of the flow fields between LES and CKSPOD are carried out. CKSPOD is able to capture instantaneous flow field, flow accuracy and mixing characteristics. Time-evolving flow dynamics, including the propagation and interactions

of vortices, are predicted with high accuracy. A good agreement is also observed for the time-averaged flow field. The time-mean density contours and mixing efficiencies from CKSPOD matches the results extracted from high-fidelity simulations. The uncertainty quantification of the predicted flow field is estimated and analyzed. The current work successfully conducted high-fidelity emulation on complex flow dynamics and mixing, and the present framework significantly reduces the computational time for evaluation of new design points, and will serve as a competitive tool for efficient survey of the design space.

CHAPTER 7.

HIGH-FIDELITY EMULATION OF REACTING FLOW DYNAMICS AND INJECTOR DESIGN OPTIMIZATION

CKSPOD, has been successfully applied to non-reacting flow of simplex swirl injector [145] and non-reacting flow of GCLSC injectors in CHAPTER 6, and has not been applied to combustion yet. Reacting flow, featured by complicated combustion dynamics and large ranges of characteristic time scales, pose challenges to the flow emulation due to the rich dynamic characteristics. In the current chapter, CKSPOD will be applied to study the spatiotemporally evolving reacting flow field and the corresponding time-averaged field. This framework is further extended to injector design optimization, based on the objective functions of mixing efficiency and injector wall thermal protection

7.1 Results and Discussions

7.1.1 Prediction of Instantaneous Reacting Flow Field

Based on CKSPOD, instantaneous spatiotemporal flow fields of the test case (Case 7) is predicted with 7 training cases as input. A comparison of instantaneous mixture fraction field between high-fidelity LES and CKSPOD is depicted in Figure 7.1. The combustion process is featured by complicated flow structures. CKSPOD is able to capture the corrugated vortices-induced mixing layer in the recess region, the gradual decrement of liquid film thickness, and the further mixing processes in the taper region. CKSPOD "blurs" some fine structures in the flow field. Overall, good agreements are observed between LES results and CKSPOD results.

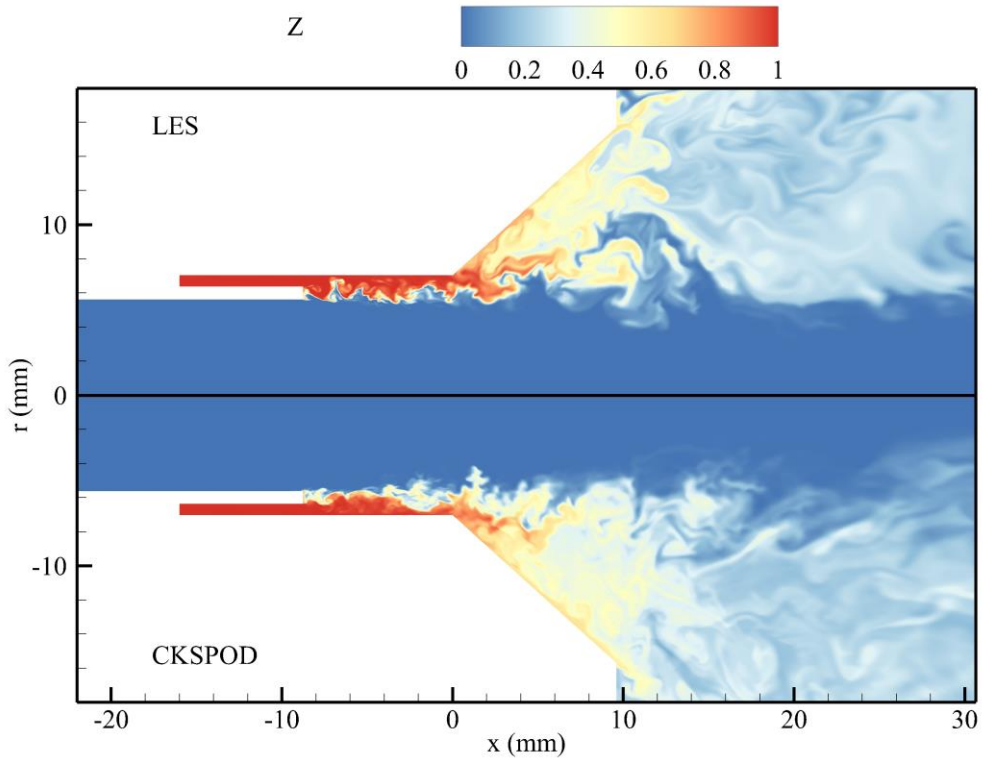

Figure 7.1 Comparison of instantaneous mixture fraction field by LES and CKSPOD

This CKSPOD implementation (depicted in Figure 3.1) can be directly applied to nearly all flow variables for either non-reacting and reacting flow field, but the direct application to temperature field prediction for reacting flow field is problematic. The temperature field is featured by large temperature range (from around 500K to 4000K) and large temperature gradients. Moreover, complex dynamics of mixing and pyrolysis take place in a small temperature range (around 500K), the contrast adds difficulty to the accurate prediction of high and low temperature regions.

As an alternative approach, in this study, temperature is obtained from the pre-calculated steady flamelet library. The look-up process of utilizes mixture fraction f, its

subgrid variance f'' and the scalar dissipation rate χ_{st} as input parameters for the flamelet library to predict filtered temperature $\tilde{T}$:

$$\tilde{T}(x,t) = \int_0^1 \int_0^\infty T(f,\chi_{st})\tilde{P}(\chi_{st})\tilde{P}(f)d\chi_{st}df \ . \tag{7.1}$$

$\tilde{P}(f)$ is dependent on mixture fraction variance, as denoted in Eq. (2.76). The intermediate mixture fraction field avoids temperature range issue, and will ensure accurate prediction of temperature flow field, as will be presented in the following sections.

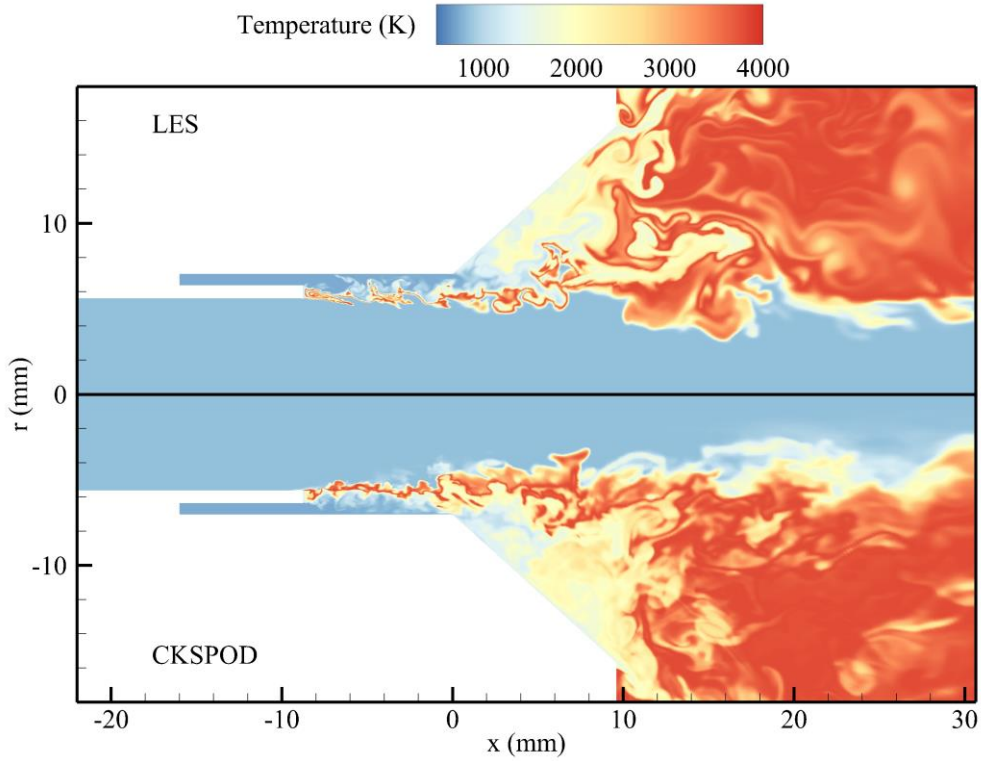

Figure 7.2 Comparison of instantaneous temperature field by LES and CKSPOD

Implementing the method mentioned above, the instantaneous temperature fields from LES and flamelet-based CKSPOD are compared in Figure 7.2. In the recess region, diffusion flame leads to the cluster of high temperature region near the mixing layer. In the

taper and downstream region, with the development of mixing layer, the reacting region rolls up, recirculates and further develops. Low temperature is observed near the taper wall due to the pyrolysis of kerosene.

CKSPOD also allows for uncertainty quantification of the predicted flow fields. The standard deviation of the emulated instantaneous mixture fraction field is presented in Figure 7.3. In the recess region, the area with higher uncertainty initiates in the immediate downstream of the shielding collar rim, and gradually develops and expands in the downstream. This corresponds to the dynamic evolving of GOX-kerosene mixing layer. Regions of high uncertainty matches the areas with richer dynamic characteristics, which further validates the current CKSPOD method.

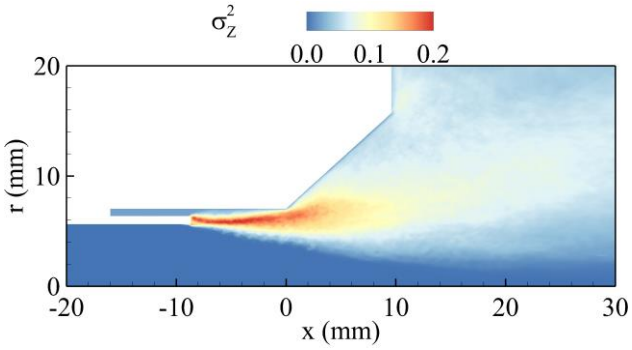

Figure 7.3 Uncertainty quantification of predicted instantaneous mixture fraction flow field by CKSPOD

7.1.2 Prediction of Time-averaged Reacting Flow Field

CKSPOD is also capable of predicting time-averaged reacting flow field. A comparison of time-averaged mixture fraction field between high-fidelity simulation and CKSPOD is presented in Figure 7.4. In the recess region, the kerosene film thickness first increases and then decreases. In the immediate downstream of shielding collar rim,

kerosene flow is decelerated in the azimuthal direction, leading to a weaker centrifugal force and thicker liquid film. In further downstream, due to the oxidization and diffusion of kerosene, the liquid film thickness decreases [167]. In the taper region, kerosene-rich flow stays attached to the taper wall. The predicted density field from CKSPOD is able to accurately capture the time-averaged flow structures in both recess and taper regions.

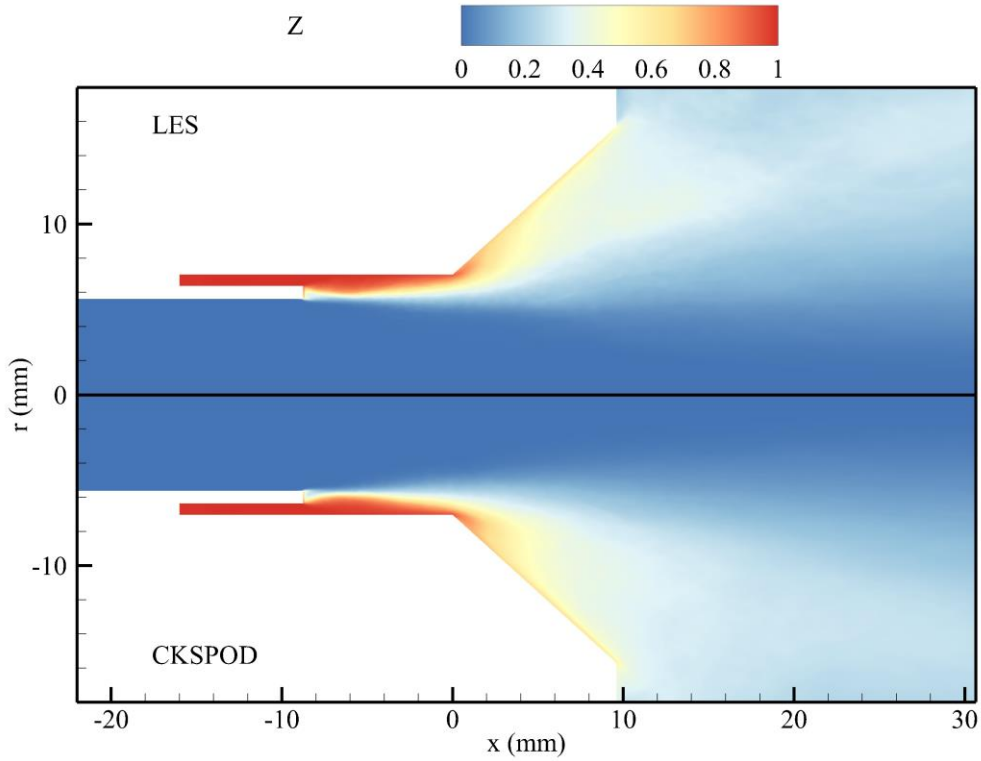

Figure 7.4 Comparison of instantaneous pressure distribution by LES and CKSPOD

In order to quantify the accuracy of CKSPOD-based emulations, thickness of mixture fraction contours are plotted and compared. Figure 7.5 shows time-averaged mixture fraction contours of 0.2248 (stoichiometric), 0.4, 0.6 and 0.8. These contours quantify the development of the shear layer, which initializes from the shielding collar rim, and gradually expands in the downstream. For each contour, a close match is observed between

the results obtained from simulation and emulation, and the error is within 1% in the recess region, within 5% in the taper region, except some extreme locations.

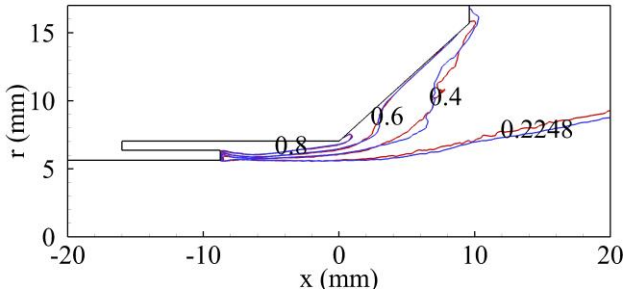

Figure 7.5 Mixture fraction contours by LES and CKSPOD

In this study, mixing / combustion efficiencies are quantified and analyzed through estimation of spatial mixing deficiency (SMD) at multiple cross sections in the near field. SMD is defined in Section 4.4.2. From the definitions, smaller values of SMD indicate more complete mixing, and a zero SMD corresponds to perfect mixing. The evolution of SMD at multiple axial locations for reacting flows from both LES and CKSPOD are depicted in Figure 7.6. SMD covers recess and taper region with an axial interval of 0.1mm. Mixing efficiency is promoted as mixture flows downstream, thus SMD decreases with increasing axial location. More efficient mixing is observed in the taper region, due to the influence of slower axial velocities and the formation of recirculation regions. From the figure, SMD of CKSPOD agrees well with that of simulation, in both recess region and taper region, and the error is within 4%. Both mixture fraction contours and mixing efficiencies verified the accuracy of CKSPOD when predicting the time-averaged flow field.

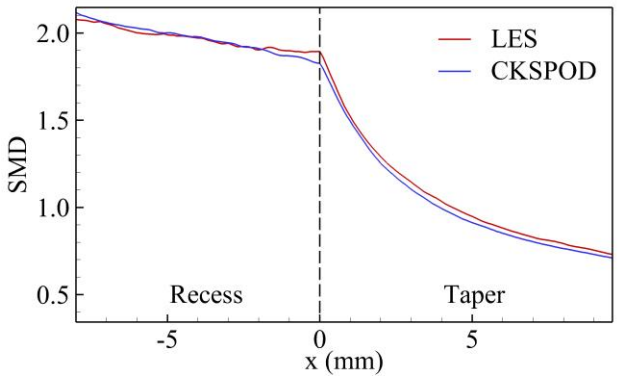

Figure 7.6 SMD in recess region and taper region by LES and CKSPOD

7.1.3 GCLSC Injector Design Optimization

The implemented surrogate model can be used to find the optimal design geometry, given a few specified performance measurements, i.e. objective functions. The design variable (recess length, L_r) is the input variable, and two objective functions, which evaluate the mixing / combustion efficiency and thermal protection to the injector wall, are defined and employed to pick the optimal design. In the current study, a set of evenly spaced sampling points with recess length interval of $\Delta L_r = 0.5mm$ is employed. For each sample point, CKSPOD is employed to predict flow field and evaluate objective functions. For comparison, LES results of 8 cases are also presented.

The first objective function, which quantifies the mixing efficiency, is defined as the SMD at the beginning of taper region. Figure 7.7 shows the current objective function as a function of recess length. LES results of 8 training cases are presented in red line, and the emulated results from CKSPOD are shown in blue symbols. As mentioned in the previous work [167], the recess length is crucial for achieving effective mixing of propellants in the early stage and subsequent intensive combustion in the downstream region. Longer recess

length corresponds to more efficient mixing, and smaller SMD. For both symbols, the similar decreasing trend is observed, indicating the high accuracy of CKSPOD.

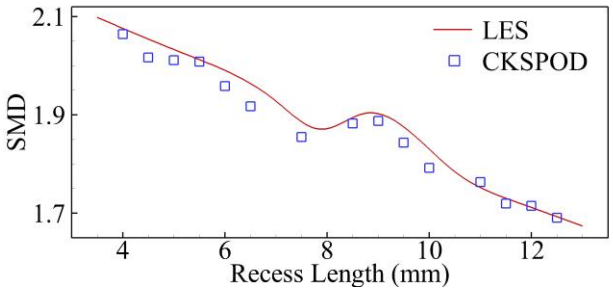

Figure 7.7 SMD vs recess length

Another concern for injector design is thermal protection. Injector wall and chamber wall are vulnerable to high temperature, and in extreme circumstances, large heat flux may result in engine meltdown. A straightforward way of evaluating thermal protection is to quantify wall temperature. In recess and taper region, the wall temperature increases in the axial direction. And in practical engines, the faceplate in the current simulation will be replaced by nearby injectors. Therefore, in the current study, the wall temperature at the end of taper region, denoted as T_{wall}, is employed as objective function and plotted in Figure 7.8 as a function of recess length. Red and blue symbols correspond to LES and CKSPOD results, respectively. The function of T_{wall} with respect to L_r follows an S-curve. T_{wall} varies slowly for $L_r < 8\text{mm}$ and $\text{L}_\text{r} > 10\text{mm}$, and increases drastically from around 600K to around 1400K in the range of $8\text{mm} < L_r < 10\text{mm}$. The same trend is also observed between LES and CKSPOD results.

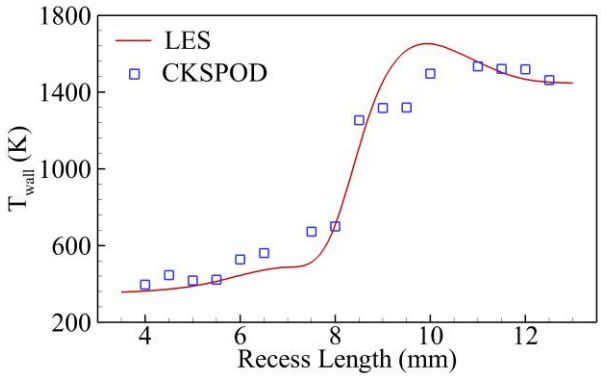

Figure 7.8 Wall temperature vs recess length

The same procedure is applicable to other objective functions, including the combustion instability, and can also be extended to inverse problem optimization, as discussed in a previous study [168], but is not demonstrated here.

7.2 Conclusions

In this chapter, a high-fidelity framework that is able to predict spatiotemporally evolving reacting flow field in reasonable turnaround time is proposed and implemented, and then extended to injector design optimization. Common kernel-smoothed proper orthogonal decomposition (CKSPOD) is employed as the surrogate model, which utilizes hadamard-based POD and allows for extraction of dominant coherent flow structures. The current work focuses on the reacting flow field of GCLSC injectors, operating at supercritical conditions. Flame initializes and anchors in the shielding collar rim, and intensifies in further downstream. The mixing and reaction between gaseous oxygen and swirling kerosene renders complicated dynamic characteristics. Common kernel-smoothed proper orthogonal decomposition (CKSPOD), which utilizes training data from high-fidelity Large Eddy Simulations (LES) and enables flow field emulation in reasonable turnaround time, is improved and employed as a surrogate model. The employed

framework is able to predict time-evolving reacting flow field, as well as the corresponding uncertainty quantification with high accuracy. A good agreement is also observed for the time-averaged flow field, as well as the time-mean mixture fraction contours and mixing / combustion efficiencies. The proposed method is further extended to injector design optimization, based on the objective functions of mixing efficiency and injector wall thermal protection. This current framework significantly reduces the computational time for efficient survey of the design space, and will serve as a promising tool in the early design stages.

CHAPTER 8.

COMBUSTION INSTABILITY IDENTIFICATION

In the previous section, injector design optimization has been conducted based on combustion efficiency and thermal protection to the injector walls. Another important factor for injector design is combustion instability, which has plagued almost all high-performance power generation and propulsion systems. Uncontrolled combustion instabilities may produce excessive noise, reduce combustion efficiency, trigger large pressure oscillations, and lead to possible engine failure. As a consequence, a comprehensive study of combustion instability identification technique, as well as its application to multi-injector engines, is desired.

8.1 Motivations

Combustion dynamics have been a key concern in the design and operation of the modern air-breathing engines and rocket engines [169]. The challenges come from several aspects. First, these engines operate at pressures much higher than the critical pressures of propellants, leading to the extreme nonlinearity and complexity of physical phenomenon as fluid transits from subcritical temperature to supercritical temperature [10]. Second, demand of high energy density leads to harsh operating conditions in a small confined space, which causes the instability hard to predict and control.

To tackle the problem of combustion dynamics, high-fidelity tools, such as LES have been extensively used [24, 170]. They are able to provide accurate results, but the high demands for computational resources hinder the broader application of LES. Consequently,

lower fidelity approaches have been developed and used. Some of the methods are designed to work jointly with high-fidelity simulations to provide information of combustion dynamics in modest amount of CPU hours.

One common practice is to model combustor by a network of homogeneous one- or two-dimensional axisymmetric acoustic elements [171, 172]. Flame is supposed infinitely thin with jump relations. Amplitudes of forward and backward waves are estimated by matching boundary conditions and jump relations across the flame. This method is simple, extendable, and is able to describe a complex system by decomposing it to a few simplified elements. The major drawbacks is the incapability to solve a complex coupled system. The description of flame is also over-simplified, not able to describe turbulent combustion accurately.

Another widely used lower order modelling approach is reduced order model, which reduces higher-order partial differential equations (PDE) to ordinary differential equations (ODE). POD-Galerkin based approach is often used [173, 174]. The flow field is decomposed into several orthogonal modes, whose time-evolving coefficients are estimated through ODEs derived from governing equations. This method is able to extract information and reconstruct the flow field, but may have difficulty handling complex boundary impedances.

Another framework is to analyze combustion dynamics through wave equations, which solve the whole set of thermoacoustic modes and generate modal information in frequency space. Under low-Mach number and small fluctuation assumptions, the

equation, Helmholtz equation, can be derived through linearization of PDE of fluctuating variables. Given proper modeling of unsteady heat release, the system of Helmholtz equation is able to generate mode shape, frequency and growth rate for each mode. Due to its ability to capture all modes, adaptability to complex geometry and boundary impedances, this framework is adopted.

As mentioned above, the framework of Helmholtz method requires appropriate modeling of unsteady heat release. A well-received model is the sensitive time lag model $Q'(t)/\bar{Q} = nu'(t-\tau)/\bar{u}$, also known as the n-τ model [169, 175, 176], which correlates heat release rate fluctuations to flow properties during injection. During the combustion process, propellants undergo the processes of injection, atomization, vaporization (these two not applicable under supercritical conditions), heating, diffusion, turbulent mixing and reaction. This model considers the chemical reaction, which takes place towards the end of flow evolution as the most important process for the modeling of combustion response. Effects of other processes are therefore ignored. In this model, time delay τ is defined as the time between the injection of propellant element and the time at which the element is burned, which represents the time lapse of all those neglected processes. Another variable n is defined as the response amplitude of the chemical reaction process to flow injection. Similar idea can be extended to frequency domain. The flame transfer function (FTF), of the form $\hat{Q}'(\omega)/\bar{Q} = F(\omega)\hat{u}'(\omega)/\bar{u}$, is defined with the assumption that all flow field oscillations are harmonic.

In general, it is not realistic to predict flame response analytically, especially for systems with complex geometries and harsh operating conditions. Experiments and

numerical simulations are highly relied upon to obtain the FTF of a system. For single-in, single-out (SISO) systems, the Wiener-Hopf equation has been widely used for FTF modeling [177, 178]. In spite of the important role FTF plays in instability analyses, its identification implementation (Wiener-Hopf) is still primitive. One pioneering work on improvement of traditional FTF identification methodology is the application of Tikhonov regularization (ridge regularization) [179]. Other works tries to enforce Gaussian fit [178] and rational fit [180] to these flame transfer functions. These works offer interesting perspectives to the modeling of FTF, but the process of modeling and fitting does not incorporate physical understanding of the response. In this chapter, a new modeling strategy for FTF that incorporates both data analytics and physical understanding.

In the study of combustion dynamics, uncertainties are inherently contained in the quantification process of flow variables. Uncertainty quantifications (UQ) of these flow variables, as well as the propagation behaviors to other parameters, provide valuable information on the quality of an engine design, but is a topic less-studied in the literature. A few pioneering works [181, 182] applied classical Monte Carlo to study the UQ of thermoacoustic instabilities. These works model UQ by perturbing parameters such as inlet air temperature, amplitude and time delay of $n-\tau$ model, and boundary impedances. The $n-\tau$ model these works employ is capable of capturing only one significant response. Moreover, the perturbations do not represent the physical variance of the system, making results of these works less accurate. To remedy the limitations of these works, the novel Bayesian framework to estimate UQ of FTF is developed. The framework employs modern statistical and machine-learning methods to learn a broader class of impulse functions with

multiple time-lags (able to capture multiple responses). The incorporation of observed data allows for more accurate estimations of UQ. It can (a) quantify uncertainty in the identification of impulse function, and (b) propagate such uncertainty to understand the FTF. This proposed framework is then applied to study four bi-swirl injectors with different geometric designs. The UQ range flame transfer function and thermoacoustic instabilities of these four injectors are then estimated and compared.

8.2 Methodology

8.2.1 Flame Transfer Function

8.2.1.1 Wiener-Hopf Method

A traditional way of analyzing a transfer function is to regard the combustion system as a single-in, single-out (SISO) system (such a system is often used in signal processing, see [183]). Here, the input is the dynamic system of a chosen variable $P'(t)$, and the output is the dynamic system of global heat release rate $\dot{Q}'(t)$. Flow variables are normalized by their temporal mean, $P(t) = P'(t)/\bar{P}(t)$, $\dot{Q}(t) = \dot{Q}'(t)/\bar{Q}(t)$.

An impulse function h is typically used to represent the relation between input and output:

$$\dot{Q}(t) = \int_0^t h(\alpha)P(t-\alpha)d\alpha \tag{8.1}$$

The Wiener-Hopf approach [183] can be described as follows. Taking the convolution of Eq. (8.1) with the input system $P(t)$, the following identity can be derived:

$$r_{P\dot{Q}}(\tau) = \int_0^{\tau} h(\alpha) r_{PP}(\tau - \alpha) d\alpha, \tag{8.2}$$

where $r_{P\dot{Q}}(\tau)$ is the cross-correlation between input and output at lag τ, and $r_{PP}(\tau)$ is the autocorrelation for the input dynamic system at lag τ. After estimating $h(\alpha)$ based on the above equation, the desired transfer function can be obtained by Fourier transform of this impulse function. This can be verified by the direct definition of a transfer function, $\mathrm{H}(\omega) = \mathrm{S}_{P\dot{Q}}(\omega)/S_{PP}(\omega)$.

In practice, the impulse function $h(\alpha)$ in Eq. (8.2) is estimated by first discretizing the underlying dynamic systems, then constructing a cross-correlation vector $\boldsymbol{r}_{P\dot{Q}}$ between input and output, and an auto-correlation matrix $\boldsymbol{R}_{PP}$ for the input system. Letting $\boldsymbol{h}$ be the discretized impulse function, Eq. (8.2) can be written as the so-called Wiener-Hopf equation:

$$\boldsymbol{h} = \boldsymbol{R}_{PP}^{-1} \boldsymbol{r}_{P\dot{Q}} \tag{8.3}$$

The estimation of transfer function via Eq. (8.3) is known as the Wiener-Hopf method.

From a statistical perspective, the Wiener-Hopf method has several intrinsic limitations as mentioned in [178]. Such limitations can be seen by rephrasing Eq. (8.3) as the optimization problem:

$$\min_{\boldsymbol{h}} ||\boldsymbol{r}_{P\dot{Q}} - \boldsymbol{R}_{pp}\boldsymbol{h}||_2^2. \tag{8.4}$$

In this sense, the Wiener-Hopf method can be seen as the least-squares estimator for a standard linear regression problem. Viewed this way, this method has two disadvantages.

First, the statistical properties of such an estimator can be suboptimal, especially when the auto-correlation matrix $\boldsymbol{R}_{PP}$ is ill-conditioned. Second, such an approach disregards the fact that only a significant few impulses are truly active, a phenomenon commonly known as *sparsity*. For the problem at hand, this means only a small number of impulse responses are non-zero, with the remaining impulses equal to zero. An identification of active impulses from inert impulses also provides a method for learning and identifying physically meaningful response.

To this end, a two-stage transfer function identification procedure is presented which jointly addresses the above concerns. The first stage employs an L_1 regularization term to provide improved impulse estimation and to select the significant few impulses. The second stage uses a physics-based method for selecting the optimal FTF model from the sequence of potential FTFs returned by the first stage.

8.2.1.2 First Stage: Estimation and Selection via L_1 Regularization

As mentioned in the Introduction, there has been some work on using regularization techniques for improving estimation performance, most notably the use of Tikhonov regularization (or ridge regression) in a similar application [179]. However, the use of an L_2 regularization term in ridge regression does not address the underlying sparsity for the problem at hand. To achieve better estimation performance under sparsity, it is well-known from statistics literature that an L_1 regularization term is needed [184]. For the problem at hand, this imposes a penalty term on the least-squares formulation in Eq. (8.4):

$$\min_{\boldsymbol{h}} ||\boldsymbol{r}_{P\dot{Q}} - \boldsymbol{R}_{pp}\boldsymbol{h}||_2^2 + \lambda||\boldsymbol{h}||_1 \tag{8.5}$$

where $||\boldsymbol{h}||_1 = \sum_\alpha |h(\alpha)|$ is the L_1 norm of $\boldsymbol{h}$, and $\lambda > 0$ is a parameter controlling the magnitude of this penalty. This formulation is better known in statistics as the Lasso estimator [185].

One of the primary appeals for Eq. (8.5) is that the impulse function $\boldsymbol{h}$ which optimizes such a formulation implicitly sets most of its entries as zero. In other words, this optimization provides a way to select which impulse responses are significant (i.e., entries with non-zero values for the optimal solution), and which impulse responses are inert (i.e., entries with zeros). This machine-learning framework can be used to extract physically meaningful FTF information from data.

The optimization of regularized problem is achieved through the assumption that for each step, only the impulse response $h(i)$ is desired, and the other impulse responses $h(j), j \neq i$ are known and fixed. The optimization for $h(i)$ then has the following closed-form solution:

$$h(i) \leftarrow \max\left(\boldsymbol{R}_{pp,i}^T\left\{\boldsymbol{r}_{P\dot{Q}} - \sum\nolimits_{j\neq i} \boldsymbol{R}_{pp,j}\, h(j)\right\} - \boldsymbol{\lambda}\,, 0\right) \tag{8.6}$$

where $\boldsymbol{R}_{pp,i}$ is the i-th column of $\boldsymbol{R}_{pp}$**.** Eq. (8.6) can be viewed as applying a soft-threshold filter (with threshold equal to λ) on the residual impulse signal leftover from the fixed responses $h(j), j \neq i$. By iterating the update scheme in Eq. (8.6) for each $h(i)$ until the entire solution vector $\boldsymbol{h}$ converges, a locally optimal solution to the desired problem in Eq. (8.5) is obtained.

8.2.1.3 Second Stage: Physics-based Model Selection

While the first stage of our method allows us to select and estimate impulse responses from data, a second refinement stage is needed to calibrate the statistical parameters used in the first stage. Such parameters include the penalty coefficient λ and the total number of lags to account for in Eq. (8.5). The goal here is to tune an optimal value for these parameters to provide the best model fit, from both a statistical and physical perspective. In particular, a smaller value of λ allows more impulse responses to be selected, while a larger value of λ restricts the number of selected responses. A selection criterion is therefore needed to find an optimal point in this trade-off. Likewise, the number of considered lags N is also an important parameter. From physical intuition, when more temporal information is used for computing auto-correlations and cross-correlations, accuracy of results should be improved. However, from a statistical perspective, this may not be the case, because high-frequency noise will contaminate FTF with unnatural numerical oscillations (this will be shown later). Again, a physics-based selection criterion is needed to arrive at an optimal point in this trade-off.

The novelty in the proposed selection criterion is that it incorporates physical prior information within a statistical model selection framework. Statistically, the model selection procedure for L_1 regularization is typically performed by choosing the model which returns the lowest prediction error (see, e.g., [186]). However, as will be demonstrated in latter chapters, this purely data-driven technique may not be able to select the best model which captures significant responses. A new selection criterion which incorporates physical prior information is proposed below.

First, define the mean-squared-error (MSE) criterion:

$$MSE(\lambda, \mathrm{N}) = \left\| \boldsymbol{r}_{P\dot{Q}} - \boldsymbol{R}_{pp}\boldsymbol{h} \right\|_2^2 \tag{8.7}$$

which measures the statistical goodness-of-fit of the impulse function $\boldsymbol{h}$ using parameters λ and N. Assume now the number of dominant responses is m, with frequencies $f_1, \cdots, f_m$ and amplitudes $A_1, \cdots, A_m$, and consider the following weighing function:

$$\begin{aligned} \mathrm{w(i)} = \sum_{j=1}^{m} A_j \delta\left(2\pi t_i f_j - 2n\pi\right) - A_j \delta\left(2\pi t_i f_j - (2n+1)\pi\right), \mathrm{i} \\ = 0, 1, 2, \ldots \end{aligned} \tag{8.8}$$

The vector of this function has identical length to that of the impulse response vector $\boldsymbol{h}$. Mathematically, this $w(i)$ provides alternation at the dominant responses and gives a framework for physics extraction. One implicit assumption is the parametric form of the weights in Eq. (8.7). Here, the Dirac function is set at the selected impulses from the L_1 regularized framework in Eq. (8.5), which, as mentioned previously, is able to capture a limited number of significant response and set other responses to be zero.

For a fixed choice of λ and N, consider now the selection number $S(\lambda, N)$, which quantifies how closely the impulse function $\boldsymbol{h}$ **(**estimated using the parameters λ and N) mimics the desired physics from the weighing function:

$$S(\lambda, N) = \max_k \sum_{i=0}^{N} \omega(i+k)h(i), k = -N, -N+1, \ldots, 0, 1, \ldots, N \tag{8.9}$$

where N is the number of time lags considered. A larger value of $S(\lambda, N)$ indicates a better fit for the selected FTF (in its capability to capture oscillations at f_1 and f_2), while a smaller value suggests poorer fit. Each model will have one unique selection number $S(\lambda, N)$. A physics-based correction factor can then be introduced as $c(\lambda, N) = \|h\|/S(\lambda, N)$. With this in hand, the proposed physics-corrected MSE selection criterion becomes:

$$MSE_c(\lambda, N) = c(\lambda, N) \times MSE(\lambda, N) \tag{8.10}$$

The final transfer function will be chosen as the transfer function with parameter settings $\hat{\lambda}$ and $\widehat{N}$ which minimizes the corrected MSE criterion $MSE_c(\lambda, N)$.

8.2.2 Uncertainty Quantification

A key contribution of this paper is the application of Bayesian formulation to the Lasso approach (Bayesian Lasso Model). Unlike flow variables, the impulse function $\boldsymbol{h}$, a collection of intermediary parameters (parameter that describe flow dynamics but is not directly measurable) that describe flame response, cannot be easily quantified through a closed-form density function. In statistical modeling, the term 'Bayesian' refers to a probabilistic approach for quantifying uncertainty in unknown intermediary parameters of interest [19]. In the Bayesian framework, prior distributions are first assigned to the unknown parameters to reflect one's prior beliefs on such parameters, before taking any observed data into account. Next, given observed data on the system, one then reconciles these prior beliefs with the observed data by computing *posterior* distributions on parameters of interest. These posterior distributions reflect an experimenter's uncertainty

on model parameters after conducting experiments, and incorporate the beliefs reflected in prior distributions as well as the experimental data.

For the current study, the Bayesian UQ approach is composed of three steps: 1) specification of the data generating model, 2) prior distribution assignment, and 3) posterior distribution sampling. We describe each of these steps briefly below.

1) Model specification for data generation

Data generation is the underlying model from which on assumes the experiment data is generated from. An appropriate statistical model is then needed to describe the relationship between intermediary parameter (i.e., impulse function $\boldsymbol{h}$) and observed data (auto-correlations $\boldsymbol{R}_{pp}$ and cross-correlations $\boldsymbol{r}_{P\dot{Q}}$). As alluded to in Chapter 8.2.1, the Wiener-Hopf equation $\boldsymbol{r}_{P\dot{Q}} = \boldsymbol{R}_{pp}\boldsymbol{h}$ provides a key relation between cross-correlations, auto-correlations and the impulse function, in the absence of noise or parameter uncertainties. From this, a natural statistical model to assume is the following:

$$\boldsymbol{r}_{P\dot{Q}} \sim \boldsymbol{N}(\boldsymbol{R}_{pp}\boldsymbol{h}, \sigma^2\boldsymbol{I}) \tag{8.11}$$

i.e, the measured auto-correlation is assumed to follow a normal distribution with mean $\boldsymbol{R}_{pp}\mathbf{h}$ and variance σ^2. In the absence of noise or uncertainty, the variance σ^2 becomes 0, which reduces to the earlier Wiener-Hopf equation.

2) Assignment of prior distributions

The data generating specification in Eq. (8.11) alone cannot support the Bayesian model specification. As noted above, prior distributions (reflecting beliefs prior to experimentation) need to be assigned to the unknown parameters before taking any observed data into account. Here, due to limited prior knowledge on the impulse function $\boldsymbol{h}$ and variance σ^2, our modeling strategy is to first assign to such parameters the following non-informative prior distributions [187] (N is assumed to be size of vector $\boldsymbol{h}$):

$$\begin{gathered}\text{(prior of } \boldsymbol{h}) \; h_i \sim N(0, \sigma^2 \psi_i), i = 1, \dots, N, \\ \text{(prior of } \sigma^2) \; \sigma^2 \sim InvGamma(a, b), \\ \text{(prior of } \psi_i) \; \psi_i \sim Expo(2\lambda^{-2}), i = 1, \dots, N.\end{gathered} \tag{8.12}$$

In the above equation, each item h_i in vector $\mathbf{h}$ is assumed to follow independent normal distributions with mean 0, and variance $\sigma^2\psi_i$. To allow for sampling from the posterior distribution (see below), the prior distributions of variance components σ^2 and ψ_i are assumed to follow the inverse gamma distribution and double exponential distribution with rate parameter $2\lambda^{-2}$, where λ is the penalty coefficient given in Eq. (8.5). The prior specification in Eq. (8.12) can be viewed as a Bayesian (or probabilistic) implementation of the L_1-regularized (Lasso) method, and hence shares the same sparsity modeling properties for the latter approach.

3) Sampling from posterior distribution

While the posterior distribution of $\boldsymbol{h}$ cannot be written in closed-form, the Bayesian specifications in Equations (8.11) and (8.12) allow for sampling from the posterior

distribution of $\boldsymbol{h}$, given observed auto-correlations $\boldsymbol{r}_{P\dot{Q}}$ and cross-correlations $\boldsymbol{R}_{pp}$. Here, sampling is defined as the selection of a subset of samples from a statistical population to estimate characteristics of this population. In current approach, the subset can be drawn through the following steps. Define m to be the desired number of posterior samples, the sampling procedure requires the iteration of the following steps from $j = 1$ to m:

a. Draw $\boldsymbol{h}^{(j)}$ from a normal distribution with mean $\boldsymbol{A}^{-1}\boldsymbol{R}_{pp}\boldsymbol{r}_{P\dot{Q}}$ and variance $(\sigma^2)^{(j-1)}\boldsymbol{A}^{-1}$, where $\boldsymbol{A} = \boldsymbol{R}_{pp}^2 + \boldsymbol{D}$, and $\boldsymbol{D} = diag(\psi_1^{(j-1)}, \dots, \psi_N^{(j-1)})$,

b. Draw $(\sigma^2)^{(j)}$ from an inverse-gamma distribution with shape parameter $a + N - 1/2$ and scale parameter $b + \frac{\left(\boldsymbol{r}_{P\dot{Q}} - \boldsymbol{R}_{pp}\boldsymbol{h}^{(j)}\right)'\left(\boldsymbol{r}_{P\dot{Q}} - \boldsymbol{R}_{pp}\boldsymbol{h}^{(j)}\right)}{2} + \frac{1}{2}\sum_{i=1}^{N}\left(\boldsymbol{h}_i^{(j)}\right)^2 / \psi_i^{(j-1)}$,

c. Draw $1/\psi_i^{(j)}$ from an inverse Gaussian distribution with mean parameter $\lambda\sqrt{(\sigma^2)^{(j)}}/\boldsymbol{h}_i^{(j)}$ and shape parameter λ^2, $i = 1, \dots, N$.

The samples $\mathcal{H}$, which correspond to posterior samples of the impulse function $\boldsymbol{h}$ under the proposed Bayesian framework, can then be interpreted as representative impulse functions given prior beliefs and observed data. Compared to the Wiener-Hopf and Lasso approach, the proposed approach offers not only a good estimate of h, but also how certain such an estimate under the samples in $\mathcal{H}$ can be. In our implementation, the initial values of $\psi_i^{(0)}$ and $(\sigma^2)^{(0)}$ are set as 1 and the variance of $\boldsymbol{r}_{P\dot{Q}}$, respectively. Further details on this posterior sampling procedure and its derivation can be found in Park and Casella [188].

With the posterior samples of $\mathcal{H}$ in hand, the forward propagation of uncertainty from the impulse function to flame transfer function can then be performed as follows, (a) for each sample in $\mathcal{H}$, compute from impulse function to FTF (or other quantities of interest), (b) use the FTFs from these posterior samples to estimate FTF uncertainty.

8.3 Numerical Implementations of Full-scale Combustor

8.3.1 Injector Configuration

In this chapter, the high-fidelity numerical framework described in CHAPTER 2 is applied to bi-swirl injectors. This design has been broadly used in Russian rocket engines, but not explored in detail yet. The configuration of current study is depicted in Figure 8.1. This type of injectors has wide applications in Russian rockets, both as main injectors for gas generator cycle engines, and preburner injectors for staged combustion cycle engines. Injector in current case is based on the geometry RD-0110 main injector, which has been used in Soyuz space vehicle. LOX and kerosene are tangentially introduced into inner and outer swirlers respectively. Reactant flows develop individually before they mix and react in recess region. The mixing continues to develop in the taper and downstream region.

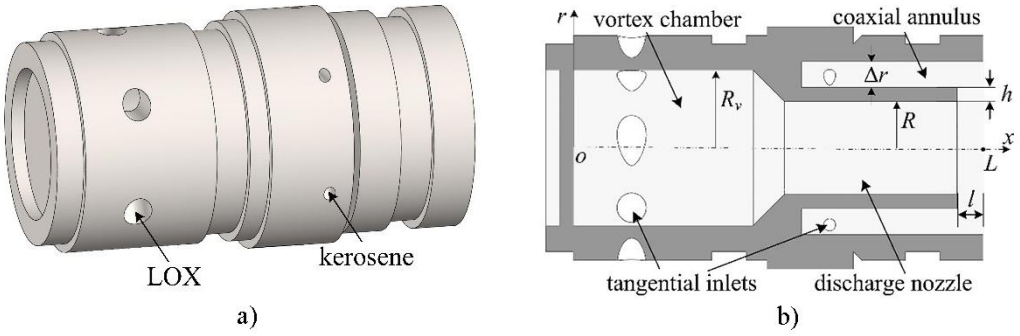

Figure 8.1: global (left) and sectional (right) view of RD-0110 liquid-liquid bi-swirl injector

The operating pressure is 100 bar, which is beyond critical pressure of oxygen and kerosene. LOX is injected 0.15 kg/s at a temperature of 120 K, while kerosene is injected 0.065 kg/s at a temperature of 300 K. A detailed description of current simulation results can be found in Wang and Yang's work. Numerical scheme and accuracy of grid resolution was justified by grid independence study. Based on current dataset, this work is to develop and test data-driven way of analyzing and quantifying combustion dynamics. White noise forcing is added to inflow velocity of LOX at the amplitude of 5% of the mean inflow velocity.

With theoretical and numerical framework elaborated above, four bi-swirl injectors with various geometric parameters are treated, with special attentions given to the influences of recess length l, post thickness h, and annulus width Δr (see Figure 8.1 for definitions) on injector performance. The geometry presented in Figure 8.1 corresponds to Case I. These geometric parameters play significant roles in flow mixing and stability characteristics, and previous works have comprehensively studied the non-reacting and reacting flow fields [9, 189]. Table 8.1 summarizes the geometric parameters of all four cases.

Table 8.1: Geometrical parameters of four cases

Case Number	Annulus Width (Δr, mm)	Post Thickness (h, mm)	Recess Length (l, mm)
I	0.5	0.8	1.5
II	0.5	0.8	**0.0**
III	0.5	**1.3**	1.5
IV	**1.0**	0.8	1.5

8.3.2 Helmholtz Solver

For the basic Navier-Stokes equations, with simple derivations and the assumption $p' = \hat{p}' e^{i\omega t}$, the inhomogeneous Helmholtz equation is listed below [190, 191]:

$$\frac{1}{\bar{c}^2}\frac{\partial^2 p'}{\partial t^2} - \bar{\rho}\nabla\left(\frac{1}{\bar{\rho}}\nabla p'\right) = \frac{(\gamma-1)}{\bar{c}^2}\frac{\partial \dot{q}'}{\partial t} \tag{8.13}$$

This study employs a commercial software "*COMSOL MULTIPHYSICS*". Based on finite element method, this software is suitable for frequency domain simulations. The *Pressure Acoustic module* in the commercial code includes a Helmholtz solver in frequency domain that is capable of generating mode shapes, frequencies and growth rates with proper setup. This solver has been validated in many previous studies [192, 193]. Moreover, the authors validated the solver with several examples in Dowling's work [190].

Due to the low-Mach-number assumption of Helmholtz solver, nozzle is removed from computation. Figure 8.2 shows the current domain, which is comprised of 91 nozzle and combustor (depicted in light red). All walls as well as LOX and kerosene inlets are treated as rigid walls. The impedance of combustor outlet is also set as zero acoustic velocity (solid wall) from theoretical model [194-197].

As elaborated in the previous section, pressure fluctuation at the outlet plane of injector is chosen as the independent flow variable of flame transfer function. The global heat release rate is also estimated. From simple derivations, source term in Eq. (8.13) will become $\frac{(\gamma-1)}{\bar{c}^2} i\omega \frac{\bar{\dot{q}}}{\bar{p}} \hat{p}'(\omega) \times \int_0^t n e^{-i\omega\tau} d\tau$.

The downstream combustor is divided into 91 sections, each one corresponds to one upstream injector. $\bar{p}$, $\bar{\dot{q}}$, $p'(t)$, $\dot{q}'(t)$ are estimated from LES simulations. According to Independent Sector Assumption, for each injector system, same response function is applied in correspondence to the extraction process from LES. More specifically,

volumetric global heat release rate response of each combustor section is correlated to average pressure at exit plane of the corresponding injector.

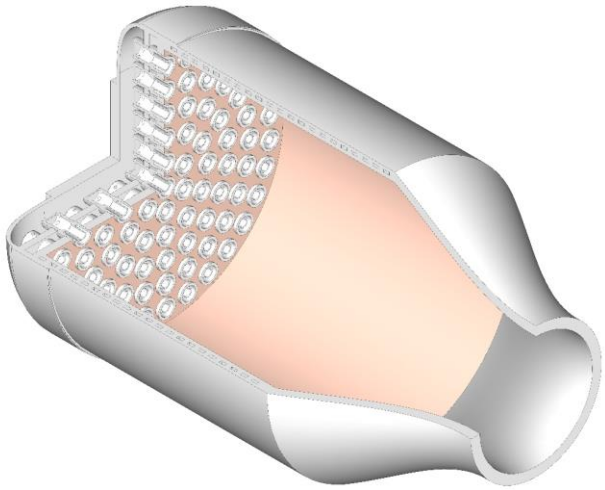

Figure 8.2: Schematics of full-scale RD-0110 combustion

8.4 Combustion Dynamics

A thorough understanding of combustion dynamics of current case is indispensable to identify and justify flame transfer function. In this chapter, among four cases, I will first analyze the combustion dynamics for Case III in detail as an example, followed by a comparison of combustion dynamics of four different geometries. A snapshot of temperature field near the injector exit is depicted in Figure 8.3. Diffusion-dominated flame anchors at the recess region and propagates downstream along the surface of the LOX stream. A wake region consisting of hot combustion products separates the LOX from the kerosene stream. Large-scale vortices induced by shear layer instability wrinkle the flame in the downstream region, where center-recirculation is generated by vortex breakdown and induces the flow reversal of hot products near the centerline of the injector. More detailed information is presented in Wang and Yang's work[198].

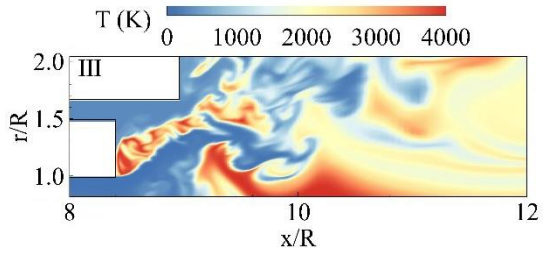

Figure 8.3: Snapshot of temperature field near the injector exit

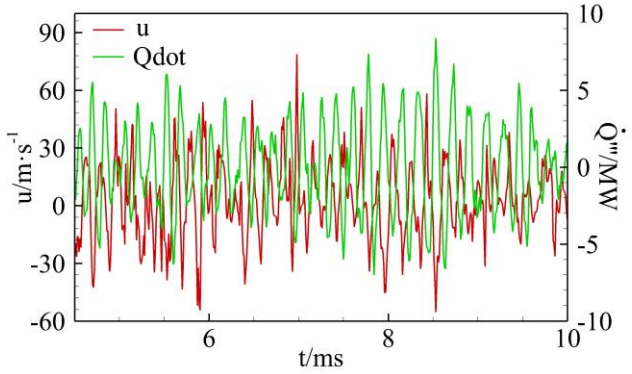

Figure 8.4: Temporal evolution of pressure at injector exit and global heat release rate

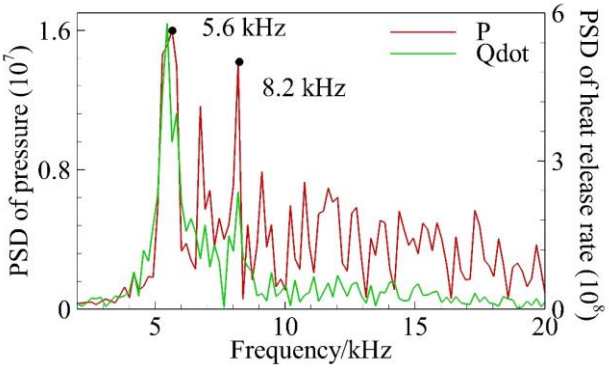

Figure 8.5: Power spectral densities of pressure at injector exit and global heat release rate

Figure 8.4 shows temporal evolution of averaged pressure at injector exit and global heat release rate. These time series are taken when the flame field reaches the stationary state. There are 550 time steps in total, covering 5.5 ms. It can be observed that heat release rate oscillations are highly correlated to pressure oscillations. Power spectral densities of both time series are plotted in Figure 8.5. Dominant frequencies are 5.6 kHz and 8.2 kHz.

Both pressure and global heat release rate have similar dominant frequencies. The former was identified as empirically determined as quarter-wave by $f = c/4(L + \Delta l)$ [152, 199].

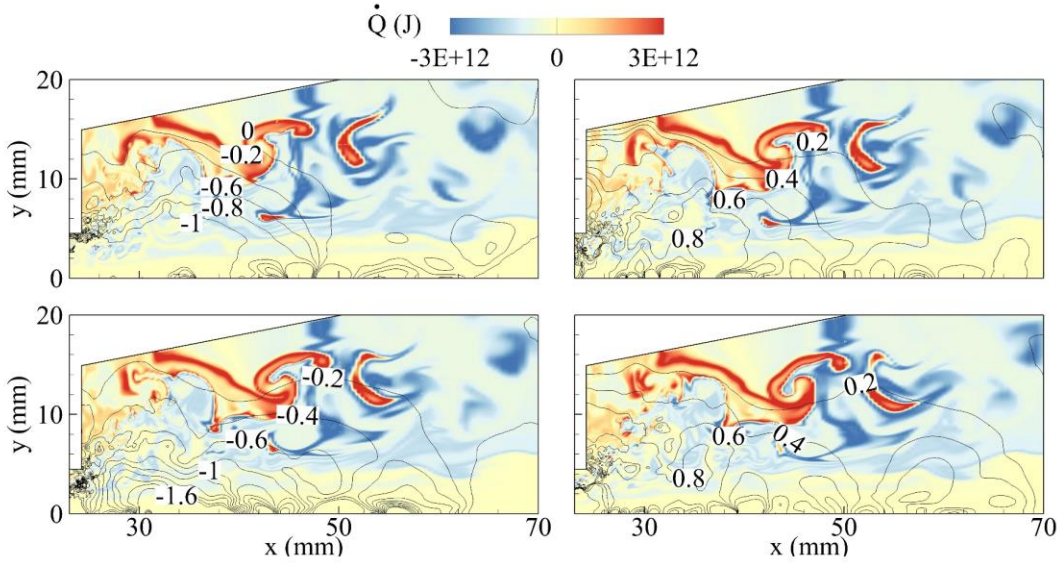

Figure 8.6: Temporal evolution of pressure and heat release rate

As stated above, pressure has direct influence on the evolution of heat release rate. Figure 8.6 shows temporal evolution of heat release rate and pressure field within two cycles. Heat release rate is plotted in color contour, and pressure is shown with solid lines. Numbers over lines are gauge pressure labels based on 100 bar, measured as bar. Phase angle Φ is calculated based on periodic flow evolution at 5.6 kHz. When Φ=0°, regions of large heat release and absorption rates are at large radial positions. Positive radial pressure gradient draws these regions to a lower radial position when Φ=180°. Negative radial pressure gradient is then formed and starts to push regions up again, when the regions reach largest radial position at Φ=360°. Alternating pressure gradients causes oscillations of regions of large heat release rate up and down at 5.6 kHz. Both analyses of PSD for time series and $p - \dot{Q}$ field evolution show the strong response of global heat release rate to

pressure at dominant frequencies. This observation will serve as a criterion for judging whether a FTF captures underlying dynamic characteristics of current combustion system accurately.

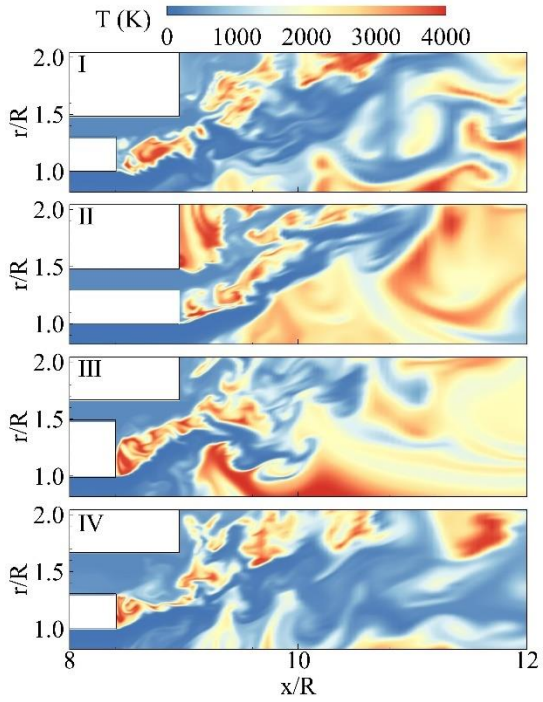

Figure 8.7: Snapshot of the temperature field near the injector exit for all cases

Figure 8.7 shows the snapshots of the temperature field near the recess region for all cases. A recess region (Case II) is found to be necessary to achieve efficient mixing and combustion. A thicker LOX post (Case III) or a wider kerosene annulus (Case IV) protects the faceplate more efficiently, and introduces larger recirculation zones near the LOX post surface and thus higher flow residence time to better anchor the flame. These geometric changes also induce a stronger heat flux to the post surface, and thus increase the risk of thermal failure of the injector device. Further details are described in the references listed above.

8.5 Flame Transfer Function Identification

8.5.1 Flame Transfer Function

Flame transfer function represents the responses of a flame to incident flow perturbations. A widely-accepted way of describing FTF for premixed flame is [200]:

$$\frac{\dot{Q}'(\omega)}{\dot{Q}} = \frac{\dot{Q}'(\omega)}{\dot{Q}}\bigg|_u + \frac{\dot{Q}'(\omega)}{\dot{Q}}\bigg|_\phi = F_u(\omega)\frac{u'(\omega)}{u} + F_\phi(\omega)\frac{\phi'(\omega)}{\phi} \tag{8.14}$$

This decomposition is originated from the definition of global heat release rate $\dot{Q} = \rho u A h$. Since effects of density can be ignored, and area fluctuations are highly dependent on local flame and flow speeds, flame response can be decomposed into contributions from velocity and equivalence ratio.

For transfer function equations, direct replications from premixed flame to non-premixed might be erroneous, as governing equations for global heat release rate are different. For non-premixed flame, $\dot{Q} = \dot{m}h$, and its global heat release rate is dominated by mass burning rate fluctuations [201]. Moreover, non-premixed flame dynamics are functions of disturbance field everywhere, while premixed flame are only at reaction sheet and determined by local flow and flame speed alone. A careful selection of covariate is needed. In previous works on combustion dynamics of non-premixed flames [201-203], transfer functions were estimated based on axial velocity. But in current study, pressure is preferred for two reasons. First, pressure directly influences heat release rate fluctuation. As stated in the previous section, propagation of pressure oscillations induces regions of high heat release rate to fluctuate. Second, other flow variables, such as axial velocity are

directly related to pressure. Moreover, while not shown here, selection of pressure over other variables for FTF calculations provides more reasonable results.

Based on times series of pressure and global heat release rate plotted in Figure 8.4, impulse functions h obtained by both methods are compared, depicted in Figure 8.8. Wiener-Hopf method loses its accuracy because it is swarmed by a large number of responses and fails to pick up significant ones. Improved method outperforms Wiener-Hopf due to its ability to select a limited number of significant responses and set unimportant responses as 0.

For the Lasso, the temporal distances between neighboring troughs / peaks are around 0.18 ms, which corresponds to dominant frequency of 5.6 kHz. Major peak of impulse response is observed at time lag of 0.33ms. This is the value of the sensitive time lag τ for the traditional $n-\tau$ model. This number matches time lag obtained from maximum value of cross-correlation.

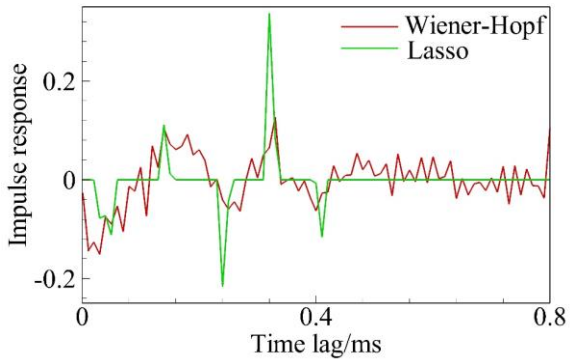

Figure 8.8: Impulse function of Wiener-Hopf method and Lasso regression

Figure 8.9 shows FTF obtained from traditional Wiener-Hopf method. Both absolute values and phases of transfer functions are estimated in frequency domain. Dominant

responses can be observed around 3 kHz, 4.8 kHz and 8.3 kHz. However, it fails to capture significant response at dominant frequency of 5.6 kHz. Moreover, it provides a poor description of phase delay which unnaturally oscillates near frequency of 4 kHz. As discussed in the methodology part, this discrepancy is caused by estimation deficiency and sparsity.

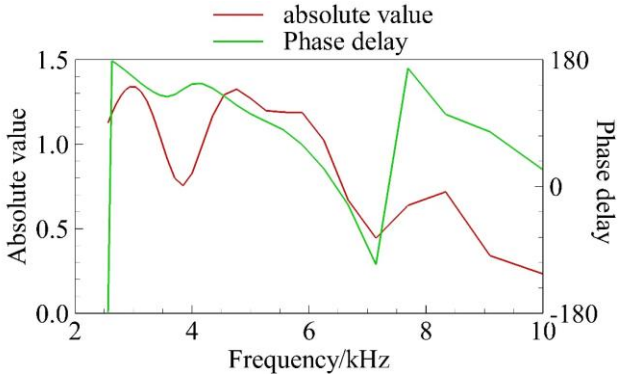

Figure 8.9: Flame transfer function based on Wiener-Hopf method

L_1 regularization is then employed to estimate physically feasible transfer function. As shown in Figure 8.10, although results from both methods have similar trends, the modified method outperforms traditional Wiener-Hopf method. The new method captures significant response 5.6 kHz, but does not capture frequency of 8.2 kHz very accurately, probably due to limitation of data availability. This situation is expected to be mitigated with higher frequency resolution. L_1 regularization is also able to capture the phase delay accurately. From the theory of sensitive time delay model, theoretical phase delay is $\Phi = -360° \cdot \tau f$. Estimated phase delay, similar to theoretical phase delay, verifies the accuracy of FTF obtained from Lasso.

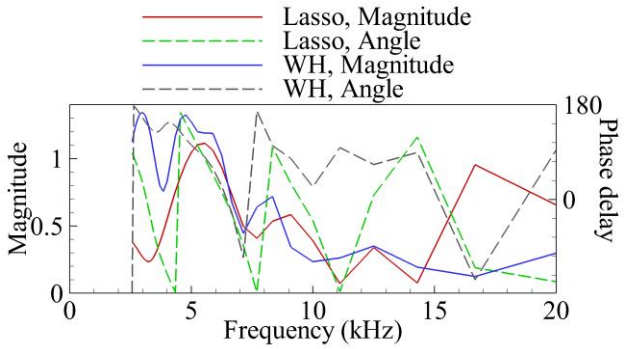

Figure 8.10: Flame transfer function with Lasso regression

8.5.2 Model Selection

As stated in Chapter 8.2, time lag that auto- and cross-correlation matrices incorporate is an important parameter and requires sophisticated selection. FTF obtained from three different time lags are chosen to demonstrate the effects. As shown in Figure 8.11, for the time lag of 0.2 ms, dominant frequency is smaller than corresponding threshold frequency, thus significant response is not captured. For the time lag of 2.0 ms, FTF is contaminated by non-physical oscillations. This verifies the necessity of a proper model selection technique.

Traditional model selection technique and the novel physics-based approach are implemented and compared. For the novel approach which requires prior knowledge of the flow field, two dominant frequencies, $f_1 = 5.6\ kHz$ and $f_2 = 8.2\ kHz$ are incorporated, and their magnitudes are obtained directly from PSD in Figure 8.5. A parametric study that incorporates a number of time lags is conducted. For this study, the MSE of various time lags are presented in red line in Figure 8.12, while corrected MSE for novel method are depicted in green. To demonstrate the deficiency of traditional method, FTF magnitudes and phase delays obtained from both methods are presented in Figure 8.13. Model selected

by physics-based method is able to capture phase delay more accurately. By incorporating physical understanding, corrected MSE is able to select optimized time lag. Although not shown here, when time lag is equal to 0.8 ms, corrected threshold is also capable to select better shrinkage parameter λ than traditional data-driven way of minimizing MSE.

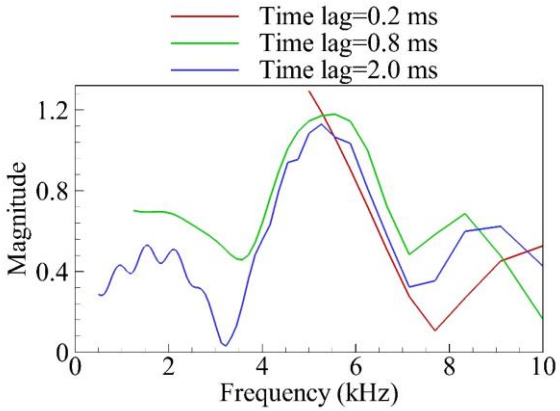

Figure 8.11: Comparison of FTF magnitude for different time lags

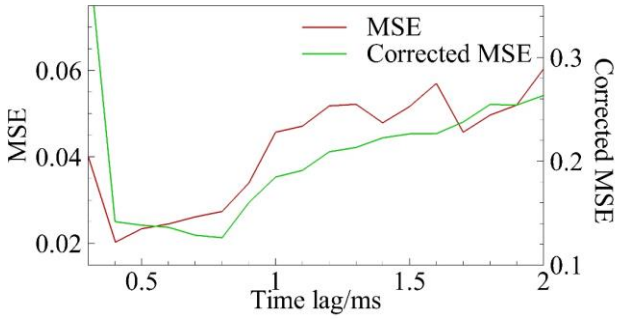

Figure 8.12: Original MSE and corrected MSE

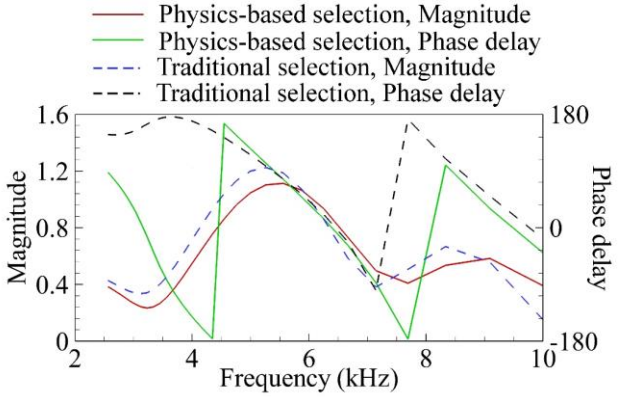

Figure 8.13: Comparison of FTF magnitude for optimized time lag

8.6 Uncertainty Quantification of Combustion Dynamics

8.6.1 Uncertainty Quantification of Impulse Function

As an example, impulse responses from both methods (Winer-Hopf and Lasso) of Case III are plotted in Figure 8.8. The building of impulse function and FTF requires a careful selection of independent flow variables. As elaborated in [204], pressure fluctuation at the outlet plane of injector is chosen. Lasso is able to pick dominant responses. The temporal distances between neighboring troughs / peaks are around 0.18 ms, which corresponds to dominant frequency of 5.6 kHz. Major peak of impulse response is observed at time lag of 0.33ms. This is the value of the sensitive time lag τ for the traditional $n-\tau$ model. This number matches time lag obtained from maximum value of cross-correlation.

Not only able to provide good estimations of impulse functions and FTFs, this framework can also describe how certain we are of such an estimate. The uncertainty in the impulse function h can be quantified by sampling from the posterior distribution of the Bayesian Lasso model. Figure 8.14 shows the resulting confidence intervals for h for all four cases. For each case, the confidence interval is estimated from $n_{samp} = 2{,}500$ posterior samples. A sensitivity analysis is performed on the number of posterior samples required for performing UQ. In this analysis, $n_{samp} = 1250, 2500$ and 5000 posterior samples yield similar results, so $n_{samp} = 2500$ samples are chosen. Here, the physical-corrected L_1-regularization (i.e., Lasso) estimate is plotted as a red line, and confidence bands for $\boldsymbol{h}$ are plotted in dotted black lines. Each band covers around 5% confidence interval, and the whole figure corresponds to 95% interval.

At nearly all time-delays, the proposed UQ approach provides a reasonable quantification of the underlying impulse function $\boldsymbol{h}$, which covers the (deterministic) Lasso estimate. Take Case III as an example, temporal distances between neighboring troughs / peaks of 0.18 ms and impulse function major peak of 0.33ms are also capture by UQ. The Lasso estimates are not centered at the confidence bands of UQ. This can be attributed to the prior assumption of impulse function, which assumes that $\boldsymbol{h}$ is centered at zero.

For each case, troughs and peaks of UQ solutions emerge alternatively with a generally regular time interval. The cyclic influence indicates the influence at one or more specific frequency. Further study indicates that for each case, this time interval matches the dominant frequencies of heat release rate and pressure (not shown here). At some time-delay, this trend is contaminated by responses with smaller time intervals, indicating the influences of higher frequencies. The impulse responses cluster near the median and spread loosely otherwise.

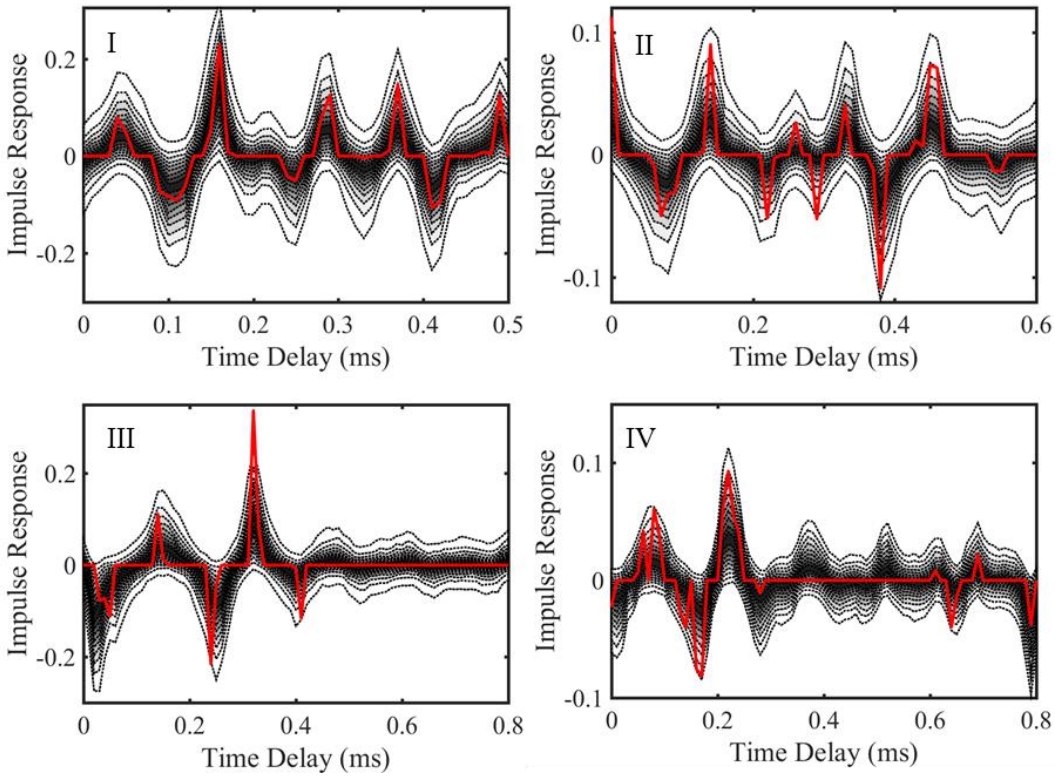

Figure 8.14: Uncertainty Quantifications of Impulse Function

8.6.2 Uncertainty Quantification of Flame Transfer Function

The FTF from both methods (Winer-Hopf and Lasso) of Case III are plotted in Figure 8.15. Lasso is able to capture dominant responses around 5.6 and 8.3 kHz more accurately. Moreover, the phase angle of FTF matches the theoretical phase angle.

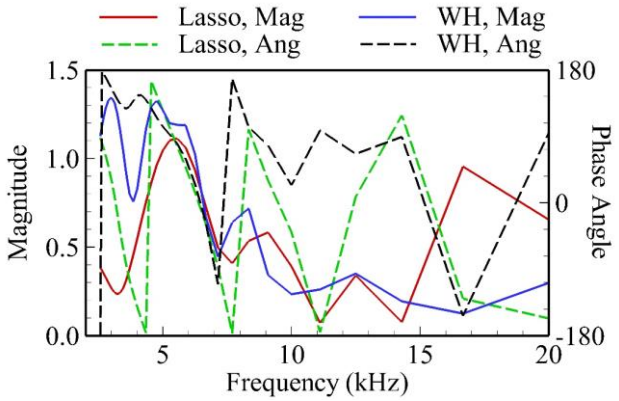

Figure 8.15 FTF of Wiener-Hopf method and Lasso

UQ of FTFs are also calculated through propagation from UQ of impulse function, and are plotted in Figure 8.16. The nearby band confidence interval of around 5% and the whole 95% confidence interval are identical to those of impulse function. All four cases capture dominant frequencies around 6 kHz. This frequency is characterized by vortex shedding, and is determined by exit velocity profile [152]: $f_v = StU/\theta$, where St and θ are Strouhal number and momentum thickness. Since Cases I, III and IV have similar exit velocity profiles, the characteristic frequencies for these cases are similar. Different from other three cases, flame zone of Case II has a dominant frequency of 19.6 kHz, which is also captured by Figure 8.16.

Both Lasso and UQ framework capture the dominant frequencies for all four cases. The UQ of responses cluster near the dominant frequencies. The UQ ranges of FTF magnitude at other frequencies are large. This indicates that the dominant responses is unaffected by noise, while responses at other frequencies are prone to noise. The confidence bands also indicate that at all frequencies, FTF clusters near the median and loosely spreads to the outer rim. The above characteristics demonstrated that similar to the Lasso, Bayesian Lasso can capture dominant combustion response and renders physical representations of combustion response.

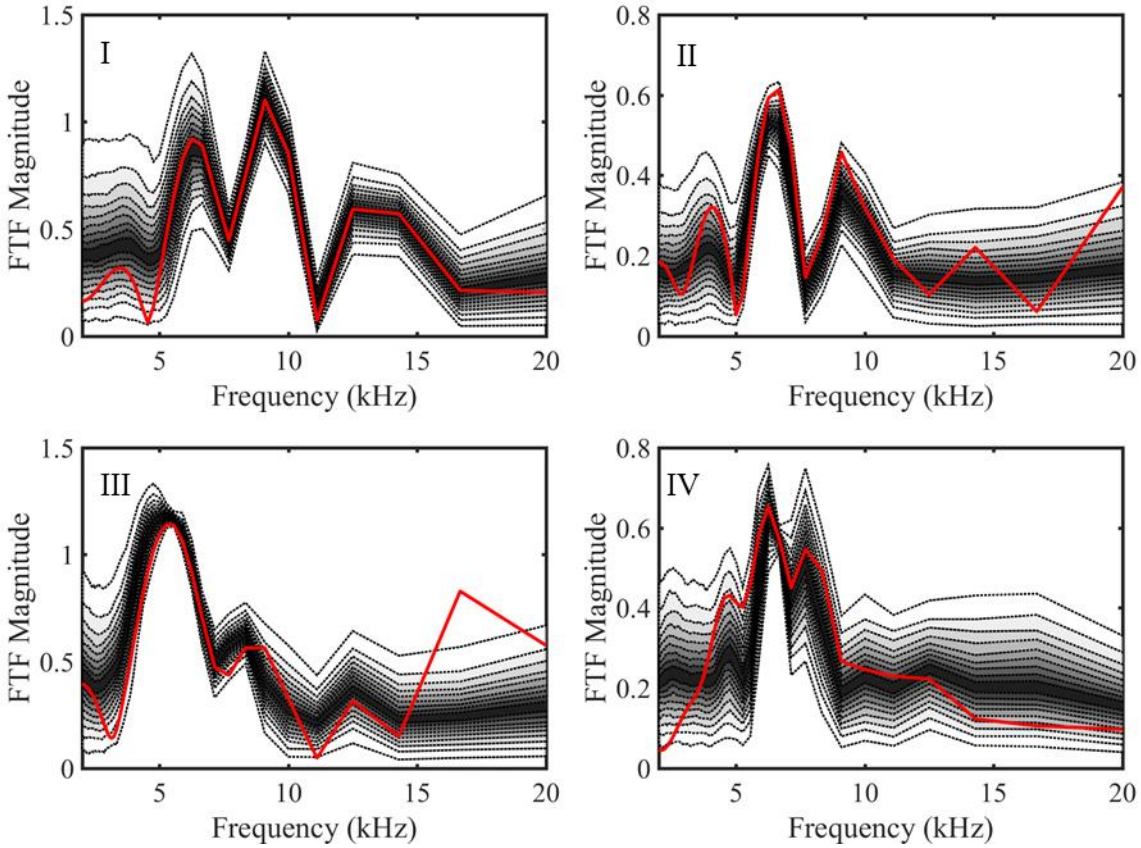

Figure 8.16 Uncertainty Quantifications of Flame Transfer Function

8.7 Thermoacoustic Instabilities

Given the estimated UQ range of combustion dynamics, UQ of thermoacoustic instabilities can then be quantified through propagation of each sample. But before that, this work takes one step back, validates the implementations of traditional Helmholtz solver. Results of UQ of thermoacoustic instabilities will be shown after validation. Due to the limitation of computational resources, all the results shown in this section are based on Case III.

8.7.1 Thermoacoustic Instabilities of Baseline Case

As the baseline study, the traditional thermoacoustic analysis is conducted using FTF and Helmholtz solver. Pressure distribution and its corresponding complex frequency for each mode are captured. The frequency can be divided into two parts. The real part represents the actual frequency, and the imaginary part quantifies the corresponding growth rate. Since $p' = \hat{p}' e^{i\omega t}$ [205], a negative growth rate means that the fluctuation amplitude grows with time, and leads to an unstable mode. All modes can be categorized based on the corresponding spatial distributions of pressure fluctuations [206]. The first longitudinal mode (1L) and first transverse mode (1T) are depicted in Figure 8.17. For tangential modes, oscillation amplitude decays axially. The dominant frequency of 1T mode is 3834 Hz. This number matches the range of 3900-4000 Hz in [207]. Other frequencies and growth rates are plotted in Figure 8.18.

The homogeneous Helmholtz equation with identical conditions are computed and compared with the inhomogeneous counterpart (not shown here). The real-part frequencies and mode shapes are similar. This similarity indicates that the thermoacoustic processes (represented in the source terms) are small perturbations. This validates the current Helmholtz approach and allows the possible future use of other linearized procedures, including linearized Galerkin method [176] or the three-dimensional linearized analyses [208].

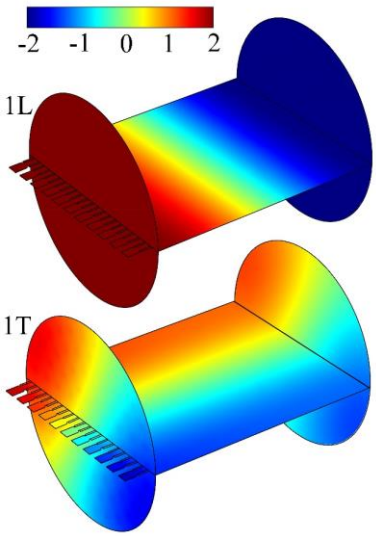

Figure 8.17 1L and 1T Mode Shape of Baseline Case

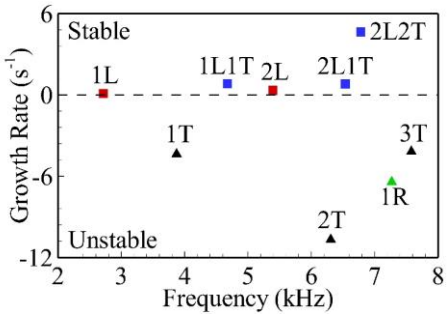

Figure 8.18 Dominant Frequencies for Baseline Case

As described and explained in Refs. [7, 176], the tangential modes tend to be more unstable than longitudinal modes for at least two reasons. First, the exhaust nozzle provides damping for longitudinal than for tangential modes (not applicable in this study); second, the physical and chemical processes near the injector faces are generally more sensitive to velocity fluctuations parallel to the injector faces than the normal unsteady motions. This is verified in Figure 8.18, as the 1T, 2T, 3T modes tend to be more unstable than longitudinal counterparts.

8.7.2 Uncertainty Quantification of Thermoacoustic Instabilities

The UQ of thermoacoustic instability is estimated by propagating the posterior samples used in the UQ of the impulse function. Because the acoustic analyses of all 2500 FTF samples can be time-consuming, we employ a common statistical technique "thinning" [187] by performing such analyses only on every k-th sample from the posterior sample chain. Specifically, in the current study, 100 cases are selected by taking every 25-th of 2500 samples.

For all 100 samples, the distributions of growth rates for 1L and 1T modes are shown in Figure 8.19. The frequencies and corresponding UQ of growth rates are listed in Table 8.2. In accordance with the analyses above, 90% confidence interval is used to quantify uncertainties. As the traditional Helmholtz approach is subject to errors, the estimation of UQ offers a better perspective. As shown in Table 8.2, compared with the deterministic growth rate in the baseline case, risk factor, the cumulative distribution function of being unstable [181, 182] is a more precise way to describe instability. In the 90% confidence interval, tangential modes have more than 80% chance to be unstable. While the other modes have only 25%, even 10% chance of being unstable. These results match the descriptions in the previous section, indicating that tangential modes have much higher chance to become unstable.

Table 8.2 UQ of Acoustic Modes

Mode	f /Hz	Growth Rates/s^{-1}	Risk Factor
1L	2719	0.19±0.39	0.22
1T	3874	-9.37±14.95	0.86
1L1T	4676	1.58±2.37	0.12
2L	5393	0.80±1.10	0.11

Table 8.2 continue

2T	6307	-21.20±28.52	0.89
2L1T	6534	1.86±2.44	0.11
2L2T	6781	6.82±9.37	0.11
1R	7268	-15.72±20.00	0.89
3T	7578	-10.85±13.55	0.90

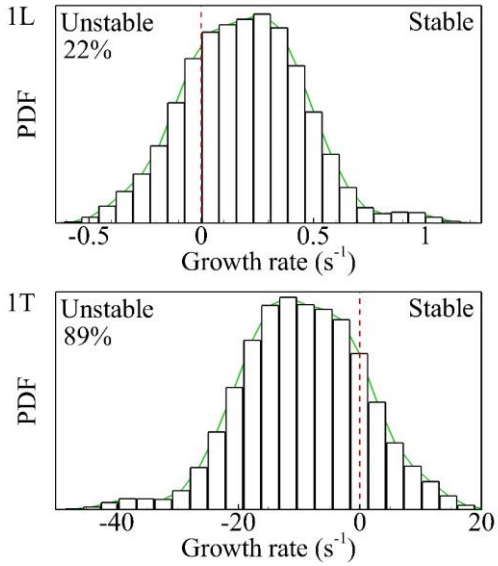

Figure 8.19 Distribution of growth rates for 1L and 1T mode

The UQ of frequencies and growth rates are further visualized in Figure 8.20. Baseline solutions (denoted as Lasso) are marked in red, and the UQ analysis results are depicted in green. Similar trends can be observed, as the tangential modes have the higher tendencies to be unstable while other modes do not. Another interesting observation is the large UQ band width of tangential modes. The traditional approach might lead to the impression that for the same geometry and operating condition, unstable modes stays unstable. On the contrary, the current study shows that the tangential modes have much wider confidence band than longitudinal and mixed modes. This study indicates the strong influence of operation on the instabilities for a single design. A small change in the pressure

and heat release rate may have significant impact on the stabilities of tangential modes. This raises a more challenging task for the combustor design. The designer should be cautious of every factor that might lead to uncertainties of pressure fluctuations, including the transient effects of throttling, the flow rates, composition of reactants, etc.

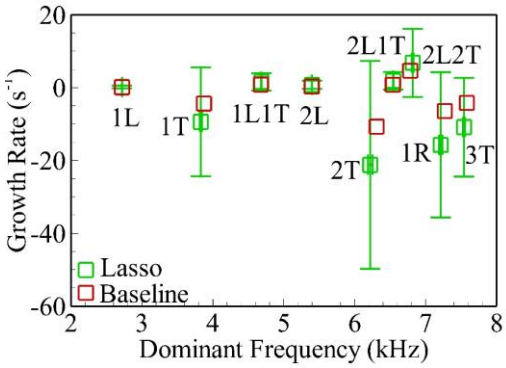

Figure 8.20 Uncertainty Quantification vs Baseline for acoustic modes

8.8 Conclusions

This proposed research is composed of two closely-related sub-topics. The first sub-topic is the two-stage flame transfer function identification method. With incorporation of L1 regularization and physics-based model selection, the proposed method is able to obtain an improved transfer function which reflects the underlying physics.

In the second sub-topic, a Bayesian framework based on Gibbs sampling and uncertainty propagation is built to estimate UQ of impulse function, transfer function. After testing a benchmark case of Helmholtz solver, the UQ is then extended to the analyses of thermoacoustic instabilities. The UQ range is able to present richer physics in terms of how large the range of flame response will be, the percentage of a mode to become unstable, etc.

CHAPTER 9.

CONCLUSIONS

This dissertation conducted a comprehensive study of gas-centered liquid-swirl coaxial (GCLSC) injectors, using both LES-based simulation and POD-based emulation. Gaseous oxygen is axially injected into the center post, while kerosene is tangentially introduced into the coaxial annulus. The operating pressure is 25.3 MPa, well above the thermodynamic critical points of the propellants involved. Major contributions will be listed in the next paragraph, followed by a summary.

In this paragraph, major contributions of the current work is summarized. For high-fidelity simulations, key dynamics characteristics of GCLSC injectors at 25.3 MPa, as well as the corresponding mechanisms, are analyzed for the first time. The flame anchoring mechanism of GCLSC injectors is also revealed for the first time. For high-fidelity simulation, CKSPOD-based emulation is improved with inclusion of common grid technique and physics-based constraints, as described in the previous sections. The improved CKSPOD is then applied to bi-fluid injector for the first time. In this study, CKSPOD is employed to predict spatio-temporally evolving flow field of gas-centered liquid-swirl coaxial injector, with complicated mixing and combustion dynamics. Moreover, CKSPOD-based emulation is applied to injector design optimization for the first time.

The study is composed of two parts. The first part investigates flow and combustion dynamics of GCLSC injectors based on high-fidelity large eddy simulations (LES). The

second part presents a high-fidelity emulation framework for the prediction of spatiotemporally evolving flow field in a significantly shorter turnaround time, and extends the framework to injector design optimization.

For the first part, LES simulations are conducted to study supercritical fluid flow dynamics and combustion characteristics of GCLSC injectors. Based on LES results, for non-reacting flows, detailed flow physics and structures are identified, followed by comprehensive analyses of key dynamic characteristics and corresponding mechanisms. The mechanisms include vortex shedding near the fuel injection slit, the shear layer instability in the recess region, and vortical expansion and merging in the taper region. For reacting flows, the flow field is categorized into four regions: propellant injection, flame initialization, flame development, and intensive combustion. Flow structures and the flame evolution are elaborated in detail. Moreover, the effects of the recess length on mixing, flow dynamics and combustion dynamics are investigated.

The second part presents a high-fidelity data-driven emulation framework, which utilizes training data from LES and enables flow field emulation in reasonable turnaround time. The framework employs common kernel-smoothed proper orthogonal decomposition (CKSPOD) as the surrogate model, which is able to extract dominant coherent flow structures through hadamard-based POD and kriging, and reconstruct the modes and coefficients to predict the flow field of a new case. Significant improvements, including common grid interpolation and physics-based conditions, are incorporated to the this framework to accommodate the prediction of complicated mixing and combustion dynamics. In the current study, CKSPOD utilizes LES results of GCLSC injectors as

training data, and recess length is chosen as the varying design parameter. Detailed evaluations of the predicted flow fields are carried out, and the current framework is able to capture spatiotemporall evolving flow fields for both non-reacting and reacting cases with high accuracy. Moreover, the improved CKSPOD presents uncertainty quantification (UQ) of the predicted flow field, providing a metric for model fit. CKSPOD is further extended to injector design and optimization, based on the objective functions of mixing efficiency and injector wall thermal protection.

A data-driven framework of combustion instability identification is proposed in the dissertation. Based on the traditional framework of identifying combustion instability through extraction and application of flame transfer function, this work proposes a novel method for the uncertainty quantification (UQ) of combustion instability. The method is implemented to estimate the UQ of thermoacoustic instability in a full-scale liquid rocket engine combustor, which comprises of 91 bi-swirl injectors burning kerosene and liquid oxygen. The proposed framework is able to present richer physics in terms of the uncertainty of flame response, the percentage of a mode to become unstable, etc.

REFERENCES

[1] Yang, V., Habiballah, M., Hulka, J., and Popp, M., *Liquid Rocket Thrust Chambers: Aspects of Modeling, Analysis, and Design*: AIAA, 2004.

[2] Lefebvre, A., *Atomization and Sprays*: CRC Press, 1988.

[3] Lieuwen, T. C., and Yang, V., "Combustion instabilities in gas turbine engines(operational experience, fundamental mechanisms and modeling)," *Progress in astronautics and aeronautics*, 2005.

[4] Huang, Y., and Yang, V., "Dynamics and stability of lean-premixed swirl-stabilized combustion," *Progress in Energy and Combustion Science* Vol. 35, No. 4, 2009, pp. 293-364.

[5] Bazarov, V. G., and Yang, V., "Liquid-propellant rocket engine injector dynamics," *Journal of Propulsion and Power* Vol. 14, No. 5, 1998, pp. 797-806.

[6] Bazarov, V., Yang, V., and Puri, P., "Design and dynamics of jet and swirl injectors," *Liquid Rocket Thrust Chambers: Aspects of Modeling, Analysis, and Design* Vol. 200, 2004, pp. 19-103.

[7] Oefelein, J. C., and Yang, V., "Comprehensive review of liquid-propellant combustion instabilities in F-1 engines," *Journal of Propulsion and Power* Vol. 9, No. 5, 1993, pp. 657-677.

[8] Huang, Y., Wang, S., and Yang, V., "Systematic analysis of lean-premixed swirl-stabilized combustion," *AIAA Journal* Vol. 44, No. 4, 2006, pp. 724-740.

[9] Wang, X., Li, Y., Wang, Y., and Yang, V., "Near-field flame dynamics of liquid oxygen/kerosene bi-swirl injectors at supercritical conditions," *Combustion and Flame* Vol. 190, 2018, pp. 1-11.

[10] Yang, V., "Modeling of supercritical vaporization, mixing, and combustion processes in liquid-fueled propulsion systems," *Proceedings of the Combustion Institute* Vol. 28, No. 1, 2000, pp. 925-942.

[11] Bellan, J., "Supercritical (and subcritical) fluid behavior and modeling: drops, streams, shear and mixing layers, jets and sprays," *Progress in energy and combustion science* Vol. 26, No. 4, 2000, pp. 329-366.

[12] Urbano, A., Selle, L., Staffelbach, G., Cuenot, B., Schmitt, T., Ducruix, S., and Candel, S., "Exploration of combustion instability triggering using Large Eddy Simulation of a multiple injector Liquid Rocket Engine," *Combustion and Flame* Vol. 169, 2016, pp. 129-140.

[13] Benner, P., Gugercin, S., and Willcox, K., "A survey of projection-based model reduction methods for parametric dynamical systems," *SIAM review* Vol. 57, No. 4, 2015, pp. 483-531.

[14] Rowley, C. W., and Dawson, S. T., "Model reduction for flow analysis and control," *Annual Review of Fluid Mechanics* Vol. 49, 2017, pp. 387-417.

[15] Eldred, M., and Dunlavy, D., "Formulations for surrogate-based optimization with data fit, multifidelity, and reduced-order models," *11th AIAA/ISSMO Multidisciplinary Analysis and Optimization Conference*. 2006, p. 7117.

[16] Newman, J. A., and Brzustowski, T., "Behavior of a liquid jet near the thermodynamic critical region," *AIAA Journal* Vol. 9, No. 8, 1971, pp. 1595-1602.

[17] Mayer, W., Schik, A., Sch-aring, M., ffler, and Tamura, H., "Injection and mixing processes in high-pressure liquid oxygen/gaseous hydrogen rocket combustors," *Journal of Propulsion and Power* Vol. 16, No. 5, 2000, pp. 823-828.

[18] Chehroudi, B., Cohn, R., and Talley, D., "Cryogenic shear layers: experiments and phenomenological modeling of the initial growth rate under subcritical and supercritical conditions," *International Journal of Heat and Fluid Flow* Vol. 23, No. 5, 2002, pp. 554-563.

[19] Branam, R., and Mayer, W., "Characterization of cryogenic injection at supercritical pressure," *Journal of Propulsion and power* Vol. 19, No. 3, 2003, pp. 342-355.

[20] Candel, S., Juniper, M., Singla, G., Scouflaire, P., and Rolon, C., "Structure and dynamics of cryogenic flames at supercritical pressure," *Combustion Science and Technology* Vol. 178, No. 1-3, 2006, pp. 161-192.

[21] Oefelein, J. C., and Yang, V., "Modeling high-pressure mixing and combustion processes in liquid rocket engines," *Journal of Propulsion and Power* Vol. 14, No. 5, 1998, pp. 843-857.

[22] Zong, N., Meng, H., Hsieh, S.-Y., and Yang, V., "A numerical study of cryogenic fluid injection and mixing under supercritical conditions," *Physics of fluids* Vol. 16, 2004, p. 4248.

[23] Oefelein, J. C., "Thermophysical characteristics of shear-coaxial LOX-H-2 flames at supercritical pressure," *Proceedings of the Combustion Institute* Vol. 30, 2005, pp. 2929-2937.

[24] Zong, N., and Yang, V., "Near-field flow and flame dynamics of LOX/methane shear-coaxial injector under supercritical conditions," *Proceedings of the Combustion Institute* Vol. 31, No. 2, 2007, pp. 2309-2317.

[25] Juniper, M., and Candel, S., "Edge diffusion flame stabilization behind a step over a liquid reactant," *Journal of Propulsion and Power* Vol. 19, No. 3, 2003, pp. 332-341.

[26] Juniper, M. P., and Candel, S. M., "The stability of ducted compound flows and consequences for the geometry of coaxial injectors," *Journal of Fluid Mechanics* Vol. 482, 2003, pp. 257-269.

[27] Masquelet, M., Menon, S., Jin, Y., and Friedrich, R., "Simulation of unsteady combustion in a LOX-GH(2) fueled rocket engine," *Aerospace Science and Technology* Vol. 13, No. 8, 2009, pp. 466-474.

[28] Masquelet, M., and Menon, S., "Large-eddy simulation of flame-turbulence interactions in a shear coaxial injector," *Journal of Propulsion and Power* Vol. 26, No. 5, 2010, pp. 924-935.

[29] Rubinsky, V. R., ed. *Combustion instability in the RD-0110 engine*: Progress in Astronautics and Aeronautics, 1995.

[30] Huang, Y., and Yang, V., "Effect of swirl on combustion dynamics in a lean-premixed swirl-stabilized combustor," *Proceedings of the Combustion Institute* Vol. 30, No. 2, 2005, pp. 1775-1782.

[31] Syred, N., and Beer, J., "Combustion in swirling flows: a review," *Combustion and Flame* Vol. 23, No. 2, 1974, pp. 143-201.

[32] Ahn, K., and Choi, H.-S., "Combustion dynamics of swirl coaxial injectors in fuel-rich combustion," *Journal of Propulsion and Power* Vol. 28, No. 6, 2012, pp. 1359-1367.

[33] Bazarov, V., Yang, V., and Puri, P., "Design and dynamics of jet and swirl injectors," *Liquid Rocket Thrust Chambers: Aspects of Modeling, Analysis, and Design*. Vol. 200, Progress in Astronautics and Aeronautics, 2004, pp. 19-103.

[34] Datta, A., and Som, S., "Numerical prediction of air core diameter, coefficient of discharge and spray cone angle of a swirl spray pressure nozzle," *International journal of heat and fluid flow* Vol. 21, No. 4, 2000, pp. 412-419.

[35] Kim, D., Im, J.-H., Koh, H., and Yoon, Y., "Effect of ambient gas density on spray characteristics of swirling liquid sheets," *Journal of propulsion and power* Vol. 23, No. 3, 2007, pp. 603-611.

[36] Fu, Q.-f., Yang, L.-j., and Wang, X.-d., "Theoretical and experimental study of the dynamics of a liquid swirl injector," *Journal of Propulsion and Power* Vol. 26, No. 1, 2010, pp. 94-101.

[37] Fu, Q.-F., Yang, L.-J., Zhang, W., and Cui, K.-D., "Spray Characteristics of an Open-end Swirl Injector," Vol. 22, No. 5, 2012, pp. 431-445.

[38] Richardson, R., Park, H., Canino, J., and Heister, S., "Non Linear Dynamic Response Modeling of a Swirl Injector," *43rd AIAA/ASME/SAE/ASEE Joint Propulsion Conference & Exhibit*. 2007.

[39] Ismailov, M., and Heister, S. D., "Dynamic Response of Rocket Swirl Injectors, Part I: Wave Reflection and Resonance," *Journal of Propulsion and Power* Vol. 27, No. 2, 2011, pp. 402-411.

[40] Ismailov, M., and Heister, S. D., "Dynamic Response of Rocket Swirl Injectors, Part II: Nonlinear Dynamic Response," *Journal of Propulsion and Power* Vol. 27, No. 2, 2011, pp. 412-421.

[41] Cho, S., Park, G., Chung, Y., Yoon, Y., and Bazarov, V. G., "Surface Instability on Cryogenic Swirl Flow at Sub-to Supercritical Conditions," *Journal of Propulsion and Power*, 2014, pp. 1-9.

[42] Zong, N., and Yang, V., "Cryogenic fluid dynamics of pressure swirl injectors at supercritical conditions," *Physics of Fluids* Vol. 20, No. 5, 2008.

[43] Huo, H., Zong, N., and Yang, V., "Cryogenic fluid dynamic response of swirl injector to external forcing at supercritical conditions," *47th AIAA Aerospace Sciences Meeting*, AIAA Paper 2009-233, 2009.

[44] Huo, H., Wang, X., and Yang, V., "Flow dynamics of a simplex swirl injector at supercritical conditions," *52nd Aerospace Sciences Meeting*. National Harbor, Maryland, 2014.

[45] Sasaki, M., Sakamoto, H., Takahashi, M., Tomita, T., and Tamura, H., "Comparative study of recessed and non-recessed swirl coaxial injectors," AIAA Paper 1997-2907, 1997.

[46] Inamura, T., Tamura, H., and Sakamoto, H., "Characteristics of liquid film and spray injected from swirl coaxial injector," *Journal of propulsion and Power* Vol. 19, No. 4, 2003, pp. 632-639.

[47] Han, P.-G., Seol, J., Hwang, S., and Yoon, Y., "The spray characteristics of swirl coaxial injectors," *41st Aerospace Sciences Meeting and Exhibit*, AIAA Paper 2003-0490, 2003.

[48] Soltani, M., Ghorbanian, K., Ashjaee, M., and Morad, M., "Spray characteristics of a liquid–liquid coaxial swirl atomizer at different mass flow rates," *Aerospace science and technology* Vol. 9, No. 7, 2005, pp. 592-604.

[49] Lightfoot, M. D., Schumaker, S. A., Villasmil, L. A., and Danczyk, S. A., "The Effect of Swirl on Gas-Centered Swirl Coaxial Injector Sprays." DTIC Document, 2011.

[50] Im, J.-H., Cho, S., Yoon, Y., and Moon, I., "Comparative study of spray characteristics of gas-centered and liquid-centered swirl coaxial injectors," *Journal of Propulsion and Power* Vol. 26, No. 6, 2010, pp. 1196-1204.

[51] Kim, S.-H., Han, Y.-M., Seo, S., Moon, I.-Y., Kim, J.-K., and Seol, W.-S., "Effects of LOX post recess on the combustion characteristics for Bi-swirl coaxial injector," *41st AIAA/ASME/SAE/ASEE Joint Propulsion Conference & Exhibit*, AIAA Paper 2005-4445, 2005.

[52] Ahn, K., Han, Y.-M., Seo, S., and Choi, H.-S., "Effects of injector recess and chamber pressure on combustion characteristics of liquid–liquid swirl coaxial injectors," *Combustion Science and Technology* Vol. 183, No. 3, 2010, pp. 252-270.

[53] Ahn, K., Han, Y.-M., and Choi, H.-S., "Effects of recess length on discharge coefficients of swirl coaxial injectors," *Combustion Science and Technology* Vol. 184, No. 3, 2012, pp. 323-336.

[54] Bazarov, V., Yang, V., and Puri, P., "Design and dynamics of jet and swirl injectors," *Liquid Rocket Thrust Chambers (Progress in Astronautics and Aeronautics): Aspects of Modeling, Analysis, and Design, AIAA* Vol. 200, 2004, pp. 19-103.

[55] Manski, D., Goertz, C., Saßnick, H.-D., Hulka, J. R., Goracke, B. D., and Levack, D. J., "Cycles for earth-to-orbit propulsion," *Journal of Propulsion and Power* Vol. 14, No. 5, 1998, pp. 588-604.

[56] Vasin, A. A., Kamensky, S. D., Katorgin, B. I., Kolesnikov, A. I., Nosov, V. P., Stavrulov, A. I., Fedorov, V. V., and Chvanov, V. K., "Liquid-propellant rocket engine chamber and its casing," *US Patents, US 6,244,041 B1*, 2001.

[57] Dranovsky, M. L., Yang, V., Culick, F., and Talley, D. G., *Combustion instabilities in liquid rocket engines: testing and development practices in Russia*: Progress in Astronautics and Aeronautics, 2007.

[58] Soller, S., Wagner, R., Kau, H., Martin, P., and Mäding, C., "Combustion stability characteristics of coax-swirl-injectors for oxygen/kerosene," AIAA Paper 2007-5563, 2007.

[59] Miller, K., Sisco, J., Nugent, N., and Anderson, W., "Combustion instability with a single-element swirl injector," *Journal of Propulsion and Power* Vol. 23, No. 5, 2007, pp. 1102-1112.

[60] Lightfoot, M. D. A., Schumaker, S. A., and Danczyk, S. A., "Atomization uniformity in gas-centered swirl-coaxial injectors," *AFRL-RZ-ED-TP-2010-095*, 2010.

[61] Schumaker, S. A., Danczyk, S. A., and Lightfoot, M. D., "Effect of cup length on film profiles in gas-centered swirl-coaxial injectors," AIAA Paper 2010-368, 2010.

[62] Kulkarni, V., Sivakumar, D., Oommen, C., and Tharakan, T., "Liquid sheet breakup in gas-centered swirl coaxial atomizers," *Journal of Fluids Engineering* Vol. 132, No. 1, 2010, p. 011303.

[63] Jeon, J., Hong, M., Han, Y.-M., and Lee, S. Y., "Experimental study on spray characteristics of gas-centered swirl coaxial injectors," *Journal of Fluids Engineering* Vol. 133, No. 12, 2011, p. 121303.

[64] Schumaker, S. A., Danczyk, S. A., and Lightfoot, M., "Effect of swirl on gas-centered swirl-coaxial injectors," AIAA Paper 2011-5621. 2011.

[65] Trask, N., Schmidt, D. P., Lightfoot, M., and Danczyk, S., "Compressible modeling of the internal flow in a gas-centered swirl-coaxial fuel injector," *Journal of Propulsion and Power* Vol. 28, No. 4, 2012, pp. 685-693.

[66] Kim, J. G., Han, Y. M., Choi, H. S., and Yoon, Y., "Study on spray patterns of gas-centered swirl coaxial (GCSC) injectors in high pressure conditions," *Aerospace Science and Technology* Vol. 27, No. 1, 2013, pp. 171-178.

[67] Matas, J.-P., Hong, M., and Cartellier, A., "Stability of a swirled liquid film entrained by a fast gas stream," *Physics of fluids* Vol. 26, No. 4, 2014, p. 042108.

[68] Sisco, J. C., Yu, Y., Sankaran, V., and Anderson, W. E., "Examination of mode shapes in an unstable model combustor," *Journal of Sound and Vibration* Vol. 330, No. 1, 2011, pp. 61-74.

[69] Morgan, C. J., Shipley, K. J., and Anderson, W. E., "Comparative Evaluation Between Experiment and Simulation for a Transverse Instability," *Journal of Propulsion and Power* Vol. 31, No. 6, 2015, pp. 1696-1706.

[70] Park, G., Lee, J., Oh, S., Yoon, Y., and Sohn, C. H., "Characteristics of Gas-Centered Swirl Coaxial Injector with Acoustic Excitation of Gas Flow," *AIAA Journal* Vol. 55, No. 3, 2017, pp. 894-901.

[71] Han, P.-G., Seol, J., Hwang, S., and Yoon, Y., "The spray characteristics of swirl coaxial injectors," *AIAA Paper* Vol. 2003-0490, 2003.

[72] Kim, B.-D., Heister, S. D., and Collicott, S. H., "Three-dimensional flow simulations in the recessed region of a coaxial injector," *Journal of Propulsion and Power* Vol. 21, No. 4, 2005, pp. 728-742.

[73] Couplet, M., Basdevant, C., and Sagaut, P., "Calibrated reduced-order POD-Galerkin system for fluid flow modelling," *Journal of Computational Physics* Vol. 207, No. 1, 2005, pp. 192-220.

[74] Kalb, V. L., and Deane, A. E., "An intrinsic stabilization scheme for proper orthogonal decomposition based low-dimensional models," *Physics of fluids* Vol. 19, No. 5, 2007, p. 054106.

[75] Ly, H. V., and Tran, H. T., "Modeling and control of physical processes using proper orthogonal decomposition," *Mathematical and computer modelling* Vol. 33, No. 1-3, 2001, pp. 223-236.

[76] Audouze, C., De Vuyst, F., and Nair, P., "Reduced ‐ order modeling of parameterized PDEs using time ‐ space ‐ parameter principal component analysis," *International journal for numerical methods in engineering* Vol. 80, No. 8, 2009, pp. 1025-1057.

[77] Mainini, L., and Willcox, K., "Surrogate modeling approach to support real-time structural assessment and decision making," *AIAA Journal* Vol. 53, No. 6, 2015, pp. 1612-1626.

[78] Mak, S., Sung, C.-L., Wang, X., Yeh, S.-T., Chang, Y.-H., Joseph, V. R., Yang, V., and Wu, C. J., "An efficient surrogate model for emulation and physics extraction of large eddy simulations," *Journal of the American Statistical Association*, 2018, pp. 1-14.

[79] Yeh, S.-T., Wang, X., Sung, C.-L., Mak, S., Chang, Y.-H., Zhang, L., Wu, C. J., and Yang, V., "Common proper orthogonal decomposition-based spatiotemporal emulator for design exploration," *AIAA Journal* Vol. 56, No. 6, 2018, pp. 2429-2442.

[80] Chang, Y.-H., Zhang, L., Wang, X., Yeh, S.-T., Mak, S., Sung, C.-L., Wu, C. F. J., and Yang, v., "Kernel-smoothed proper orthogonal decomposition (KSPOD)-based emulation for spatiotemporally evolving flow dynamics prediction," *Submitted to AIAA Journal*, 2019.

[81] Chang, Y.-H., Zhang, L., Li, Y., Wang, X., and Yang, V., "Common kernel-smoothed proper orthogonal decomposition (CKSPOD): An advanced surrogate model to predict spatiotemporally evolving flow dynamics," 2019.

[82] Benedict, M., Webb, G. B., and Rubin, L. C., "An Empirical Equation for Thermodynamic Properties of Light Hydrocarbons and Their Mixtures I. Methane, Ethane, Propane and n ‐ Butane," *The Journal of Chemical Physics* Vol. 8, No. 4, 1940, pp. 334-345.

[83] Peng, D. Y., and Robinson, D. B., "A new two-constant equation of state," *Industrial & Engineering Chemistry Fundamentals* Vol. 15, No. 1, 1976, pp. 59-64.

[84] Soave, G., "Equilibrium constants from a modified Redlich-Kwong equation of state," *Chemical Engineering Science* Vol. 27, No. 6, 1972, pp. 1197-1203.

[85] Wang, X., "Swirling Fluid Mixing and Combustion Dynamics at Supercritical Conditions."PhD Thesis, Georgia Institute of Technology, 2016.

[86] Poling, B. E., Prausnitz, J. M., and O'Connell, J. P., *The properties of gases and liquids*. New York: McGraw-Hill, 2001.

[87] Ely, J. F., and Hanley, H. J. M., "Prediction of Transport-Properties .1. Viscosity of Fluids and Mixtures," *Industrial & Engineering Chemistry Fundamentals* Vol. 20, No. 4, 1981, pp. 323-332.

[88] Piomelli, U., "Large-eddy simulation: achievements and challenges," *Progress in Aerospace Sciences* Vol. 35, No. 4, 1999, pp. 335-362.

[89] Sagaut, P., *Large eddy simulation for incompressible flows : an introduction*. Berlin ; New York: Springer, 2001.

[90] Moin, P., and Mahesh, K., "Direct numerical simulation: A tool in turbulence research," *Annual Review of Fluid Mechanics* Vol. 30, 1998, pp. 539-578.

[91] Miller, R. S., Harstad, K. G., and Bellan, J., "Direct numerical simulations of supercritical fluid mixing layers applied to heptane-nitrogen," *Journal of Fluid Mechanics* Vol. 436, 2001, pp. 1-39.

[92] Okong'o, N., Harstad, K., and Bellan, J., "Direct numerical simulations of O-2/H-2 temporal mixing layers under supercritical conditions," *AIAA Journal* Vol. 40, No. 5, 2002, pp. 914-926.

[93] Vervisch, L., and Poinsot, T., "Direct numerical simulation of non-premixed turbulent flames," *Annual Review of Fluid Mechanics* Vol. 30, 1998, pp. 655-691.

[94] Pope, S. B., *Turbulent flows*. Cambridge ; New York: Cambridge University Press, 2000.

[95] Leonard, A., "Energy cascade in large-eddy simulations of turbulent fluid flows," *Turbulent diffusion in environmental pollution; Proceedings of the Second Symposium, Charlottesville*. New York, Academic Press, Inc., Proceedings of the Second Symposium, Charlottesville, Va ; United States, 1974.

[96] Ghosal, S., and Moin, P., "The Basic Equations for the Large-Eddy Simulation of Turbulent Flows in Complex-Geometry," *Journal of Computational Physics* Vol. 118, No. 1, 1995, pp. 24-37.

[97] Vanderven, H., "A Family of Large-Eddy Simulation (Les) Filters with Nonuniform Filter Widths," *Physics of Fluids* Vol. 7, No. 5, 1995, pp. 1171-1172.

[98] Le Ribault, C., Sarkar, S., and Stanley, S. A., "Large eddy simulation of a plane jet," *Physics of Fluids* Vol. 11, No. 10, 1999, pp. 3069-3083.

[99] Moin, P., "Progress in large eddy simulation of turbulent flows," 1997.

[100] Favre, A., "Statistical equations of turbulent gases (Statistical equations for compressible gas, discussing turbulent quantities separated into fluctuating and macroscopic parts)," 1969.

[101] Calhoon, W. H., Jr., and Menon, S., "Subgrid modeling for reacting large eddy simulations," *AIAA, Aerospace Sciences Meeting and Exhibit, 34th, Reno*. United States, 1996.

[102] Smagorinsky, J., "General Circulation Experiments with the Primitive Equations. I-the Basic Experiment. ," *Monthly Weather Review* Vol. 91, 1963, pp. 99-164.

[103] Lilly, D. K., "The representation of small scale turbulence in numerical simulation experiments," 1967.

[104] Erlebacher, G., Hussaini, M. Y., Speziale, C. G., and Zang, T. A., "Toward the Large-Eddy Simulation of Compressible Turbulent Flows," *Journal of Fluid Mechanics* Vol. 238, 1992, pp. 155-185.

[105] Moin, P., and Kim, J., "Numerical Investigation of Turbulent Channel Flow," *Journal of Fluid Mechanics* Vol. 118, No. May, 1982, pp. 341-377.

[106] Martın, M. P., Piomelli, U., and Candler, G. V., "A Priori Test of SGS Models in Compressible Turbulence," *Proceedings of the 3rd ASME/JSME Joint Fluid Engineering Conference*. San Francisco, California, USA, 1999.

[107] Germano, M., Piomelli, U., Moin, P., and Cabot, W. H., "A Dynamic Subgrid-Scale Eddy Viscosity Model," *Physics of Fluids a-Fluid Dynamics* Vol. 3, No. 7, 1991, pp. 1760-1765.

[108] Juneja, A., and Brasseur, J. G., "Characteristics of subgrid-resolved-scale dynamics in anisotropic turbulence, with application to rough-wall boundary layers," *Physics of Fluids* Vol. 11, No. 10, 1999, pp. 3054-3068.

[109] Klimenko, A., "Multicomponent diffusion of various admixtures in turbulent flow," *Fluid Dynamics* Vol. 25, No. 3, 1990, pp. 327-334.

[110] Bilger, R. W., "Conditional Moment Closure for Turbulent Reacting Flow," *Physics of Fluids a-Fluid Dynamics* Vol. 5, No. 2, 1993, pp. 436-444.

[111] Kerstein, A. R., "Linear-Eddy Modeling of Turbulent Transport .7. Finite-Rate Chemistry and Multistream Mixing," *Journal of Fluid Mechanics* Vol. 240, 1992, pp. 289-313.

[112] Kerstein, A. R., "Linear-Eddy Modeling of Turbulent Transport .4. Structure of Diffusion Flames," *Combustion Science and Technology* Vol. 81, No. 1-3, 1992, pp. 75-96.

[113] Mcmurtry, P. A., Menon, S., and Kerstein, A. R., "Linear Eddy Modeling of Turbulent Combustion," *Energy & Fuels* Vol. 7, No. 6, 1993, pp. 817-826.

[114] Sankaran, V., and Menon, S., "Subgrid combustion modeling of 3-D premixed flames in the thin-reaction-zone regime," *Proceedings of the Combustion Institute* Vol. 30, 2005, pp. 575-582.

[115] Peters, N., *Turbulent combustion*. Cambridge, England: Cambridge University Press, 2000.

[116] Légier, J., Poinsot, T., and Veynante, D., "Dynamically thickened flame LES model for premixed and non-premixed turbulent combustion," *Proceedings of the Summer Program*. 2000, p. 12.

[117] DesJardin, P. E., and Frankel, S. H., "Large eddy simulation of a nonpremixed reacting jet: Application and assessment of subgrid-scale combustion models," *Physics of Fluids* Vol. 10, No. 9, 1998, pp. 2298-2314.

[118] Cook, A. W., and Riley, J. J., "Subgrid-scale modeling for turbulent reacting flows," *Combustion and Flame* Vol. 112, No. 4, 1998, pp. 593-606.

[119] Girimaji, S. S., and Zhou, Y., "Analysis and modeling of subgrid scalar mixing using numerical data," *Physics of Fluids* Vol. 8, No. 5, 1996, pp. 1224-1236.

[120] Pierce, C. D., and Moin, P., "Progress-variable approach for large-eddy simulation of non-premixed turbulent combustion," *Journal of Fluid Mechanics* Vol. 504, 2004, pp. 73-97.

[121] Choi, Y. H., and Merkle, C. L., "The Application of Preconditioning in Viscous Flows," *Journal of Computational Physics* Vol. 105, No. 2, 1993, pp. 207-223.

[122] Shuen, J. S., Chen, K. H., and Choi, Y. H., "A Coupled Implicit Method for Chemical Nonequilibrium Flows at All Speeds," *Journal of Computational Physics* Vol. 106, No. 2, 1993, pp. 306-318.

[123] Turkel, E., "Review of Preconditioning Methods for Fluid-Dynamics," *Applied Numerical Mathematics* Vol. 12, No. 1-3, 1993, pp. 257-284.

[124] Hsieh, S. Y., and Yang, V., "A preconditioned flux-differencing scheme for chemically reacting flows at all Mach numbers," *International Journal of Computational Fluid Dynamics* Vol. 8, No. 1, 1997, pp. 31-49.

[125] Meng, H., and Yang, V., "A unified treatment of general fluid thermodynamics and its application to a preconditioning scheme," *Journal of Computational Physics* Vol. 189, No. 1, 2003, pp. 277-304.

[126] Zong, N., and Yang, V., "An efficient preconditioning scheme for real-fluid mixtures using primitive pressure-temperature variables," *International Journal of Computational Fluid Dynamics* Vol. 21, No. 5-6, 2007, pp. 217-230.

[127] Zong, N., "Modeling and simulation of cryogenic fluid injection and mixing dynamics under supercritical conditions."PhD Thesis, The Pennsylvania State University, 2005.

[128] Buelow, P., "Convergence enhancement of Euler and Navier-Stokes algorithms," 1997.

[129] Venkateswaran, S., and Merkle, C., "Dual time-stepping and preconditioning for unsteady computations," *33rd Aerospace Sciences Meeting and Exhibit*. 1995, pp. AIAA Paper 95-0078.

[130] Huo, H., "Large-eddy simulation of supercritical fluid flow and combustion."PhD Thesis, 2011.

[131] Hoffmann, K. A., and Chiang, S. T., *Computational fluid dynamics*. Wichita, Kan.: Engineering Education System, 1998.

[132] Kordulla, W., and Vinokur, M., "Efficient Computation of Volume in Flow Predictions," *AIAA Journal* Vol. 21, No. 6, 1983, pp. 917-918.

[133] Apte, S., and Yang, V., "Unsteady flow evolution in porous chamber with surface mass injection, part 1: Free oscillation," *AIAA Journal* Vol. 39, No. 8, 2001, pp. 1577-1586.

[134] Poinsot, T. J., and Lele, S. K., "Boundary-Conditions for Direct Simulations of Compressible Viscous Flows," *Journal of Computational Physics* Vol. 101, No. 1, 1992, pp. 104-129.

[135] Rudy, D. H., and Strikwerda, J. C., "A Nonreflecting Outflow Boundary-Condition for Subsonic Navier-Stokes Calculations," *Journal of Computational Physics* Vol. 36, No. 1, 1980, pp. 55-70.

[136] Baum, M., Poinsot, T., and Thevenin, D., "Accurate Boundary-Conditions for Multicomponent Reactive Flows," *Journal of Computational Physics* Vol. 116, No. 2, 1995, pp. 247-261.

[137] Manski, D., Goertz, C., Sabnick, H.-D., Hulka, J. R., Goracke, B. D., and H. Levack, D. J., "Cycles for earth-to-orbit propulsion," *Journal of Propulsion and Power* Vol. 14, No. 5, 1998, pp. 588-604.

[138] Yang, V., Ku, D. D., Walker, M. L. R., Williams, L. T., and Leahy, J. C., "Liquid Oxygen/Kerosene Staged Combustion Rocket Engines With Oxidizer-Rich Preburners," *NASA/TP 2015–218203*, 2015.

[139] Yang, V., Ku, D. D., Lioi, C. B., Yeh, S.-T., Leahy, J. C., and Kenny, R. J., "Liquid Oxygen/Kerosene Oxygen-Rich, Staged Combustion Engine Technology Development," *NASA/TP 2016-218226*, 2016.

[140] Lioi, C., Ku, D., and Yang, V., "Linear Acoustic Analysis of Main Combustion Chamber of an Oxidizer-Rich Staged Combustion Engine," *Journal of Propulsion and Power* Vol. 34, No. 6, 2018, pp. 1505-1518.

[141] Bodony, D. J., "Analysis of sponge zones for computational fluid mechanics," *Journal of Computational Physics* Vol. 212, No. 2, 2006, pp. 681-702.

[142] Li, Y., Wang, X., Zhang, L., and Yang, V., "Effects of Recess Length on Flow Dynamics of Gas-Centered Liquid-Swirl Coaxial Injector under Supercritical Conditions," *submitted to Physics Review Fluids*, 2019.

[143] Rasmussen, C. E., "Gaussian processes in machine learning," *Advanced lectures on machine learning*. Springer, 2004, pp. 63-71.

[144] Goovaerts, P., *Geostatistics for natural resources evaluation.* New York: Oxford University Press, 1997.

[145] Chang, Y.-H., "High-Fidelity Emulation of Spatiotemporally Evolving Flow Dynamics."PhD Thesis, Georgia Institute of Technology, 2018.

[146] Casella, G., and Berger, R. L., *Statistical inference*: Duxbury Pacific Grove, CA, 2002.

[147] Liu, D. C., and Nocedal, J., "On the limited memory BFGS method for large scale optimization," *Mathematical programming* Vol. 45, No. 1-3, 1989, pp. 503-528.

[148] Santner, T. J., Williams, B. J., and Notz, W. I., *The design and analysis of computer experiments*: Springer Science & Business Media, 2013.

[149] Lumley, J., "The structure of inhomogeneous turbulence," *Atmospheric Turbulence and Wave Propagation*, 1967, pp. 166-178.

[150] Zong, N., and Yang, V., "Cryogenic fluid dynamics of pressure swirl injectors at supercritical conditions," *Physics of Fluids* Vol. 20, No. 5, 2008, p. 056103.

[151] Berkooz, G., Holmes, P., and Lumley, J. L., "The proper orthogonal decomposition in the analysis of turbulent flows," *Annual review of fluid mechanics* Vol. 25, No. 1, 1993, pp. 539-575.

[152] Wang, X., Huo, H., Wang, Y., and Yang, V., "Comprehensive Study of Cryogenic Fluid Dynamics of Swirl Injectors at Supercritical Conditions," *AIAA Journal* Vol. 55, 2017, p. 9.

[153] Zong, N., Meng, H., Hsieh, S.-Y., and Yang, V., "A numerical study of cryogenic fluid injection and mixing under supercritical conditions," *Physics of Fluids* Vol. 16, No. 12, 2004, pp. 4248-4261.

[154] Meng, H., Hsiao, G., Yang, V., and Shuen, J., "Transport and dynamics of liquid oxygen droplets in supercritical hydrogen streams," *Journal of Fluid Mechanics* Vol. 527, 2005, pp. 115-139.

[155] Yu, M. H., and Monkewitz, P. A., "The effect of nonuniform density on the absolute instability of two-dimensional inertial jets and wakes," *Physics of Fluids A: Fluid Dynamics* Vol. 2, No. 7, 1990, pp. 1175-1181.

[156] Brown, G. L., and Roshko, A., "On density effects and large structure in turbulent mixing layers," *Journal of Fluid Mechanics* Vol. 64, No. 4, 1974, pp. 775-816.

[157] Zhang, L., Choi, J. Y., and Yang, V., "Supersonic combustion and flame stabilization of coflow ethylene and air with splitter plate," *Journal of Propulsion and Power* Vol. 31, No. 5, 2015, pp. 1242-1255.

[158] Panda, J., and McLaughlin, D., "Experiments on the instabilities of a swirling jet," *Physics of Fluids* Vol. 6, No. 1, 1994, pp. 263-276.

[159] Lu, X., Wang, S., Sung, H.-G., Hsieh, S.-Y., and Yang, V., "Large-eddy simulations of turbulent swirling flows injected into a dump chamber," *Journal of Fluid Mechanics* Vol. 527, 2005, pp. 171-195.

[160] Ho, C.-M., and Huerre, P., "Perturbed free shear layers," *Annual Review of Fluid Mechanics* Vol. 16, No. 1, 1984, pp. 365-422.

[161] Zhang, L., and Yang, V., "Flow Dynamics and Mixing of a Transverse Jet in Crossflow—Part I: Steady Crossflow," *Journal of Engineering for Gas Turbines and Power* Vol. 139, No. 8, 2017, p. 082601.

[162] Zhang, L., and Yang, V., "Flow Dynamics and Mixing of a Transverse Jet in Crossflow—Part II: Oscillating Crossflow," *Journal of Engineering for Gas Turbines and Power* Vol. 139, No. 8, 2017, p. 082602.

[163] Zhang, L., Wang, X., Li, Y., Yeh, S.-T., and Yang, V., "Supercritical fluid flow dynamics and mixing in gas-centered liquid-swirl coaxial injectors," *Physics of Fluids* Vol. 30, No. 7, 2018, p. 075106.

[164] Wang, X., Huo, H., Wang, Y., and Yang, V., "Comprehensive study of cryogenic fluid dynamics of swirl injectors at supercritical conditions," *AIAA Journal* Vol. 55, No. 9, 2017, pp. 3109-3119.

[165] Balance, H. C., Bibik, O., Cook, T. S., Danczyk, S., Schumaker, S. A., Yang, V., and Lieuwen, T. C., "Optical Diagnostics in a High-Pressure Combustor with Gaseous Oxygen and Kerosene," *Journal of Propulsion and Power* Vol. 1, 2018, p. 13.

[166] Wang, X., and Yang, V., "Supercritical mixing and combustion of liquid-oxygen/kerosene bi-swirl injectors," *Journal of Propulsion and Power* Vol. 33, No. 2, 2016, pp. 316-322.

[167] Wang, X., Zhang, L., Li, Y., Yeh, S.-T., and Yang, V., "Supercritical combustion of gas-centered liquid-swirl coaxial injectors for staged-combustion engines," *Combustion and Flame* Vol. 197, 2018, pp. 204-214.

[168] Wang, X., Yeh, S.-T., Chang, Y.-H., and Yang, V., "A high-fidelity design methodology using LES-based simulation and POD-based emulation: A case study of swirl injectors," *Chinese Journal of Aeronautics* Vol. 31, No. 9, 2018, pp. 1855-1869.

[169] Crocco, L., and Cheng, S.-I., *Theory of combustion instability in liquid propellant rocket motors*: Cambridge University Press, 1956.

[170] Huang, Y., Sung, H.-G., Hsieh, S.-Y., and Yang, V., "Large-eddy simulation of combustion dynamics of lean-premixed swirl-stabilized combustor," *Journal of Propulsion and Power* Vol. 19, No. 5, 2003, pp. 782-794.

[171] Polifke, W., Poncet, A., Paschereit, C., and Döbbeling, K., "Reconstruction of acoustic transfer matrices by instationary computational fluid dynamics," *Journal of Sound and Vibration* Vol. 245, No. 3, 2001, pp. 483-510.

[172] Evesque, S. p., and Polifke, W., "Low-Order Acoustic Modelling for Annular Combustors: Validation and Inclusion of Modal Coupling," *ASME Turbo Expo 2002: Power for Land, Sea, and Air*. American Society of Mechanical Engineers, 2002, pp. 321-331.

[173] Munipalli, R., Zhu, X., Menon, S., and Hesthaven, J., "Model reduction opportunities in detailed simulations of combustion dynamics," *52nd Aerospace Sciences Meeting*. 2014.

[174] Huang, C., Anderson, W. E., and Merkle, C., "Exploration of POD-Galerkin Techniques for Developing Reduced Order Models of Nonlinear Euler Equations," *55th AIAA Aerospace Sciences Meeting*, AIAA Paper 2017-0378, 2017.

[175] Harrje, D. T., "Liquid propellant rocket combustion instability," 1972.

[176] Culick, F. E., and Yang, V., "Overview of combustion instabilities in liquid-propellant rocket engines," *Liquid Rocket Engine Combustion Instability*. Vol. 169, 1995, pp. 3-37.

[177] Komarek, T., and Polifke, W., "Impact of swirl fluctuations on the flame response of a perfectly premixed swirl burner," *Journal of Engineering for Gas Turbines and Power* Vol. 132, No. 6, 2010, p. 061503.

[178] Polifke, W., "Black-box system identification for reduced order model construction," *Annals of Nuclear Energy* Vol. 67, 2014, pp. 109-128.

[179] Föller, S., and Polifke, W., "Advances in identification techniques for aero-acoustic scattering coefficients from large eddy simulation," *18th International Congress on Sound and Vibration (ICSV18)*. 2011.

[180] Subramanian, P., Blumenthal, R. S., Polifke, W., and Sujith, R., "Distributed time lag response functions for the modelling of combustion dynamics," *Combustion Theory and Modelling* Vol. 19, No. 2, 2015, pp. 223-237.

[181] Bauerheim, M., Ndiaye, A., Constantine, P., Iaccarino, G., Moreau, S., and Nicoud, F., "Uncertainty quantification of thermo-acoustic instabilities in annular combustors," *Proceedings of the Summer Program*. 2014, pp. 209-218.

[182] Silva, C. F., Magri, L., Runte, T., and Polifke, W., "Uncertainty quantification of growth rates of thermoacoustic instability by an adjoint Helmholtz solver," *Journal of Engineering for Gas Turbines and Power* Vol. 139, No. 1, 2017, p. 011901.

[183] Bendat, J. S., and Piersol, A. G., *Random data: analysis and measurement procedures*: John Wiley & Sons, 2011.

[184] Zhao, P., and Yu, B., "On model selection consistency of Lasso," *Journal of Machine learning research* Vol. 7, No. Nov, 2006, pp. 2541-2563.

[185] Tibshirani, R., "Regression shrinkage and selection via the lasso," *Journal of the Royal Statistical Society. Series B*, 1996, pp. 267-288.

[186] Friedman, J., Hastie, T., and Tibshirani, R., *The elements of statistical learning*: Springer series in statistics Springer, Berlin, 2001.

[187] Gelman, A., Carlin, J. B., Stern, H. S., Dunson, D. B., Vehtari, A., and Rubin, D. B., *Bayesian data analysis*: CRC press Boca Raton, FL, 2014.

[188] Park, T., and Casella, G., "The bayesian lasso," *Journal of the American Statistical Association* Vol. 103, No. 482, 2008, pp. 681-686.

[189] Wang, X., Wang, Y., and Yang, V., "Geometric Effects on Liquid Oxygen/Kerosene Bi-Swirl Injector Flow Dynamics at Supercritical Conditions," *AIAA Journal* Vol. 55, No. 10, 2017, pp. 3467-3475.

[190] Dowling, A. P., "The calculation of thermoacoustic oscillations," *Journal of sound and vibration* Vol. 180, No. 4, 1995, pp. 557-581.

[191] Dowling, A. P., and Stow, S. R., "Acoustic analysis of gas turbine combustors," *Journal of propulsion and power* Vol. 19, No. 5, 2003, pp. 751-764.

[192] Camporeale, S., Fortunato, B., and Campa, G., "A finite element method for three-dimensional analysis of thermo-acoustic combustion instability," *Journal of Engineering for Gas Turbines and Power* Vol. 133, No. 1, 2011, p. 011506.

[193] Nicoud, F., Benoit, L., Sensiau, C., and Poinsot, T., "Acoustic modes in combustors with complex impedances and multidimensional active flames," *AIAA Journal* Vol. 45, No. 2, 2007, pp. 426-441.

[194] Wolf, P., Staffelbach, G., Gicquel, L. Y., Müller, J.-D., and Poinsot, T., "Acoustic and large eddy simulation studies of azimuthal modes in annular combustion chambers," *Combustion and Flame* Vol. 159, No. 11, 2012, pp. 3398-3413.

[195] Marble, F., and Candel, S., "Acoustic disturbance from gas non-uniformities convected through a nozzle," *Journal of Sound and Vibration* Vol. 55, No. 2, 1977, pp. 225-243.

[196] Stow, S., Dowling, A., and Hynes, T., "Reflection of circumferential modes in a choked nozzle," *Journal of Fluid Mechanics* Vol. 467, 2002, pp. 215-239.

[197] Lamarque, N., and Poinsot, T., "Boundary conditions for acoustic eigenmode computations in gas turbine combustion chambers," *AIAA Journal* Vol. 46, No. 9, 2008, p. 2282.

[198] Wang, X., and Yang, V., "Supercritical Mixing and Combustion of Liquid-Oxygen/Kerosene Bi-Swirl Injectors," *Journal of Propulsion and Power* Vol. 33 (2), 2017, pp. 316-332.

[199] Wang, X., Li, Y., Wang, Y., and Yang, V., "Near-Field Flame Dynamics of Liquid Oxygen/Kerosene Bi-Swirl Injections at Supercritical Conditions," *Combustion and Flame*.

[200] Lieuwen, T., "Modeling premixed combustion-acoustic wave interactions: A review," *Journal of propulsion and power* Vol. 19, No. 5, 2003, pp. 765-781.

[201] Magina, N., Shin, D.-H., Acharya, V., and Lieuwen, T., "Response of non-premixed flames to bulk flow perturbations," *Proceedings of the Combustion Institute* Vol. 34, No. 1, 2013, pp. 963-971.

[202] Balasubramanian, K., and Sujith, R., "Non-normality and nonlinearity in combustion–acoustic interaction in diffusion flames," *Journal of Fluid Mechanics* Vol. 594, 2008, pp. 29-57.

[203] Tyagi, M., Jamadar, N., and Chakravarthy, S., "Oscillatory response of an idealized two-dimensional diffusion flame: Analytical and numerical study," *Combustion and Flame* Vol. 149, No. 3, 2007, pp. 271-285.

[204] Li, Y., Wang, X., Mak, S., Yeh, S.-T., Lin, L.-H., Wu, C. F. J., and Yang, V., "A Two-stage Transfer Function Identification Methodology and Its Applications to Bi-swirl Injectors," *53rd AIAA/SAE/ASEE Joint Propulsion Conference*, AIAA Paper 2017-4933, 2017.

[205] Multiphysics, C., "v. 5.2," *COMSOL AB, Stockholm, Sweden*, 2015.

[206] Lieuwen, T. C., *Unsteady combustor physics*: Cambridge University Press, 2012.

[207] Rubinsky, V. R., "Combustion instability in the RD-0110 engine," *Progress in Astronautics and Aeronautics* Vol. 169, 1995, pp. 89-112.

[208] Lieuwen, T. C., and Yang, V., eds. *Combustion instabilities in gas turbine engines(operational experience, fundamental mechanisms and modeling)*: Vol. 210, Progress in Astronautics and Aeronautics, AIAA, Reston, VA, 2005.